Tailoring magnetic phenomena and disorder in ultra-thin films with He^+ irradiation

Johannes Wilhelmus van der Jagt

To cite this version:

Johannes Wilhelmus van der Jagt. Tailoring magnetic phenomena and disorder in ultra-thin films with He^+ irradiation. Condensed Matter [cond-mat]. Université Paris-Saclay, 2023. English. NNT : 2023UPAST045 . tel-04085644

HAL Id: tel-04085644
https://theses.hal.science/tel-04085644v1
Submitted on 29 Apr 2023

Tailoring magnetic phenomena and disorder in ultra-thin films with He^+ irradiation

Contrôle des propriétés magnétiques et du désordre dans des couches ultra-minces par irradiation par des ions He^+

Thèse de doctorat de l'université Paris-Saclay

École doctorale n°575, electrical, optical, bio : physics and engineering (EOBE)
Spécialité de doctorat : Physique
Graduate School : Sciences de l'ingénierie et des systèmes.
Référent : Faculté des sciences d'Orsay

Thèse préparée dans l'unité de recherche **Centre de Nanosciences et de Nanotechnologies (CNRS, Université Paris-Saclay)**, sous la direction de **Dafiné RAVELOSONA**, directeur de recherche et la co-direction de **Liza HERRERA DIEZ**, chargée de recherche

Thèse soutenue à Paris-Saclay, le 27 mars 2023, par

Johannes Wilhelmus VAN DER JAGT

Composition du jury

Membres du jury avec voix délibérative

André THIAVILLE Directeur de Recherche, Laboratoire de Physique des Solides, Université Paris-Saclay	Président
Gilles GAUDIN Directeur de Recherche, CEA SPINTEC, Université Grenoble-Alpes	Rapporteur & Examinateur
Laura THEVENARD Directrice de Recherche, INSP, Sorbonne Université	Rapporteure & Examinatrice
Gianfranco DURIN Professeur, Instituto Nazionale di Ricerca Metrologica	Examinateur
Joo-Von KIM Directeur de Recherche, C2N, Université Paris-Saclay, CNRS	Examinateur

THESE DE DOCTORAT

NNT : 2023UPAST045

université
PARIS-SACLAY

ÉCOLE DOCTORALE
Physique et ingénierie :
Electrons, Photons,
Sciences du vivant (EOBE)

Titre : Contrôle des propriétés magnétiques et du désordre dans des couches ultra-minces par irradiation par des ions He$^+$

Mots clés : irradiation ionique, parois magnetiques, mouvement de parois, couches ultra-minces, magnetisme, spintronique

Résumé : Les dispositifs spintroniques promettent des améliorations significatives par rapport aux technologies CMOS actuelles en termes d'efficacité, de vitesse et de consommation d'énergie pour des applications telles que le stockage de données, la logique et le calcul neuromorphique. En particulier dans les dispositifs tels que les MRAMs (magnetic random access memory) ou ceux basés sur le mouvement des parois magnétiques (c'est-à-dire l'interface entre les domaines magnétiques), l'un des principaux challenges concerne l'optimisation des paramètres magnétiques tels que l'anisotropie et la réduction du désordre structural présent dans les matériaux et dispositifs. Dans cette thèse, nous abordons ces problèmes en utilisant l'irradiation par des ions légers. Des ions He$^+$ à haute énergie sont utilisés pour déplacer à l'echelle atomique les atomes du réseau cristallin dans les matériaux magnétiques, ce qui entraîne un réarrangement du réseau et une modification des propriétés magnétiques des matériaux. Dans la première partie de cette thèse, nous montrons que l'irradiation par des ions He$^+$ peut être utilisée pour moduler plusieurs paramètres magnétiques dans des films ultra-minces. Dans la deuxième partie de cette thèse, nous utilisons l'irradiation par des ions He$^+$ pour réduire le désordre intrinsèque du matériau et le désordre extrinsèque induit par les techniques de nanofabrication. Plus précisément, dans la première partie, nous étudions comment l'irradiation avec des ions He$^+$ à température modérée peut induire la cristallisation d'un film ultramince amorphe de W/CoFeB/MgO et montrons que nous pouvons obtenir une anisotropie magnétique similaire ou supérieure par rapport à un procédé de recuit à haute température. Nous montrons également comment l'irradiation de films ultraminces de W/CoFeB/MgO pré-cristallisés peut moduler les propriétés magnétiques interfaciales et améliorer le mouvement des parois magnétiques. Nous présentons en outre des preuves que l'efficacité de la commutation tout-optique de l'aimantation dans les ferrimagnétiques synthétiques Co/Gd peut être améliorée de 30% et que la magnétostriction des multicouches Ni/Fe peut être supprimée par irradiation par des ions He$^+$. Dans la deuxième partie, nous montrons que le désordre à l'échelle nanométrique dans le W/CoFeB/MgO cristallisé peut être revelé en étudiant le mouvement des parois magnétiques et que les échantillons cristallisés par irradiation ionique présentent une réduction du désordre à l'échelle nanométrique entrainant une augmentation de la vitesse des parois magnétiques. Nous soulignons en particulier que le contrôle du désordre à l'échelle nanométrique est un facteur essentiel pour les dispositifs spintroniques basés sur le mouvement des parois magnétiques. Même dans des échantillons ayant des propriétés magnétiques similaires, le désordre à l'échelle nanométrique peut induire des changements significatifs du mouvement de parois magnétiques. Les défauts extrinsèques, qui peuvent être générés par les techniques de nanofabrication, réduisent également le mouvement de parois magnétiques. A la fin de cette thèse, nous montrons que l'interaction entre les défauts extrinsèques et les parois magnétiques peut être minimisée et même supprimée par une irradiation locale avec des ions He$^+$ sur les bords des nanostructures. Les parois magnétiques qui se déplacent dans les dispositifs dont les bords sont irradiés ne sont plus influencées par les défauts de bord et se déplacent à la même vitesse que dans un film continu. Nous montrons également que le "patterning" magnétique sans gravure physique peut créer des structures avec un effet de bord considérablement réduit. En conclusion, les résultats de cette thèse montrent que l'irradiation par des ions He$^+$ est un outil puissant permettant de moduler les propriétés des matériaux magnétiques et de réduire les défauts intrinsèques et extrinsèques de tout dispositif spintronique.

université
PARIS-SACLAY

ÉCOLE DOCTORALE
Physique et ingénierie :
Electrons, Photons,
Sciences du vivant (EOBE)

Title : Tailoring magnetic phenomena and disorder in ultra-thin films with He$^+$ irradiation

Keywords : ion irradiation, magnetic domain walls, domain wall motion, ultra-thin films, magnetism, spintronics

Abstract : Spintronic devices promise significant improvement over current CMOS-based technology in terms of efficiency, speed, and energy consumption for applications such as data storage, logic, and neuromorphic computing. Particularly in devices such as magnetic random access memory or those based on the motion of magnetic domain walls (i.e., the interface between magnetic domains), one of the main challenges is related to the optimization of magnetic parameters such as anisotropy and the reduction of disorder. In this thesis, we tackle these problems by employing light ion irradiation. A high-energy He$^+$ ion is used to induce interatomic displacements of lattice atoms in magnetic materials, which can result in a rearrangement of the local structure, affecting the magnetic properties of the materials. In the first part of this thesis, we show that He$^+$ ion irradiation can be used to tune several magnetic properties in ultrathin films. In the second part of this thesis, we use He$^+$ ion irradiation to tune the intrinsic material disorder and the extrinsic disorder induced by the patterning processes. Specifically, in part one, we study how irradiation with light ions at moderate temperatures can result in the crystallization of an amorphous W/CoFeB/MgO ultrathin film and show that we can achieve similar or improved magnetic anisotropy compared to a standard annealing process at high temperatures. We also show how irradiation of pre-crystallized W/CoFeB/MgO ultrathin films can tune the interfacial magnetic properties and enhance domain wall motion. We further present evidence that the efficiency of all-optical switching of magnetization in Co/Gd synthetic ferrimagnets can be improved by 30% and that the magnetostriction of Ni/Fe multilayers can be efficiently tuned by light ion irradiation. In part two, we show that the nanoscale disorder in crystallized W/CoFeB/MgO can be revealed by studying domain wall motion and that samples crystallized by ion irradiation show reduced nanoscale disorder for efficient domain wall motion. We particularly highlight that the nanoscale disorder is an essential factor for spintronic devices based on domain wall motion. Even in samples with similar magnetic properties, nanoscale disorder can induce significant changes in domain wall motion. Extrinsic defects, which can be generated by lithography techniques, also strongly reduce domain wall motion. Towards the end of this thesis, we show that the interaction between extrinsic defects and domain walls can be tuned and even quenched through local irradiation with light ions at the edges of nanostructures. Domain walls that move through devices with irradiated edges show almost no reduction in velocity caused by edge defects and propagate as fast as in non-patterned films. We also show that magnetic patterning without physical etching can create structures with a significantly reduced edge effect. In conclusion, the results in this thesis show that irradiation with He$^+$ ions is a versatile tool to engineer the properties of magnetic materials and to reduce the intrinsic and extrinsic defects in any spintronic device.

Alle kritiek is goddank nutteloos. De schrijvers zijn te eigenwijs, de lezers te dom om er hun voordeel mee te doen.
Jan Greshoff, Dutch author and literary scholar, 1888-1971

Acknowledgements

La gratitude est le secret de la vie.
Albert Schweitzer

After three(-ish) years of hard work and a good 140 pages or so later, this journey comes to an end. Although my name is on the front of this manuscript, by no means am I its sole contributor. There is a large number of people that I need to thank for their contributions, each of them valuable, as without even a single one of them, the pages that follow would look completely different.

I would like to start with a group of people that have had arguably the biggest contribution to this work; my supervisors: Dafiné, Liza, Roméo, and Mamour. Dafiné, it was a real pleasure and honor to be able to work with you. Your optimistic, can-do attitude (and love for celebrations) hasn't made a single moment in these three years boring. I am particularly grateful for your open-door policy (which I happily abused on more than one occasion) and frequent opportunities for discussion about all manners, big or small, scientific or industrial, professional or private. Add working together in a dynamic start-up to this mix, and my experience has only become more unique and interesting, for which I am ever grateful. Liza, although on a scientific basis we might not have worked together very intensely, your input, (sometimes brutal) honesty, and do-it-yourself mindset have been instrumental in the advancement of my experiments. Whether it is building a new Kerr microscope from scratch, or quickly building a rig to move coils around, no challenge was to big with your input on my side. Roméo, even though you only just finished your own PhD when you became involved with mine, it did certainly not feel that way. Not only has your recent experience been a boon, but also your hands-on approach to fixing issues has saved me from awkwardly staring at a broken irradiation machine on more than one occasion. While perhaps a touch careless (R.I.P. to the four AGFM probes), I certainly learned to be more decisive when fixing issues, both experimentally as well as in my personal life. Your name should also be mentioned in many of the paragraphs that follow, as I am happy to say that outside of work we have become good friends. Your support and the many distractions have helped me through some of the harder parts of my PhD. I would also be remiss not to mention the fact that you agreed to correct this manuscript after you had already left Spin-Ion, for which I can only express my gratitude and admiration. Mamour, while you left Spin-Ion only half a year into my PhD, your contribution to this work should not be understated. Your expertise in materials science and ion irradiation have been essential for the development of my scientific knowledge in the early stages of my PhD, and I always regret not having been able to continue these discussions to the end. Not to mention, your patience in teaching me the ropes of the irradiation machine has been impressive, and I can only aspire to channel this patience whenever I am on the giving end of such training.

A big thank you also goes to the members of the jury; first to Gilles Gaudin and Laura Thevenard for accepting the arduous task of reviewing this manuscript. I am aware that reviewing a manuscript takes a long time, and thus I can only be grateful for all your efforts in improving the work presented in the following. Second to Gianfranco Durin, Joo-Von Kim, André Thiaville, and Tiffany Santos for accepting to be examiners of my defense. I immensely enjoyed our discussions, which have only widened my scope on the potential of the work presented here.

The nature of modern science is collaboration, which has been a cornerstone of this thesis. Hence,

I will now try[1] to thank everyone that has been involved, in one way or another, in the multitude of collaborations that led to the results of my thesis. To start with the various researchers of the C2N. Nicolas, I would call you the expert of MOKE and Kerr microscopy, but I know you hate that term. Nonetheless, your *expertise* has kick-started my understanding of Kerr microscopy, which resulted in many of the measurements presented here. I would also like to thank you for taking the time to answer my many Kerr microscopy related questions, even after you had left the C2N. Dominique, I have always enjoyed the time we spent together at the FIB (even though the majority of the time it has been down). Your always useful comments about the design of my irradiation patterns have made my experimental preparations significantly easier. I would also like to thank Jean-Luc, David, Teo, Christophe, and Abdou for their help in the cleanroom, saving me from headlessly running around while trying to make devices. A very special thank you goes to Maryam. You have not only dealt with my antics in the cleanroom while making devices (cleanroom disco not excluded), but you have also become one of my best friends. Thank you for distracting and supporting me when things got difficult, celebrating with me when things were working well, for allowing me to vent frustrations, and all-in-all just for being a good friend.

The collaborative nature of this work goes beyond the C2N. To start with Vincent Jeudy and André Thiaville from LPS. Vincent, thank you for all the nice discussions about domain wall motion. Without your help in the analysis of some of the results, this thesis would contain a lot less physics! André, not only should I thank you for being part of the jury, but also for the many discussions we have had these past few years. I don't think I have ever met someone more passionate about science than you, which has reinvigorated me every time I came to LPS for a discussion or BLS measurements. When talking about BLS measurements, an honorable thank you should also go to Mohamed Belmeguenai from LSPM. A big thank you also goes to Luis Lopez Diaz from the University of Salamanca, Stefania Pizzini from Institut Néel, and Reinoud Lavijsen from TU/e, who have hosted me during my secondments in Salamanca, Grenoble, and Eindhoven. It was a pleasure to work in your labs, and I must thank you, not only for all the nice discussions we have had, but also for taking the time in accommodating me in your labs in sometimes short time-frames. I would also like to thank Randy Dumas from Quantum Design and Fredrik Magnusson from NanOsc for performing FMR measurements, Thomas Hauet from Institut Jean Lamour for performing SQUID-VSM measurements, and Alessio Lamperti from CNR-IMM for performing the ToF-SIMS measurements for the results in Section 3.2 of this thesis.

Next I would like to move on to my other colleagues at Spin-Ion Technologies; Benjamin, Elmer, Maïkane, Song, and Corina. I am super grateful for the opportunity to work in such a dynamic start-up with all of you. I should particularly thank Benjamin and Elmer, not only for their help as colleagues, but for their support as friends. A special thank you goes to Corina, not only for *helping* (read forcing) me to learn French by refusing to speak English (merci!), but also for your tireless efforts in helping me get settled in la France and dealing with the insane administration that comes along with moving abroad. An honorable mention also goes to Julien, whose internship I had the pleasure to supervise. Although our experiments did not work our as planned, I am very happy to have been able to work with such an eager and fast learning student.

Spin-Ion is hosted at the C2N, meaning I had the opportunity to interact with many fellow PhD students, post-docs, and researchers in the academic scene. In particular I would like to thank everyone from the Integnano group; Damien, Tanvi, Marie, Clément, Atreya, Kamel, Rohit, Subhajit, Adrien, Thomas, and former members Xing, Axel, Tifenn, Maxence, Bogdan, and Thibaut. Thank you for the countless big and small interactions that we have had on a daily basis, it was a pleasure to work among you.

I consider myself extremely lucky, because I had the chance to do my PhD in a European ITN called MagnEFi. Not only has this stimulated many collaborations, some of which can be found in Chapter 5 of this thesis, but I have also gained many new friends in the process. I should start off by thanking Liza and Clare, who poured their life and soul into managing this project. It

---

[1] I am lucky to have been able to work with so many people, and hence it is likely I might forget some people. To all those who feel addressed by this: thank you!

was not easy, especially with Covid at the beginning of the project, but your obvious passion and commitment have made this a very successful project. I must also thank all the partners of the ITN, in particular my fellow ESRs; Rohit, Subhajit, Adriano, Jintao, Golam, Adithya, Beatrice, Adrien, Pingzhi, Mouad, Sreeveni, Cristina, Mandy, and Giovanni. Even though we are all spread-out throughout Europe, it was a pleasure to go through the ups and downs of a PhD project together, and I am very glad that I can call each and everyone of you my friend.

The last group of people that I need to thank is my family and friends. Even though they did not have a scientific contribution to this thesis, it would not exist without their support. In particular I should thank Lucas for our many gaming sessions and “apes together strong” mentality which have kept me going when things got tough, and everyone from the *little* big band Orsay for their musical distractions. My last but not least thank you goes to my family; Papa en Mama, Jorin en Tamara, en Lysa en Mike. Zonder jullie was ik nooit zo ver gekomen.

Thank you, merci, dankjewel!

Résumé

Les dispositifs spintroniques promettent des améliorations significatives par rapport aux technologies CMOS actuelles en termes d'efficacité, de vitesse et de consommation d'énergie pour des applications telles que le stockage de données, la logique et le calcul neuromorphique. En particulier dans les dispositifs tels que les MRAMs (magnetic random access memory) ou ceux basés sur le mouvement des parois magnétiques (c'est-à-dire l'interface entre les domaines magnétiques), l'un des principaux challenges concerne l'optimisation des paramètres magnétiques tels que l'anisotropie et la réduction du désordre structural présent dans les matériaux et dispositifs. Dans cette thèse, nous abordons ces problèmes en utilisant l'irradiation par des ions légers. Des ions He^+ à haute énergie sont utilisés pour déplacer à l'echelle atomique les atomes du réseau cristallin dans les matériaux magnétiques, ce qui entraîne un réarrangement du réseau et une modification des propriétés magnétiques des matériaux. Dans la première partie de cette thèse, nous montrons que l'irradiation par des ions He^+ peut être utilisée pour moduler plusieurs paramètres magnétiques dans des films ultra-minces. Dans la deuxième partie de cette thèse, nous utilisons l'irradiation par des ions He^+ pour réduire le désordre intrinsèque du matériau et le désordre extrinsèque induit par les techniques de nanofabrication. Plus précisément, dans la première partie, nous étudions comment l'irradiation avec des ions He^+ à température modérée peut induire la cristallisation d'un film ultra-mince amorphe de W/CoFeB/MgO et montrons que nous pouvons obtenir une anisotropie magnétique similaire ou supérieure par rapport à un procédé de recuit à haute température. Nous montrons également comment l'irradiation de films ultraminces de W/CoFeB/MgO pré-cristallisés peut moduler les propriétés magnétiques interfaciales et améliorer le mouvement des parois magnétiques. Nous présentons en outre des preuves que l'efficacité de la commutation tout-optique de l'aimantation dans les ferrimagnétiques synthétiques Co/Gd peut être améliorée de 30% et que la magnétostriction des multicouches Ni/Fe peut être supprimée par irradiation par des ions He^+. Dans la deuxième partie, nous montrons que le désordre à l'échelle nanométrique dans le W/CoFeB/MgO cristallisé peut être revelé en étudiant le mouvement des parois magnétiques et que les échantillons cristallisés par irradiation ionique présentent une réduction du désordre à l'échelle nanométrique entrainant une augmentation de la vitesse des parois magnétiques. Nous soulignons en particulier que le contrôle du désordre à l'échelle nanométrique est un facteur essentiel pour les dispositifs spintroniques basés sur le mouvement des parois magnétiques. Même dans des échantillons ayant des propriétés magnétiques similaires, le désordre à l'échelle nanométrique peut induire des changements significatifs du mouvement de parois magnétiques. Les défauts extrinsèques, qui peuvent être générés par les techniques de nanofabrication, réduisent également le mouvement de parois magnétiques. A la fin de cette thèse, nous montrons que l'interaction entre les défauts extrinsèques et les parois magnétiques peut être minimisée et même supprimée par une irradiation locale avec des ions He^+ sur les bords des nanostructures. Les parois magnétiques qui se déplacent dans les dispositifs dont les bords sont irradiés ne sont plus influencées par les défauts de bord et se déplacent à la même vitesse que dans un film continu. Nous montrons également que le “patterning” magnétique sans gravure physique peut créer des structures avec un effet de bord considérablement réduit. En conclusion, les résultats de cette thèse montrent que l'irradiation par des ions He^+ est un outil puissant permettant de moduler les propriétés des matériaux magnétiques et de réduire les défauts intrinsèques et extrinsèques de tout dispositif spintronique.

Abstract

Spintronic devices promise significant improvement over current CMOS-based technology in terms of efficiency, speed, and energy consumption for applications such as data storage, logic, and neuromorphic computing. Particularly in devices such as magnetic random access memory or those based on the motion of magnetic domain walls (i.e., the interface between magnetic domains), one of the main challenges is related to the optimization of magnetic parameters such as anisotropy and the reduction of disorder. In this thesis, we tackle these problems by employing light ion irradiation. A high-energy He^+ ion is used to induce interatomic displacements of lattice atoms in magnetic materials, which can result in a rearrangement of the local structure, affecting the magnetic properties of the materials. In the first part of this thesis, we show that He^+ ion irradiation can be used to tune several magnetic properties in ultra-thin films. In the second part of this thesis, we use He^+ ion irradiation to tune the intrinsic material disorder and the extrinsic disorder induced by the patterning processes. Specifically, in part one, we study how irradiation with light ions at moderate temperatures can result in the crystallization of an amorphous W/CoFeB/MgO ultrathin film and show that we can achieve similar or improved magnetic anisotropy compared to a standard annealing process at high temperatures. We also show how irradiation of pre-crystallized W/CoFeB/MgO ultrathin films can tune the interfacial magnetic properties and enhance domain wall motion. We further present evidence that the efficiency of all-optical switching of magnetization in Co/Gd synthetic ferrimagnets can be improved by 30% and that the magnetostriction of Ni/Fe multilayers can be efficiently tuned by light ion irradiation. In part two, we show that the nanoscale disorder in crystallized W/CoFeB/MgO can be revealed by studying domain wall motion and that samples crystallized by ion irradiation show reduced nanoscale disorder for efficient domain wall motion. We particularly highlight that the nanoscale disorder is an essential factor for spintronic devices based on domain wall motion. Even in samples with similar magnetic properties, nanoscale disorder can induce significant changes in domain wall motion. Extrinsic defects, which can be generated by lithography techniques, also strongly reduce domain wall motion. Towards the end of this thesis, we show that the interaction between extrinsic defects and domain walls can be tuned and even quenched through local irradiation with light ions at the edges of nanostructures. Domain walls that move through devices with irradiated edges show almost no reduction in velocity caused by edge defects and propagate as fast as in non-patterned films. We also show that magnetic patterning without physical etching can create structures with a significantly reduced edge effect. In conclusion, the results in this thesis show that irradiation with He^+ ions is a versatile tool to engineer the properties of magnetic materials and to reduce the intrinsic and extrinsic defects in any spintronic device.

Table of Contents

Introduction

With the advent of big data, quantum computing, and artificial intelligence, information technologies are put under increasing pressure. The drive for ever increasing data storage capacity, speed, and low energy consumption poses a great challenge for the development of next generation storage and processing devices. A promising class of devices that can address this challenge is found in the field of spintronics.

In spintronics, we use not only the charge of an electron, but also an additional degree of freedom - their magnetic moment, or spin - to perform operations. The field of spintronics was kick-started by the discovery of the giant magnetoresistance (GMR) [1,2], the discovery of which resulted in the 2007 Nobel prize in Physics for Albert Fert and Peter Grünberg for revolutionizing data storage technology by vastly improving the storage density and efficiency of hard disk drives. Further developments came with the advent of the tunnel magnetoresistance (TMR) [3,4] in so-called magnetic tunnel junctions (MTJ). These breakthroughs led to the development of a new type of memory called magnetic random access memory (MRAM), which, due to its non-volatile data storage, high speed, and low energy consumption, promises to replace many current forms of data storage, such as NOR-Flash, SRAM, DRAM, and even NAND-Flash [5].

MRAM encodes information in cells, each containing a single MTJ. The value of the bit-cell depends on the relative orientation of the magnetic moment of two ferromagnetic (FM) layers within the MTJ. Information can be written to the bit-cell by manipulating the magnetic moment of a FM through the spin-transfer torque (STT) [6,7] and spin-orbit torque (SOT) [8]. While STT-MRAM is already commercially available, SOT-MRAM is still under development. Beyond information storage, MRAM can be integrated into neural networks in a grid-layout, as researchers from Samsung have recently demonstrated [9]. Despite advances in integration, MRAM still faces scalability issues, in particular related to manufacturing, including material disorder and chip defects, which affect the data storage density, data retention time, and yield [10].

Another spintronic device that has been developed along with MRAM is the racetrack memory [11]. Instead of storing information in individually addressable cells, racetrack memory encodes the information in a long strip of magnetic domains, with the value of the bit depending on the direction of the magnetic moment in the domain. The region between these domains, known as the domain wall (DW), can be moved through the strip with STT or SOT currents, effectively moving the domains (or bits) themselves. This type of device is not only interesting for data storage [11–13] but also for logic [14–17] and neural network applications [18–22]. However, like MRAM, DW-racetrack memories exhibit crucial issues. The main roadblock for DW-motion-based devices is disorder, both in the form of intrinsic disorder caused by the growth of the materials used to make the devices, as well as extrinsic disorder that is created by nanofabrication processes. Disorder gives rise to spatial distributions of magnetic properties, which can cause strong pinning. Pinning reduces the efficiency of the entire DW-device, as it requires a minimum current to move the DW forward and introduces randomness in the device which makes it harder to control the DW position. It is clear that the improvement of these applications depends on the ability to accurately control the material disorder and magnetic properties.

This Thesis

In this thesis, we make use of a very powerful technique based on He^+ ion irradiation to improve the performance of MRAM materials and DW-devices through post-growth control of inter-atomic displacements. The materials used in these devices consist of layers of different metallic compounds, typically a heavy metal (HM)/FM/non-magnetic (NM) configuration, where each layer is only a few atoms thick. The magnetic properties of these materials heavily depend on the structure of the interfaces between the different layers. For example, the magnetic anisotropy - important for achieving high data storage density - and Dzyaloshinskii-Moriya interaction - important for achieving fast DW motion - are both highly dependent on the interface structure, and typically improved when the interfaces between the layers are smoother. Interface intermixing, one important form of disorder in these ultra-thin films, thus heavily affects the magnetic properties.

During the irradiation, He^+ ions traverse the material and collide with atoms in the lattice, causing them to be displaced. This process can significantly impact the interface structure of the HM/FM/NM ultra-thin films, giving rise to a modification of the magnetic properties. Since He^+ ions have a low mass, they transfer a low energy to the target atoms, and only inter-atomic displacements are induced without cascade collisions and surface sputtering, making He^+ irradiation the most versatile post-growth technique to control the magnetic properties of ultra-thin films [23].

Ion irradiation of magnetic materials has been used since the discovery by Chappert *et al.* that the magnetic properties of a Co/Pt ultra-thin film can be controlled by He^+ irradiation induced intermixing of the Co/Pt interfaces [24]. Since then, many new challenges have emerged with the development of MRAM and racetrack memory technologies that can be tackled by He^+ irradiation. In this thesis we focus particularly on W/CoFeB/MgO materials, which are archetypical materials in MTJs and DW-motion based devices due to their large TMR, high anisotropy, and low magnetic damping, which increase the efficiency of these devices. As mentioned previously, intrinsic and extrinsic disorder is one of the main showstoppers for the further integration of MRAM and racetrack memory. In this thesis we investigate the possibility to both control order through irradiation induced crystallization and disorder through irradiation induced interface intermixing. More specifically, this thesis aims to address several challenges:

1. Improvement of the crystallization process of W/CoFeB/MgO ultra-thin films by designing a fast He^+ irradiation process at moderate temperature, as the current crystallization processes based on high temperature annealing are plagued with long annealing times and structural damages induced by the large temperatures required.

2. Improvement of the DW motion in W/CoFeB/MgO materials and better understanding of the role of disorder through irradiation induced crystallization and irradiation induced interface intermixing.

3. Improvement of DW motion in W/CoFeB/MgO wires by reducing the influence of extrinsic edge defects through He^+ irradiation.

This thesis is prepared at Spin-Ion Technologies [25], a start-up company originating from the Centre de Nanosciences et de Nanotechnologies (Université Paris-Salcay and CNRS) that develops ion irradiation processes to enhance magnetic materials for semiconductor applications, and is part of an international training network (ITN) funded by the European Union named Magnetism and the effects of Electric Fields (MagnEFi) [26]. Part of the results shown in this thesis will be used by Spin-Ion Technologies to further develop their ion beam processes. Furthermore, the ITN has stimulated many opportunities for collaboration that has allowed us to explore the effects of He^+ irradiation on other spintronic concepts such as all-optical switching, magnetostriction, spin-wave transmission, and magneto-ionics. This thesis will contain the results of several of these collaborations to demonstrate the power of He^+ irradiation.

Outline

Chapter 1 provides an introduction to the main concepts required to understand the various magnetic effects in ultra-thin films. It covers the various magnetic properties present in ultra-thin films, focusing on properties that are dependent on the interfaces between the layers, as these are most susceptible to irradiation. It also explains how magnetic DWs move throughout the layers and how they interact with the disorder in the material. The chapter concludes with an introduction to the various experimental techniques used throughout the thesis to characterize the magnetic properties of the ultra-thin films.

Chapter 2 provides a detailed introduction to the concept of ion irradiation, particularly in magnetic materials. It covers the basic physics of ion-matter interactions and the effect of irradiation on the material structure. It specifically explains how irradiation can be used to induce both ordering and mixing of the atoms in the layers and provides a comprehensive overview of the state of the art regarding irradiation of magnetic materials.

In Chapter 3 we use He^+ irradiation at moderate temperatures to induce crystallization in an amorphous W/CoFeB/MgO ultra-thin film, and investigate how the magnetic properties of such films evolve. We also propose a method to measure the disorder of polycrystalline films using DW motion, and provide evidence that irradiation induced crystallization can result in an optimized nanoscale disorder for easy DW motion.

In Chapter 4 we use He^+ irradiation at room temperature to induce interface intermixing in pre-crystallized W/CoFeB/MgO ultra-films. We investigate how the magnetic properties and disorder of the film evolve with irradiation, and how the DW motion is affected. We also study how the extrinsic disorder in the form of edge effects can be changed with irradiation, resulting in a massive improvement of DW motion due to the absence of edge damage.

In Chapter 5 we show results from two collaborations investigating the effects of He^+ irradiation on other spintronic interfacial phenomena, particularly the all-optical switching of magnetization in a Co/Gd artificial ferrimagnet and the magnetoelasticity of Ni/Fe multi-layers.

Chapter 6 contains a summary of the main results presented in Chapters 3, 4, and 5, and perspectives on further developments based on these results.

Chapter 1

Essential concepts in nanomagnetism and domain wall physics

> *Magnetism, as you recall from physics class, is a powerful force that causes certain things to be attracted to refrigerators.*
> Dave Barry

In this chapter, we introduce the basic underlying theoretical concepts and experimental techniques required to appreciate the results presented in this thesis. We start with an overview of the magnetic interactions that play a role in the material systems treated in this thesis, with a specific focus on thin films. We highlight that the magnetic interactions depend strongly on the local atomic arrangement and that these interactions are thus tunable with techniques that impact the local atomic ordering - such as He^+ irradiation. We will then discuss how the interplay between these interactions results in the formation of domains and domain walls. We explore how domain walls move through systems when external forces are applied to them, with a specific focus on the role that material disorder plays. Finally, we discuss how we can experimentally characterize magnetic materials through magnetometry and imaging techniques.

1.1 Magnetic energies and interactions

1.1.1 An introduction to magnetic ordering and micromagnetism

An atom i in a magnetic material has an intrinsic magnetic moment, also called spin $\mathbf{S}_i$ (in A m^2). The collection of these spins defines the magnetization $\mathbf{M}$ (in A m^{-1}). In *ferromagnets* (FM) like iron (Fe), cobalt (Co), and nickel (Ni), the magnetic moments align parallel to each other, resulting in a net non-zero magnetization. The maximum value of the magnetization, i.e. when all the moments align in the same direction, is called the saturation magnetization $|\mathbf{M}| = M_\mathrm{s}(T)$ and is temperature dependent. Thermal fluctuations compete with the inter-moment interactions, meaning that above the critical ordering temperature T_c, the so-called Curie temperature, the net magnetization is zero. This state ($M_\mathrm{s}\,(T > T_\mathrm{c}) = 0$) is called the *paramagnetic* state. In other materials, like chromium (Cr), manganese (Mn), or nickel-oxide (NiO), the magnetic moments like to align anti-parallel to each other. These materials are called *anti-ferromagnets* (AF), which do not present a net magnetization ($M_\mathrm{s} = 0$). AFs are governed by a different ordering temperature called the Néel temperature T_N. Certain material alloys that have AF coupling do present a net magnetization, due to a mismatch in magnetization between the AF coupled sub-lattices of the different magnetic materials. These materials, like cobalt-gadolinium (CoGd), are called *ferrimagnets.* In this thesis we will mainly discuss FM materials, with a brief excursion into ferrimagnetic materials in Chapter 5.

In systems larger than the atomic scale, the behavior of the magnetization can be described with the micromagnetic model. This model is based on a continuum-approximation: the minimum distance over which the magnetization can be varied - the exchange length, typically 2-10 nm for FMs and given by $l_{\mathrm{ex}} = \sqrt{\frac{2A}{\mu_0 M_{\mathrm{s}}^2}}$, where A denotes the strength of the exchange interaction - is larger than the inter-atomic distance. In this model we can describe the magnetization vector $\mathbf{M}(\mathbf{r})$ with spatial coordinates $\mathbf{r}$ as a continuous vector field, instead of treating each individual atomic magnetic moment as a discrete vector. $\mathbf{M}(\mathbf{r})$ varies in direction only, with its value being equal to the saturation magnetization $M_{\mathrm{s}}(T)$. We can then define the reduced magnetization vector $\mathbf{m}(\mathbf{r}) = \mathbf{M}(\mathbf{r})/M_{\mathrm{s}}(T)$.

For the materials studied in this thesis, several interactions compete with each other. The resulting magnetic state can be determined by minimizing the total free energy, to which these interactions contribute. The total free energy can be summarized in the following volume integral [27,28]:

$$E = \int_V \left(\underbrace{-\mu_0 M_{\mathrm{s}} \mathbf{m} \cdot \mathbf{H}_{\mathrm{ext}}}_{\text{Zeeman}} + \underbrace{A \left(\nabla \mathbf{m}\right)^2}_{\text{Heisenberg}} + \underbrace{D \left(\left(\mathbf{m} \cdot \nabla \right) \mathbf{m} \right) - \mathbf{m} \left(\nabla \cdot \mathbf{m} \right)}_{\text{DMI}} + \underbrace{K_{\mathrm{eff}} \sin^2 \left(\theta\right)}_{\text{Anisotropy}} \right) \mathrm{d}V. \tag{1.1}$$

Here $\mathbf{H}_{\mathrm{ext}}$ represents an external applied magnetic field, A is the exchange stiffness constant, D denotes the strength of the Dzyaloshinskii-Moriya interaction (DMI), and K_{eff} is the effective anisotropy constant. In the following, we will examine the terms in Equation 1.1 one by one in more detail.

1.1.2 Zeeman interaction

The first term in Equation 1.1 represents the Zeeman interaction, which describes how the magnetic moments interact with an externally applied magnetic field $\mathbf{H}_{\mathrm{ext}}$. μ_0 represents the vacuum permeability. This term promotes alignment between the magnetic moments and the applied magnetic field, with any deviation of the magnetic moment from the applied field direction incurring an energy penalty.

1.1.3 Exchange interactions

The second and third terms in Equation 1.1 describe two different exchange interactions; the symmetric Heisenberg exchange interaction and the anti-symmetric DMI. Other exchange interactions exist [28], but they do not concern the material systems studied in this thesis and hence they will not be discussed here. The (anti-)symmetric exchange interaction is short ranged, describing the magnetic interactions between atoms. We start by describing the Heisenberg exchange interaction, before moving on to the DMI.

1.1.3.1 Symmetric exchange interaction: the Heisenberg exchange interaction

The symmetric exchange interaction, also called direct exchange or Heisenberg exchange, is an interaction that promotes the alignment of neighboring spins and is represented by the second term in Equation 1.1. This exchange interaction arises due to the interplay between the Coulomb repulsion between electrons on neighboring atoms i and j, and the Pauli exclusion principle, which says that two indistinguishable particles cannot be in the same state. As a result, the two electrons together can be in two different states; a spin triplet and spin singlet state, with either parallel or anti-parallel spins, respectively. The energy difference between these states is governed by an exchange integral J (in J). Expanding this view in a lattice of atoms leads to the Heisenberg Hamiltonian, given by

$$\mathcal{H}_{\mathrm{ex}} = -2 \sum_{i<j} J_{ij} \mathbf{S}_i \cdot \mathbf{S}_j. \tag{1.2}$$

Here J_{ij} is the exchange integral between neighboring atoms i and j, and $\mathbf{S}_i$ and $\mathbf{S}_j$ denote the atomic spins. The sum is taken over all neighboring atoms.[1] Considering only nearest neighboring atoms, J_{ij} can be taken as a constant, J. The sign of J governs the alignment between the spins, with $J > 0$ denoting an FM or parallel state, and $J < 0$ denoting an AF or anti-parallel state.

Going back to the continuum approximation made in the micromagnetic model, we obtain the exchange energy as written in the second term of Equation 1.1. Here, A is the exchange stiffness or exchange constant, given by

$$A \approx \frac{S^2 Z_\mathrm{c}}{a} J, \tag{1.3}$$

with S the spin, Z_c the number of atoms in a unit cell and a the lattice constant. Typical values for the exchange constant in ferromagnetic materials are in the range of 10 - 30 pJ m^{-1}. Note that in the exchange energy term in Equation 1.1, $(\nabla \mathbf{m})^2$ is shorthand for $(\nabla m_x)^2 + (\nabla m_y)^2 + (\nabla m_z)^2$.

1.1.3.2 Anti-symmetric exchange interaction: the Dzyaloshinskii-Moriya interaction

The DMI is an anti-symmetric exchange interaction that promotes perpendicular alignment between neighboring spins, and is represented by the third term in Equation 1.1. The Hamiltonian that governs the DMI is given by

$$\mathcal{H}_\mathrm{DMI} = -\mathbf{D}_{ij} \cdot \left(\mathbf{S}_i \times \mathbf{S}_j\right), \tag{1.4}$$

where $\mathbf{D}_{ij}$ represents the DMI vector. As a result of the cross-product of $\mathbf{S}_i$ and $\mathbf{S}_j$, the DMI promotes rotation of the spins around $\mathbf{D}_{ij}$. In this thesis, we adopt the following sign convention: $D < 0$ ($D > 0$) denotes anti-clockwise (clockwise) rotation of the spins.[2]

There are several mechanisms that cause the appearance of DMI, which depend mostly on the class of materials that is considered. One common property of these material classes is that there must be a broken inversion symmetry. This was first shown by Dzyaloshinskii in 1958 [29] and later expanded upon by Moriya in 1960 [30] for low symmetry crystals, where the DMI is considered as a super-exchange interaction between magnetic atoms. An example of a crystal with DMI is the non-centrosymmetric B20 crystallographic structure, to which materials like FeGe and MnSi belong. However, a low symmetry is not necessarily limited to bulk crystals. Inversion symmetry is broken at interfaces. To describe the appearance of interfacial DMI, two different models are typically used; the Fert-Levy model [31] and the Rashba model [32].

A sketch of the working principles of the Fert-Levy type DMI at the interface between a FM and a non-magnetic (NM) material is shown in Figure 1.1. In the Fert-Levy model, the DMI is mediated through a third atom at distances $\mathbf{r}_i$ and $\mathbf{r}_j$ from the magnetic atoms with spins $\mathbf{S}_i$ and $\mathbf{S}_j$, respectively (Fig. 1.1a). In this view, the DMI constant can be written as

$$\mathbf{D}_\mathrm{ij} \propto V \left(\mathbf{r}_\mathrm{i} \times \mathbf{r}_\mathrm{j}\right), \tag{1.5}$$

where V is a constant that represents the coupling between the electron spin and the atomic lattice, also called spin-orbit coupling (SOC). Equation 1.5 implies that the position of the third atom can control the sign of $\mathbf{D}_{ij}$ - placing the third atom below or above the magnetic atoms inverses the sign of $\mathbf{D}_{ij}$ - as is shown in Figure 1.1b. This means that in systems where the same NM is present at both sides of the FM (e.g. NM/FM/NM), the inversion symmetry is no longer broken and the DMI contributions cancel each other out.[3]

---

[1] Different conventions exist, omitting the factor 2 and/or counting each neighboring pair in the sum twice.

[2] Note that in the literature different conventions exist for the sign of the Hamiltonian. To avoid confusion, we will keep this convention throughout this thesis.

[3] In real systems without inversion symmetry this is not always the case. Franken et al. [33] showed that Pt/Co/Pt stacks can show a measurable DMI depending on the thickness of the top layer, as well as on the growth conditions of the layers.

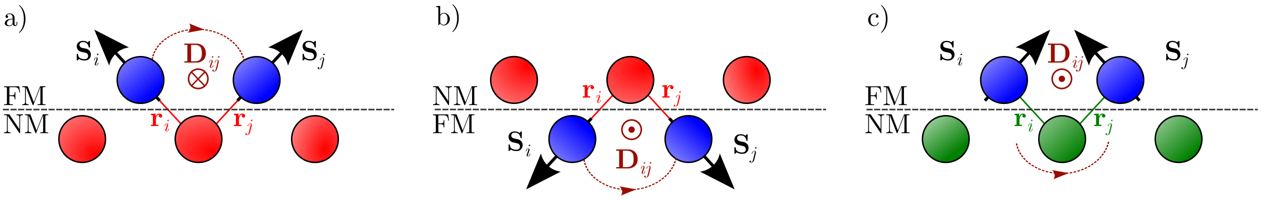

Fig. 1.1: Fert-Levy model for interfacial DMI | Sketch of the interfacial DMI at the interface between a FM (blue) and a NM (red/green) as described in the Fert-Levy model [31]. a) and b) show the cases for two FM/NM interfaces with opposite signs for the DMI vector $\mathbf{D}_{ij}$ (brown) due to the inversion of the NM/FM interface. c) shows the case for a FM/NM interface with a different NM that results in the opposite sign for $\mathbf{D}_{ij}$. $\mathbf{S}_i$ and $\mathbf{S}_j$ represent the spins of the FM atoms. $\mathbf{r}_i$ and $\mathbf{r}_j$ represent the distance between the NM and the FM atom at sites i and j, respectively. Image adapted from Ref. [34].

Furthermore, the significant role that is played by the SOC also impacts the sign and strength of the DMI [30–32]. In a semi-classical description, SOC describes the coupling between the electron spin and its angular momentum due to the electron orbit in the atom. The sign and magnitude of the SOC coupling are material dependent. Heavier atoms typically have larger SOC, since SOC scales with Z^4, with Z the atomic number. This means that the sign of $\mathbf{D}_{ij}$ is not only dependent on the position of the NM atom, but on the type of NM atom as well. This is depicted in Figure 1.1c, where the sign of $\mathbf{D}_{ij}$ is flipped due to an exchanged NM material with opposite SOC.

Typical systems with strong Fert-Levy type iDMI have an interface between a FM and a heavy metal (HM) due to their large SOC. Examples of such interfaces are Pt/Co, Ir/Co, W/Co, and Ta/Co, which are often combined to create samples with large DMI [35].

As mentioned before, Fert-Levy type DMI is not the only interfacial phenomenon which can describe DMI. Rashba type DMI occurs due to so-called Rashba SOC [36,37]. Due to the broken symmetry at an interface, a residual potential can exist. This potential creates an electric field $\mathbf{E} = E\hat{\mathbf{z}}$, with $\hat{\mathbf{z}}$ the direction normal to the interface. An electron moving through this electric field experiences a magnetic field $\mathbf{B}_{\mathrm{R}}(\mathbf{k})$, which is momentum dependent. The interaction between the electron spins and this magnetic moment is captured in the Rashba Hamiltonian [32,38]

$$\mathcal{H}_{\mathrm{R}} = -\boldsymbol{\sigma} \cdot \mathbf{B}_{\mathrm{R}}(\mathbf{k}) = \frac{\alpha_{\mathrm{R}}}{\hbar} \boldsymbol{\sigma} \cdot (\mathbf{k} \times \hat{\mathbf{z}}) \,, \tag{1.6}$$

where $\alpha_{\mathrm{R}} \propto E$ is the Rashba coefficient, $\hbar$ the reduced Planck constant, $\boldsymbol{\sigma}$ a Pauli matrix representing the electron spin, and $\mathbf{k}$ the electron wave-vector representing its momentum. The precessing electron spins around $\mathbf{B}_{\mathrm{R}}(\mathbf{k})$ interact with the local magnetic moments through *s*-*d* coupling [39], inducing a tilt in the magnetization whose direction is dependent on $\mathbf{B}_{\mathrm{R}}(\mathbf{k})$. In the Rashba DMI model, the DMI constant is given by $D = 4\alpha_{\mathrm{R}} m_{\mathrm{e}} A/\hbar^2$ [32], with m_{e} the effective mass of the electron and A the exchange stiffness.

Rashba type DMI is often used to explain the appearance of DMI at FM/Oxide (FM/Ox) interfaces, such as Co/MgO, Fe/MgO, and Co/AlOx [40]. Combinations of HM/FM and FM/Ox interfaces such as Pt/Co/AlOx can thus show significant DMI values [35].

The DMI energy in the third term of Equation 1.1 represents the total bulk DMI. In this thesis, we study materials that are combinations of very thin layers in the order of a few nanometers. In this geometry, the micromagnetic description of the DMI energy can be written as [41]

$$\varepsilon_{\mathrm{DMI}} = D \left((\mathbf{m} \cdot \nabla) \, m_z - m_z \, (\nabla \cdot \mathbf{m}) \right) . \tag{1.7}$$

Here we assume that the bulk DMI is negligible compared to the interface DMI, which is true for thin films. The effective field representing the DMI interaction is then given by [42]

$$\mathbf{H}_{\mathrm{DMI}} = -\frac{D}{\mu_0 M_{\mathrm{s}}} \left(\nabla m_z - (\nabla \cdot \mathbf{m})\, \hat{\mathbf{z}}\right). \tag{1.8}$$

Note that, due to the interfacial nature of the DMI, D depends inversely on the FM layer thickness t. We can then define an interfacial DMI parameter D_{s}, which is thickness independent, $D = D_{\mathrm{s}}/t$. Typical values of D_{s} are in the order of 1 pJ m^{-1}, around a factor 10 smaller than the exchange stiffness constant A.

So far we have seen that the interfacial DMI, whether in the Fert-Levy or Rashba model, is dependent on interactions with nearby NM or Ox atoms. The arrangement of these atoms with respect to the FM atoms is of crucial importance. As we will see in the coming chapters of this thesis, the DMI is thus one of the parameters that is strongly dependent on disorder and can be modified with ion irradiation.

1.1.4 Magnetic anisotropies and demagnetization

The fourth and last term in Equation 1.1 denotes the anisotropy energy, which describes the overall preferential direction of the magnetization in the material. Several factors contribute to this energy, including the crystal structure, interfacial effects, and the shape of the material, which we will discuss one by one in the following.

1.1.4.1 Magneto-crystalline anisotropy

Magneto-crystalline anisotropy (MCA) describes the contribution from the crystal structure to the magnetic anisotropy. Due to SOC, the magnetic moments tend to align to a certain crystallographic axis. The associated MCA energy depends on the symmetry in the material. For hcp Co with hexagonal symmetry around the c axis, the associated energy density of the MCA is given by [43]

$$\varepsilon_{\mathrm{MC}} = K_1 \sin^2(\theta) + K_2 \sin^4(\theta) + \mathcal{O}\left(\sin^6(\theta)\right), \tag{1.9}$$

where K_1 and K_2 are the second and fourth order anisotropy constants (in J m^{-3}) and θ is the angle between the magnetization vector and the high symmetry axis of the crystal.[1] The form of the preferential magnetization direction depends on the relative sign and strength of K_1 and K_2, which can be described with the phase diagram obtained by minimizing the MCA energy in Equation 1.9 shown in Figure 1.2.

For large positive K_1, the material shows easy axis anisotropy. For $K_1 < 0$ and $K_2 > -K_1/2$, an easy cone appears instead, which turns into an easy plane if $K_2 < -K_1/2$. In the meta-stable region, two energy minima exist; $\theta = 0$ and $\theta = \pi/2$. In the case of uniaxial easy-axis anisotropy (large positive K_1 and small K_2), the fourth order term in Equation 1.9 can be neglected, which is what we will do in the remainder of this section.

1.1.4.2 Interface anisotropy

Similar to the DMI, interfaces contribute to the anisotropy. This was first realized by Néel in 1954 [44]. In thin magnetic films, the contribution of the interface anisotropy takes the form of a uniaxial anisotropy [43–48];

$$\varepsilon_{\mathrm{s}} = \frac{K_{\mathrm{s}}}{t} \sin^2(\theta), \tag{1.10}$$

---

[1] The MCA energy for tetragonal and cubic systems energy can be written in the form of Equation 1.9 with slightly different higher order terms [28].

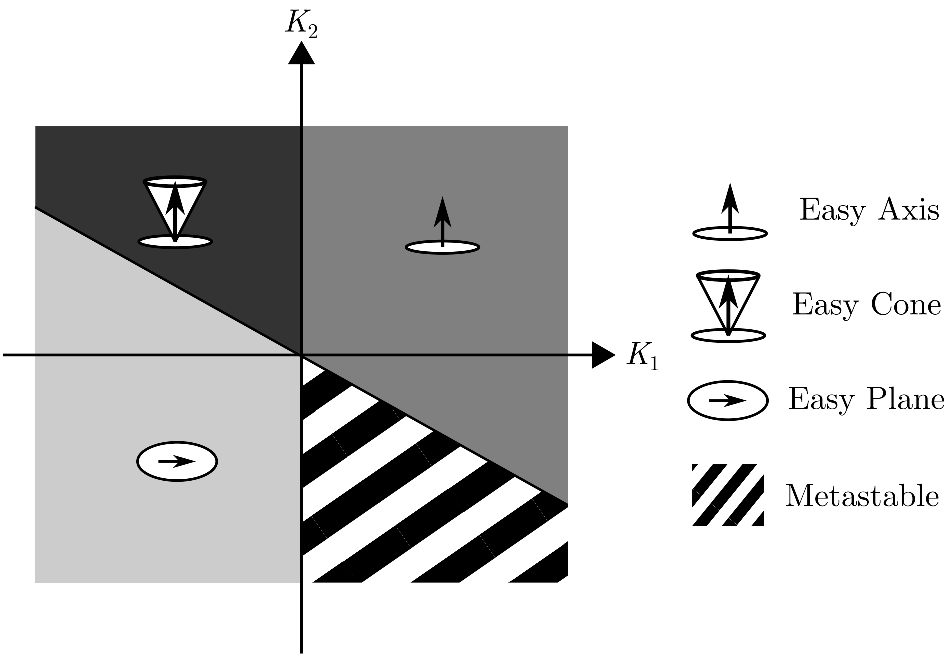

Fig. 1.2: Uniaxial anisotropy phase diagram | Phase diagram showing the easy anisotropy directions of uniaxial magnets for different values of the second and fourth order anisotropy constants K_1 and K_2. Figure adapted from Ref. [28].

where K_s is the surface anisotropy constant (in J m^{-2}) and t is the thickness of the magnetic layer.[1] This means that we can describe the volume and surface contribution in a single uniaxial anisotropy constant K_u, given by

$$K_\mathrm{u} = K_\mathrm{v} + \frac{K_{\mathrm{s},1} + K_{\mathrm{s},2}}{t}. \tag{1.11}$$

Here, K_v represents the volume contribution to the anisotropy, typically the MCA, and $K_{\mathrm{s},1}$ and $K_{\mathrm{s},2}$ represent the contributions from the interfaces on either side of the FM layer. In the thin magnetic films studied in this thesis, the bulk contribution to the anisotropy is very small compared to the surface contribution. Hence in the remainder we will assume $K_\mathrm{v} = 0$.

The surface anisotropy typically favors alignment of the magnetic moment perpendicular to the sample surface. This is a phenomenon known as perpendicular magnetic anisotropy (PMA). The origin of the surface anisotropy is often attributed to the hybridization of the 3d orbitals of the FM with an adjacent material. In FM/HM interfaces, the 5d orbitals of the HM hybridize with the 3d orbitals of the FM, modifying the local crystal field and adding to the PMA. For FM/Ox interfaces, the 3d orbitals of the FM instead hybridize with the 2p orbitals of the oxygen [49]. Given that the surface anisotropy term thus heavily depends on the atomic arrangement at the interfaces, sharp interfaces are important to obtain large surface anisotropy values. Moreover, this indicates that the surface anisotropy will be sensitive to ion irradiation.

1.1.4.3 Dipolar interaction and shape anisotropy

A magnetic moment generates a dipolar field. In a magnetic material, this field $\mathbf{H}_\mathrm{D}$ interacts with other magnetic moments. This is called the dipolar or dipole(-dipole) interaction, and its associated energy can be written in the same form as the Zeeman energy (first term in Eq. 1.1):

---

[1] This description is only valid when t is smaller than the exchange length $l_\mathrm{ex} = \sqrt{\frac{2A}{\mu_0 M_\mathrm{s}^2}}$, which for the materials studied in this thesis is the case.

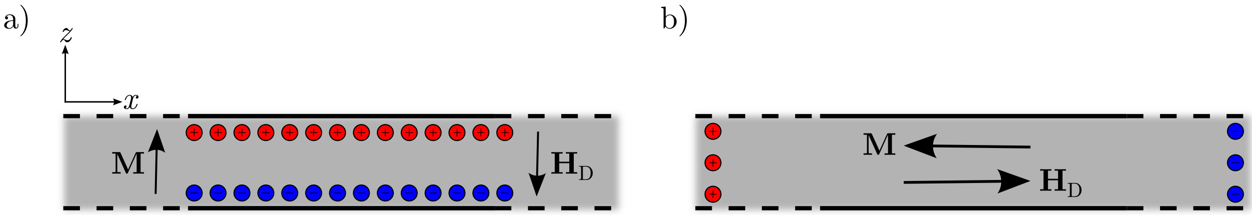

Fig. 1.3: Magnetic surface charges in thin films | Schematic representation of the magnetic charges (red and blue) and resulting demagnetizing field $\mathbf{H}_\mathrm{D}$ in a thin film with uniform magnetization $\mathbf{M}$ pointed a) perpendicular to the sample normal and b) in the sample plane.

$$\varepsilon_\mathrm{D} = -\frac{1}{2}\mu_0 M_\mathrm{s}\mathbf{m}\cdot\mathbf{H}_\mathrm{D}. \tag{1.12}$$

Note that there is an added factor 1/2 to prevent including the interaction between two magnetic moments twice.

To evaluate ε_D, we can make use of *magnetic charges* [28]. We can use Gauss' law $\nabla\cdot\mathbf{B} = \mu_0\nabla\cdot(\mathbf{H}+\mathbf{M}) = 0$ to find $\nabla\cdot\mathbf{H} = -\nabla\cdot\mathbf{M}$. In the absence of currents, we can express the demagnetizing field as a scalar potential $\mathbf{H}_\mathrm{D} = -\nabla\Phi_\mathrm{m}$. Combining this with the resulting expression from Gauss' law we find $\nabla^2\Phi_\mathrm{m} = \nabla\cdot\mathbf{M} = -\rho_\mathrm{m}$, with ρ_m the magnetic charge density. This is analogous to the Poisson equation, but now in the framework of magnetic charges.[1] This analogy works in the bulk, but to prevent $\mathbf{M}$ from going abruptly to zero at the edges, we introduce magnetic surface charges, whose density is given by $\sigma_\mathrm{m} = \mathbf{M}\cdot\hat{\mathbf{z}}$, with $\hat{\mathbf{z}}$ the direction normal to the surface plane.

Figure 1.3 shows how we can use the concept of magnetic charges to evaluate ε_D. Figure 1.3a shows a thin film with uniform magnetization perpendicular to the sample normal, and Figure 1.3b shows the same film but now magnetized in the plane. In both cases, only surface charges exist ($\nabla\cdot\mathbf{M} = 0$). The magnetic charges create the opposing field $\mathbf{H}_\mathrm{D}$, which due to its direction antiparallel to $\mathbf{M}$ is often called the *demagnetizing field*. To reduce its energy, the system tries to reduce the number of magnetic charges. Hence, the dipolar energy is minimized when the magnetization is pointed in the plane.

The fact that the dipolar energy in thin films prefers magnetization in the plane can be considered as an anisotropy term which works against the surface anisotropy that we discussed before. This anisotropy is called *shape anisotropy*, since its exact contribution depends on the shape of the sample. To evaluate its contribution, we can write $\mathbf{H}_\mathrm{D}$ as

$$\mathbf{H}_\mathrm{D} = -\mathcal{N}\mathbf{M} = -\begin{pmatrix} N_\mathrm{x} & 0 & 0 \\ 0 & N_\mathrm{y} & 0 \\ 0 & 0 & N_\mathrm{z} \end{pmatrix}\mathbf{M}, \tag{1.13}$$

where $\mathcal{N}$ is the so-called demagnetization tensor, which follows the shape of the sample. In keeping with the thin-film analogy, the thickness of the film is much smaller than its length and width. This means the contribution of the shape will be dominated by the film thickness. We can thus set $N_\mathrm{x} = N_\mathrm{y} \approx 0$ and $N_\mathrm{z} \approx 1$. We can then write $\mathbf{H}_\mathrm{D}$ as $\mathbf{H}_\mathrm{D} = -M_\mathrm{z}\hat{\mathbf{z}}$. Inserting this into Equation 1.12 gives

$$\varepsilon_\mathrm{D} = \frac{\mu_0 M_\mathrm{s}^2}{2}\cos^2(\theta) = K_\mathrm{D}\cos^2(\theta), \tag{1.14}$$

where $K_\mathrm{D} = \mu_0 M_\mathrm{s}^2/2$ is the shape anisotropy constant.

---

[1] Note that magnetic monopoles do not exist [50]. Hence, the magnetic charges we speak of here are merely a mathematical device to evaluate ε_D, and not real physical objects.

1.1.4.4 Effective Anisotropy

In the previous sections we have seen the various contributions to the magnetic anisotropy, with in particular the surface anisotropy and shape anisotropy found to be working against each other; the surface anisotropy prefers out-of-plane magnetization - or PMA - while the shape anisotropy prefers in-plane magnetization. Due to this competition, we can define an effective anisotropy constant $K_{\text{eff}} = K_{\text{u}} - K_{\text{D}}$ which takes into account both contributions. It is this constant which we use in the fourth term of Equation 1.1. K_{eff} is given by

$$K_{\text{eff}} = \frac{K_{\text{s},1} + K_{\text{s},2}}{t} - \frac{1}{2}\mu_0 M_{\text{s}}^2. \tag{1.15}$$

The sign of K_{eff} describes the transition between PMA and in-plane anisotropy. If $K_{\text{eff}} > 0$ the sample has PMA, whereas if $K_{\text{eff}} < 0$ the sample shows in-plane anisotropy. Moreover, K_{eff} is thickness dependent due to the surface term. In very thin samples, the surface anisotropy contribution is larger than the shape anisotropy, and thus the sample shows PMA. Increasing the thickness past the critical point where the shape and surface anisotropies cancel each other out ($K_{\text{eff}} = 0$), the easy axis transitions to in-plane anisotropy.

The associated effective anisotropy field can be found when calculating the field required to saturate a uniaxial magnet along its hard axis direction, which is perpendicular to the easy axis. If only considering the effective anisotropy and Zeeman energies, it is given by

$$H_{K_{\text{eff}}} = \frac{2K_{\text{eff}}}{\mu_0 M_{\text{s}}}. \tag{1.16}$$

This concludes our discussion of all the energy terms in Equation 1.1. In the next section we will see the magnetic configuration resulting from the interplay of those different energies.

1.2 Magnetic domains and domain walls

In the previous section, we have seen the various magnetic interactions that play a role in the thin-film samples that we study in this thesis. In this section we will describe the ground state that results from the interplay between these magnetic interactions in samples with PMA and without the application of an external magnetic field.

Let us first consider a thin film sample with only exchange, PMA, and dipolar energy. In a uniformly magnetized film, the exchange and anisotropy energies are minimized. However, the sample contains very large dipolar energy as the surface charges are very close (see Fig. 1.3a). Due to the PMA, it is unfavorable for the magnetization to turn in the plane. Another way the sample can reduce its dipolar energy is by forming smaller regions with uniform and opposite magnetization - *magnetic domains* - that are aligned with the easy axis. Whether the magnetization is pointing up or down, the domains have the same energy, but the overall dipolar energy is significantly reduced. The area in between the magnetic domains, where the magnetization rotates gradually from one direction to the other, is called a *domain wall* (DW). The manner in which the magnetization rotates depends on the micromagnetic energy of the DW. Generally speaking, two limiting cases exist; a Bloch and a Néel DW, which are schematically represented in Figure 1.4. In a Bloch wall, the magnetization rotates in the DW plane (yz-plane in Fig. 1.4), while in a Néel wall the magnetization rotates perpendicular to the DW plane (xz-plane in Fig. 1.4).

In the absence of DMI, Bloch DWs are energetically favored since a Néel wall requires the creation of additional magnetic charges ($\nabla \cdot \mathbf{M} \neq 0$ for a Néel wall) although this depends on the lateral dimension of the sample, i.e. in the y-direction. Below a certain width, Néel DWs are favored [52]. For this thesis however, this condition does not apply and thus we will ignore this effect in the remainder.

We can find the expression for the energy of a Bloch wall by considering its micromagnetic energy, which, when only considering exchange and anisotropy energies, is given by [28,53]

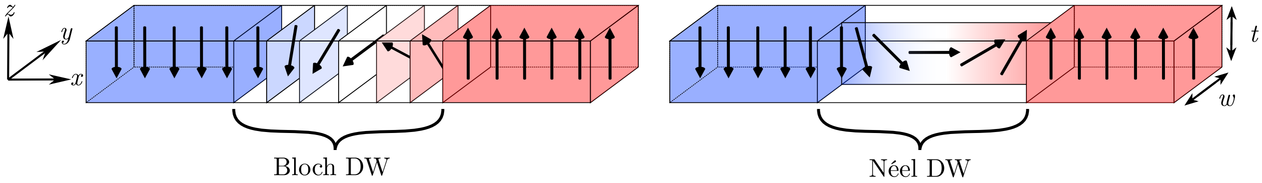

Fig. 1.4: Bloch and Néel domain walls | Schematic representations of a Bloch and Néel DW in thin films of thickness t and width w with PMA. Figure adapted from Ref. [51].

$$\varepsilon_{\text{tot}} = \varepsilon_{\text{ex}} + \varepsilon_{\text{K}} = \int \left[A \left[\left(\frac{\partial \theta}{\partial x} \right)^2 + \left(\sin\left(\theta\right) \frac{\partial \phi}{\partial x} \right)^2 \right] + K_{\text{eff}} \sin^2\left(\theta\right) \right] dx. \tag{1.17}$$

Note that here we switched to a spherical coordinate system, with θ denoting the polar angle in the yz-plane and ϕ the azimuthal angle in the xy-plane. To find the energy we first need to find the profile of the Bloch wall, which can be done by minimizing the Euler-Lagrange equations for Equation 1.17. A solution can be found by assuming that the magnetization in the DW only rotates in the yz-plane, i.e. $\phi = \text{constant}$. Assuming the DW separates an $\uparrow$-domain for negative x and a $\downarrow$-domain at positive x, the domain wall profile for a Bloch wall is given by

$$\begin{aligned} \theta\left(x\right) &= 2 \arctan\left[\exp\left(\frac{x-q}{\Delta_0} \right) \right], \\ \phi\left(x\right) &= \phi. \end{aligned} \tag{1.18}$$

Here q is the center of the domain wall, and Δ_0 is the width of the Bloch wall given by

$$\Delta_0 = \sqrt{\frac{A}{K_{\text{eff}}}}. \tag{1.19}$$

Plugging this profile back into Equation 1.17 gives the Bloch DW surface energy density

$$\sigma_0 = 4\sqrt{A K_{\text{eff}}}. \tag{1.20}$$

The situation becomes more complex when considering a Néel wall. As mentioned before the difference in energy between a Bloch and Néel wall comes from the additional magnetic charges created by the Néel wall. Obtaining the width and energy of a Néel wall forces us to take into account the shape anisotropy of the DW from the induced magnetic charges. The analysis, performed in detail in Ref. [53], is very similar to what has been shown before, except now we replace the anisotropy constant K_{eff} in Equation 1.17 by $K_{\text{eff}} + K_{\text{DW}} \cos^2\left(\phi\right)$, where K_{DW} is the shape anisotropy of the DW, given by

$$K_{\text{DW}} \approx \frac{t \ln\left(2\right)}{\pi \Delta_0} \frac{\mu_0 M_{\text{s}}^2}{2}. \tag{1.21}$$

We then find for the width and energy

$$\Delta\left(\phi\right) \approx \frac{\Delta_0}{\sqrt{1 + \kappa \cos^2\left(\phi\right)}}, \tag{1.22}$$

$$\sigma\left(\phi\right) \approx \sigma_0 \sqrt{1 + \kappa \cos^2\left(\phi\right)}, \tag{1.23}$$

with $\kappa = K_{\text{DW}}/K_{\text{eff}}$. For $\kappa \ll 1$, e.g. when a sample has strong PMA, Equation 1.23 can be approximated to

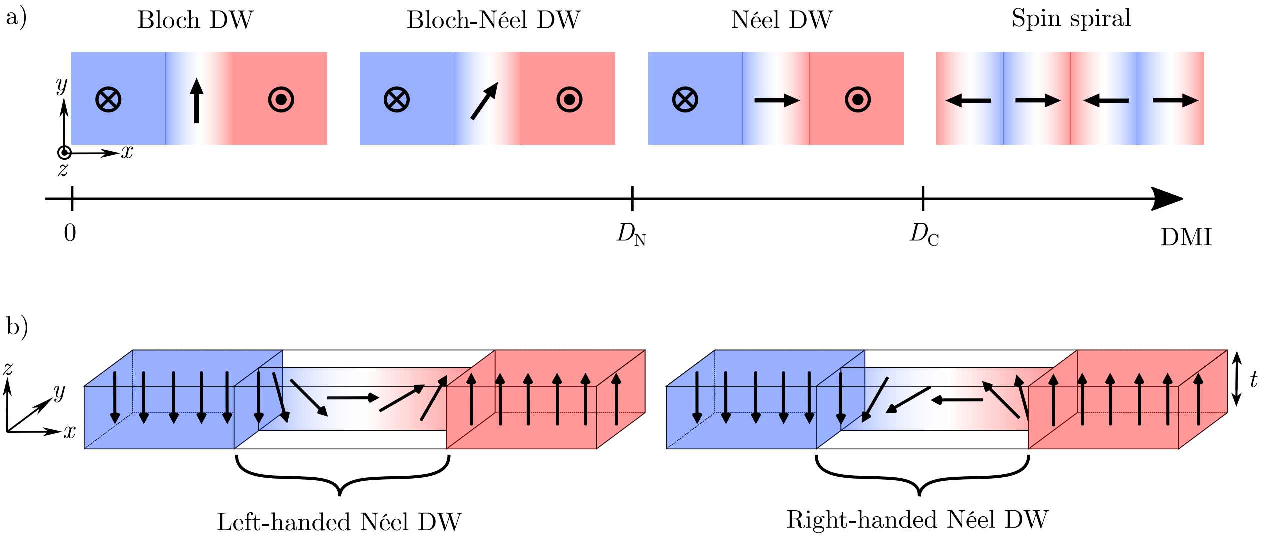

Fig. 1.5: The influence of DMI on a domain wall | a) Schematic representation of the transition from a Bloch DW to a Néel DW with increasing DMI strength. For $D_\mathrm{N} < D < D_\mathrm{c}$ the Néel DW becomes energetically favorable. For $D > D_\mathrm{c}$ a spin-spiral is stabilized. b) Schematic representations of a left-handed and right-handed Néel DW. Depending on the sign of D, one is energetically favored over the other. Figure adapted from Ref. [51].

$$\sigma\left(\phi\right) \approx \sigma_0 + 2\Delta_0 K_\mathrm{DW}\cos^2\left(\phi\right). \tag{1.24}$$

It should be noted that the expression for K_DW is an approximation, where it is assumed that Δ_0 does not depend on ϕ. However, as we have seen, this is not always the case, and it should be taken into account to obtain an exact solution for Equations 1.22 and 1.23. The required correction is small however, and so we will neglect it in the remainder.

The final layer of complexity is achieved when the influence of the DMI is taken into account. Indeed as discussed in Section 1.1.3.2, the DMI can be expressed as an effective field (see Eq. 1.8), which points in the plane of the sample. Hence, it affects the magnetization in the DW. We will not treat the entire derivation of the effect of an in-plane field on the DW energy here (it can be found in Ref. [53]), but for small fields and small κ the additional term to the DW energy can be written as $-\pi\Delta_0\mu_0 M_\mathrm{s} H_\mathrm{DMI}\cos\left(\phi\right)$, with a minus sign because it counteracts the DW shape anisotropy, i.e. it tries to stabilize Néel DWs. The full static DW energy without the influence of external magnetic fields is thus given by

$$\sigma\left(\phi\right) \approx \sigma_0 + \Delta_0\mu_0 M_\mathrm{s}\left(H_{K_\mathrm{DW}}\cos^2\left(\phi\right) - \pi H_\mathrm{DMI}\cos\left(\phi\right)\right), \tag{1.25}$$

where H_{K_DW} is the DW shape anisotropy field, which has the same form as Equation 1.16.

The effect of the DMI on the DW is visualized in Figure 1.5. The DMI favors the stabilization of Néel walls, depending on its value; the stronger the DMI, the more Néel walls are favored. As shown in Figure 1.5b, its sign determines the handedness of the DW that the DMI favors, with $D < 0$ ($D > 0$) favoring left-handed, or anti-clockwise (right-handed, clockwise) Néel walls. In the evolution from a Bloch to Néel wall (Fig. 1.5a), there are several threshold values. For $D_\mathrm{N} < D < D_\mathrm{c}$ a pure Néel DW is stabilized. Increasing the DMI above a critical value D_c, where $\sigma < 0$, it becomes favorable to continuously rotate the magnetization: this phenomenon is called a spin spiral.

So far we have only considered a static DW. In the next section we will discuss what happens when an external magnetic field is applied.

1.3 Magnetization Dynamics

In the previous section we have seen that magnetostatic interactions lead to the formation of DWs, whose structure strongly depends on the sign and value of DMI. In the this section, we discuss what happens when we apply external magnetic fields, which will cause the DW to move.

1.3.1 The Landau-Lifshitz-Gilbert Equation

The spatial and temporal evolution of the magnetization is described by the Landau-Lifshitz-Gilbert (LLG) equation [54,55],

$$\frac{\partial \mathbf{m}(t)}{\partial t} = \underbrace{-\gamma_0 \left(\mathbf{m} \times \mathbf{H}_{\mathrm{eff}}\right)}_{\text{Precession}} + \underbrace{\alpha \left(\mathbf{m} \times \frac{\partial \mathbf{m}(t)}{\partial t}\right)}_{\text{Damping}}, \tag{1.26}$$

where $\gamma_0 = \mu_0 \gamma$, with the gyromagnetic ratio $\gamma = g|e|/2m_{\mathrm{e}}$, and $g \approx 2$ the Landé factor, e the electron charge and m_{e} the electron mass. α is the Gilbert damping parameter. $\mathbf{H}_{\mathrm{eff}}$ is the effective field, which contains all the micromagnetic contributions described in Section 1.1, any externally applied magnetic field, as well as any other effective field that affects the magnetization. Figure 1.6 schematically shows the resulting dynamics, which is a spiralling motion around $\mathbf{H}_{\mathrm{eff}}$. The two terms on the right-hand side of Equation 1.26 describe two torques; $\mathbf{T}_{\mathrm{p}}$ and $\mathbf{T}_{\mathrm{d}}$, which describe the precessional motion of the magnetization around $\mathbf{H}_{\mathrm{eff}}$ and the damping of this precessional motion, respectively. The damping term thus describes the dissipation of energy in the system, and is analogous to a viscous force.

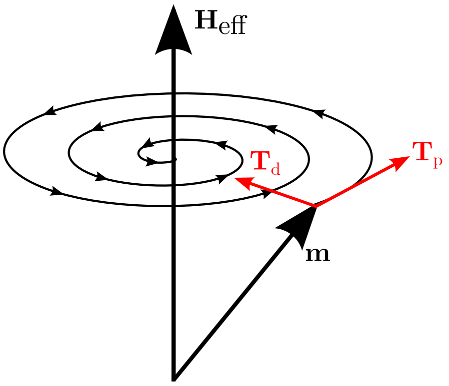

Fig. 1.6: Magnetization dynamics as described by the LLG equation | Schematic representation of the magnetization dynamics around an effective field $\mathbf{H}_{\mathrm{eff}}$ as described by the LLG equation. $\mathbf{T}_{\mathrm{p}}$ and $\mathbf{T}_{\mathrm{d}}$ denote the precessional and damping torques, represented by the right-hand terms of Equation 1.26. Figure adapted from Ref. [51].

1.3.2 Field-driven domain wall dynamics in perfect films

In this section we will discuss the effects of the magnetization dynamics described by the LLG equation on domain walls. For this discussion, we will limit ourselves to domain wall motion in thin-films with PMA. Moreover, we will only consider out-of-plane applied magnetic fields, where $\mathbf{H} = H\hat{\mathbf{z}}$.

When an external field is applied, the precession and damping torques $\mathbf{T}_{\mathrm{p}}$ and $\mathbf{T}_{\mathrm{d}}$ will be exerted on the magnetization. $\mathbf{T}_{\mathrm{p}}$ and $\mathbf{T}_{\mathrm{d}}$ are only non-zero in the DW, since the magnetization in the domains is (anti-)parallel to the applied field. The effects of the torques on the magnetization in the DW are schematically visualized in Figure 1.7. For simplicity's sake we show only the effects on a Néel DW and only in the center of the DW, but the same approach can easily be performed

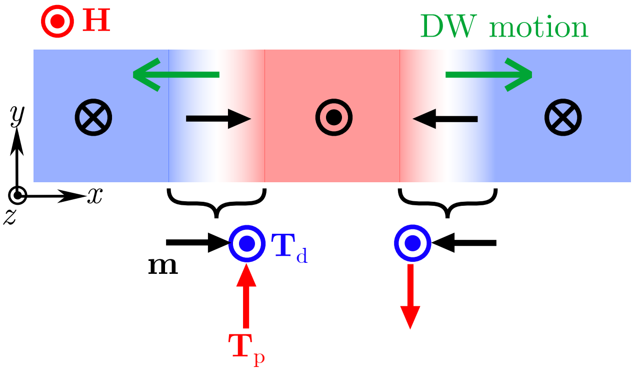

Fig. 1.7: Field-driven domain wall motion | Schematic representation of the torques $\mathbf{T}_\mathrm{p}$ and $\mathbf{T}_\mathrm{d}$ acting on the magnetization in a Néel DW upon the application of an external magnetic field $\mathbf{H} = H\hat{\mathbf{z}}$. The green arrows denote the direction in which the DW moves as a result of the torques. Figure adapted from Ref. [51].

for a Bloch DW as well. As a result of the applied torques, the DW starts to move in the direction indicated by the green arrows.

The dynamics of DWs in materials with uniaxial anisotropy were first described by Walker in 1956[1] [58], and can be described by introducing time dependence to the DW profile described with Equation 1.18:

$$\begin{aligned} \theta\left(x,t\right) &= 2\arctan\left[\exp\left(\frac{x-q\left(t\right)}{\Delta_0}\right)\right], \\ \phi\left(x,t\right) &= \phi\left(t\right). \end{aligned} \tag{1.27}$$

The equations of motion for q and ϕ can be found by solving the Euler-Lagrange equations derived by Slonczewski in 1972 [59]. Because we only use the q and ϕ coordinates to describe the DW dynamics, this model is often called the q-ϕ model. We will first consider a DW without the influence of DMI. The resulting equations of motion are given by [53]

$$\begin{aligned} \alpha\frac{\dot{q}}{\Delta_0} + \dot{\phi} &= \gamma_0 H, \\ \frac{\dot{q}}{\Delta_0} - \alpha\dot{\phi} &= -\gamma_0 H_{K_\mathrm{DW}}\sin\left(\phi\right)\cos\left(\phi\right), \end{aligned} \tag{1.28}$$

where $\dot{\phi}$ and $\dot{q}$ denote the partial derivatives with respect to t of ϕ and q respectively. It can be shown that a steady state solution $\dot{\phi} = 0$ exists for $H \leq H_\mathrm{W} = \alpha H_{K_\mathrm{DW}}/2$, where H_W is the so-called Walker field. Below the Walker field, also called the steady-state regime, the DW moves steadily with a velocity given by

$$\dot{q} = v_\mathrm{DW} = \frac{\gamma_0\Delta_0}{\alpha}H. \tag{1.29}$$

The mobility of the DW in this regime, given by $\mu_\mathrm{DW} = \dot{q}/H$ is large and constant. When describing this regime with the torques from the LLG equation, we can see that $\mathbf{T}_\mathrm{p}$ first rotates the magnetization in the DW in the xy-plane. This creates additional magnetic charges and thus a demagnetization field, which aligns the magnetization out of the plane. This is what makes the DW move. $\mathbf{T}_\mathrm{d}$ opposes the effect from $\mathbf{T}_\mathrm{p}$, meaning that, in equilibrium, the DW moves with a steady velocity.

For fields larger than H_W, $\mathbf{T}_\mathrm{d}$ can no longer compensate the effect of $\mathbf{T}_\mathrm{p}$. Indeed no solutions of $\dot{\phi} = 0$ exist for $H > H_\mathrm{W}$, and thus the magnetization starts precessing. This is called the Walker breakdown.

---

[1] Walker's original work is unpublished [56], but an account can be found in Ref. [57]. The complete analytical model can be found in Ref. [58].

Above the Walker breakdown, the DW dissipates energy by precessing. Due to the precession, we can no longer describe the velocity of the DW with an expression $\dot{q}$ as given in Equation 1.29, since its position and thus velocity varies along the length of the DW. Instead, we can describe the velocity of the DW by considering the average velocity along the DW $\langle \dot{q} \rangle$. It can be shown [53] that the velocity in this regime is given by

$$\langle \dot{q} \rangle = \frac{\gamma_0 \Delta_0}{\alpha \left(1+\alpha^2\right)} \left[H \left(1+\alpha^2\right) - \sqrt{H^2 - H_{\mathrm{W}}^2} \right]. \tag{1.30}$$

Equation 1.30 shows that for fields just above H_{W}, the velocity drops significantly due to the precessional behavior of the magnetization in the DW. The mobility in this regime, $\mu_{\mathrm{DW}} = \langle \dot{q} \rangle / H$, is negative. Further increasing the field, the velocity asymptotically approaches another steady state regime, but with a lower mobility. In the limit for $H \to \infty$, the velocity is given by

$$\lim_{H \to \infty} \langle \dot{q} \rangle = \frac{\gamma_0 \Delta_0 \alpha}{1+\alpha^2} H. \tag{1.31}$$

The full DW velocity curve as governed by Equations 1.29, 1.30, and 1.31 is shown in Figure 1.8a.

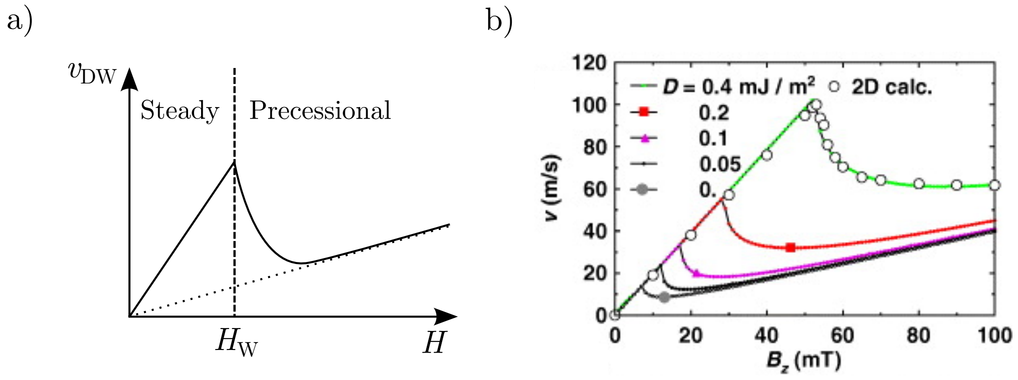

Fig. 1.8: Domain wall velocity as described by the q-ϕ model | a) DW velocity as a function of the applied magnetic field as described by the q-ϕ model. The dashed line indicates the Walker field H_{W}. The dotted line represents the limit for large fields given in Equation 1.31. b) DW velocity from the q-ϕ model and 2D calculations for different values of the DMI strength D. Figure adapted from Ref. [41].

Let us now consider the effect of adding DMI to the model. As shown in Figure 1.5, the DMI favors a DW to be in the Néel configuration, and its effect can be considered as an effective DMI field that points in the direction of the plane (see Eqs. 1.8 and 1.25). Taking this into account, the equations of motion for q and ϕ are now given by [41]

$$\begin{aligned} &\alpha \frac{\dot{q}}{\Delta_0} + \dot{\phi} = \gamma_0 H, \\ &\frac{\dot{q}}{\Delta_0} - \alpha \dot{\phi} = \gamma_0 \left(H_{\mathrm{D}} \sin(\phi) - H_{K_{\mathrm{DW}}} \sin(\phi) \cos(\phi) \right), \end{aligned} \tag{1.32}$$

where $H_{\mathrm{D}} = \frac{\pi}{2} H_{\mathrm{DMI}}$. An elegant solution to these equations can be found, although the derivation is somewhat cumbersome. We will not provide the entire derivation here, but it can be found in detail in Ref. [53]. It was Thiaville *et al.* [41] that first showed that the solution to Equation 1.32 is still given by Equations 1.29, 1.30, and 1.31, and that only H_{W} is modified. In the presence of DMI, H_{W} is now given by

$$H_{\mathrm{W}} = \alpha \sin(\phi) \left(H_{\mathrm{D}} - H_{K_{\mathrm{DW}}} \cos(\phi) \right), \tag{1.33}$$

where $\cos(\phi) = \frac{1}{4}\left(\delta - \sqrt{\delta^2+8}\right)$, and $\delta = H_\mathrm{D}/H_{K_\mathrm{DW}}$. The corresponding velocity is given by

$$v_\mathrm{W} = \frac{\gamma_0 \Delta_0}{\alpha} H_\mathrm{W} = \gamma_0 \Delta_0 H_\mathrm{D} \left(\sin(\phi) - \frac{\sin(2\phi)}{2\delta}\right). \tag{1.34}$$

The DMI thus does not significantly change the physics in the q-ϕ model, and extends the steady state regime to larger fields. This is visible in Figure 1.8b, where can be seen that the Walker field is pushed to larger magnetic fields when the value for the DMI is increased. Note that for very large DMI ($H_\mathrm{D} \gg H_{K_\mathrm{DW}}$), $H_\mathrm{W} \approx \alpha H_\mathrm{D}$, and Equation 1.34 is then given by [41,60]

$$v_\mathrm{W} = \frac{\pi}{2}\gamma \frac{D}{M_\mathrm{s}}. \tag{1.35}$$

While the q-ϕ model can be very powerful, there are several limitations that one does need to be aware of. They stem mostly from the fact that the q-ϕ model considers the DW as a rigid object that moves only in x, and thus only describes one-dimensional (1D) dynamics. It thus works reasonably well in systems which are inherently 1D, such as nanowires [61], but in thin film samples the extra dimension needs to be taken into account. The DMI also introduces two-dimensional (2D) effects, with notably the observation of the Walker breakdown as shown in Figure 1.8b being absent. Instead, at the Walker field, v_DW reaches a plateau [60,62–64], as shown using micromagnetic simulations in Figure 1.9.

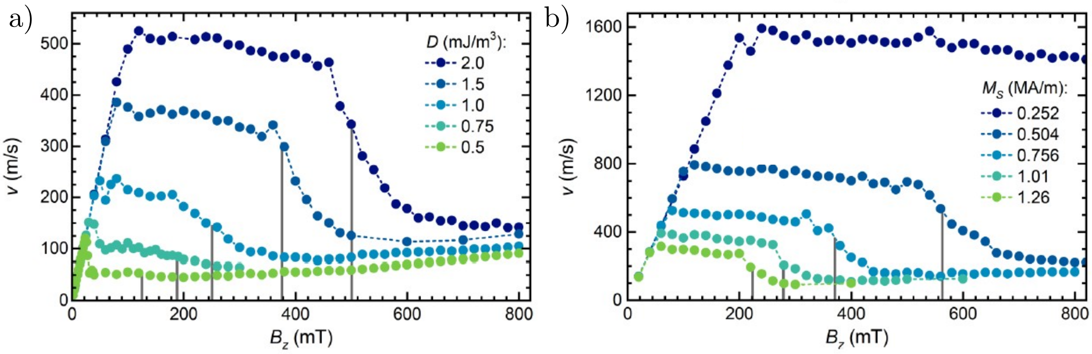

Fig. 1.9: Velocity plateau in the presence of DMI | Simulated field-driven DW velocity with varying values of a) the DMI and b) M_s. The vertical lines indicate the calculated Slonczewski fields. Figure adapted from Ref. [63].

From Figure 1.9 can be seen that the height of the velocity plateau follows the approximated v_W described in Equation 1.35, scaling with D/M_s. Recent studies of the velocity plateau have shown that the end of the plateau seems to correspond to the so-called Slonczewski field H_S [63,64], which is the field where the q-ϕ model predicts the velocity to be at a minimum. When either $H_{K_\mathrm{DW}} \ll H_\mathrm{D}$ or $H_\mathrm{D} \ll H_{K_\mathrm{DW}}$, the Slonczewski field and velocity are well approximated by [64]

$$H_\mathrm{S} = H_\mathrm{W}\left(\frac{1+\alpha^2}{\alpha\sqrt{\alpha^2+2}}\right), \tag{1.36}$$

$$v_\mathrm{S} = v_\mathrm{W}\left(\frac{\alpha\sqrt{\alpha^2+2}}{1+\alpha^2}\right), \tag{1.37}$$

although the actual experimental value will depend strongly on the value of δ. After the velocity plateau, the velocity comes back to the steady state precessional regime described by Equation 1.31.

Another notable contributor to 2D effects is disorder in the material, which can introduce roughness and stochastic effects to the DW motion. In the next section, we discuss the effects of disorder on DW motion in more detail.

1.3.3 Field-driven domain wall dynamics in films with disorder

In the previous section we have discussed how a DW moves under an applied field. However, these models assume that the sample is homogeneous, i.e. it does not contain any disorder or defects. Realistic samples are not homogeneous. Crystalline texture, material defects, grain boundaries, and spacial variation of magnetic properties due to intermixing and interface roughness can all contribute to the disorder. This disorder is typically characterized as a potential through which the DW must move, schematically shown in Figure 1.10a. To model the effects of the potential on the DW shape and dynamics, we consider the DW as an elastic line [65]. Its shape is determined by the competition of its elastic energy and the energy in the pinning landscape. The former describes the tendency for the DW to reduce its length - less length costs less energy - and the latter describes the fact that the DW wants to be in the energy minimum of the potential landscape. Due to this competition, the DW is no longer straight, as assumed in the q-ϕ model.

Under a magnetic field, the pinning landscape introduces an energy barrier, which acts as pinning sites for the DW. In order for the DW to move forward, the applied force needs to be large enough to overcome these energy barriers. The resulting characteristic curve for the DW velocity is shown in Figure 1.10b. The critical field H_{dep} required to overcome the pinning energy barrier is called the depinning field. Below the depinning field, the DW motion is thermally activated and dominated by pinning. This regime is called the *creep* regime. Around the depinning field we enter the *depinning* transition, where the field is large enough to overcome the pinning forces. When further increasing the field, the influence of the disorder is reduced and the DW dynamics enter the *flow* regime, where it is mostly described by the q-ϕ model as discussed in the previous section.

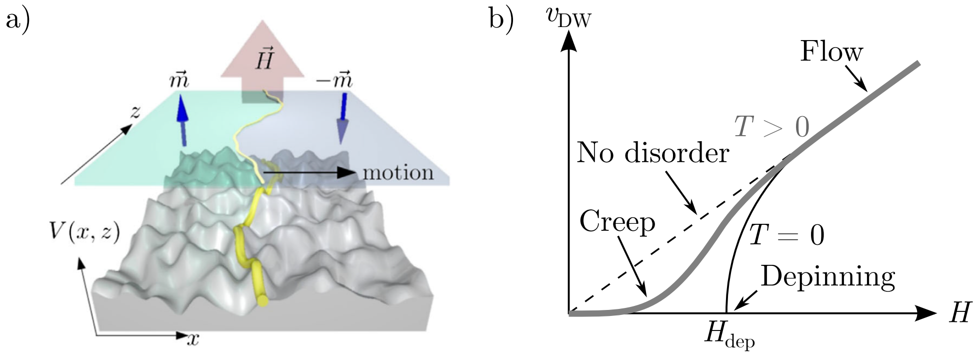

Fig. 1.10: Domain wall (motion) in a disordered landscape | a) DW (yellow) in a pinning landscape $V(x,z)$ (grey). The applied magnetic field causes the DW to move over the potential landscape. Figure adapted from Ref. [66]. b) Theoretical curve for field driven DW motion in a disordered landscape. The dashed line indicates the DW velocity as described by the q-ϕ model. The solid black line indicates the scenario at $T = 0$, where below H_{dep} the DW velocity is zero. The thick grey line indicates the scenario at $T > 0$, where the DW moves by thermal activation at $H < H_{\text{dep}}$. Figure adapted from Ref. [65].

It is thus evident that below and around the depinning transition, the q-ϕ model is inadequate to describe the DW dynamics. Instead, we resort to statistical models that describe DW dynamics on the microscopic level [67–70]. We will not treat the details of these statistical models in this thesis. Instead we refer to Refs. [53,70] for an excellent review and treatment. In the following we will discuss the resulting DW dynamics in the creep, depinning and flow regimes.

1.3.3.1 Creep regime

In creep dynamics, we describe the dynamics of an elastic 1D interface in 2D quenched disorder with the aforementioned statistical models. The statistical physics behind these dynamics do not only describe magnetic DWs, but can be applied for a whole range of systems; among others, these include ferroelectric DWs [71], fracture fronts [72], strained amorphous materials [73], and liquid contact lines [74].

In the creep regime, the applied magnetic field is not strong enough for the DW to overcome the energy barriers imposed by the pinning potential. This means that the DW motion is thermally driven, and that we can thus use an Arrhenius law to describe its motion [75]:

$$v(H \leq H_{\text{dep}}, T) = v\left(H_{\text{dep}}, T\right) \exp\left(-\frac{\Delta E(H)}{k_{\text{B}} T}\right), \tag{1.38}$$

where $\Delta E(H)$ is the energy barrier created by the disorder landscape, and $k_{\text{B}}T$ is the thermal energy, with k_{B} the Boltzmann constant. The energy barrier depends on the applied magnetic field, and typically scales as $\Delta E \sim H^{-\mu}$, where $\mu = 1/4$ is a universal exponent [75,76]. ΔE thus diverges when $H \to 0$, and $\Delta E \to 0$ with increasing H.

Jeudy *et al.* [66] showed that the energy barrier can be written as

$$\Delta E(H) = k_{\text{B}} T_{\text{d}} \left(\left(\frac{H}{H_{\text{dep}}}\right)^{-\mu} - 1\right), \tag{1.39}$$

with T_{d} the depinning temperature, with $k_{\text{B}}T_{\text{d}}$ describing the order of magnitude of the pinning energy barrier. The creep dynamics as described by Equations 1.38 and 1.39 are universal. This means that the creep dynamics only depend on the dimensionality and type of DW-disorder interaction of the system: the reduced energy barrier $\Delta E/k_{\text{B}}T_{\text{d}}$ as a function of the reduced force H/H_{dep} follows the form described by Equation 1.39. The exponential behavior of the velocity with the applied magnetic field in the creep regime is visible for the $T > 0$ curve in Figure 1.10b.

1.3.3.2 Depinning transition

The depinning transition describes the transition from the creep regime to the flow regime. At very low temperatures compared to T_{d}, it can be described with a power law [76,77]:

$$v\left(H > H_{\text{dep}}, T \ll T_{\text{d}}\right) = v_{\text{T}} \left(\frac{H - H_{\text{dep}}}{H_{\text{dep}}}\right)^{\beta}, \tag{1.40}$$

where v_{T} is the DW velocity in the absence of pinning and $\beta = 0.25$ is the depinning exponent [78]. Indeed the velocity is 0 when $H = H_{\text{dep}}$, and increases steeply with increasing H, as shown for $T = 0$ in Figure 1.10b. When the temperature does become significantly large enough, so-called thermal rounding occurs. The velocity is non-zero at the depinning field:

$$v\left(H_{\text{dep}}, T\right) = v_{\text{T}} \left(\frac{T}{T_{\text{d}}}\right)^{\psi}, \tag{1.41}$$

where $\psi \approx 0.15$ is the thermal rounding exponent [79]. This rounding is visible around the depinning transition for the $T > 0$ curve in Figure 1.10b.

Much like the creep regime, the depinning transition can also be described with universal dynamics. Diaz Pardo *et al.* [77] showed that the velocity in the depinning regime can be written as

$$v(H > H_{\text{dep}}, T) = \frac{v\left(H_{\text{dep}}\right)}{x_0} \left(\frac{T_{\text{d}}}{T}\right)^{\psi} \left(\frac{H - H_{\text{dep}}}{H_{\text{dep}}}\right)^{\beta}, \tag{1.42}$$

where $x_0 = 0.65$ is a universal constant.

The depinning transition ends with a crossover to the flow regime. However this crossover is not yet well understood.

1.3.3.3 Flow regime

In the flow regime, the effect of the disorder on the DW dynamics is reduced, and the velocity as predicted by the q-ϕ model is recovered. However, depending on the relative values of H_{W} and H_{dep}, the flow velocity can either be in the steady-state regime or in the precessional regime. This is schematically illustrated in Figure 1.11. In the case where $H_{\mathrm{W}} > H_{\mathrm{dep}}$ (Fig. 1.11a), the measured DW velocity in the flow regime is the steady-state regime. After passing the Walker field, the breakdown towards the precessional regime can be observed. When $H_{\mathrm{W}} < H_{\mathrm{dep}}$ (Fig. 1.11b), the Walker breakdown can be hidden in the creep regime. The observed velocity in the flow regime is thus the precessional regime.

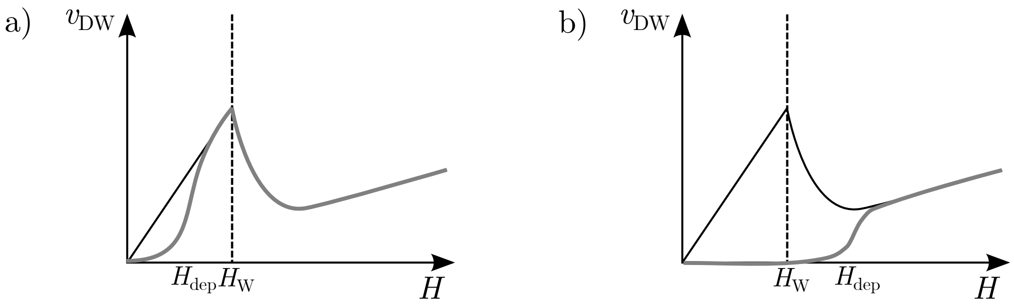

Fig. 1.11: Domain wall velocity in the flow regime | Schematic representation showing two cases for DW dynamics in the flow regime. The black curve shows the DW velocity as predicted by the q-ϕ model, the thick grey curve shows the DW velocity in samples with disorder. a) $H_{\mathrm{W}} > H_{\mathrm{dep}}$. The measured velocity in the flow regime is the steady-state velocity, after which the Walker breakdown can be observed. b) $H_{\mathrm{W}} < H_{\mathrm{dep}}$. The Walker breakdown in hidden in the creep regime, and only the precessional regime is visible in the flow regime.

The inclusion of the velocity plateau that occurs above H_{W} due to 2D effects further complicates the velocity curves that can be observed in the flow regime. The behavior as described in Figure 1.11 still holds, where, depending on the values of H_{W}, H_{dep} and H_{S}, the plateau might be fully visible ($H_{\mathrm{dep}} < H_{\mathrm{W}}$), partly visible ($H_{\mathrm{dep}} \approx H_{\mathrm{W}} < H_{\mathrm{S}}$), or not visible at all ($H_{\mathrm{dep}} > H_{\mathrm{S}} > H_{\mathrm{W}}$) [64].

Moreover, recent micromagnetic simulations have predicted that polycrystalline disorder also affects the flow dynamics; through per-grain variation of magnetic parameters [81,82] and grain size distribution [80]. The effects of grain size distribution are shown in Figure 1.12. Figure 1.12a shows the field driven DW velocity for samples with differing average polycrystalline grain size d. Indeed, the value of d has a strong effect on the height of the velocity plateau. This effect is modelled through the dissipation of energy through emission of so-called spin waves (see Section 1.4.2.2 for

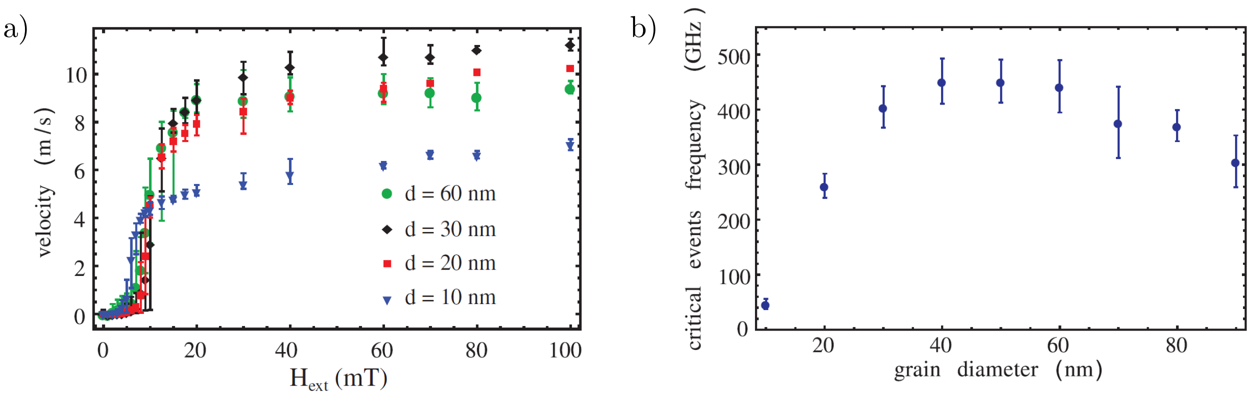

Fig. 1.12: Effect of disorder on flow domain wall velocity | a) DW velocity in samples with varying grain sizes d obtained from micromagnetic simulations. b) Frequency of critical depinning events for a DW moving in the flow regime for different grain diameters. Figure adapted from Ref. [80].

more details) at local DW depinning events [80,83]. The frequency of these depinning events as a function of grain size is shown in Figure 1.12b, where a clear dependence is revealed.

Varying approaches to model the contribution of disorder exist, either through adding an extrinsic component to the effective damping [81,82], or considering in-plane variations of the anisotropy easy axis [83]. H_{W}, H_{S}, and their corresponding velocities v_{W} and v_{S}, depend strongly on the damping. Care should be taken when analyzing DW velocity in samples with disorder, since it is still unclear how to separate the effects of disorder and other magnetic properties [64,83].

In Chapter 3 of this thesis we will show that we can use DW motion techniques to obtain information about the nanoscale disorder.

1.3.4 Current-driven domain wall dynamics

Magnetic fields are not the sole means of moving DWs. In this section, we provide a brief overview of the current-driven motion of DWs. Although we will not delve into this topic in-depth, we refer to Ref. [51] and the references therein for more information. The dynamics of current-driven DWs rely on spin torques that result from the flow of electrons with a preferred spin direction, known as a spin-polarized current (or spin current). Two dominant types of spin torques can move DWs: spin-transfer torque (STT) and spin-orbit torque (SOT).

STT involves the scattering of spin-up and spin-down electrons in a FM material. As current flows through a magnetic domain, the flowing electrons naturally become spin-polarized in the same direction as the domain's magnetization due to the different scattering rates between spin-up and spin-down electrons. When the current crosses the DW into an oppositely magnetized domain, the electron's spin flips. Its angular momentum transfers to the local magnetization within the DW due to the spin-conservation of the s-d exchange interaction. The resulting torques move the DW.

SOT involves the conversion of orbital angular momentum to spin angular momentum via SOC. In HM/FM/NM stacks similar to those studied in this thesis, the spin current generates in the bulk of the HM or at the HM/FM interface due to the HM's significant SOC. SOT can be explained by two different effects: the spin-Hall effect (SHE) and the Rashba-Edelstein effect. In SHE, electrons are deflected when they flow through the metal, depending on their spin. Electrons with opposite spins deflect in opposite directions, generating a spin current that flows towards and away from the HM/FM interface, depending on the spin direction. The spin current flowing towards the FM layer transfers its angular momentum to the local magnetic moments, resulting in a torque on the magnetization. In the Rashba-Edelstein effect, electrons near the HM/FM interface align their spin with the Rashba field, generating a spin density near the HM/FM interface that exerts a torque on the FM magnetization through the s-d exchange interaction.

We can use the same analysis as in Section 1.3.2, with an adapted LLG equation that includes the torques generated by STT and SOT. The details are available in Ref. [51]. In general, the STT causes the DW to move in the opposite direction of the current flow. For SOT, the DW's direction of motion depends on the sign of the deflection angle, i.e., spin-Hall angle (SHA), the current direction, and the DW's magnetization rotation direction (also known as its chirality). Despite the different torques driving the DW, it still experiences a Walker-like breakdown and pinning due to material disorder. Thus, the overall physics of DW dynamics described in Sections 1.3.2 and 1.3.3 is expected to stay the same.

In this thesis, we have yet to focus on current-driven DW motion directly. However, for applications, it is vital to mention that our results are expected to apply to current-driven DW motion as well.

1.3.5 A brief word on skyrmion dynamics

The above discussion can be extended to skyrmions, which are magnetic quasi-particles that can be visualized as a 360-degree DW. Skyrmions have recently generated interest for their potential applications. In Section 2.4, we will elaborate on how irradiation affects them. Although we do not directly study skyrmion dynamics in this thesis, we will briefly touch upon their significant physics, unique properties, and motion peculiarities for future applications. For more information, please refer to Ref. [51] and the references therein.

Skyrmions are defined as non-collinear spin textures comprising circular domains enclosed by a DW of the same chirality. This results in a magnetization profile that continuously rotates 360 degrees along the diameter of the skyrmion. Due to this specific profile, skyrmions are relatively stable theoretically. Moreover, skyrmions can be driven by a polarized current and can be reduced to a few nanometers in size, similar to DWs. Intriguingly, the critical depinning current for a skyrmion to move is four to five orders of magnitude lower than that required to move a DW, making skyrmions particularly appealing for applications such as racetrack memory and logic. Skyrmions were first observed experimentally in non-centro-symmetric bulk crystals such as MnSi and FeGe. More recently, they have also been found in many different HM/FM/HM and HM/FM/NM single- and multilayers.

The stability and nucleation of skyrmions depend on the same interplay of magnetic parameters as discussed in Sections 1.1 and 1.2. Skyrmions usually exist within a narrow range of values for the exchange interaction, DMI, anisotropy, and applied magnetic field. Typically, skyrmions are stable when the DMI is relatively large compared to the anisotropy and the exchange interaction. This results in a low DW energy (see Eq. 1.25), favoring the non-collinear rotation of spins characteristic of skyrmions.

Skyrmion motion can be modeled using the Thiele formalism, treating the skyrmion as a rigid particle and enabling consideration of only the motion of the center of mass of the skyrmion. In addition to the current-driven force from the SOT and the damping dissipative force present for regular DWs, skyrmions experience an extra gyrotropic force. This gyrotropic force is similar to a Magnus force and causes a deflection of the skyrmion's path from its SOT force-imposed direction. This deflection is known as the skyrmion Hall effect (SkHE), and the deflection angle is the skyrmion Hall angle (SkHA), which depends only on the center spin's direction.

Thus, skyrmion motion is similar to DW motion, encountering similar issues with pinning at low driving forces and instability at large driving forces. Therefore, the results presented in this thesis are also expected to apply to skyrmion motion. The SkHE introduces another challenge in controlling skyrmion motion. However, promising recent results indicate that ion irradiation can be used to counteract the SkHE (see Section 2.4s).

1.4 Measuring Magnetism

So far in this chapter, we focused our discussion on the magneto-static interactions, domains and DWs, as well as the dynamics of said DWs that are induced when a magnetic field is applied. As we have seen, in order to predict the magnetic ground state and the magnetization dynamics, we need to be able to measure these magnetic interactions. In this section, we will treat various experimental techniques that allow us to measure magnetic interactions. These techniques will be used throughout the experimental chapters of this thesis to gain a better understanding of the physics in our magnetic samples. This section is split into two parts. In Section 1.4.1, we discuss techniques that measure the entire magnetic state, also called magnetometry. In Section 1.4.2, we will discuss techniques that make use of magnetization dynamics and collectively precessing magnetic moments, also called *magnons*.

1.4.1 Magnetometry techniques

Magnetometry describes the measurement of the magnetic moment of a sample, typically as a function of an external magnetic field. The corresponding M-H curve shows the characteristic *hysteresis loop*, which is a result of the competition of the micromagnetic energies discussed in Section 1.1. A sketch of a hysteresis loop for a sample showing PMA is shown in Figure 1.13. Three cases with different angles between the easy-axis and $\mathbf{H}$ are shown. At large fields, the sample is saturated and we can determine M_s. The remanant magnetization $M_\mathrm{r} = M\left(H = 0\right)$ changes with the applied field angle. The coercive field H_c, where $M\left(H_\mathrm{c}\right) = 0$, indicates the field where the

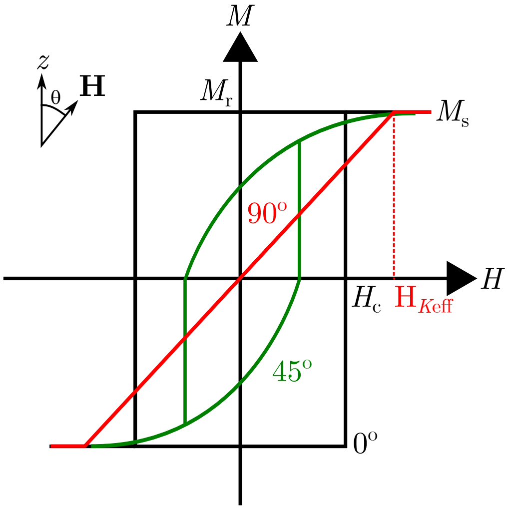

Fig. 1.13: Hysteresis loop | An example of a hysteresis loop of a uniaxial magnet for different angles $\theta = 0°$ (black), 45° (green), and 90° (red) between the applied field $\mathbf{H}$ and the easy axis ($\hat{\mathbf{z}}$ in case of PMA). The red dotted line shows the anisotropy field $H_{K_{\text{eff}}}$.

magnetization switches direction. From the hard axis loop (red), we can determine the anisotropy field (see also Section 1.1.4.4). Of note is that the hysteresis loop shown in Figure 1.13 is only valid for the so-called macro-spin approximation, where we consider the magnetization in the sample to behave like a single magnetic moment. In reality, magnetization reversal is more complicated and can result in differently shaped hysteresis loops [28], although the basic principles discussed here still apply.

In the following we will discuss the working principles of various techniques that have been used to probe the magnetic moment in the experiments in this thesis.

1.4.1.1 Vibrating Sample Magnetometry

In vibrating sample magnetometry (VSM) [84–86], the magnetization of a sample can be measured by vibrating the sample at a certain frequency in a static magnetic field. The vibrating magnetization of the sample perturbs the static DC field from the electromagnets. This perturbation can be measured by some pick-up coils. The current generated in the pick-up coils is a result of Faraday's law, and is proportional to the magnetization of the sample. The pick-up coils can be arranged in different orientations depending on the orientation of the field and the desired component of the magnetization to be measured. The strength of the static field determines the magnetization in the sample. By using a lock-in technique, noise from other vibrational sources can be eliminated. VSMs can reach sensitivities of up to 10^{-8} A m^2.

In this thesis we used several VSMs to measure hysteresis loops and the saturation magnetization of thin film samples. Among them are an EZ9 VSM from ADE and an EZ9 VSM from Microsense, capable of measuring up to 2.5 T at temperatures between 0 and 800 K, with a sensitivity of up to 10^{-8} A m^2. Furthermore a homemade VSM has been used, which is capable of measuring up to fields of 1 T with a sensitivity of 10^{-8} A m^2.

1.4.1.2 Superconducting Quantum Interference Device with VSM

To enhance the sensitivity of a VSM even further, it is often combined with a superconducting quantum interference device (SQUID) [87]. A SQUID makes use of parallel Josephson junctions, which are used to count the quantized magnetic flux. Vibrating the sample through superconducting pick-up coils generates a current, which is analyzed by the SQUID circuit. This provides a very accurate measurement of the magnetic moment in the sample, with typical sensitivities ranging from 10^{-10} A m^2 all the way down to 10^{-12} A m^2 [28]. A downside of SQUID-VSM compared to regular VSM is that a SQUID-VSM measurement is very time consuming and more sensitive to external perturbations.

For the measurements in this thesis, we used a MPMS SQUID VSM from Quantum Design. It is capable of applying magnetic fields up to 7 T, at temperatures ranging from 2 K to 1000 K. It can reach sensitivities up to 10^{-10} A m^2. In this thesis it is used to obtain accurate measurements of the saturation magnetization.

1.4.1.3 Alternating Gradient Field Magnetometry

Alternating gradient field magnetometry[1] (AGFM) is often cited as a technique which combines the speed of VSM with the accuracy of SQUID measurements [88]. A magnetic sample is suspended in a DC field which controls the magnetization of the sample. Small gradient coils create an alternating magnetic field gradient. The force applied to the sample is proportional to the magnetization and the gradient strength. The AC field gradient causes the sample to vibrate, which is converted into an electrical signal via the piezo-electric sample holder. By varying the AC field gradient close to the mechanical resonance frequency of the sample rod, the signal can be greatly enhanced. A lock-in technique is used to reduce noise from external vibrations. While this technique is very fast and sensitive, it is also quite susceptible to ambient mechanical and acoustic noise.

In this thesis, we used a PMC MicroMag 2900 Series AGM from LakeShore. It has a sensitivity of roughly 10^{-10} A m^2, and can apply fields up to 2 T. It is used to obtain hysteresis loops and measurements of the saturation magnetization.

1.4.2 Magnon-based techniques

In this section we describe how we can use magnetic excitations to obtain information about the magnetic parameters discussed in Section 1.1. These excitations are typically called magnons, and can be pictured as a collection of magnetic moments precessing around an effective field, as described by the LLG equation (see Section 1.3.1).

Magnons can exhibit a phase difference between neighbouring spins and can be seen as a $k \neq 0$ excitation, showing wave-like behavior with a wavelength $\lambda = 2\pi/k$, where k is its wave vector. The $k = 0$ magnon then describes uniform precession. Figure 1.14 schematically shows a higher-order magnon. It is often referred to as a *spin wave*, as we will also do for the remainder of this thesis.

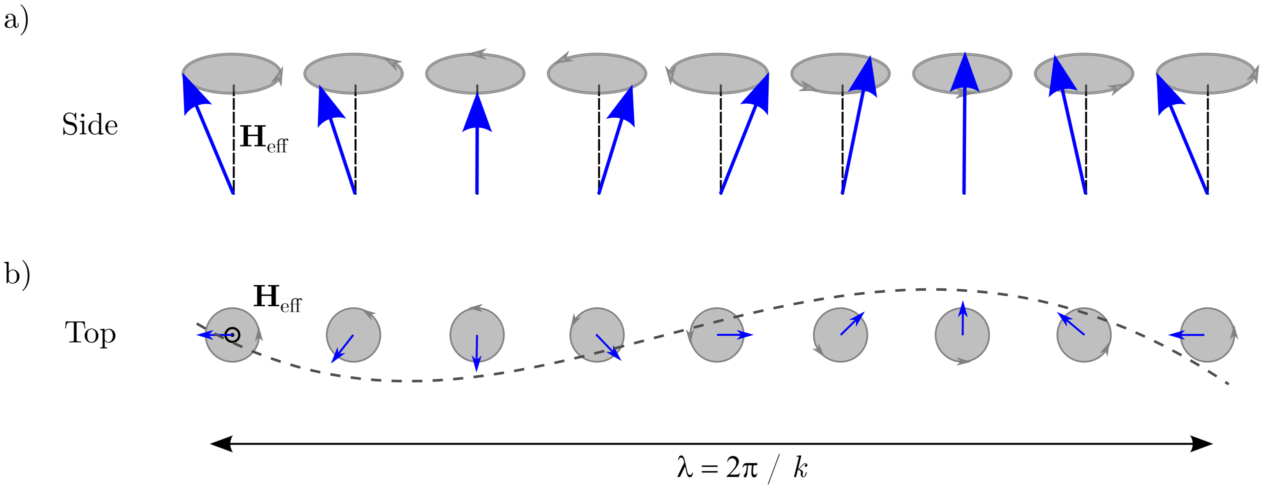

Fig. 1.14: Schematic representation of a spin wave | a) Side b) and top view of a spin wave with wavelength λ. The magnetization precesses around the effective field, with a phase difference between neighboring spins. Figure adapted from Ref. [89].

---

[1] Also called Alternating Gradient Magnetometry (AGM) or Alternating Gradient Force Magnetometry (AGFM).

In this section, we describe two techniques that probe spin waves. $k = 0$ spin waves can be probed by studying ferromagnetic resonance phenomena, whereas $k \neq 0$ spin waves can be studied by Brillouin light scattering measurements.

1.4.2.1 Ferromagnetic Resonance

Ferromagnetic resonance (FMR) measurements make use of resonance phenomena of precessing magnetic moments to gain information about a range of magnetic properties. The resonance can be induced by periodically exciting the magnetic system. When exciting the system at the resonance frequency f_{res}, the oscillations in the system are the largest. The resonance conditions can be derived from the LLG equation when considering a static field $\mathbf{H}_{\mathrm{DC}}$ that is perturbed by a small RF field $\mathbf{h}_{\mathrm{RF}}$, typically applied perpendicular to the direction of $\mathbf{H}_{\mathrm{DC}}$. We will not treat the entire derivation here, instead for a complete description we refer to Refs. [90,91].

The resonance condition is given by the famous Kittel formula, which, for ultra-thin films with PMA, $\mathbf{H}_{\mathrm{DC}} = H\hat{\mathbf{z}}$ out of the plane, and $\mathbf{h}_{\mathrm{RF}}$ applied in the plane, reads

$$f_{\mathrm{res}} = \frac{\gamma_0}{2\pi}\left(H + H_{K_{\mathrm{eff}}}\right). \tag{1.43}$$

Similarly, for films with in-plane anisotropy (i.e. $H_{K_{\mathrm{eff}}} < 0$), $\mathbf{H}_{\mathrm{DC}} \perp \mathbf{h}_{\mathrm{RF}}$ applied both in the plane, the Kittel formula is given by

$$f_{\mathrm{res}} = \frac{\gamma_0}{2\pi}\sqrt{H\left(H - H_{K_{\mathrm{eff}}}\right)}. \tag{1.44}$$

In a typical FMR measurement as performed in this thesis, the resonance conditions are found by setting the frequency f of $\mathbf{h}_{\mathrm{RF}}$, and then sweeping the DC magnetic field H to find the resonance. The absorbed power, which is measured by comparing the input with the output RF power, has the shape of an anti-Lorentzian [90], given by

$$\chi'' = A_{\mathrm{sym}}\frac{\left(\frac{1}{2}\Delta H\right)^2}{\left(\frac{1}{2}\Delta H\right)^2 + \left(H - H_{\mathrm{res}}\right)^2} - B_{\mathrm{asym}}\frac{\left(\frac{1}{2}\Delta H\right)\left(H - H_{\mathrm{res}}\right)}{\left(\frac{1}{2}\Delta H\right)^2 + \left(H - H_{\mathrm{res}}\right)^2}, \tag{1.45}$$

where ΔH is the full width at half maximum (FWHM) of the Lorentzian, A_{sym} and B_{asym} the amplitudes of the Lorentzian and the asymmetric correction, respectively, and H_{res} the field at which resonance occurs. Due to the lock-in technique that is used, the actual measured signal is the derivative of Equation 1.45, given by [90]

$$\frac{d\chi''}{dH} = -2A_{\mathrm{sym}}\frac{\left(\frac{1}{2}\Delta H\right)^2\left(H - H_{\mathrm{res}}\right)}{\left(\left(\frac{1}{2}\Delta H\right)^2 + \left(H - H_{\mathrm{res}}\right)^2\right)^2} - B_{\mathrm{asym}}\frac{\left(\frac{1}{2}\Delta H\right)\left(\left(\frac{1}{2}\Delta H\right)^2 - \left(H - H_{\mathrm{res}}\right)^2\right)}{\left(\left(\frac{1}{2}\Delta H\right)^2 + \left(H - H_{\mathrm{res}}\right)^2\right)^2}. \tag{1.46}$$

All FMR spectra obtained from experiments performed in this thesis have been analyzed with Equation 1.46. An example of an FMR spectrum is shown in Figure 1.15. The measured absorption is shown in black, with the solid red line showing the fit with Equation 1.46. The integrated data is shown in grey, and fitted with Equation 1.45 shown in red dots. It follows the anti-Lorentzian shape. H_{res} corresponds to the point where the derivative crosses 0 in between the two peaks, and is indicated with a blue dotted line. The FWHM of the Lorentzian ΔH, shown with the pink horizontal line, can be extracted from the peak-to-peak width of the raw signal via $\Delta H_{\mathrm{pp}} = \Delta H/\sqrt{3}$ [90], which is shown in green.

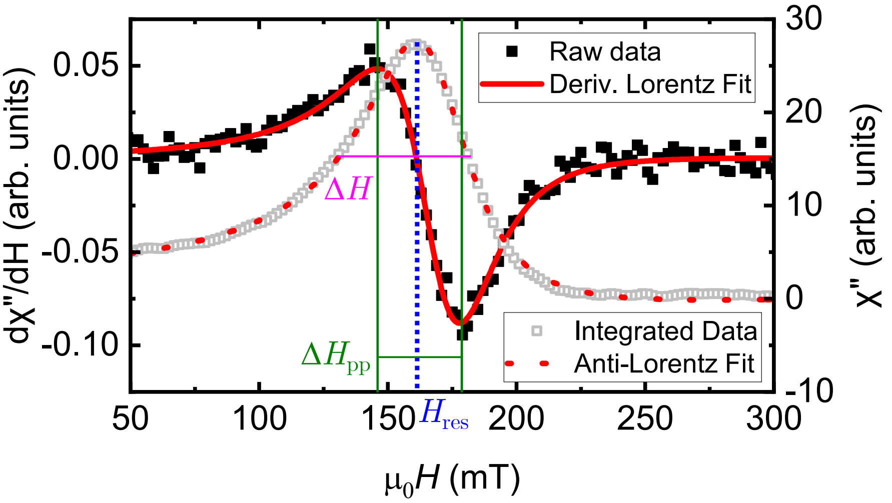

Fig. 1.15: An example of an FMR spectrum | Measured FMR spectrum of a W(4)/CoFeB(1)/MgO(2)/Ta(3) (thickness of each layer between brackets in nm) thin film sample, with the raw data in black and the fit with Equation 1.46 indicated with a solid red line. The integrated data showing the anti-Lorentzian form is shown in grey, with the fit indicated with a red dotted line. The blue line indicates H_{res}. ΔH_{pp} is shown with green lines, and the pink horizontal line shows the FWHM of the Lorentzian ΔH.

The FWHM of the anti-Lorentzian depends on the damping, and is given by

$$\Delta H = \frac{4\pi\alpha}{\gamma_0} f + \Delta H_0, \tag{1.47}$$

where ΔH_0 is a catch-all term called the *inhomogeneous broadening* that is often used to denote the influence of inhomogeneities in the system. Grains in polycrystalline materials can have slightly varying magnetic parameters, which in turn result in slightly different resonance fields, which contribute to the additional linewidth. Note that Equation 1.47 is not a complete equation: different mechanisms, such as two-magnon scattering [92], can further contribute to the linewidth of the FMR spectra. For measurements with $\mathbf{H}_{\mathrm{DC}}$ perpendicular to the sample plane, Equation 1.47 is valid. Equations 1.43 and 1.47 thus show that FMR can be a powerful technique to probe the anisotropy, damping and disorder in a magnetic sample.

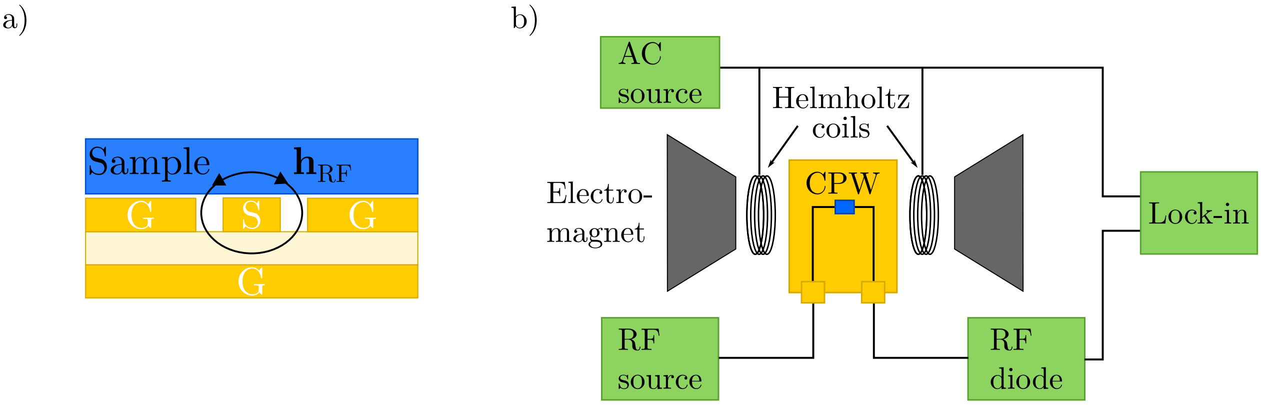

Fig. 1.16: A broadband FMR spectroscopy setup | a) Cross-section of a CPW (gold) with a sample (blue) on top. $\mathbf{h}_{\mathrm{RF}}$ generated by the CPW is shown in black. b) Schematic drawing of the FMR setup with lock-in detection.

A schematic representation of a typical FMR measurement setup is shown in Figure 1.16. Figure 1.16a shows a cross-section of a co-planar waveguide (CPW) with a sample on top. The RF signal travelling through the CPW generates $\mathbf{h}_{\mathrm{RF}}$. Figure 1.16b is a schematic representation of the entire setup. The CPW as shown in Figure 1.16a is placed between the poles of an electromagnet, which generates $\mathbf{H}_{\mathrm{DC}}$. A lock-in is used to filter out noise contributions at other frequencies than the reference frequency. Helmholtz coils are used to modulate the FMR signal with a small AC field[1] parallel to $\mathbf{H}_{\mathrm{DC}}$.

For the experiments in this thesis, we used a PhaseFMR and CryoFMR from NanOsc Instruments AB. It is capable of probing frequencies between 2 GHz and 40 or 60 GHz, respectively, at DC fields up to 0.9 T when the field is in the plane of the sample, and 1.4 T when the field is perpendicular to the plane of the sample. Is has been used to accurately measure $H_{K_{\mathrm{eff}}}$, the Gilbert damping constant α, and the inhomogeneous broadening ΔH_0.

1.4.2.2 Brillouin Light Scattering

Brillouin light scattering (BLS) [93,94] is a powerful technique in which we use light scattering with higher-order magnons to probe material parameters. Notably, it is a very powerful method to measure the strength of the DMI [35].

In BLS, a photon interacts with a spin wave in the material. This scattering process is inelastic, meaning the energy of the photon and the spin wave is not conserved. Two types of scattering processes exist; a Stokes process, where a spin wave is created as a result of the scattering, and an anti-Stokes process, where a spin wave is destroyed. After the Stokes (anti-Stokes) process, the backscattered photon has lost (gained) energy, and will thus show a slight shift in its frequency. This frequency shift is very small, but can be resolved with a Fabry-Perot interferometer. We will not treat the exact working principles of Fabry-Perot interferometry here, but an overview can be found in Ref. [93].

For the experiments in this thesis, the BLS measurements were performed with a strong in-plane field $H > H_{K_{\mathrm{eff}}}$, so that the samples with PMA are saturated in the plane. The spin waves that are probed are then in the so-called Damon-Eshbach mode [95]. An example of a resulting spectrum as measured by BLS is shown in Figure 1.17. Apart from the central peak, which represents phonon scattering,[2] two clear peaks are visible. They correspond to the Stokes and anti-Stokes scattering processes. The solid lines are fits with Lorentzians.

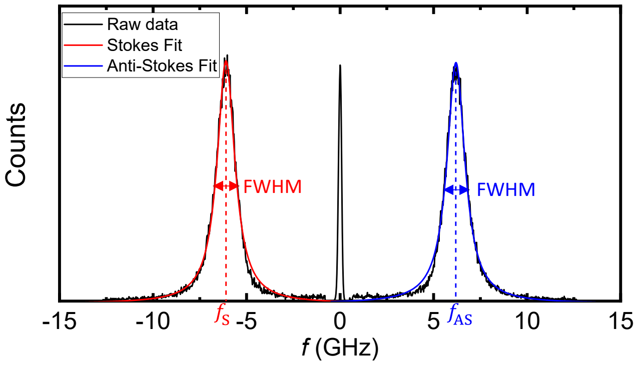

Fig. 1.17: Example spectrum as obtained with BLS | A typical BLS spectrum containing an manually attenuated central peak, and the Stokes and Anti-Stokes peaks. The solid red and blue lines are fits with Lorentzians on the Stokes and anti-Stokes peaks, respectively.

---

[1] Not to be confused with the RF field generated by the CPW.

[2] The central peak in Figure 1.17 is manually attenuated.

Like in FMR, we can obtain information about the magnetic properties from the center frequency and width of the Stokes and anti-Stokes peaks. For $H > H_{K_{\text{eff}}}$ and samples with PMA, this frequency is given by [96]

$$
\begin{aligned}
f &= f_0 \pm f_{\text{DMI}} \\
&= \frac{\gamma\mu_0}{2\pi}\sqrt{\left(H + J_0 k_{\text{SW}}^2 + P\left(k_{\text{SW}}t\right) M_{\text{s}}\right)\left(H + J_0 k_{\text{SW}}^2 - P\left(k_{\text{SW}}t\right) M_{\text{s}} - H_{K_{\text{eff}}}\right)} \pm \frac{\gamma}{\pi M_{\text{s}}} D k_{\text{SW}},
\end{aligned}
\tag{1.48}
$$

where k_{SW} is the spin-wave wave vector, $J_0 = 2A/\left(\mu_0 M_{\text{s}}\right)$ is the spin wave stiffness factor, $P\left(k_{\text{SW}}t\right) = 1 - \left(1 - e^{-|k_{\text{SW}}|t}\right)/\left(|k_{\text{SW}}|\,t\right)$, and K_{eff} is the effective anisotropy field. Note that the center frequency f_0 is shifted due to the DMI with a term f_{DMI}. This is because the DMI favors spin waves with either a negative or positive wave vector, depending on its sign [97,98].

We can thus extract the DMI strength from BLS spectra by measuring the difference between the Stokes and anti-Stokes peaks. This difference is given by[1]

$$
\Delta f = f_{\text{AS}} - f_{\text{S}} = 2 f_{\text{DMI}} = \frac{2\gamma}{\pi M_{\text{s}}} D k_{\text{SW}}. \tag{1.49}
$$

To obtain a more accurate measurement of the DMI, Δf is usually measured for several k_{SW}. We can set the value of k_{SW} that is probed in the BLS experiment, since it depends only on the measurement geometry and the wavelength of the light λ through the following relation

$$
k_{\text{SW}} = \frac{4\pi \sin\left(\theta_{\text{inc}}\right)}{\lambda}. \tag{1.50}
$$

Here θ_{inc} is the incidence angle of the light with respect to the sample plane.

Similarly to FMR, the width of the peaks in the BLS spectrum can give us more information about damping phenomena. For $H > H_{K_{\text{eff}}}$, the FWHM is given by

$$
\text{FWHM} = \frac{\alpha\gamma_0}{2\pi}\left(2H - H_{K_{\text{eff}}}\right) + \delta f_0. \tag{1.51}
$$

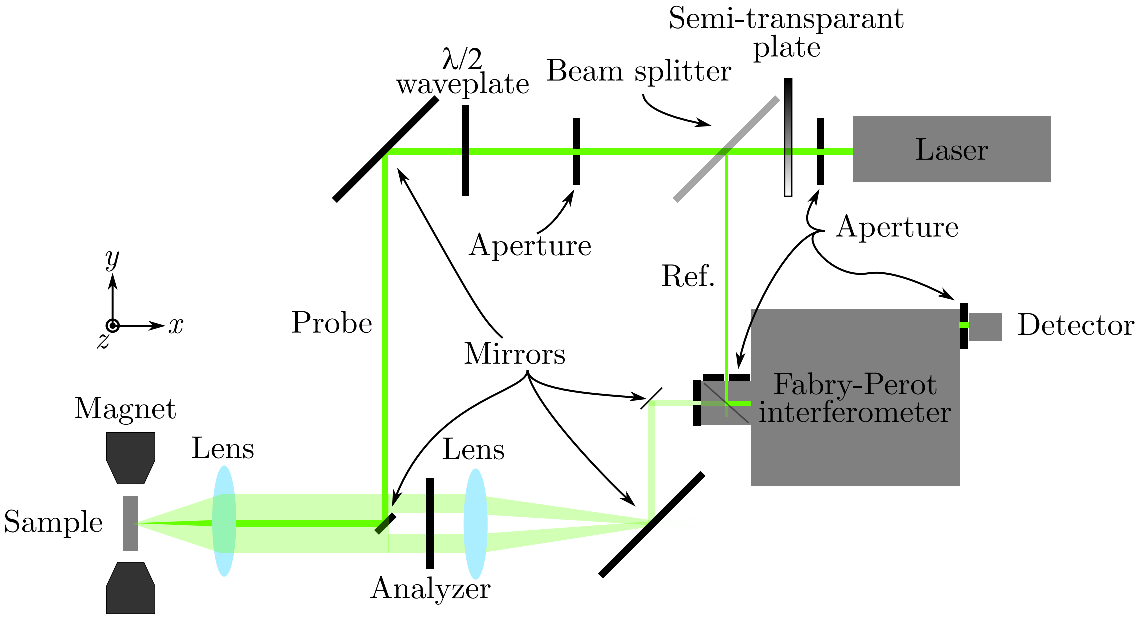

Fig. 1.18: Diagram of the Brillouin light spectroscopy setup | See text for details.

---

[1] Note that depending on the measurement geometry, care needs to be taken to obtain the correct sign of the DMI when calculating Δf. For a left-handed geometry, the correct sign is obtained when using Equation 1.49. For right-handed geometries, one should take $\Delta f = f_{\text{S}} - f_{\text{AS}}$ instead [96]. In general, we used a left-handed geometry for the measurements in this thesis. When a right-handed geometry was used, we will explicitly mention it.

The first term in Equation 1.51 describes the increase in width due to damping. Similar to FMR, the second term describes the inhomogeneous broadening that occurs due to other damping mechanisms, disorder, and the broadening that arises from the finesse of the Fabry-Perot spectrometer cavity. The latter is equal to the width of the central peak in the BLS spectra. Under the assumption that the main inhomogeneous broadening is due to disorder in the form of variations in the anisotropy field, δf_0 is given by [99]

$$\delta f_0 = \frac{\gamma_0 H}{4\pi\sqrt{H^2 - HH_{K_{\mathrm{eff}}}}} \Delta H_{K_{\mathrm{eff}}}, \tag{1.52}$$

where $\Delta H_{K_{\mathrm{eff}}}$ is the distribution of effective anisotropy fields.

The measurement geometry of the BLS setup used for the experiments in this thesis is shown in Figure 1.18. A 200-mW laser with wavelength $\lambda = 532$ nm is guided towards the sample. A semi-transparent plate is used to set the power of the beam, which for our measurements is set to 30 mW. A part of the beam is split off from the main beam to act as a reference for the Fabry-Perot interferometer. The probe beam passes through a $\lambda/2$-waveplate to set the direction of the linear polarization. The back-scattered light is cross-polarized, and thus passes through an analyzer, which is set to the vertical direction,[1] before being focused onto the Fabry-Perot interferometer. Magnets are placed close to the sample in order to apply an in-plane field in the y direction. The sample can rotate in the x-z plane to define θ_{inc} (with respect to the z-axis). This geometry is called the back-scattering geometry.

1.5 Imaging Magnetism: magneto-optics

Throughout this thesis we use optical techniques to study DW motion. These optical techniques allow us to visualize domains and how they change when magnetic fields are applied. These techniques make use of the magneto-optical Kerr effect (MOKE), discovered by John Kerr in 1877 [100]. In this section we will discuss MOKE and its use in microscopy in more detail. There are several different geometries of MOKE that are used in microscopes, but for this discussion we will limit ourselves to the polar geometry; the incident light and magnetization are aligned perpendicular to the plane.

1.5.1 Magneto-Optical Kerr effect

The principles of polar MOKE are shown in Figure 1.19. For a detailed treatment of the physics of MOKE, we refer to Ref. [101]. Linearly polarized light, which can be seen as an equal contribution of left-handed circularly polarized (LCP) and right-handed circularly polarized (RCP) light, reflects off the surface of a magnetic material. Due to the magnetization in the sample, the reflective indices for LCP and RCP are not equal. Hence, in the case of Figure 1.19, more RCP is reflected than LCP. In total, this means that the polarization has rotated and gained some ellipticity. The strength of this effect is proportional to the magnetization of the sample.

Although a full quantum mechanical description is required to accurately describe MOKE due to its dependence on SOC, an intuitive understanding for the origin of MOKE can be obtained through a classical description. The magnetization in the material can be described using an effective magnetic field. The electrons in the material, which follow the electric field of the LCP and RCP light travelling through the material, experience an extra Lorentz force. Since the Lorentz force depends on the direction of rotation, this will result in the reduction of the radius of one sense of rotation and an increase in the other. This effectively results in different dielectric constants for LCP and RCP light, which in turn results in different reflective indices for LCP and RCP light.

---

[1] This polarization direction is chosen to correspond with the working polarization direction of the Fabry-Perot interferometer.

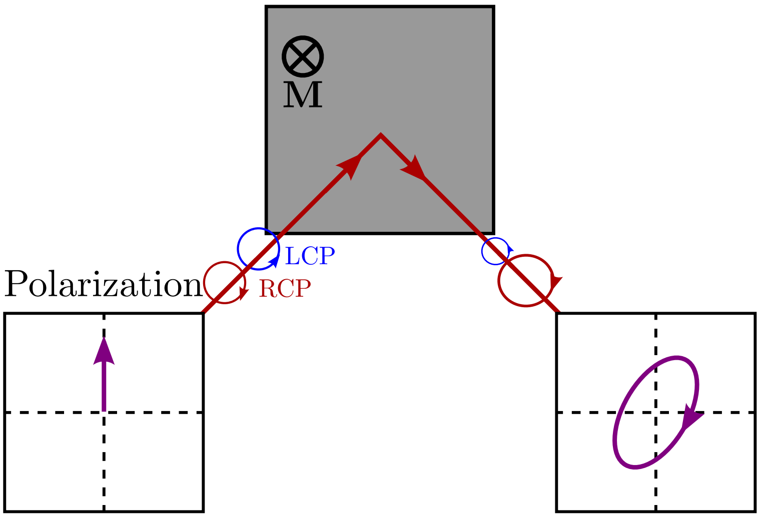

Fig. 1.19: The principles of polar MOKE | Linearly polarized light reflects off the sample surface. After reflection, the polarizaion has rotated and gained some ellipticity. This effect is proportional to the magnetization and is based on different refraction indices for left-handed circularly polarized (LCP) and right-handed circularly polarized (RCP) light. Image adapted from Ref. [89].

1.5.2 Kerr microscopy

We will now explain how we can use MOKE to “see” magnetism. Indeed it is impossible to see magnetization with the naked eye or under a regular microscope. However, by clever use of polarizers, we can use MOKE to visualize domains. Such a microscope is called a Kerr microscope [27].

An optical diagram of a typical Kerr microscope is shown in Figure 1.20a. Light from an LED is collected by a collimating lens and subsequently linearly polarized. A beam splitter directs the light towards the objective lens, which focuses the light onto the sample. If the sample has domains, the reflected light now contains a mixture of polarization; turned in one direction in areas with magnetization in one direction, and turned in the opposite direction in areas with opposite magnetization. A coil is placed close to the sample so that the magnetic state can be manipulated with magnetic fields. The reflected light travels back through the objective lens and beam splitter. It passes through an analyzer which is set almost perpendicular to the polarizer. This ensures that one sense of Kerr rotation is preferred over the other, and hence photons from areas with a certain Kerr rotation are collected in greater numbers by the camera. This shows up as a brighter spot compared to the areas where the Kerr rotation is in the opposite direction, and hence we can image magnetic domains. A typical image obtained from a Kerr microscope is shown in Figure 1.20b. The white domain in the center corresponds to one direction of the magnetization, while the grey area surrounding it corresponds to the opposite direction.

For the experiments in this thesis we used a range of different microscopes. For the majority of experiments shown in this thesis, we used a homemade Kerr microscope with an optical scheme as shown in Figure 1.20a. The spectrum of light from the LED has a center wavelength of roughly 640 nm, with a FWHM of around 20 nm. Using 20x, 50x, and 100x objectives, the microscope can reach sub-micrometer resolution when properly stabilized. The CMOS camera is a Moment camera from Teledyne photometrics, capable of imaging up to 50 frames per second. A range of coils is used, depending on the duration and strength of the magnetic field that is applied. This includes low-wind coils (~ 20) with short rising times (~ 100 ns) capable of reaching 45 mT, but also higher-wind coils (~ 120) with higher rising times (~ 1 μs) when longer pulses are required.

The DW motion experiments at very large fields in Chapter 4 have been performed using a commercial Kerr microscope from Evico magnetics. A micro-coil with ultra-short rising time (~ 1 ns) capable of reaching fields well above 100 mT has been used to obtain the data.

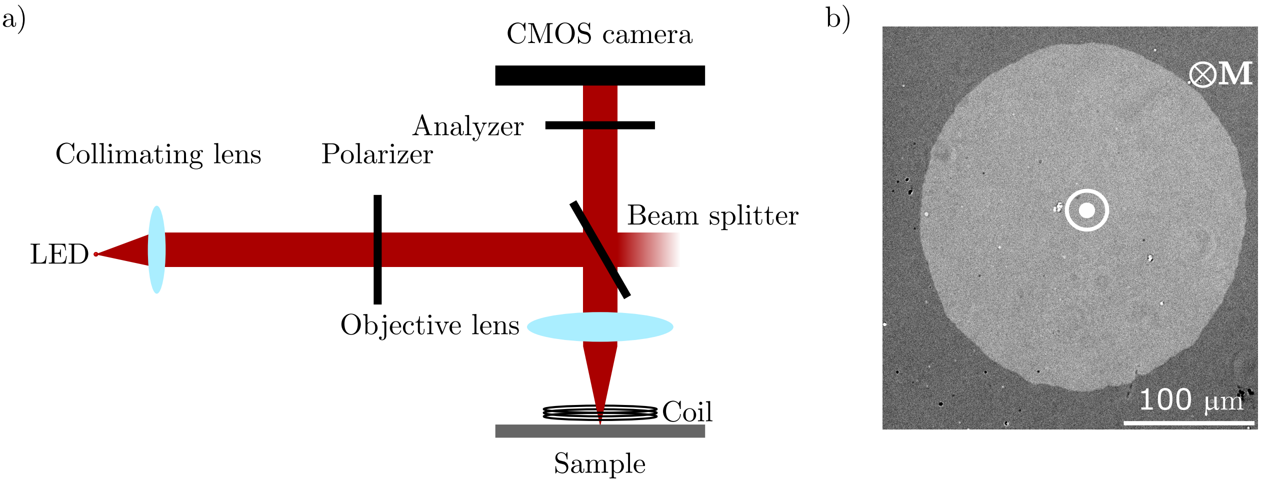

Fig. 1.20: A basic polar Kerr microscopy setup | a) Optical diagram of a basic polar Kerr microscope setup. Light is collected from an LED. It is subsequently polarized and focused onto the sample. The reflected light then passes through an analyzer and is collected by a CMOS camera. A coil is placed close to the sample to allow for the application of magnetic fields. b) Typical image as obtained with a Kerr microscope. The magnetic domain with magnetization opposite to its surroundings is shown in white.

1.5.3 Measuring domain wall motion with Kerr microscopy

Throughout this thesis we use Kerr microscopy to study DW motion. In this section we will discuss in more detail how this is done.

Most of the DW motion experiments have been performed using a quasi-static procedure, which is shown in Figure 1.21. It makes use of a set of magnetic field pulses with images taken in between them. It is schematically shown in Figure 1.21a. First the sample is saturated with a long, negative field pulse. A domain is subsequently nucleated using a short, strong, and positive field pulse. A first image is taken, which corresponds to the image shown in Figure 1.21b. The nucleated domain is shown in light grey. A measurement pulse is then applied, with the magnetic field in the same direction of the nucleated domain, causing it to grow. A second image is then taken, which is shown in Figure 1.21c. The original domain has grown. The distance over which the DW has traveled can be obtained by taking a differential image of Image 2 - Image 1. This is shown in Figure 1.21d. The grey area now shows the distance L over which the DW has traveled, which can be determined from its radius. The DW velocity is then obtained by

$$v_{\mathrm{DW}} = \frac{L}{t_{\mathrm{pulse}}}, \tag{1.53}$$

where t_{pulse} is the length of the applied pulse.

There are two important factors to consider when discussing the limitations of this technique. The first concerns the duration of the applied magnetic field pulse with respect to the coil rising time. If the magnetic field pulse is on the same order as the rising time, a significant amount of t_{pulse} is dominated by the non-linear shape of the pulse during the rising time. Equation 1.53 is then no longer valid. A way around this limitation is to measure L at the same magnetic field for different pulse times. The velocity is then extracted from the slope of the L-t_{pulse} curve. In the experiments in this thesis, the applied pulses were never shorter than 40 rise times, and so Equation 1.53 is accurate enough. The second limitation to consider is that the images are taken when the DW is at rest (hence the name quasi-static). This means that we are not probing the steady-state velocity of the DW during the magnetic field pulse. Instead the velocity is only calculated after the DW has relaxed. Furthermore, due to the inherent pinning of the DW in the materials studied in this thesis, thermal activation on the time scale of the image sequence is not strong enough to move the DW.

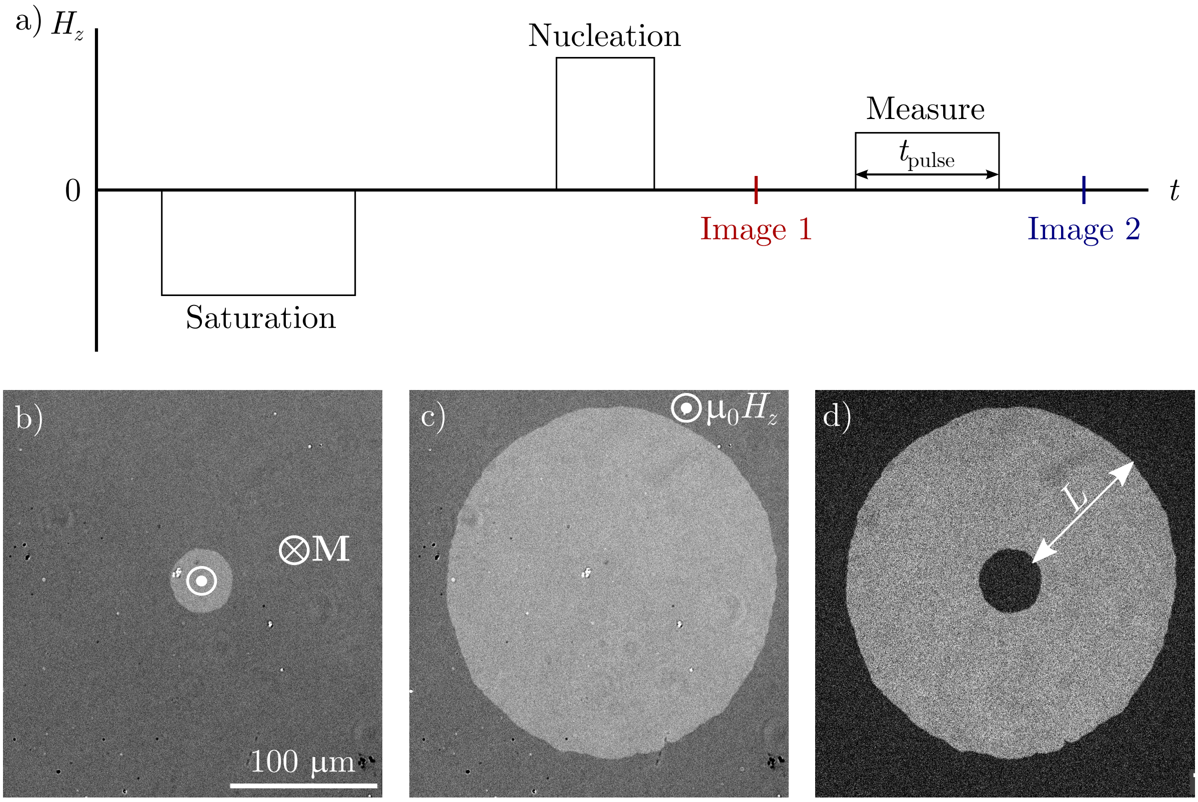

Fig. 1.21: Procedure for measuring domain wall motion | a) Scheme of magnetic field pulses applied during the measurement. The sample is first saturated by a long, negative field pulse. A domain is nucleated using a short, strong, and positive field pulse. A first image is taken, which corresponds to the image shown in b. A measurement pulse is then applied, which varies in height and length. After the pulse a second image is taken, which corresponds to the image shown in c. Figure adapted from Ref. [53]. b) Image after nucleation corresponding to image 1 in a. c) Image after the measurement pulse corresponding to image 2 in a. d) Image 2 - Image 1. The grey area now shows the distance over which the DW has traveled during the measurement pulse. L can be determined from the radius. The DW velocity can then be calculated by dividing L by t_{pulse}. Figures b-d inspired by Ref. [102].

Dynamic measurements have been performed for some of the data shown in Chapter 4. A movie is taken during the application of the pulse, and t_{pulse} is calculated from the difference between 2 frames: $\Delta t = t_2 - t_1$. The effect of DW relaxation is very small in the experiments in this thesis. Moreover, the velocity of the DW during these measurements is slow enough for the frame rate at which the movies where taken in order not to blur the image of the DW. Hence the two techniques can be interchanged without introducing a significant error.

1.6 Summary and conclusions

In this chapter, we have seen all the magnetic interactions that are at play in the materials that are studied in this thesis: ultra-thin films with PMA. We have seen how acting together they form magnetic domains and DWs. We have discussed dynamical effects, particularly how DWs move under an applied field. We have also discussed how these static and dynamic effects can be measured using magnetometry and various spectroscopy techniques. Furthermore we have seen how we can use MOKE to image magnetic domains and measure DW motion.

Throughout this chapter we have revealed that disorder plays a large role. On the atomic scale it influences the strength of various magnetic interactions, for example the DMI and (surface) anisotropy, which depend on smooth interfaces between materials. On a larger scale, i.e. several nanometers, disorder plays an important role in DW motion, since the DW width is in the same scale as the disorder - roughly 10s of nm. Furthermore, the typical energy barriers involved in pinning are similar to the DW energy and energies of the micromagnetic parameters - on the order of several $\mathrm{mJ/m^2}$. To optimize these magnetic parameters and DW motion, it is imperative to understand the role of nanoscale disorder on magnetic properties and control the atomic ordering.

In this thesis, we control and modify the atomic ordering using $\mathrm{He^+}$ irradiation. In the next chapter, we will discuss how $\mathrm{He^+}$ ions interact with magnetic materials and how it can be used to control the atomic ordering.

Chapter 2

Ion beam physics in magnetic materials

It's like playing pool, but with atoms!

Ion irradiation is a central topic in this thesis. In the last chapter, we have evidenced that many interactions and phenomena in magnetic materials are susceptible to rearrangements of atoms caused by He$^+$ irradiation. In this chapter, we aim at giving more insight into the interaction of ions with matter. We first treat the basic interactions between ions and matter, with a focus on the ion trajectory in Section 2.1, before discussing the effects in the target material in Section 2.2. There, we will also discuss how ion irradiation can enhance ordering through crystallization, which is a technique that we use in Chapter 3 of this thesis. In Section 2.3, we discuss the working principles of ion irradiation. At the end of this chapter - in Section 2.4 - we will give an overview of the latest results regarding ion beam physics in magnetic materials. It should be noted that in this chapter, we will mostly restrict ourselves to the effects caused by light atoms, particularly He$^+$. Comprehensive reviews of ion beam physics and ion-matter interactions, including the effects caused by heavy ions, can be found in Refs. [103–106].

2.1 Basic interactions between light ions and matter

A fast ion moving in an atomic lattice can collide with the nuclei of the atoms in the lattice - a so called *nuclear collision* - and with the electrons in the solid, which is called an *electronic collision*. During these collisions, the ion loses energy and can be deflected as it traverses the atomic lattice. In this section, we will describe the basic physics behind these collisions and the different stopping forces that play a role.

2.1.1 Binary elastic ion-matter collisions

2.1.1.1 Classical scattering kinematics

The easiest method to describe the nuclear and electronic collisions is by using the so-called binary elastic collision approach, in which the two particles are seen as two point charges. A basic sketch of such a collision is shown in Figure 2.1.

To best describe the collision, we will make use of two reference frames. In the laboratory system (LS, Fig. 2.1a), we will assume a stationary atom being hit by a moving ion. After the collision, the path of the ion is deflected by an angle Θ, and the recoil atom starts moving with an angle Λ with respect to the initial path of the ion. Since momentum is conserved due to the elastic nature of the collision, we can also describe the two particles using a center-of-mass system (CMS, Fig. 2.1b). In this case, the two particles can be described as a single particle with reduced mass

$$\mu = \frac{m_\mathrm{i} m_\mathrm{a}}{m_\mathrm{i} + m_\mathrm{a}}, \tag{2.1}$$

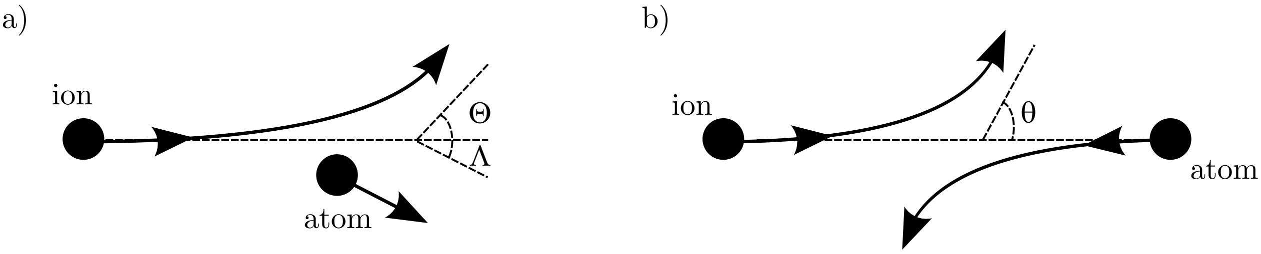

Fig. 2.1: A binary elastic collision | A sketch of a binary elastic collision in two different reference frames. a) Laboratory system. b) Center-of-mass system. Image adapted from Ref. [106].

and scattering angle θ, where m_i and m_a are the masses of the ion and atom, respectively.

Through conservation of momentum, the transformation between the reference frames is given by

$$\begin{aligned}\tan(\Theta) &= \frac{\sin(\theta)}{\frac{m_\mathrm{i}}{m_\mathrm{a}} + \cos(\theta)},\\ \Lambda &= \frac{\pi - \theta}{2},\\ \theta &= \Theta + \arcsin\left(\frac{m_\mathrm{i}}{m_\mathrm{a}}\sin(\Theta)\right).\end{aligned} \tag{2.2}$$

For light ions compared to target atoms, i.e. $m_\mathrm{i} \ll m_\mathrm{a}$, the transformation rules for Θ reduce simply to $\Theta = \theta$.

In the CMS, we can describe the relative kinetic energy of the system with

$$E_\mathrm{r} = \frac{m_\mathrm{a}}{m_\mathrm{i} + m_\mathrm{a}} E, \tag{2.3}$$

where E is the kinetic energy of the ion in the LS system. During the collision, energy is transferred from the ion to the atom. The transferred energy during the collision is given by

$$T = \gamma E \sin^2\left(\frac{\theta}{2}\right), \tag{2.4}$$

where $\gamma = 4m_\mathrm{i}m_\mathrm{a}/\left(m_\mathrm{i} + m_\mathrm{a}\right)^2$ is the so-called energy transfer factor. The maximum transferred energy $T_\mathrm{max} = \gamma E$ thus depends on the masses of the particles involved, as well as the ion energy. Some typical values for He^+ and Ga^+ ions with a kinetic energy of 30 keV colliding with different species of target particles are shown in Table 2.1.

Table 2.1: Typical maximum energy transfer values | Maximum energy transfer of 30 keV He^+ and Ga^+ ions in various target materials, according to Eq. 2.4.

$He^+ \to Co$	$He^+ \to W$	$He^+ \to B$	$Ga^+ \to Co$	$Ga^+ \to W$	$Ga^+ \to B$
13.5 keV	5.8 keV	29.6 keV	29.9 keV	25.0 keV	14.3 keV

The values reported in Table 2.1 are typically much larger than experimental values, and are only valid in the limit for very large scattering angles. The actual trajectory of the ion and the scattering geometry thus play a large role in determining the energy transfer. Furthermore, we have so far ignored any interaction between the two particles.

Figure 2.2 shows a sketch of the classical scattering trajectory of an ion scattering with atom. An ion entering the differential area dσ scatters with an atom, and is deflected into a differential solid angle dω. The deflection angle θ is the same as defined in the CMS system. We can find the scattering angle using a standard classical trajectory integral, given by [106]

$$\theta = \pi - 2p \int_{R_{\mathrm{min}}}^{\infty} \frac{1}{R^2} \left[1 - \frac{V(R)}{E_{\mathrm{r}}} - \frac{p^2}{R^2} \right]^{-1/2} \mathrm{d}R, \tag{2.5}$$

where p is the so-called collision parameter as sketched in Figure 2.2, and $V(R)$ is a symmetric atomic interaction potential which depends on the distance R between the ion and the atom. R_{min} is the minimal approach distance, corresponding to

$$1 - \frac{V(R_{\mathrm{min}})}{E_{\mathrm{r}}} - \frac{p^2}{R_{\mathrm{min}}^2} = 0. \tag{2.6}$$

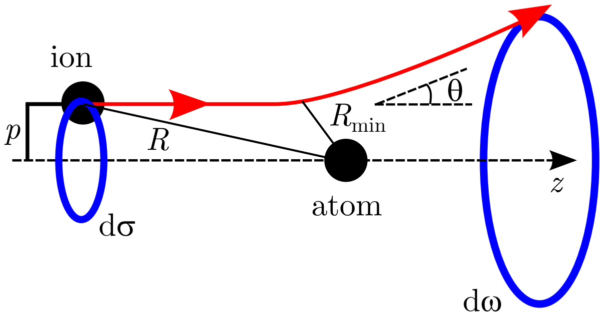

Fig. 2.2: Classical scattering trajectory | Sketch of the classical scattering trajectory (in red) of an ion scattering with an atom. The differential surfaces that define the scattering cross-section are denoted in blue. Image adapted from Ref. [106]

.

From Figure 2.2 we can also define the scattering cross-section, which denotes the probability of ion scattering with atom. The scattering cross-section depends on the scattering geometry, and, in the CMS, is given by [106]

$$\frac{\mathrm{d}\sigma}{\mathrm{d}\omega} = \frac{p}{\sin(\theta)} \left| \frac{\mathrm{d}p}{\mathrm{d}\theta} \right|. \tag{2.7}$$

Using the transformation rules of Equation 2.2, the LS scattering cross-section is defined by

$$\frac{\mathrm{d}\sigma}{\mathrm{d}\Omega} = \frac{\mathrm{d}\sigma}{\mathrm{d}\omega} \frac{\left((\alpha_{\mathrm{m}} + \cos(\theta))^2 + \sin^2(\theta) \right)^{3/2}}{1 + \alpha_{\mathrm{m}} \cos(\theta)}, \tag{2.8}$$

where $\alpha_{\mathrm{m}} = m_{\mathrm{i}}/m_{\mathrm{a}}$. For very light ions compared to the target atoms, i.e. $\alpha_{\mathrm{m}} \ll 1$, the scattering cross-section is the same in both the LS and CMS systems.

Due to the cylindrical geometry of the scattering problem, the majority of collisions will result in forward scattering of the ion, i.e. small scattering angles. We can thus approximate the trajectory integral by a straight line [107]. The ion, which is now traveling along the z-direction, experiences a force pulse when scattering with the atom, resulting in the transfer of momentum perpendicular to its direction of motion. The scattering angle is then determined by the ratio of the transverse and longitudinal momentum, and is given by

$$\theta = -\frac{1}{2E_{\mathrm{r}}} \int_{-\infty}^{+\infty} \frac{\partial}{\partial p} V\left(\sqrt{p^2 + z^2}\right) dz, \tag{2.9}$$

where $R = \sqrt{p^2 + z^2}$ follows from Pythagoras' theorem. In this approximation, Equation 2.2 is now reduced to

$$\Theta = \frac{m_{\mathrm{a}}}{m_{\mathrm{i}} + m_{\mathrm{a}}} \theta, \tag{2.10}$$

so that in the LS, Equation 2.9 is given by

$$\Theta = -\frac{1}{2E} \int_{-\infty}^{+\infty} \frac{\partial}{\partial p} V\left(\sqrt{p^2 + z^2}\right) dz. \tag{2.11}$$

To obtain more information about the scattering geometry and transferred energy in the collision, we need a suitable interaction potential. In the next section, we will discuss several applicable atomic potentials.

2.1.1.2 Inter-atomic potentials and screening

Since we are dealing with the scattering of charged particles, we can make use of a Coulomb potential:

$$V(R) = \frac{Z_\mathrm{i} Z_\mathrm{a} e^2}{4\pi\varepsilon_0 R}, \tag{2.12}$$

where Z_i and Z_a denote the atomic number of the ion and atom, respectively, where ε_0 is the vacuum permittivity, and e the elementary charge.

Inserting this potential into the trajectory integral of Equation 2.5 gives

$$\tan\left(\frac{\theta}{2}\right) = \frac{b}{2p}, \tag{2.13}$$

where $b = Z_\mathrm{i} Z_\mathrm{a} e^2 / 4\pi\varepsilon_0 E_\mathrm{r}$ is the so-called collision diameter, which represents the minimum distance of approach for two particles with the same charge polarity. In the low-angle approximation, the scattering angle for this potential becomes

$$\theta = \frac{b}{p}. \tag{2.14}$$

The simple Coulomb potential has a few important limitations. Firstly, depending on the energy of the ion, the charges on either particle can be susceptible to screening, effectively hiding the charges. Secondly, a charged ion can capture charges from the atomic lattice, becoming effectively uncharged. Lastly, the electron cloud of the ion can penetrate the electron cloud of the atom before scattering, which breaks the point-charge assumption from the beginning of this chapter. To more accurately describe these effects, statistical methods are required.

When dealing with screening, we typically use a modified screened Coulomb potential:

$$V(R) = \frac{Z_\mathrm{i} Z_\mathrm{a} e^2}{4\pi\varepsilon_0 R} \phi\left(\frac{R}{a}\right), \tag{2.15}$$

where ϕ is a screening function, with a the typical screening radius. Thomas [108] and Fermi [109] first obtained a numerical solution for the screening function of a single atom, which was expanded by Lindhard [107] to fit the interaction of two neutral atoms. The function is numerical, with a screening length that depends on the species of the scattered ion and atom, given by

$$a_\mathrm{L} = 0.88534 \frac{a_0}{\left(Z_\mathrm{i}^{2/3} + Z_\mathrm{a}^{2/3}\right)^{1/2}}, \tag{2.16}$$

where $a_0 = 4\pi\varepsilon_0 \hbar^2 / e^2 m_\mathrm{e}$ is the radius of the first Bohr orbit.

A more universal solution for the screened Coulomb potential was found by Ziegler, Biersack, and Littmark [110]. This so-called ZBL potential is valid for all combinations of ions and target atoms, and is given by

$$\phi_\mathrm{ZBL}(R) = \sum_{j=1}^{4} a_\mathrm{j} \exp\left(-b_\mathrm{j} \frac{R}{a_\mathrm{ZBL}}\right), \text{with } a_\mathrm{ZBL} = \frac{a_0}{Z_\mathrm{i}^{0.23} + Z_\mathrm{a}^{0.23}}, \tag{2.17}$$

where $a_\mathrm{j} = (0.1818, 0.5099, 0.2802, 0.02817)$, and $b_\mathrm{j} = (3.2, 0.9423, 0.4028, 0.2016)$.

A useful approximation that we can use to obtain an analytical solution to the problem is the so-called power law approximation, where we approximate the atomic potential to follow a power law behavior $V(R) \propto R^{-s}$, with s a fitting parameter between 1 and 5. In this case, the screening function is given by

$$\phi_{\mathrm{PL}}(R) = \frac{k_{\mathrm{s}}}{s}\left(\frac{R}{a_{\mathrm{ZBL}}}\right)^{1-s}, \tag{2.18}$$

with k_{s} another fitting parameter.

The applicability of the screened Coulomb potential depends on the velocity of the incoming ion. For sufficiently fast ion velocities, the electrons of the target atom essentially stand still, and thus no screening occurs. In this case, we can use the regular Coulomb potential as described in Equation 2.12. For slower ions, electrons no longer stand still and can thus mask the charge of the target nucleus. In this case, screening needs to be taken into account. Furthermore, electrons can be exchanged between the ion and the target system depending on the velocity of the ion compared to the typical electron velocity.

The velocity that governs the applicability of the screening effects is the Bohr velocity of the first orbit, given by

$$v_{\mathrm{Bohr}} = \frac{e^2}{4\pi\varepsilon_0\hbar}\frac{Z}{n}, \tag{2.19}$$

where, Z is the atomic number of the considered material, and $n = 1$ for the first orbit. The velocity condition that governs electron exchange and screening effects is given by $v_{\mathrm{Bohr}}Z_{\mathrm{i}}^{2/3}$ [106]. For $v \gg v_{\mathrm{Bohr}}Z_{\mathrm{i}}^{2/3}$, no screening effects occur, whereas for $v \ll v_{\mathrm{Bohr}}Z_{\mathrm{i}}^{2/3}$, screening effects need to be taken into account. In the case of He^{+} ions, this velocity condition is given at several 100 keV to 1 MeV.

The exchange of electrons between the ion and target system changes the effective charge of the ion. As a consequence, we can write the effective charge as [106]

$$Z_{\mathrm{i}}^{\mathrm{eff}} = Z_{\mathrm{i}}\left(1 - \exp\left(-\frac{v}{v_{\mathrm{Bohr}}}Z_{\mathrm{i}}^{-2/3}\right)\right). \tag{2.20}$$

At low velocities, electrons are captured and $Z_{\mathrm{i}}^{\mathrm{eff}} \to 0$. Screening is then strong. At larger velocities, $Z_{\mathrm{i}}^{\mathrm{eff}}$ approaches Z_{i}, since the ion becomes deprived of its electrons due to the scattering events [106].

With the definitions for the atomic potentials in this section, we can obtain more detailed information about the energy transfer in a collision, as well as the scattering cross-sections.

2.1.1.3 Transferred energy and scattering cross-sections

For $v \gg v_{\mathrm{Bohr}}Z_{\mathrm{i}}^{2/3}$, screening can be ignored. For the pure Coulomb potential (Eq. 2.12), the trajectory integral gives the solution in Equation 2.13. Inserting this into Equation 2.7 results in the standard Rutherford scattering cross-section:

$$\left(\frac{\mathrm{d}\sigma}{\mathrm{d}\omega}\right)_{\mathrm{R}} = \frac{1}{16}\left(\frac{Z_{\mathrm{i}}Z_{\mathrm{a}}e^2}{4\pi\varepsilon_0}\right)^2\frac{1}{E_{\mathrm{r}}^2}\frac{1}{\sin^4\left(\frac{\theta}{2}\right)}, \tag{2.21}$$

which scales inversely with the ion energy. This inverse dependence on the energy signals that scattering is more likely at low ion energies.

Plugging the result from Equation 2.13 into Equation 2.4 gives us the trajectory dependent energy transfer:

$$T(p) = \frac{\gamma E}{1 + \left(\frac{2p}{b}\right)^2}. \tag{2.22}$$

.

At high impact parameter, the energy transfer is thus reduced. The cross-section after transformation with Equations 2.4 and 2.7 is given by

$$\left(\frac{\mathrm{d}\sigma}{\mathrm{d}T}\right)_{\mathrm{R}} = \frac{\pi}{4}\left(\frac{Z_{\mathrm{i}}Z_{\mathrm{a}}e^2}{4\pi\varepsilon_0}\right)^2 m_{\mathrm{i}}\left(m_{\mathrm{i}}+m_{\mathrm{a}}\right) \times \frac{1}{ET^2}. \tag{2.23}$$

The dependence on T^{-2} highlights that small energy transfers are by far the most likely.

At low velocity, $v \ll v_{\mathrm{Bohr}} Z_{\mathrm{i}}^{2/3}$, screening needs to be taken into account, and the analysis becomes more complicated. It involves extrapolating the low-angle approximation to larger angles in order to define a universal scattering function, which can be used to obtain the scattering cross-section, depending on the chosen screening function. We will not treat the entire derivation here, but more details can be found in Refs. [106,107]. In the power-law approximation, the cross-section is given by

$$\frac{\mathrm{d}\sigma}{\mathrm{d}T} = C_{\mathrm{s}}\frac{1}{E^{1/s}T^{1+1/s}}, \tag{2.24}$$

where C_{s} is a constant given by

$$C_{\mathrm{s}} = \frac{\pi}{2}\lambda_{\mathrm{s}} a_{\mathrm{L}}^2 \left(\frac{2Z_{\mathrm{i}}Z_{\mathrm{a}}e^2}{4\pi\varepsilon_0 a_{\mathrm{L}}}\right)^{2/s} \alpha_{\mathrm{m}}^{1/s}, \tag{2.25}$$

with $\lambda_{\mathrm{s}} = 2/s \cdot (k_{\mathrm{s}}\gamma_{\mathrm{s}}/s)^{2/s}$, $\gamma_{\mathrm{s}} = 1/2 \cdot B\left(1/2, (s+1)/2\right)$, and B denoting the Beta function. Indeed, low energy transfers are also favorable in a screened potential. Light ions, with small α_{m}, have a much lower chance to transfer energy. Only at low energies do they have a more significant probability to transfer energy by the Coulomb interaction.

2.1.2 Ion stopping

In the previous section, we have seen that ions transfer energy to nuclei and electrons of the target through collisions. The ion will keep moving through the target lattice, until it has transferred all of its energy, at which point it stops. An ion traversing the lattice thus experiences a stopping force. This is defined as the loss of energy per pathlength s, via

$$B\left(E\right) = -\frac{\mathrm{d}E}{\mathrm{d}s}. \tag{2.26}$$

Since it is the areal atomic density n and not the thickness itself that determines the energy loss, we define the stopping cross-section as

$$S\left(E\right) = -\frac{1}{n}\frac{\mathrm{d}E}{\mathrm{d}s}. \tag{2.27}$$

The differential probability per unit pathlength of a collision is given by $n\mathrm{d}\sigma\left(T\right)$, corresponding to an energy loss of $nT\mathrm{d}\sigma\left(T\right)$. When integrating over all possible energy transfers, the stopping cross-section is given by

$$S\left(E\right) = \int T\mathrm{d}\sigma\left(E,T\right). \tag{2.28}$$

In the remainder of this section, we will assume that we can separate the stopping cross-section according to

$$S\left(E\right) = S_{\mathrm{n}}\left(E\right) + S_{\mathrm{e}}\left(E\right), \tag{2.29}$$

where S_{n} and S_{e} represent the nuclear and electronic stopping cross-sections. This assumption is not immediately obvious. We can justify it by looking at the contribution of electrons and nuclei for different impact parameters p. For large impact parameters, the scattering is mostly dominated by electronic effects due to screening. Small impact parameters result in a mixed effect of nuclear and electronic stopping. As we have seen in Equations 2.22, 2.23, and 2.24, small impact parameters result in large energy transfers, which are very rare. Hence, the majority of collisions will have larger impact parameters, and we can assume that the effects can be separated.

In the following, we will thus treat each contribution separately. At the end, we will see how we can use the stopping cross-sections to determine the distance the ion travels in the target material.

2.1.2.1 Nuclear stopping

Nuclear stopping can be determined using the same procedure as the screened scattering cross-section in Section 2.1.1.3 [111]. The fitting formula depends on the chosen screening function. For the universal ZBL potential, which is valid for all combinations of ion and target atom, the nuclear energy loss per pathlength is given by

$$\left(-\frac{\mathrm{d}\varepsilon}{\mathrm{d}\rho}\right)_{\mathrm{n}} = \frac{0.5\ln\left(1+1.2288\varepsilon\right)}{\varepsilon+0.1728\varepsilon^{1/2}+0.0008\varepsilon^{0.1504}}, \tag{2.30}$$

where ε is the reduced energy, given by $\varepsilon = a/b$, with a the screening radius and b the minimum approach distance of the screened Coulomb potential, and $\rho = \pi a^2 n\gamma s$ the reduced pathlength [111]. The energy loss per pathlength is graphically shown in Figure 2.3. Nuclear stopping is strongest only in a specific window of reduced energy, and gradually drops at energies above and below this window.

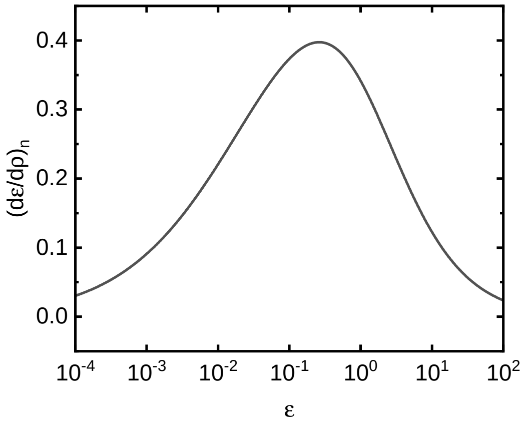

Fig. 2.3: Reduced nuclear stopping according to the ZBL potential | Reduced nuclear stopping as described by the ZBL potential and Equation 2.30.

In the power-law approximation, integration of Equation 2.28, after inserting Equation 2.24, with $T_{\mathrm{max}} = \gamma E$ as upper bound, gives

$$S_{\mathrm{n}}\left(E\right) = \frac{C_{\mathrm{s}}\gamma^{1-1/s}}{1-1/s}E^{1-2/s}, \tag{2.31}$$

which, when only extracting the dependence on the particle masses goes as

$$S_{\mathrm{n}}\left(E\right) \propto m_{\mathrm{a}}^{1-2/s}\left(\frac{m_{\mathrm{i}}}{m_{\mathrm{i}}+m_{\mathrm{a}}}\right)^{2-2/s}\left(\frac{E}{m_{\mathrm{i}}}\right)^{1-2/s}. \tag{2.32}$$

Nuclear stopping thus depends strongly on the velocity of the ion, as well as the masses of the particles involved in the nuclear scattering process. In the case of light ions, i.e. $m_{\mathrm{i}} \ll m_{\mathrm{a}}$, nuclear stopping only weakly depends on the mass of the target atom $\sim m_{\mathrm{a}}^{-1}$, and thus depends more strongly on the mass and energy of the ions, with heavier ions showing in general larger nuclear stopping.

2.1.2.2 Electronic stopping

In the case of electronic stopping, the scattering mechanism depends strongly on the velocity of the ion. As mentioned in Section 2.1.1.2, scattering at low ion velocities is susceptible to charge transfer and screening effects. We thus separate electronic stopping in different velocity regimes.

For low ion velocities, $v \ll v_{\mathrm{Bohr}} Z_{\mathrm{i}}^{2/3}$, electronic stopping takes place through momentum exchange with the target electrons. This view, which follows the picture first proposed by Fermi *et al.* in 1947 [112], states the the electronic stopping is proportional to the collision rate and the average momentum transfer per collision event. In essence, the electronic stopping is proportional to the velocity of the ion. This was expanded upon by Lindhard and Scharff in 1961 [113] to obtain the full low-velocity electronic stopping cross-section, given by

$$S_{\mathrm{e}}(v) = \frac{2e^2 a_0}{\varepsilon_0} \frac{Z_{\mathrm{i}}^{7/6} Z_{\mathrm{a}}}{\left(Z_{\mathrm{i}}^{2/3} + Z_{\mathrm{a}}^{2/3}\right)^{3/2}} \frac{v}{v_{\mathrm{Bohr}}}. \tag{2.33}$$

The proportionality of the stopping to the ion velocity $v \sim \sqrt{E}$ can be seen as a viscous friction. For light ions, $Z_{\mathrm{i}} \ll Z_{\mathrm{a}}$, the electronic stopping no longer depends on the mass of the target atoms, and only on the mass of the incoming ion. Low velocity electronic stopping for light ions is thus independent of the target material.

For high ion velocities, $v \gg v_{\mathrm{Bohr}} Z_{\mathrm{i}}^{2/3}$, the classical scattering mechanism described in Section 2.1.1.1, which is based on original models by Bohr [114,115], is no longer adequate to describe electronic stopping. Instead, a quantum mechanical description is required. Quantum mechanical scattering is based on the velocity difference between in-going and out-going matter waves. Bethe first gave an idea of quantum mechanical electronic stopping in 1930 [116], which results in the following stopping cross-section:

$$S_{\mathrm{e}}(v) = \frac{4\pi e^4}{(4\pi\varepsilon_0)^2} \frac{Z_{\mathrm{i}}^2 Z_{\mathrm{a}}}{m_{\mathrm{e}} v^2} \ln\left(\frac{2 m_{\mathrm{e}} v^2}{I}\right), \tag{2.34}$$

where I is the mean ionization potential, which is often approximated through $I \approx 10\mathrm{eV} \cdot Z_{\mathrm{a}}$. Small transfer of momentum leads to only small energy transfers, and will result in excitation of the target electron. Larger momentum transfers are capable of ionizing the target atom, knocking the electron from its bound state.

2.1.2.3 Total Stopping

Now that the contributions from nuclear and electronic stopping are known, we can use Equation 2.29 to find the total stopping cross-section. Due to the numerical nature of the solutions involved, the total stopping force is typically investigated using Monte Carlo simulations. These programs, such as Stopping and Range of Ions in Matter (SRIM) or Transport of Ions in Matter (TRIM) [117], solve the above equations at each binary collision and follow the ion along its path through the material. In regards of ion stopping, results for typical ion-target combinations are shown in Figure 2.4.

Figures 2.4a and b show the stopping for light He^+ ions in Co and W targets, respectively. We see that the contribution from nuclear stopping is small compared to electronic stopping. Hence, for light ions, electronic stopping dominates. Furthermore, we also see that the electronic stopping is independent of the target material, as stated previously. The strength of the electronic stopping is the same in both Co and W targets. Figures 2.4c and d show the stopping for heavier Ga^+ ions in Co and W targets, respectively. Here we see the opposite behavior, the stopping is dominated by nuclear stopping, and electronic stopping only becomes significant at much larger energies. Furthermore, the total stopping is also an order of magnitude larger for Ga^+ ions compared to lighter He^+ ions. As we will highlight in Section 2.2, the lower stopping of He^+ results in less target damage, which allows for more precise control of atomic displacements in the target.

With the total stopping we can determine the ion range, which is the subject of the next section.

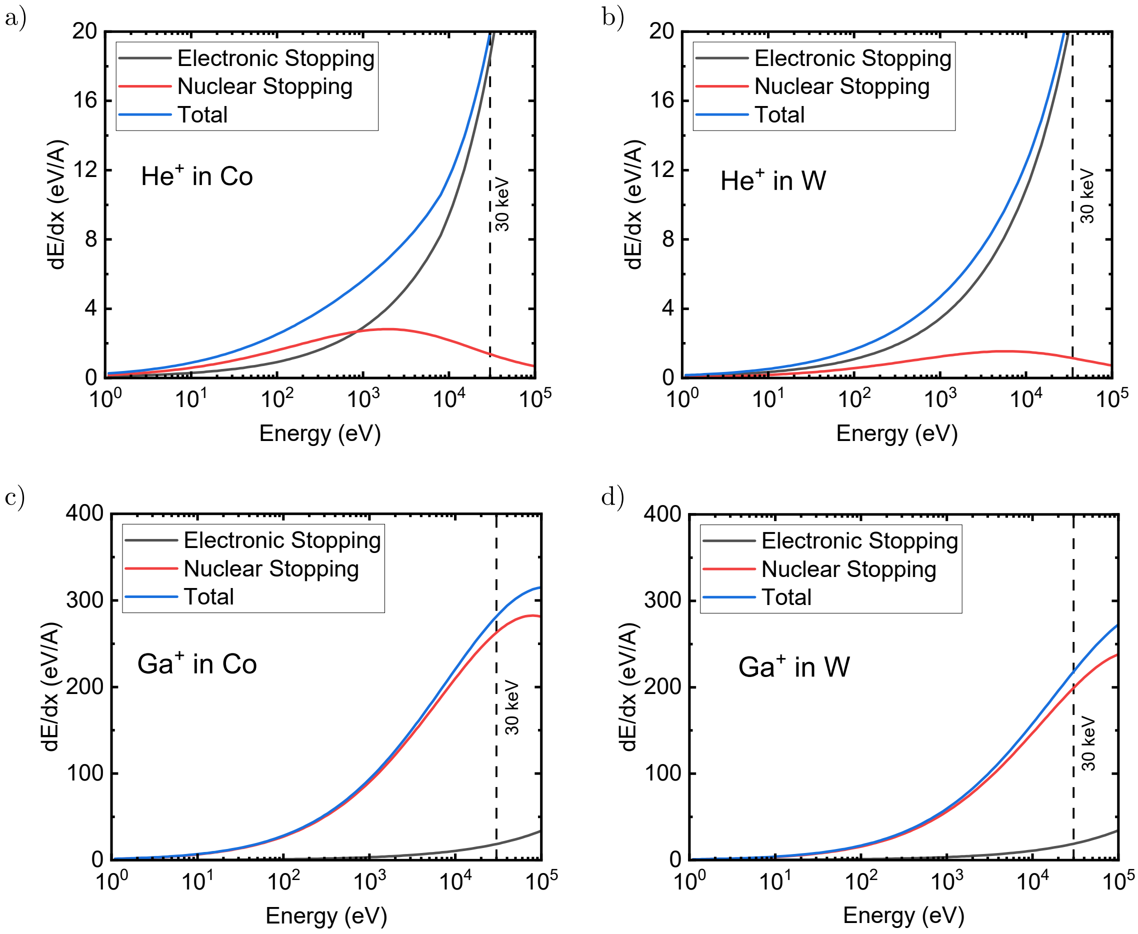

Fig. 2.4: Ion stopping for various ion-target combinations | Simulated energy loss values from nuclear (red) and electronic (black) stopping for various ion-target combinations. The blue line shows the total stopping contribution. Vertical dotted line indicates an ion energy on 30 keV. Results obtained with SRIM.

2.1.2.4 Ion range

In the previous section we have seen the energy loss per pathlength of the ion due to nuclear and electronic collisions. An ion will keep traversing the target material until it has transferred all its energy. We can investigate the total ion pathlength from the ion stopping. The total pathlength for an ion with starting energy E is defined by[1]

$$\overline{R}_{\mathrm{t}}\left(E\right) = \frac{1}{n}\int_{0}^{E}\frac{\mathrm{d}E'}{S\left(E'\right)}. \tag{2.35}$$

In the case of light ions, where $S_{\mathrm{n}}\left(E\right) \approx 0$, the low velocity electronic stopping can be approximated by $S_{\mathrm{e}}\left(E\right) \approx k_{\mathrm{e}}\sqrt{E}$, where k_{e} is a constant. In that case, the total pathlength is given by

$$\overline{R}_{\mathrm{t}}\left(E\right) = \frac{2}{nk_{\mathrm{e}}}\sqrt{E}. \tag{2.36}$$

At high velocities, the electronic stopping scales inversely with the energy (Eq. 2.34), meaning the total pathlength scales as $\overline{R}_{\mathrm{t}}\left(E\right) \propto E^{2}$. Larger ion energy thus equals a longer pathlength. This

---

[1] It should be noted that the following expressions are only accurate in amorphous materials. In crystalline materials, the ion can be scattered in the direction of a crystallographic axis, scattering significantly less often than in an amorphous material with randomly distributed atoms. This phenomenon is called channeling. Hence, in the case of channeling, the following expressions typically underestimate the actual traveled distance.

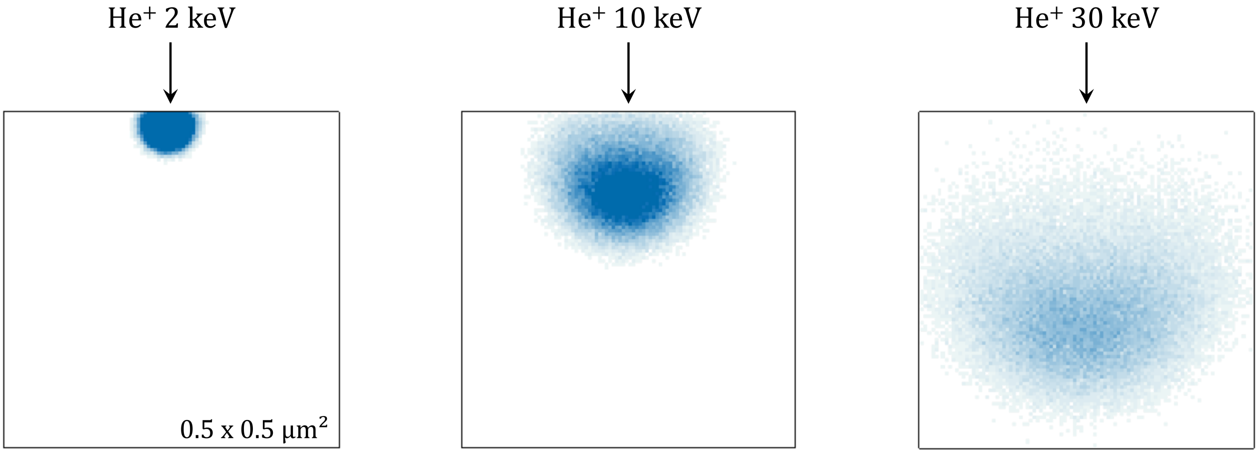

Fig. 2.5: Ion distributions for different ion energies | Distribution of He$^+$ ions with different energies in a Si target. Results obtained with SRIM. The blue color denotes the quantity of He$^+$ ions that stop at a certain location, with darker blue denoting more ions.

is also visible in SRIM results for He$^+$ ions with different energy traversing a Si target, which are showed in Figure 2.5.

In the case where nuclear stopping is dominant, only approximate solutions exist. In the power-law approximation, the total range is given, in reduced units, by [118]

$$\overline{\rho}_\mathrm{t}\left(\varepsilon\right) = \frac{s-1}{\lambda_\mathrm{s}}\varepsilon^{2/s}. \tag{2.37}$$

The total pathlength still increases with increasing ion energy, but reduces very fast with increasing ion mass. This means that heavier ions typically travel shorter distances at the same energy compared to light ions.

Figure 2.5 shows not only that more energetic ions travel further, but also that the distribution of ions changes. Furthermore, the ions do not travel in a straight line. In the remainder of this section we will describe the implantation distribution in more detail. To do so, we will define a few projected ion ranges, which are schematically shown in Figure 2.6. R_p is the projected range in the direction of the surface normal, along the depth axis, $R_\mathrm{p}^{=}$ is the longitudinal projected range, along the original incidence angle θ with the surface normal, and $R_\mathrm{p}^{\perp}$ is the lateral projected range, perpendicular to the axis of original incidence. The latter is also often called the lateral straggling of the ion. From Figure 2.6 it is obvious that care should be taken when determining the implantation depth, since the actual value can significantly differ from $\overline{R}_\mathrm{t}$.

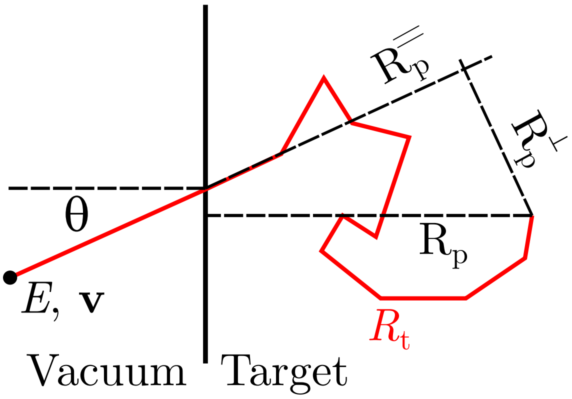

Fig. 2.6: Path of an ion in a target material | Sketch of the path of an ion with starting energy E, velocity $\mathbf{v}$, and incidence angle θ in a target material. The total pathlength as described by Eq. 2.35 is shown in red. The longitudinal, lateral, and normal projected ranges are shown with $R_\mathrm{p}^{=}$, $R_\mathrm{p}^{\perp}$, and R_p, respectively. These are also often called straggling.

The distribution of ion ranges can be obtained with a transport integral. Let us define the distribution of projected longitudinal ranges as $f_{\mathrm{R}}(x, E, \boldsymbol{\eta})$, where x denotes the depth, E the energy of the particle, and $\boldsymbol{\eta}$ the direction of incidence of the particle. $f_{\mathrm{R}}(x, E, \boldsymbol{\eta})\,\delta x$ then denotes the probability that a particle stops between x and $x + \delta x$. The transport integral considers three possibilities for an ion traversing δx: (1) A nuclear collision occurs, changing the incidence and the energy of the ion, (2) an electronic collision occurs, changing the energy of the ion by ΔE, but not the direction, and (3) nothing happens. The analysis of this integral is not trivial, and the details can be found in Ref. [106] and references therein. In general, we can use the different moments of the distribution function to obtain the solutions, via

$$f_{\mathrm{R}}^{(\nu)}(E) = \int_{-\infty}^{+\infty} f_{\mathrm{R}}(x, E)\, x^{\nu} \mathrm{d}x, \tag{2.38}$$

where we can drop the dependence on $\boldsymbol{\eta}$ by assuming an infinite medium.

The first moment, $\nu = 1$, describes the longitudinal mean projected range $\overline{R}_{\mathrm{p}}^{=}$. The second moment, $\nu = 2$ describes the width of the distribution, which is related to the longitudinal straggling, i.e. variation of longitudinal projected range. In special cases, such as for light ions, analytical solutions exist. Schiøtt obtained, for light ions at large electronic stopping [119]:

$$\frac{\overline{R}_{\mathrm{p}}^{=}(E)}{\overline{R}_{\mathrm{t}}(E)} = \lambda(1 - 2\lambda), \tag{2.39}$$

where $\lambda = m_{\mathrm{i}}/m_{\mathrm{a}} \cdot S_{\mathrm{e}}(E)/S_{\mathrm{n}}(E) < 0.5$.

For more practical purposes, the range distribution is usually approximated by a Gaussian. Predictions can then be made using the SRIM software package. Some typical results for He^{+} ions in a Co target are shown in Figure 2.7. Indeed, as the energy of the He^{+} ion increases, so do the projected range and straggling components.

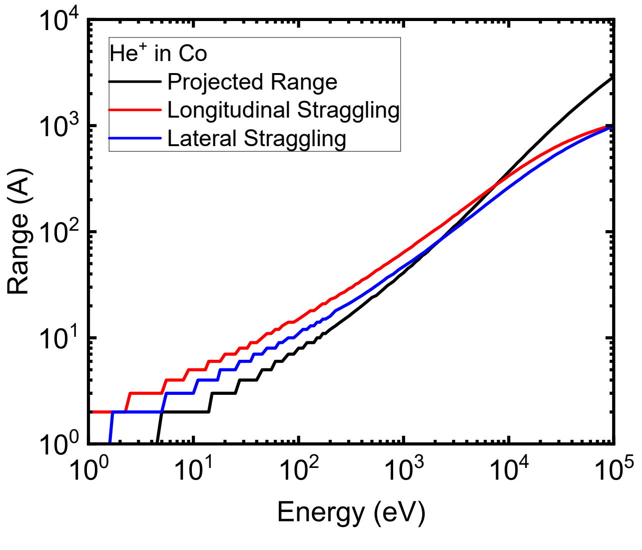

Fig. 2.7: Range and straggling of a He^{+} ion | SRIM results for the range and straggling of a He^{+} ion in a Co target as a function of the He^{+} ion energy. The steps at low energy are due to the discretisation of the SRIM simulation.

2.2 Ion energy deposition: evolution of the target material

In the previous section, we have seen that an ion traversing an atomic lattice can transfer energy to the atomic lattice through nuclear and electronic collisions. In this section, we will describe the effects of this energy deposition in the atomic lattice. Specifically, we will describe the structural modification of the lattice caused by the ballistic energy deposition, how this can result in atomic mixing in compound materials, as well as induced crystallization of amorphous target materials.

2.2.1 Damage: cascades, spikes, defects, and sputtering

Energy from collisions is transferred to the atomic lattice. This is either done directly by nuclear collisions, or indirectly by electronic collisions and subsequent electron-phonon coupling. Collisions thus increase the kinetic energy of the lattice atoms, allowing them to be displaced.

Depending on the amount and type of energy that is deposited into the lattice, we can identify three distinct regimes, which are shown schematically in Figure 2.8. In the case of primarily nuclear energy deposition, a linear collision cascade can be created (Fig. 2.8a). In the linear collision cascade, binary collisions take place between moving particles and stationary target atoms. Recoil atoms can displace other stationary atoms if their energy is large enough. When the nuclear energy deposition is very large, a lot of ions are moving, and collisions now mostly take place between already moving atoms (Fig. 2.8b). This so-called non-linear collision cascade can result in a quick thermalization of the lattice, and is often called an elastic thermal spike. At very large electronic energy deposition, the hot electron gas that is created can heat up the atomic lattice through electron-phonon coupling (Fig. 2.8c). This can also result in a thermalization of the lattice, and is often called an inelastic thermal spike. For both types of thermal spike, atomic motion and thermal energy dissipation is governed mainly by dissipation laws. In this section we focus mostly on linear cascade collisions, as this is the dominant contribution for light ions.

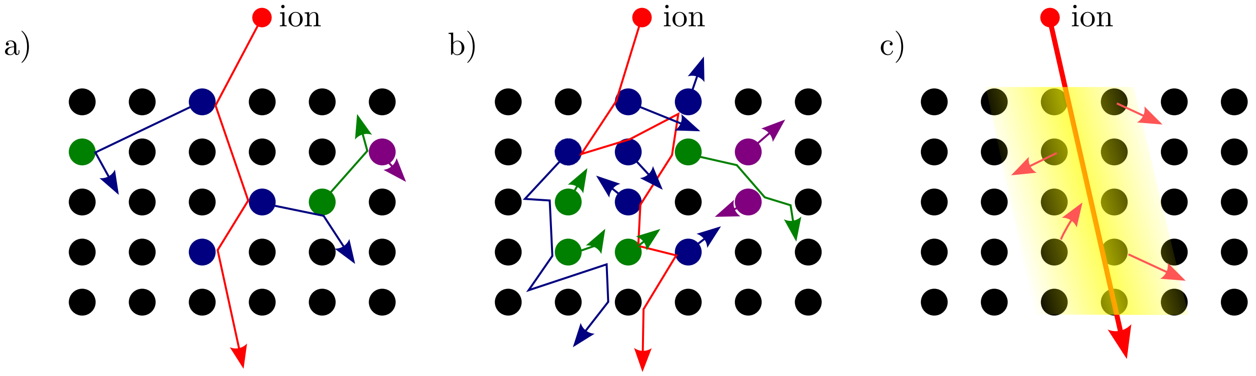

Fig. 2.8: The different balistic energy deposition regimes | Sketches of the three different balistic energy deposition regimes. a) A linear collision cascade. b) Non-linear collision cascade and elastic thermal spike. The path of the ion in shown in red, primary recoil atoms in blue, secondary recoil atoms in green, and tertiary recoil atoms in purple. c) Inelastic thermal spike. The spike zone is shown in yellow. Figure inspired by Ref. [106].

2.2.1.1 Linear cascade collisions

A wide range of linear cascade morphologies exist, depending on the ion species and target material. Figure 2.9 shows examples of two collision cascades, one for light He^+ ions, and one for heavier Ga^+ ions. In both cases, the ions have a starting energy of 30 keV. Each window shows results for 6 ions. The black dots show primary collisions between the ion and the lattice atoms, the grey dots show secondary and higher order collisions between lattice atoms. The results have been obtained with the SRIM simulation package. Light ions, with low nuclear energy deposition, create very dilute cascades. Heavier ions create very dense cascades due to the larger nuclear energy deposition. With increasing nuclear energy deposition, the linear cascade can transform into a non-linear cascade or elastic thermal spike.

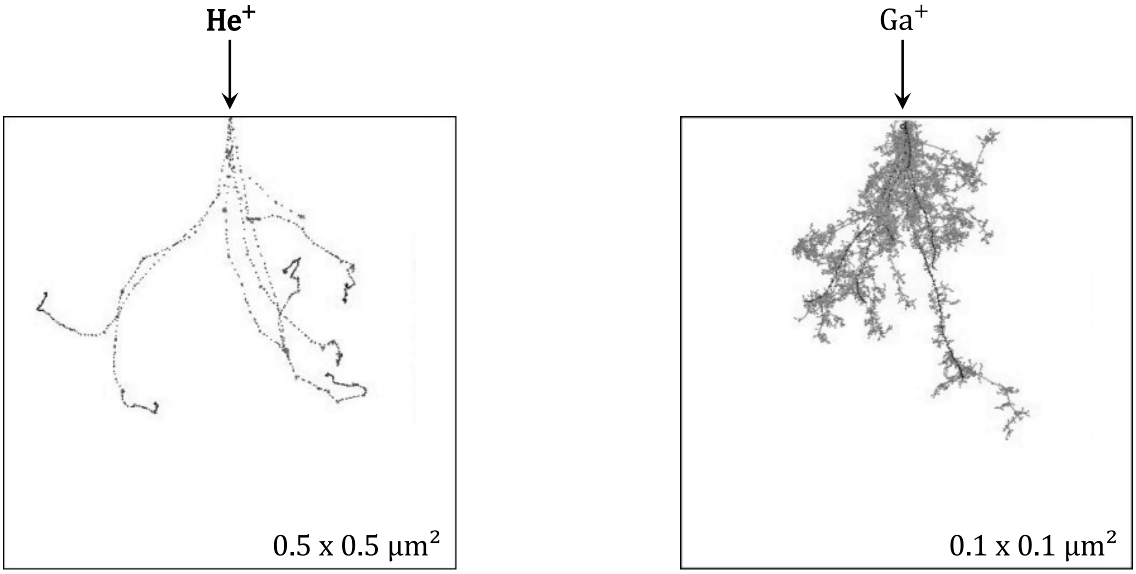

Fig. 2.9: Linear collision cascades for He$^+$ and Ga$^+$ ions | SRIM simulation of 6 He$^+$ and Ga$^+$ ions at 30 keV in a Si target. The black line shows the path of the ion, which each dot a primary collision. The grey dots show secondary and higher order collisions.

In order to get a better idea of the damage and recoil distributions in a linear cascade, we can use transport physics [120–122], similar to the discussion for ion ranges in Section 2.1.2.4. For the cascade caused by a single ion, we can define a distribution function f, such that the probability to find a cascade atom with energy $E_0 + \mathrm{d}E_0$ in a volume element $\mathrm{d}^3\mathbf{r}$ around $\mathbf{r}$ for an incident ion at $\mathbf{r} = 0$ with direction $\boldsymbol{\eta}$ and energy E is written as

$$\mathrm{d}N\left(E, \boldsymbol{\eta}, E_0, \mathbf{r}\right) = f\left(E, \boldsymbol{\eta}, E_0, \mathbf{r}\right) \mathrm{d}E_0 \mathrm{d}^3\mathbf{r}. \tag{2.40}$$

By taking into account that high energy ions contribute very little due to the small nuclear stopping, and that cascade ions must have an energy $E_0 < E$, i.e. $f \to 0$ for $E > E_0$, we can extend the distribution function for $E_0 \to \infty$. In that case, for higher order moments ($\nu > 0$), f can be factorized into

$$f\left(E, \boldsymbol{\eta}, E_0, \mathbf{r}\right) = C f_{\mathrm{D}}\left(E, \boldsymbol{\eta}, \mathbf{r}\right) f_{\mathrm{E}}\left(E, E_0\right), \tag{2.41}$$

where f_{D} is the spatial energy deposition distribution in the cascade, also called the damage distribution, and f_{E} is the recoil density. C is a re-normalization constant. Equation 2.41 assumes that the energy distribution is independent of the position within the cascade itself.

In order to obtain the distribution of relocated atoms, we consider only the energy deposited into atomic motion, i.e. nuclear energy deposition. To make the analysis easier, we restrict ourselves to primary recoil atoms from the collisions between an ion and stationary lattice atom, which is a valid assumption for light ions. In that case, the fraction of energy deposited into atomic motion is given by the volume integral of the energy distribution:

$$\nu_{\mathrm{D}}\left(E\right) = \int f_{\mathrm{D}}\left(E, \boldsymbol{\eta}, \mathbf{r}\right) \mathrm{d}^3\mathbf{r}. \tag{2.42}$$

For small recoil energies, i.e. those caused by light ions, this fraction can be approximated to $\nu_{\mathrm{D}}\left(E\right) \approx 0.9 \cdot E$.

Analogous to the range calculations, we can now calculate the spatial energy deposition in the target material. A schematic of the ion range and energy deposition distributions is shown in Figure 2.10. In the case of an ion with an energy below the maximum for electronic stopping, but where

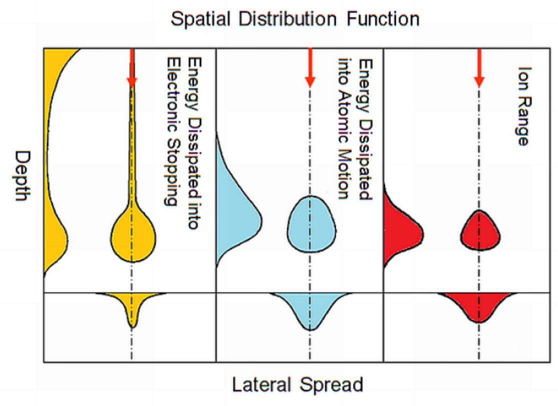

Fig. 2.10: Distribution of ion range and energies | Spatial distribution of ion ranges and deposited nuclear and electronic energy, for an ion with normal incidence. The center of each frame shows a contour cut. A projection onto the plane of incidence is shown on the left of each frame. A projection onto the plane normal to the plane of incidence is shown on the bottom of each frame. Figure from Ref. [106], after Ref. [123].

electronic energy dissipation still dominates, the energy deposition is as follows (see Fig. 2.10): Initially, the stopping is dominated by electronic collisions. The more the ion slows down, the less electronic energy is deposited. Once the nuclear stopping becomes relevant, the spatial energy dissipation increases due to atomic motion around the path of the ion. The contributions of the recoil atoms increase the total electronic energy dissipation at the end of the ion range.

At very low recoil energies and in the power law approximation, the recoil density f_E can be approximated to

$$f_\mathrm{E}\left(E, E_0\right) = \frac{6}{\pi^2}\frac{\nu_\mathrm{D}\left(E\right)}{E_0^2}, \tag{2.43}$$

which, if properly normalized, allows us to write the total cascade distribution function as

$$f\left(E, \boldsymbol{\eta}, E_0, \mathbf{r}\right) = \frac{6}{\pi^2}\frac{f_\mathrm{D}\left(E, \boldsymbol{\eta}, \mathbf{r}\right)}{E_0^2}. \tag{2.44}$$

For practical purposes however, like in the case for range calculations, Monte Carlo simulations like the SRIM package are often used to calculate the damage distributions.

2.2.1.2 Thermal spikes

If either the nuclear or electronic energy deposition is very high, thermal spikes can occur in the target lattice. These spikes are very small for light ions at intermediate energies, and thus we will not provide a detailed description. For more information, see Ref. [106].

A thermal spike can be described with the temporal and spatial evolution of a temperature field $T\left(r, t\right)$. In a cylindrical geometry, the radial energy dissipation is governed by the following differential equation

$$\frac{\partial}{\partial t}T\left(r, t\right) = \frac{1}{r}\frac{\partial}{\partial r}\left(r\kappa\left(T\left(r, t\right)\right)\frac{\partial T\left(r, t\right)}{\partial r}\right), \tag{2.45}$$

where $\kappa = \lambda/\rho c$ is the thermal diffusivity, λ the thermal conductivity, ρ the mass density, and c the specific thermal capacity. If κ is temperature independent, the solution is given by

$$T\left(r, t\right) = \left|\frac{\mathrm{d}E}{\mathrm{d}x}\right|\frac{1}{4\pi\lambda t}\exp\left(-\frac{r^2}{4\kappa t}\right). \tag{2.46}$$

In the case of an elastic thermal spike, the atomic motion can be described as a gas of hot atoms. The thermal diffusivity is then dependent on the temperature, and can be described in terms of atomic collisions. A solution for the temperature field can then be found by inserting this thermal conductivity into Equation 2.45.

In the case of in-elastic thermal spikes, with high electronic stopping, we can instead describe the thermal spike using a hot electron gas and by introducing electron-phonon coupling. The thermal energy dissipation is then described by a coupled differential equation for the electron lattice and the phonon lattice.

2.2.1.3 Sputtering

Collisions with atoms at the surface of a target lattice can result in the ejection of said atoms from the target lattice. This phenomenon is called sputtering. Sputtering is significant when the nuclear deposited energy is high, i.e. for heavier ions. Since sputtering is negligible for light ions such as He^+, we will not treat it in detail here. Details can be found in Ref. [106].

The sputtering yield, or number of sputtered atoms per incoming ion with energy E and incidence angle θ, is given by

$$Y_{\mathrm{s}}(E,\theta) = \frac{3}{2\pi^3\lambda_0 a^2}\frac{1}{U_{\mathrm{s}}}\frac{S_{\mathrm{n}}(E)}{\cos(\theta)}\alpha(m_{\mathrm{i}},m_{\mathrm{a}})\,. \tag{2.47}$$

Here U_{s} is the surface binding energy, $\lambda_0 = 24$ is a constant, a is any appropriate screening radius, and α a target-ion mass correction factor. For He^+ ions, $\alpha \approx 0.1$. It grows with increasing $m_{\mathrm{i}}/m_{\mathrm{a}}$, i.e. α is larger for heavy ions. Surface atoms are only ejected when the transferred energy is larger than the sputtering threshold energy, which depends on the surface binding energy. The fact that T is typically small for light ions, combined with the low nuclear stopping cross-section and small mass correction factor, indeed shows that sputtering is almost negligible for light ions. From SRIM simulations, a typical sputtering yield for 15 keV He^+ ions in a Ta target layer is 0.04 Ta atoms/ion. The typical sputtering yield for Ga^+ ions at the same energy is 6.00 Ta atoms/ion, 150 times larger than He^+.

2.2.1.4 Damage

Collisions with atoms in the bulk can create vacancies in the atomic lattice after an atom is displaced from its original site. The combination of a vacancy and a displaced atom is called a *Frenkel pair*. We can thus describe the damage in the atomic lattice from collisions with ions with the number of Frenkel pairs created per ion [124]. A Frenkel pair is not always stable. Its stability depends on the energy that is converted in atomic motion. Different processes for Frenkel pair creation thus exist, which are summarized in Figure 2.11.

An incident ion with energy E scatters off the atomic lattice, and transfers an energy T. For very small T, the atom is not moved far enough, and the Frenkel pair recombines instantly. Hence, only for $T > U_{\mathrm{d}}$, where U_{d} is the displacement threshold energy, a (meta-)stable Frenkel pair can be created. Typical values for displacement thresholds are 15 to 80 eV [126]. For intermediate T, the created Frenkel pair can either recombine in its original configuration, or the vacancy can be taken by another atom. The latter is called a replacement collision, or substitution. If the transferred energy is very large, the distance between vacancy and interstitial atom is too large to recombine. Hence, a stable vacancy is created, and the crystal is destroyed.

In a linear cascade, the number of Frenkel pairs created after an atomic collision is given by

$$N_{\mathrm{F}}(T) = \int_{U_{\mathrm{d}}}^{T} f_{\mathrm{E}}(T,E_0)\,P_{\mathrm{d}}(E_0)\,\mathrm{d}E_0, \tag{2.48}$$

where $f_{\mathrm{E}}(T,E_0)$ is the recoil density as described in Equation 2.43, and $P_{\mathrm{d}}(E_0)$ is the probability that a recoil atom with energy E_0 is displaced. Taking into account substitutions, P_{d} can be described by

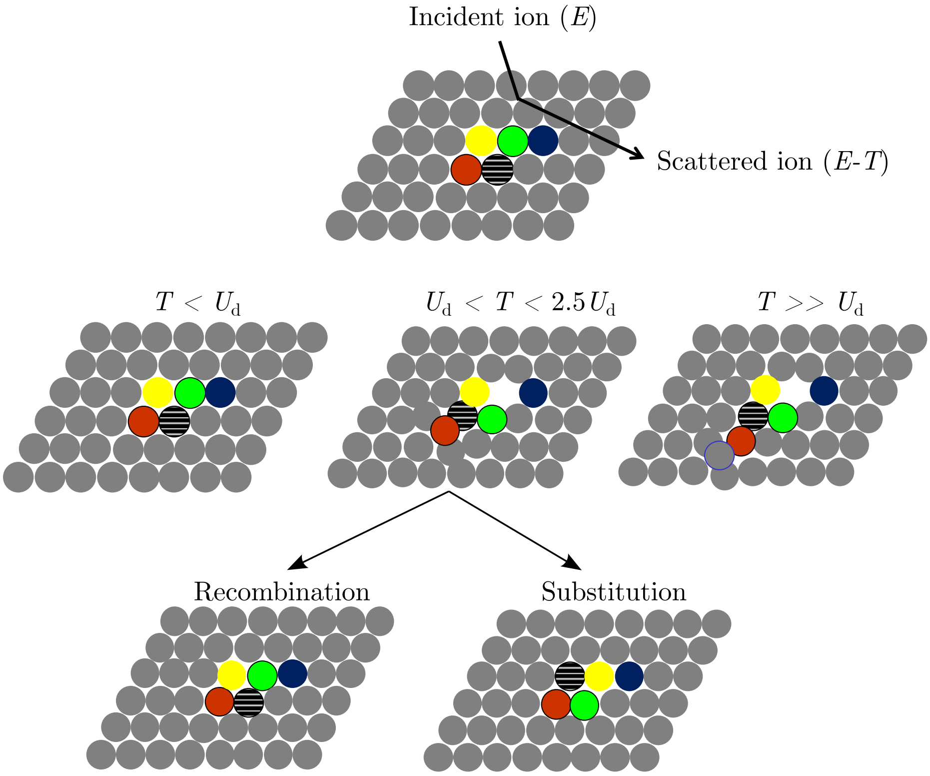

Fig. 2.11: Frenkel pair creation | Schematic representation of the processes for Frenkel pair creation, depending on the value of the transferred energy T. If T is below the threshold energy U_d, nothing happens. For intermediate values, a stable Frenkel pair is created, which can then recombine to its original location, or take the place of another lattice site. For very large transferred energies, the crystal is destroyed and the Frenkel pair does not recombine. Figure adapted from Ref. [125].

$$P_\mathrm{d}\left(E_0\right) = \begin{cases} 0 & E_0 < U_\mathrm{d}, \\ \frac{E_0 - U_\mathrm{d}}{U_\mathrm{d}} & U_\mathrm{d} < E_0 < 2U_\mathrm{d}, \\ 1 & E > 2U_\mathrm{d}. \end{cases} \tag{2.49}$$

Equation 2.48 is then given by the modified Kinchin-Pease formula [127]

$$N_\mathrm{F}\left(T\right) = \begin{cases} 0 & T < U_\mathrm{d}, \\ 1 & U_\mathrm{d} < T < 2.5U_\mathrm{d}, \\ 0.4\frac{\nu_\mathrm{D}(T)}{U_\mathrm{d}} & \text{else}. \end{cases} \tag{2.50}$$

The Frenkel pair yield Y_FP per pathlength s can be defined in terms of a damage cross-section σ_D:

$$\frac{\mathrm{d}Y_\mathrm{FP}}{\mathrm{d}s} = n\sigma_\mathrm{D}. \tag{2.51}$$

σ_D results from the probability of a nuclear collision: [106]

$$\sigma_\mathrm{D}\left(E'\right) = \int_{U_\mathrm{d}}^{\gamma E'} N_\mathrm{F}\left(T\right)\frac{\mathrm{d}\sigma_\mathrm{n}\left(E',T\right)}{\mathrm{d}T}\mathrm{d}T, \tag{2.52}$$

where E' is the instantaneous energy of the ion. Y_FP then follows from integration along the pathlength:

$$Y_\mathrm{FP}\left(E\right) = \int_{U_\mathrm{d}/\gamma}^{E} \frac{\sigma_\mathrm{D}\left(E'\right)}{S\left(E'\right)}\mathrm{d}E'. \tag{2.53}$$

At low energies, Y_{FP} is dominated by nuclear collisions, and increases with increasing energy. At high energies, the influence of electronic energy losses becomes larger, and thus Y_{FP} saturates for increasing electronic energy loss. The dependence on nuclear energy deposition also means that Y_{FP} is typically larger for heavier ions, since nuclear energy deposition is larger for heavy ions.

For light ions, the energy transfer is typically small. Due to the small cascade and the heavy prevalence of primary recoils, $N_{\mathrm{F}}(T)$ can be taken as 1. In the power-law approximation, with $s \to 2$ [106], we can use the scattering cross-section (Eqs. 2.24 and 2.25) to obtain an estimation for the Frenkel pair yield for light ions:

$$Y_{\mathrm{FP}}(E) = \frac{2C_2}{k_{\mathrm{e}}\sqrt{U_{\mathrm{d}}}}\left[\ln\left(\frac{\gamma E}{U_{\mathrm{d}}}\right) - 2\left(1 - \sqrt{\frac{U_{\mathrm{d}}}{\gamma E}}\right)\right]. \tag{2.54}$$

Here we assumed negligible nuclear stopping, and $S_{\mathrm{e}}(E) \approx k_{\mathrm{e}}\sqrt{E}$ (see Sec. 2.1.2.2). Indeed following Equation 2.54, Y_{FP} increases with increasing $T_{\max} = \gamma E > U_{\mathrm{d}}$.

So far we have only described the damage caused by a single ion. However, in a realistic sample and under continuous irradiation, target atoms are displaced continuously. How can we describe accumulating damage in the sample, and how does this damage evolve over time? This is what we will focus on in the remainder of this section.

Consider a beam of ions with flux ϕ (in ions/cm^2/s). We can describe the evolution of the concentration of defects per unit volume as [128]

$$\frac{\mathrm{d}C_{\mathrm{D}}}{\mathrm{d}t} = P_{\mathrm{D}}\left(1 - \frac{C_{\mathrm{D}}}{n}\right) - L, \tag{2.55}$$

where P_{D} represents the raw defect production rate, $(1 - C_{\mathrm{D}}/n)$ is a term that takes into account pre-existing defects, and L is a loss term. P_{D} grows with increasing flux, and can be written as $P_{\mathrm{D}} = n\sigma_{\mathrm{D}}\phi$. When assuming that the defect losses are only due to recombinations, we can write $L = RC_{\mathrm{D}}$, where R is the recombination rate coefficient [129]. In that case, we can rewrite the evolution of the defect concentration as

$$\frac{\mathrm{d}C_{\mathrm{D}}}{\mathrm{d}t} = n\sigma_{\mathrm{D}}\phi\left(1 - \frac{C_{\mathrm{D}}}{n}\right) - RC_{\mathrm{D}}. \tag{2.56}$$

We can rewrite Equation 2.56 in terms of the defect fraction $f_{\mathrm{d}} = C_{\mathrm{D}}/n$:

$$\frac{\mathrm{d}f_{\mathrm{d}}}{\mathrm{d}t} = \sigma_{\mathrm{D}}\phi\left(1 - f_{\mathrm{d}}\right) - Rf_{\mathrm{d}}. \tag{2.57}$$

$\sigma_{\mathrm{D}}\phi$, or the defect production rate, is often expressed in displacements per atom per second (dpa/s), where $\sigma_{\mathrm{D}}\phi = 1$ dpa/s denotes that every atom is displaced on average once per second. For constant R, Equation 2.56 has a solution given by [105]

$$f_{\mathrm{d}} = f_{\mathrm{s}}\left[1 - \exp\left(-\frac{\sigma_{\mathrm{D}}\phi t}{f_{\mathrm{s}}}\right)\right], \tag{2.58}$$

where $f_{\mathrm{s}} = \sigma_{\mathrm{D}}\phi/\left(\sigma_{\mathrm{D}}\phi + R\right)$ is the relative defect fraction at saturation. At low ion fluences $F = \phi t$ (in ions/cm^2, assuming a constant ion flux), f_{d} first increases linearly with increasing ion fluence, before exponentially levelling off to the saturation value f_{s}. At f_{s}, the defect production rate is equal to the recombination rate.

Up to now, we have not accounted for defect diffusion, as well as any effects due to temperature. Indeed, R is temperature dependent, with typically larger recombination rates at higher temperatures [105]. Furthermore, temperature also affects the diffusion of defects themselves. To better describe the diffusion of defects, we write the rate equation separately for interstitial atoms and vacancies. We also add an extra loss term that represents defect sinks. In that case, the rate equations are now given by

$$\begin{aligned}\frac{\mathrm{d}C_{\mathrm{i}}}{d_{\mathrm{t}}} &= n\sigma_{\mathrm{D}}\phi - RC_{\mathrm{i}}C_{\mathrm{v}} - \sum_{s} K_{\mathrm{i}s}C_{s}C_{\mathrm{i}},\\ \frac{\mathrm{d}C_{\mathrm{v}}}{d_{\mathrm{t}}} &= n\sigma_{\mathrm{D}}\phi - RC_{\mathrm{i}}C_{\mathrm{v}} - \sum_{s} K_{\mathrm{v}s}C_{s}C_{\mathrm{v}},\end{aligned} \tag{2.59}$$

where C_{i} and C_{v} denote the interstitial and vacancy concentrations, respectively. The recombination rate R, as well as the defect-sink reaction rate coefficients $K_{\mathrm{i}s}$ and $K_{\mathrm{v}s}$ are dependent on the defect diffusion constant D.

Finding an analytical solution to the coupled non-linear differential equations in 2.59 is not trivial. Instead, numerical techniques are often used. Equation 2.59 can be further complicated by considering different types of defect sinks, each with a different affinity for interstitials and vacancies, and the thermal production of defects at larger temperatures. Moreover, defect production in compound materials, as well as the different diffusion rates for each type of defect in each sub-lattice significantly complicates the analysis. We will not describe these additional effects here, instead we refer to Refs. [130,131] for a more detailed picture. In the next section, we will treat mixing of compound materials due to ion irradiation.

2.2.2 Mixing

So far in this chapter, we have only considered single compound targets, e.g. Co, Pt, or W lattices. However, the samples that are studied in this thesis consist of complicated stacks of thin films, which in themselves can be compounds (e.g. a stack of W (4)/$\mathrm{Co_{20}Fe_{60}B_{20}}$ (1)/MgO (2)/Ta(5), with thicknesses in nanometers). Irradiation of these samples can result in the mixing of layers [132–134], which is what we will describe here. We first discuss ballistic mixing by ion irradiation, before discussing the effect that thermodynamics and chemistry has on the ballistic mixing.

2.2.2.1 Ballistic mixing

In a binary system, such as a bilayer or a thin marker layer in a bulk sample, the relocations with distance x of the atoms at the interface can be described by the so-called relocation cross-section $\mathrm{d}\sigma(x,z)$, where z denotes the depth. For a beam of ions with fluence F, the mean displacement is given by

$$\langle \Delta x\rangle = F\int_{z} z\,\mathrm{d}\sigma(x,z)\,. \tag{2.60}$$

For small relocations, the variance of the mixing distribution is given by

$$\Omega_{\mathrm{m}}^{2} = \left\langle (\Delta x - \langle\Delta x\rangle)^{2}\right\rangle = F\int_{z} z^{2}\mathrm{d}\sigma(x,z)\,, \tag{2.61}$$

where the integral is usually named the mixing parameter M. The mixing profile in the case of a bilayer system then evolves along a broadening error function, which is schematically shown in Figure 2.12. The initial bilayer, shown in the inset on the left, corresponds to the dark-blue curve with a sharp transition of concentration at the interface. Increasing fluence broadens the concentration profile as atoms start mixing, creating an intermixed state which is schematically shown on the right. Note that the evolution of the bilayer profile in Figure 2.12 assumes symmetric mixing of the layers, in which case the standard deviation of the mixing profile is given by $\sqrt{2}\Omega_{\mathrm{m}}$.

Determination of the ballistic mixing parameter is not trivial. Several different processes happen at the same time, including displacement of atoms at the interface, displacement of atoms far away into the interface, as well as cascade mixing around the interface [135]. From analysis of these effects and assuming a power-law scattering behavior, one can obtain the mixing parameter M, given by

$$M = \frac{2\gamma}{\pi^{2}} S_{\mathrm{n}}\left(\overline{E}\right)\frac{\left(\overline{R}_{\mathrm{p}}\left(U_{\mathrm{m}}\right)\right)^{2}}{U_{\mathrm{m}}}, \tag{2.62}$$

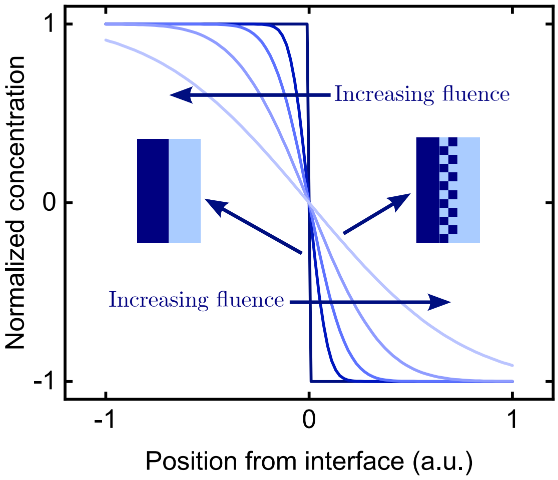

Fig. 2.12: Ballistic mixing profile of a bilayer system | Evolving concentration due to symmetric ballistic mixing in a bilayer system. The insets show the initial bilayer state and an intermixed state after irradiation. The horizontal arrows denote the progression of the concentration profile with increasing fluence.

where $\overline{E}$ is the mean energy of the ion at the interface depth, U_m is the relocation threshold energy for atoms around the interface, and $\overline{R}_\mathrm{p}\left(U_\mathrm{m}\right)$ is the mean projected range of an atom at the threshold energy.

The mixing of atoms due to irradiation is often linked to diffusion of atoms. This "ballistic diffusion" is linked to the mixing parameter through $M = 4Dt/F = 4D/\phi$, where D is the associated diffusion constant, t is the irradiation time, and ϕ the flux. Combining this with Equation 2.62, we obtain a ballistic diffusion constant for power law scattering, given by

$$D_\mathrm{bal,PL} = \frac{\gamma\phi}{2\pi^2} S_\mathrm{n}\left(\overline{E}\right) \frac{\left(\overline{R}_\mathrm{p}\left(U_\mathrm{m}\right)\right)^2}{U_\mathrm{m}}. \tag{2.63}$$

Equation 2.63 thus states that ballistic mixing is enhanced for ion-target combinations of similar mass. Heavier atoms typically have a larger ballistic mixing compared to light ions, due to their larger nuclear stopping.

The ballistic diffusion constant in Equation 2.63 does not take into account any chemical and temperature based effects. Indeed, certain elements like mixing more with some elements than other. In the next section, we discuss several models that describe the influence of thermodynamics on ballistic mixing.

2.2.2.2 Influence of thermodynamics on ballistic mixing

The simplest way to study the effects of thermodynamics on mixing is to consider Fick's law for chemical diffusion:

$$\frac{\partial C\left(x,t\right)}{\partial t} = D\nabla^2 C\left(x,t\right), \tag{2.64}$$

where C denotes the concentration. In the case of a bilayered system, D must be adapted in order to take into account the diffusive motion of the interface between the two materials A and B (the so-called Kirkendall effect). By applying Darken's method, this results in [136]

$$D \rightarrow \tilde{D} = \left[D^\circ_\mathrm{A} C_\mathrm{B} + D^\circ_\mathrm{B} C_\mathrm{A}\right]\left[1 - \frac{2\Delta H_\mathrm{mix}}{k_\mathrm{B} T}\right], \tag{2.65}$$

where D° is the intrinsic diffusivity constant, and $\Delta H_\mathrm{mix} = 2\delta C_\mathrm{A} C_\mathrm{B}$ is the enthalpy of mixing. δ is the heat of mixing parameter, which depends on the potential energies of each possible compound to be formed (A-A, B-B, and A-B), and thus determines which compounds are more favorable to be formed [136]. ΔH_{mix} can be estimated with a model by Miedema [137]. According to Equation 2.65, the diffusivity is enhanced for material combinations with a negative ΔH_{mix}, whereas material combinations with positive ΔH_{mix} have reduced diffusivity. Depending on the strength of ΔH_{mix}, materials can even "demix". Values of ΔH_{mix} for relevant material combinations in this thesis are shown in Figure 2.13.

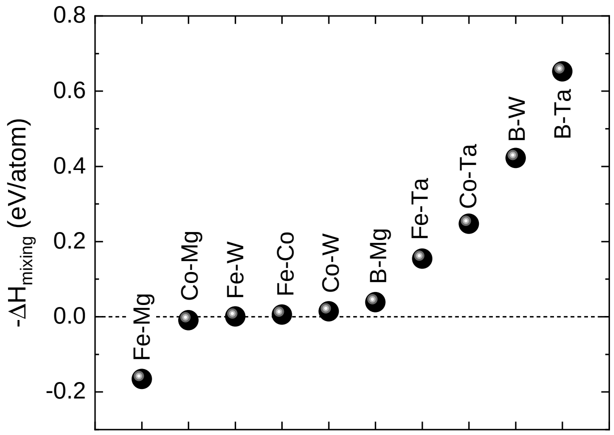

Fig. 2.13: Mixing enthalpies for different material combinations | Enthalpy of mixing of different material combinations based on Miedema's model [137]. More negative enthalpy of mixing denotes an easier mixing. Values obtained from Ref. [138].

Experimentally, a correlation is observed between $\tilde{D}$ and $\frac{1}{4}\phi\Delta H_{\mathrm{mix}}$ [136]. However, this is mostly true for high energy heavy ions, which mostly cause thermal spike mixing. Furthermore, the scaling is different for different compound combinations. Johnson *et al.* [136] proposed a phenomenological adaptation in 1985 that takes into account the enthalpy of coherence ΔH_{coh}, resulting in a radiation enhanced diffusion constant given by

$$\tilde{D} = \frac{1}{4}\phi K_1 n^{1/3} \left(\frac{S_{\mathrm{n}}\left(\overline{E}\right)}{\Delta H_{\mathrm{coh}}} \right)^2 \left[1 + K_2 \frac{\Delta H_{\mathrm{mix}}}{\Delta H_{\mathrm{coh}}} \right], \tag{2.66}$$

where $K_1 = 0.0037$ nm and $K_2 = 27$ are constants, and n is the average atomic density of the bilayer materials. Better experimental correlation can be obtained with Equation 2.66, but this model is inaccurate for light ions.

In the case of light ions, the ballistic and thermodynamic effects can be separated, as proposed in a model by Traverse *et al.* from 1989 [139]. The experimental diffusion constant can then be written as

$$\tilde{D}_{\mathrm{exp}} = \tilde{D}_{\mathrm{bal}} + \tilde{D}' \left[1 - \frac{2\Delta H_{\mathrm{mix}}}{k_{\mathrm{B}}T} \right], \tag{2.67}$$

where $\tilde{D}_{\mathrm{bal}}$ is the contribution due to ballistic effects, which can be described by Equation 2.63, and $\tilde{D}'$ is the so-called radiation enhanced diffusion constant. In the Traverse model, $\tilde{D}'$ is given by

$$\tilde{D}' = M' \frac{k_{\mathrm{B}}T}{C_{\mathrm{A}}C_{\mathrm{B}}}, \tag{2.68}$$

where $M' = MC_{\mathrm{v}}/C_{\mathrm{v}}^{\circ}$ is the enhanced atomic mobility due to the additional vacancies created by the irradiation process, with C_{v} and C_{v}° the vacancy concentration under and without irradiation, respectively.

The models describing the effect of thermodynamics on irradiation show that mixing is not a straightforward process. Indeed, the mixing varies a lot between different target atom species. Furthermore, at larger temperatures, the thermodynamic mixing effects become larger. In the case of light ions, thermodynamic effects can even dominate the mixing, as the ballistic contribution, which depends on the nuclear stopping, is typically very low.

We will use the effect of atomic mixing after irradiation throughout this thesis. In Chapters 4 and 5 we will show that the irradiation induced intermixing of layers can significantly impact various magnetic properties of ultra-thin films, and that the evolution in the magnetic state due to mixing can be exploited to eliminate edge defects. In Chapter 3, mixing plays a secondary role to irradiation induced crystallization, which is discussed in the next section. Nonetheless, mixing is an effect that should be taken into account when designing magnetic samples with different nanoscale disorder.

2.2.3 Irradiation induced crystallization

So far, we have seen that ion irradiation induces lattice atom displacements, and can cause binary layers to mix. However, ion irradiation can also enable the exploration of non-equilibrium paths toward more stable ordered structural phases. For example, if the target material is amorphous, atoms that are moved around have a chance to crystallize. Normally, this only occurs at very large temperatures, e.g. by high temperature annealing [140–142]. However, the added atomic mobility due to ion irradiation can induce the crystallization process at lower temperatures [105,143–145]. In this section, we describe this irradiation induced crystallization from two different points of view. First, we consider the so-called nanoparticle view, in which the crystallite is depicted as a particle in an amorphous environment. We will discuss the basics of crystallite growth, and how crystallite growth under irradiation can result in a narrower distribution of crystallite sizes. In the second, we will briefly consider the change in the crystallization energy barrier, which is used to explain the onset of crystallization at significantly reduced temperature under irradiation. Both points of view are described in detail in Refs. [105,144]. Here we give an overview of the essentials.

2.2.3.1 Nanoparticle model

In the nanoparticle model for irradiation induced crystallization, we consider the crystallite as a nanoparticle in an amorphous solid solution. This model makes use of the thermodynamic description of particle formations in solid solutions, which can be adapted for driven systems such as those under irradiation. Let us first consider the basic thermodynamics or regular solid solutions.

In any thermodynamic system, we can define a phase as a homogeneous, physically distinct, mechanically separable portion of the material. A phase can be defined by its atomic phase (e.g. liquid, solid or gas), its chemical composition, and crystalline structure. For the purposes of this model, we focus on the latter, where we define a crystalline phase in an amorphous surrounding phase. When multiple phases are present, an interface between the phases exist, which is also called a phase boundary. A move between phases, also called a phase transition, is characterized by the Gibbs free energy of each phase:

$$G = H - TS, \tag{2.69}$$

where H is the enthalpy, T the temperature and S the entropy. A phase transition is possible when the difference in Gibbs free energy $\Delta G = G_\mathrm{f} - G_\mathrm{i}$ between the final state f and initial state i is smaller than 0.

We now consider a binary glass-metal system of A and B, where B is the solute in host matrix A (i.e. B is the crystallite in surrounding amorphous material A). We can then summarize the different existing phases as a function of temperature and solute concentration C_B in a phase diagram. An example is shown in Figure 2.14a. We can describe the evolution of the system upon cooling down from T_1 at a stable concentration C, shown by the blue line in Figure 2.14a. At high temperature T_1 larger than the melting temperature, both phases are in liquid form (L). Upon cooling down to

T_2, A starts to form and the system is in a mixture of A and liquid A + B (A + L). Further cooling down to T_3, the system is now a solid solution of B in host matrix A (A(B)). Finally, cooling further down to T_4, phase separation occurs, where we have separate A and B phases (A+B). This region is also called the coexistence region.

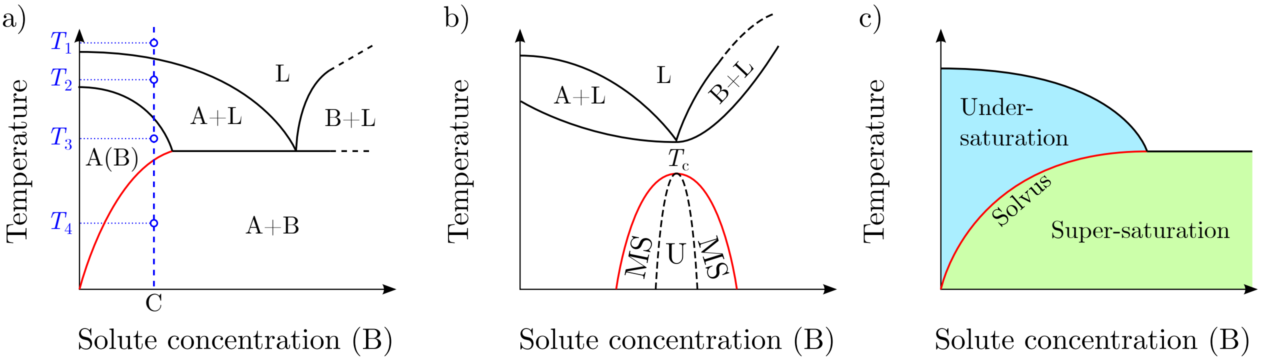

Fig. 2.14: Solid metal-glass solution phase diagrams | a) Phase diagram for a solid metal-glass solution, with A the host matrix and B the solute, as a function of temperature and solute concentration. A(B) denotes a dissolved B in A, and L denotes the phase where both A and B are a liquid. The solvus is shown in red. b) Phase diagram with a miscibility gap. Below the critical temperature T_c, the A + B phase is either unstable (U), or meta-stable (MS). c) Zoom-in of a) around the solvus (red). The area below the solvus is the super-saturated region (green), whereas the area above the solvus is the under-saturated region (blue). Figures adapted from Ref. [105].

If the coexistence region does not cross A + L or B + L, the system has a miscibility gap. An example of such a phase diagram is shown in Figure 2.14b. Below the critical temperature, depending on how the system transitions from A(B) to A + B, the system can be metastable (MS), presenting an energy barrier for particle nucleation and growth. If such an energy barrier does not exist, A + B is unstable (U).

The line separating A(B) and A + B is called the solvus, and is shown in red in all figures. It denotes the maximum solute concentration that can be added at a given temperature before phase separation occurs. At large temperature where A(B) is stable, more solute concentration can be added before phase separation occurs. This is called under-saturation. Concenquently, the region past the solvus is called the super-saturated regime. For 2 solid phases A and B, where B is in the form of a particle, the solvus is given by

$$C\left(R\right) = C_\infty\left(T\right)\exp\left(\frac{L_c}{R}\right), \tag{2.70}$$

where $C_\infty = C_0 \exp\left(-H_v^f/k_B T\right)$ is the solvus for a plane interface, with C_0 a positive pre-factor and H_v^f the vacancy formation enthalpy, R the particle size, and $L_c = 2\sigma\Omega/k_B T$ is the capillary length, with σ the surface tension and Ω the atomic volume. The solvus depends on particle size and temperature through

$$\ln\left(\frac{C\left(R\right)}{C_\infty}\right) \propto \frac{1}{RT}, \tag{2.71}$$

which shows that larger particles are more stable than smaller particles, since they have a lower $C\left(R\right)$.

So far, we have only described the equilibrium state of the system. How does the system reach its equilibrium state? We can gain insight by looking at the time evolution of the so-called supersaturation $s\left(t\right) = C\left(t\right)/C_\infty$. We can identify four distinct regimes, which are summarized in Figure 2.15.

In the first regime, called the super-saturation regime, $s\left(t\right)$ increases with the amount of monomers, i.e. crystallites, deposited in the system. $s\left(t\right)$ keeps increasing until it reaches a critical value $s_c = 1$ at t_1. At s_c, the system is at the solvus.

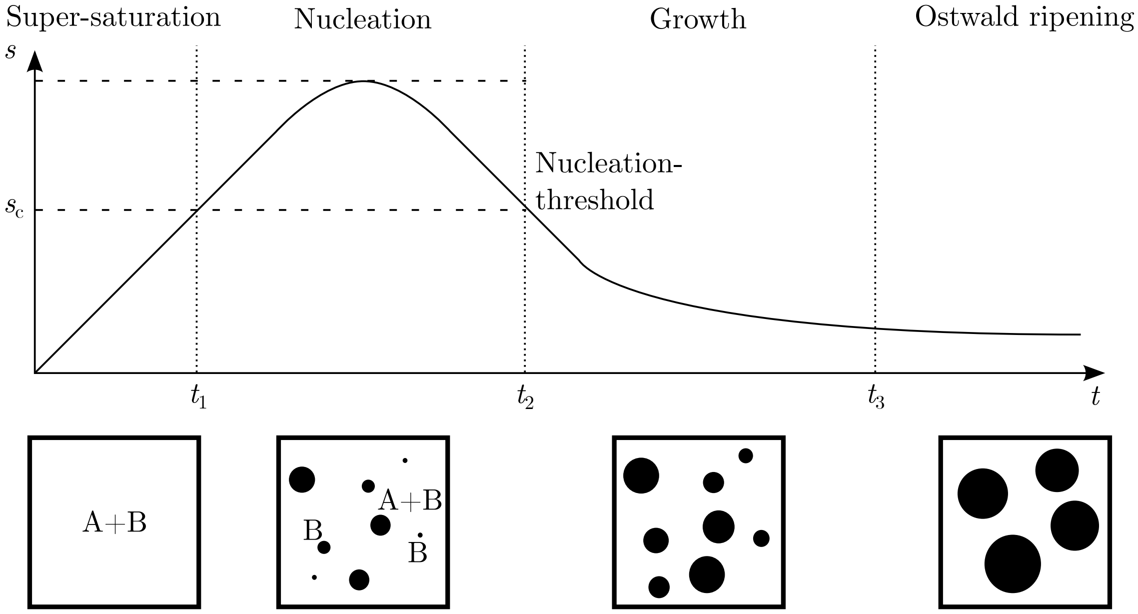

Fig. 2.15: Nanoparticle evolution | Schematic representation of the evolution of the supersaturation as a function of time. Four distinct regimes are identified, which are separated by vertical dotted lines. A schematic representation of the state is shown in the panels below each regime: (1) super-saturation for $t < t_1$, where s grows until a critical value s_c. (2) Nucleation, where particles are allowed to nucleate due to $s > s_\mathrm{c}$. This regime lasts until t_2, where s drops below s_c. (3) Growth, where new particles no longer nucleate, but existing particles are allowed to grow due to absorption of monomers, i.e. crystallites, in the solution. This lasts until t_3, where we enter (4) the Ostwald ripening regime, where smaller particles are unstable, dissolve, and further grow the larger particles. Figure adapted from Ref. [105].

Further increasing $s(t)$ leads to the second regime: nucleation. For $s(t) > 1$, embryo's are formed. The stability of these particles depends on the balance of volume and surface energies. We can define a critical energy barrier ΔG^* and critical radius R^* necessary for particle stability, which both depend on s and the temperature T. They are given by

$$\begin{aligned} \Delta G^* &\propto \frac{1}{T^2 \ln\left(s^2(t)\right)}, \\ R^* &\propto \frac{1}{T \ln\left(s(t)\right)}. \end{aligned} \tag{2.72}$$

Their scaling with s and T tells us that it is easier to nucleate at larger temperatures and larger supersaturation, while the critical radius of nucleation drops with similar scaling. In favorable nucleation conditions, smaller particles are stabilized. The nucleation rate J^*, which depends on ΔG^* through

$$J^* \propto \exp\left(-\frac{\Delta G^*}{k_\mathrm{B} T}\right), \tag{2.73}$$

thus increases at larger temperatures and higher super-saturation. The dependence of J^* on s tells us the behavior in the nucleation regime. At s just above s_c, the saturation levels are not high enough to form a lot of particles, and thus s keeps increasing due to monomer deposition, despite the nucleation of some particles. Once ΔG^* is low enough, an explosion of small particle nucleation occurs. These particles are a sink for the solute, causing s to decrease over time. Decreasing s increases ΔG^* and R^*, in turn dropping J^*. Once s is below the nucleation threshold at t_2, nucleation stops. $t_2 - t_1$ is thus the nucleation window. A broad range of particle sizes remain at the end of the nucleation window, as particles that have been nucleated at the start of the nucleation window have had more time to grow. Growth of particles does not stop below s_{c} however, and we enter the next regime.

No new particles nucleate in the growth regime, however s is still large enough to allow the particles to grow. This essentially occurs due to the fact that the super-saturation is still larger than the interface concentration of the growing particles, the latter of which is given by Equation 2.70. As long as this condition is satisfied, the particles will grow. The growth rate depends on the dominant process: monomer absorption or monomer diffusion. With time, the super-saturation is further reduced as the particles grow, which in turn affects their stability. Smaller particles will become less and less stable, eventually dissolving. At this point (t_3), we enter the next regime: *Ostwald ripening.*

Ostwald ripening, the process in which the smaller particles dissolve back into the host matrix, allows the larger particles to grow further. Ostwald ripening is thus essentially a mass redistribution: big particles grow at the expense of small particles until the supersaturation goes to zero.

How does irradiation change the processes in this model? We can get an idea by taking into account the ballistic effects from the irradiation process, which counteract the thermal effects. At very high temperatures, the thermal effects still dominate, and classical Ostwald ripening occurs. At lower temperatures, the ballistic effects can become dominant. If the ballistic effects are very strong, they can completely destroy the particles. At weaker ballistic effects, they counteract the thermal effects, reaching a steady state. Hence, smaller particles are stabilized compared to pure thermal effects. This is often called *Inverse Ostwald Ripening.*

The additional ballistic effects due to irradiation can be described by two different models. In the first, a ballistic term $G(r)$ is added to Fick's diffusion law (Equation 2.64):

$$\frac{\partial C(r,t)}{\partial t} = D\nabla^2 C(r,t) + G(r), \tag{2.74}$$

where r denotes the distance to the center of a single particle. $G(r)$ is proportional to the displacement rate $\sigma_{\mathrm{D}}\phi$. Frost and Russell proposed the source term [146]

$$G(r) = \frac{S}{4r\lambda}\left[R^2 - (r-\lambda)^2\right], \tag{2.75}$$

where $S \propto \sigma_{\mathrm{D}}\phi$ is a constant recoil generation rate, R the radius of the particle, and λ the displacement distance of the recoils. Numerical solutions to Equation 2.74 using this source term indicate the following behavior for the steady state, depending on the particle size: particles that are bigger than the steady state size will be reduced in size due to the ballistic effects (inverse Ostwald ripening), whereas particles that are smaller than the steady state size will experience growth towards the steady state size (classical Ostwald ripening).

The second model is based on the ballistic mixing model described in Section 2.2.2. For light ions, a model from Martin [147] states that the additional ballistic effects can be summarized in an effective temperature model. Basically, the evolution of the system is similar to pure thermal behavior, but now at an effective temperature

$$T_{\mathrm{eff}} = T\left(1 + \frac{\tilde{D}_{\mathrm{bal}}}{\tilde{D}'}\right). \tag{2.76}$$

Indeed the increased temperature due to the added ballistic effects and radiation enhanced diffusion reduces the steady state particle size, causing particles that are too big to shrink, and particles that are too small to grow.

In summary for the nanoparticle model, irradiation during the crystallization process can thus result in a more homogeneous distribution of crystallite sizes compared to regular crystallite formation, due to the shrinking of larger crystallites and the growing of smaller crystallites. However, this model cannot explain why the critical temperature for crystallization is reduced [144]. In the effective temperature view, due to the relatively small ballistic effect of light ions, the effective temperature increase will be relatively small to the observed changes in activation temperature for crystallization (up to several hundreds of degrees depending on the ion type [105]). In the next section, we briefly discuss the crystallization activation temperature under irradiation.

2.2.3.2 Ion beam induced epitaxial crystallization

Crystallization occurs when atoms are stimulated to rearrange their bonds to reach a lower energy state ($\Delta G < 0$). During regular thermal treatments, the energy barrier for crystallization is overcome by pure thermal energy [148]. Displacement of atoms and their subsequent recombination under ion irradiation can also act as a stimulus for crystallization [143,144]. In the case of epitaxial growth, this process is called ion beam induced epitaxial crystallization (IBIEC). IBIEC is dependent on the ratio of induced damage and atomic recombinations, both of which were discussed in Section 2.2.1.4. When recombinations outweigh damage creation, crystallization becomes more likely. Ion irradiation temperature plays a significant role here, since recombinations are more favored at larger temperatures. Even slight changes in irradiation temperature of a few degrees can mean the difference between IBIEC and ion beam induced amorphization of a material [105].

To understand why ion irradiation can cause crystallization, especially at much lower temperatures compared to pure thermal treatments, we investigate the activation energy. In the thermal case, the recrystallization velocity v can be described with an Arrhenius law [148]:

$$v = v_0 \exp\left(-\frac{E_\mathrm{a}}{k_\mathrm{B}T}\right), \tag{2.77}$$

where v_0 is a constant, and E_a the crystallization activation energy. E_a is typically very large for thermal crystallization (e.g. $E_\mathrm{a} = 2.7$ eV [148]). This is usually attributed to the fact that, for epitaxial crystallization, the energy barrier is given by $E_\mathrm{a} = E_\mathrm{n} + E_\mathrm{i}$, where E_n represents the energy barrier for nucleation of defects, and E_i the energy barrier for bond rearrangement [149].

In the case of ion irradiation, E_n is naturally overcome by the ballistic effects of the collision process. Hence, the only activation energy that plays a role in IBIEC is E_i, which is typically much lower. Typical values from experimental studies range between 0.18 eV to 0.4 eV, depending on the ion mass as mentioned in Refs. [105,144] and references therein. Although IBIEC and the crystal nucleation through the nanoparticle model described in Section 2.2.3.1 are different, it is expected that the reduced energy barrier argument is still valid, albeit qualitatively. One factor that could bridge the two descriptions lies in the fact that nucleation under annealing is preferred at locations where E_n is naturally low due to existing lattice defects, whereas under irradiation the nucleation is randomly distributed throughout the layer as it is driven by ballistic effects. This could result in more homogeneous crystallite nucleation under irradiation compared to annealing.

The above description is arguably limited. Defect production is heavily dependent on the properties of the ion, such as mass and energy, and on the properties of the target material, such as defect production and diffusivity, and other changes to the thermodynamic properties of the material under irradiation. It is also expected that the crystallization dynamics change further for very thin film amorphous layers, as the above descriptions are mainly made for bulk Si. Furthermore, beam parameters such as fluence and flux, as well as ambient conditions such as irradiation temperature exert large effects on the crystallization dynamics [105]. More in-depth studies are required to reveal the exact crystallization dynamics under ion irradiation in different materials and for different ions.

Despite these limitations, it is clear that ion irradiation can enhance the crystallization process, both through the reduced energy barrier required for crystallization, as well as the reduced particle size distribution discussed in Section 2.2.3.1. In Chapter 3 of this thesis, we will shed more light on the effect of crystallization on the magnetic properties of ultra-thin magnetic films. We will specifically show that the magnetic anisotropy is heavily dependent on the irradiation temperature and fluence. We will also show that different irradiation parameters have strong effects on the motion of a domain wall, which in turn can be used to gain insights into the structural properties of the thin films.

2.3 The working principles of ion irradiation

In this section, we discuss working principles of the ion irradiation techniques that we have used in this thesis. This includes the physics that are involved in steering the ion beam to the sample, and the possibilities to only irradiate parts of the sample through local irradiation.

2.3.1 Full film ion irradiation

The working principles of large scale ion irradiation are shown in Figure 2.16a. A helium plasma is created in an electron cyclotron resonance (ECR) source, where microwave radiation is used to excite the helium gas. Ions are extracted from the plasma using a high voltage, which forms the initial beam. The extraction voltage sets the ion energy. The beam current, i.e. the amount of ions in the beam over a certain time, is regulated by the source. Injecting more gas will create a denser plasma, and thus a stronger beam current. Similarly, increasing the ECR power will further ionize the gas, resulting in a larger beam current. The beam passes through a filter, which gets rid of impurities (e.g. C^+ or O^+), multi-charged ions (e.g. He^{++}), and other particles that do not have the right velocity. Two filter types are common; a Wien filter [150], shown schematically in Figure 2.16b, which selects the correct velocity by using the balance between the electrostatic and Lorentz forces a particle experiences traveling through perpendicular magnetic and electric fields, and a Lorentz-force filter [150], shown schematically in Figure 2.16c, which selects particles based on their deflection radius as a consequence of the Lorentz force the particle experiences when traveling through a magnetic field. After traveling through a shape controlling aperture, the shape of the beam is further controlled by electrostatic lenses, which focus the beam onto the sample. Beam sizes in the focused spot are typically a few millimeters. A final set of electrostatic lenses is used to sweep the beam across the sample.

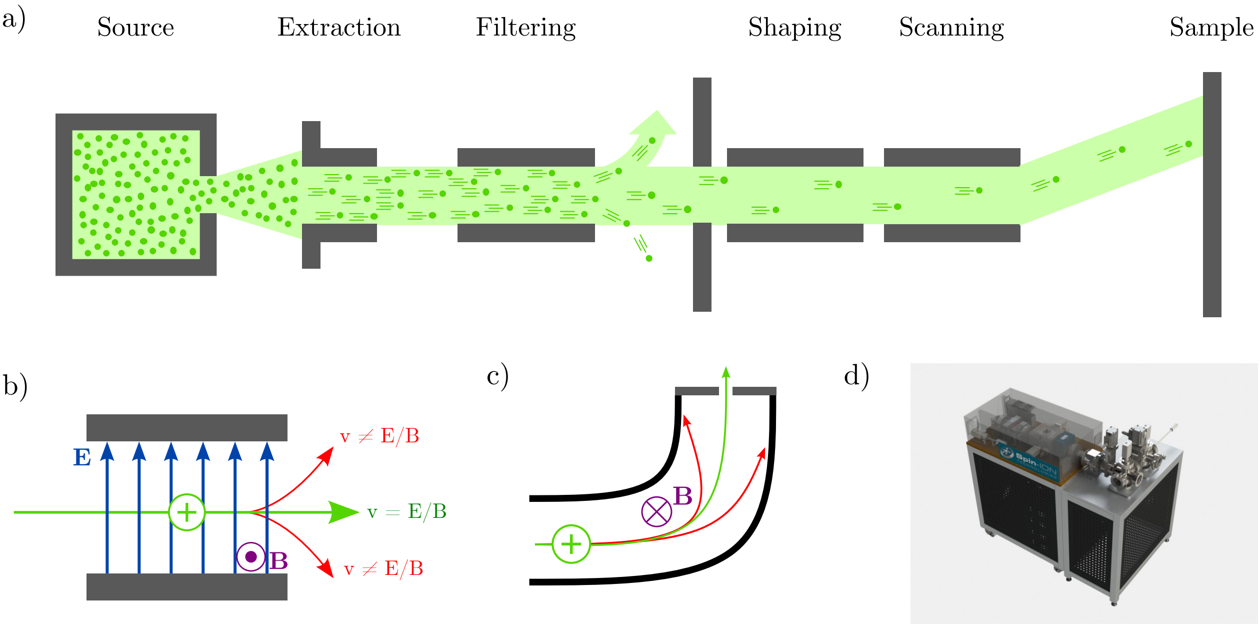

Fig. 2.16: a) The working principles of ion irradiation | He^+ ions are created in an ECR source. They are extracted at high voltage with the extraction lens, and subsequently filtered to select only the correct species of ion. The beam is then shaped and scanned on the sample by use of electrostatic lenses. b) Schematic of a Wien filter. Only particles with the correct velocity will be selected. c) Schematic of a Lorentz-force filter. Only particles with the correct velocity will be deflected in the correct way to pass through the gap. d) A rendering of the Helium-S^{TM} developed by Spin-Ion Technologies [25].

To perform the large scale irradiations for the experiments in this thesis, we use a Helium-S^{TM} from Spin-Ion Technologies [25], shown in Figure 2.16d. It is capable to create a He^+ ion beam with energies between 1 and 30 keV to homogeneously irradiate 15 × 15 mm^2 samples. Furthermore, the sample holder contains a heating element to perform irradiations at elevated temperatures. The latter will be exploited in the optimization of magnetic materials through irradiation induced crystallization, which we discuss in the next chapter.

2.3.2 Local ion irradiation

Two different techniques are typically used to achieve local irradiation; focused ion beam (FIB) and irradiation through a mask. The latter is also often called magnetic planar patterning in the case of He$^+$ irradiation through a mask, as no etching occurs. In this section, we discuss the working principles of both techniques. While the details depend strongly on the type of ions that are used - a He$^+$ FIB works differently from a Ga$^+$ FIB for example - we restrict ourselves to irradiation with He$^+$ ions. For the He$^+$ FIB, the details are excellently reviewed in Ref. [151], while a review on magnetic patterning can be found in Ref. [152].

2.3.2.1 Focused Ion Beam (FIB)

The working principles of a He$^+$ FIB are shown in Figure 2.17. He$^+$ ions are created in the source, which is schematically shown in Figure 2.17a. An atomically sharp W-tip is suspended in a He$_2$ gas. The atoms in the tip are arranged in a pyramid with three atoms at the top, which is the so-called trimer configuration. This allows for the application of very strong electric fields when a voltage is applied to the tip, which ionizes the He atoms. He$^+$ ions can be extracted from the plasma at the tip with another electric field, applied with a so-called extractor lens (blue). Although the ions are coming only from a small point at the tip, the extractor lens causes the ions to be emitted in a solid angle. Optics are thus required to control the shape of the beam, which are shown in Figure 2.17b. After the extractor, electrostatic lenses are used to refocus the beam. Quadrupole lenses correct any deviation in the beam. The beam subsequently passes through a set of apertures, which allows a user to control the beam current. Blanker lenses can be used to deflect the beam, stopping it from reaching the sample. A final set of lenses is then used to focus the beam onto the sample, where the beam can be rastered with the use of octopole lenses.

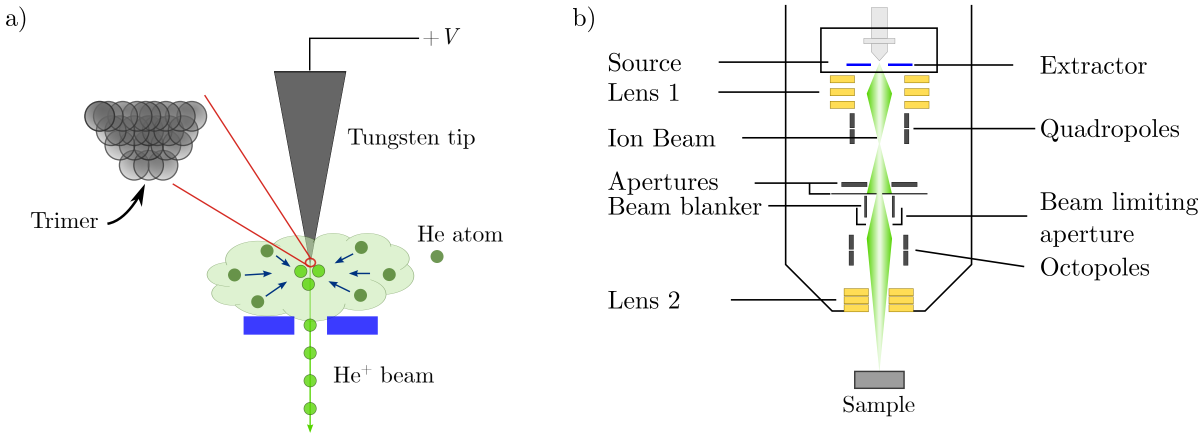

Fig. 2.17: The working principles of a He$^+$ FIB | a) He$^+$ source. A gas of He atoms is ionized by a strong electric field at the end of the tip. The atoms at the end of the tip are arranged in the so-called trimer configuration. He$^+$ is extracted from the ionized gas with extractor lenses (blue). b) Schematic of the full He$^+$ column optics. The ion beam (green) is extracted from the source, which is shown in more detail in a). It travels through several electro-static lenses that control the shape and direction of the ion beam. Apertures and beam blankers control the beam current that is sent to the sample. The beam is rastered on the sample with the octopole lenses, close to the final focusing lens.

For the local irradiations with a He$^+$ FIB in this thesis, we use a Zeiss Orion NanoFab He$^+$ FIB, capable of irradiations between 10 and 30 keV at beam currents between 0.1 and 100 pA. The FIB is capable of reaching resolutions down to 0.5 nm at 30 keV.

FIBs with advanced optics can reach very high resolutions, which is one of the main advantages when using a FIB to locally irradiate a (magnetic) material. However, when large areas are required to be irradiated, a FIB quickly becomes inefficient. Larger scale irradiation through a mask can be used to solve this issue, which is what we discuss in the next section.

2.3.2.2 Magnetic planar patterning

Figure 2.18a shows the working principles of a magnetic patterning process through a mask. A lithography process, as described in Chapter 4, is used to fabricate a protective mask on the areas of the sample that should be protected from irradiation. After the irradiation is complete, the mask is removed, and what remains is a sample where the areas that were exposed to irradiation have changed magnetic properties.

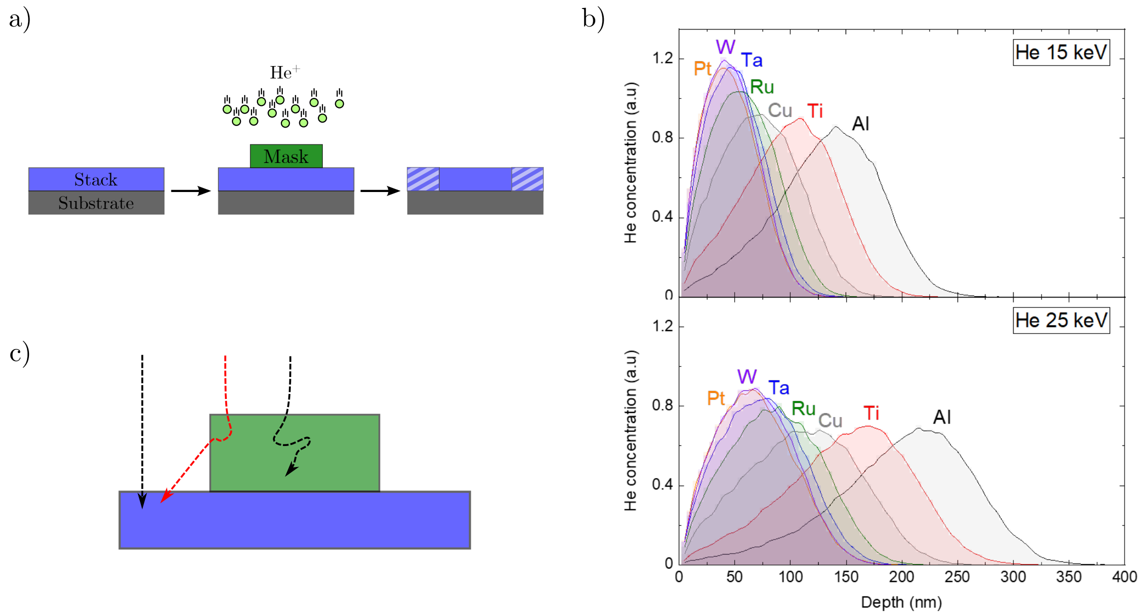

Fig. 2.18: Magnetic planar patterning through a mask | a) Schematic drawing of the magnetic planar patterning process by irradiation through a mask. The areas exposed to the He$^+$ ions have changed magnetic properties, while the area covered by the mask has been untouched. b) Stopping of He$^+$ at 15 keV (top) and 25 keV (bottom) in different mask materials with varying densities. Results obtained with SRIM. c) Schematic drawing of the different possible ion paths (dotted lines). The ion either hits the material directly, is stopped in the mask, or leaves the mask after a while. The latter results in collateral damage and is indicated in red.

The design and properties of the irradiation mask are dependent on the type of ions used for the patterning process, as showed by SRIM results for the stopping of He$^+$ with different energies in different materials in Figure 2.18b. Heavier ions require a thinner mask than lighter ions for example, as lighter ions typically travel further. Additionally, ions with larger energy also require thicker irradiation masks. Denser mask materials can reduce the total required mask thickness, as ions typically travel less far in denser materials.

The typical resolution that can be achieved with magnetic planar patterning depends strongly on the beam parameters and quality of the irradiation mask. We will not go into detail here, as mask optimization has been excellently treated in Ref. [125], but we will mention the most important factors. For ions with normal incidence, straggling in the mask can deflect their path, which can result in the ion leaving the mask at the edges, as shown in Figure 2.18c. For beams that come in under an angle, additional shading effects should be taken into account. These effects are strongly dependent on the height of the mask and can slightly displace the irradiated pattern. Furthermore, ions hitting the mask at the bottom will not be fully stopped and can thus influence the material below the mask. Masks without perfectly straight edges further influence the resolution, as part of the material around the edges will receive a different dose due to the mask covering a slightly larger area at the edge. To optimize the resolution in magnetic planar patterning through a mask, one should chose a dense mask material with straight edges [125], and minimize the mask height in the case of irradiation under an angle. Alternatively, one can use a higher resolution lithography process, such as electron beam lithography, to obtain better defined masks. Sub-50 nm resolutions can be achieved with magnetic planar patterning [153,154].

2.4 State of the art on ion beam physics in magnetic materials

In the previous two sections, we have seen that ion irradiation can significantly alter the atomic ordering in materials through mixing, crystallization, and overall damage production. In Chapter 1, we have seen that the properties of magnetic materials are heavily dependent on the atomic arrangement, especially at the interface between two materials. To see if we can tailor and/or improve the properties of magnetic materials, it is thus natural to investigate what happens to the properties of magnetic materials under ion irradiation. While we hope to contribute to this understanding in this thesis, a lot of prior work on irradiation of magnetic materials already exists, including many from our team.

Several excellent reviews on the topic have been made, such as one by Fassbender *et al.* from 2004 [23] on tailoring magnetism with light ion irradiation, or one by Fassbender and McCord from 2008 [152] summarizing advances in magnetic patterning, or a more recent one by Mahendra *et al.* [155] which discusses advances on tailoring magnetic tunnel junctions and its relevant properties with irradiation. However, some of these reviews are almost 20 years old, and therefore do not take into account advances in other directions of spintronics, such as the DMI, chiral DWs and magnetic skyrmions (essentially 360 degree DWs [156]), all-optical switching (AOS) of magnetization, magnetostriction, and novel device concepts based on the tuning of these properties.

In this section we give a comprehensive overview of these novel advances, as well as discuss any relevant works for the experiments in this thesis. For the sake of completeness, we will repeat some of the advances already described in the review papers mentioned above, albeit in less detail. We also focus mainly on thin films with PMA. The section is structured as follows: we start with a description of the effects of ion irradiation on the magnetic properties that are relevant for the results in this thesis. Following this, we discuss how the changes in these magnetic properties have been used to engineer devices based on magnetic structures such as DWs and skyrmions.

2.4.1 The effect of irradiation on the magnetic properties of PMA materials

When it comes to the modification of magnetic properties by ion irradiation, we typically describe two different effects; irradiation induced mixing and irradiation induced ordering. In this section, we describe the state-of-the-art of both processes.

2.4.1.1 Mixing and modification of magnetic parameters

In 1998, Chappert *et al.* were the first to report that He^+ irradiation can alter the anisotropy of Pt/Co/Pt thin films [24]. Their results show that 30 keV He^+ irradiation at room temperature (RT) can progressively tune the coercive field of a Pt/Co/Pt thin film and that, by irradiating through a mask, magnetic patterns can be created. This quickly spawned follow up works that both further investigated the capabilities of magnetic patterning [153,154,157–161] with various different types of ions, as well as the origin of the changes in magnetic properties [162–166]. Extensive structural characterizations by Devolder [163] show that irradiation causes mixing and alloying at the Pt/Co interfaces, which were identified to be the cause of the reduction in anisotropy. The interface roughness progressively increases with He^+ fluence, while the anisotropy decreases. The reduction of anisotropy with increasing ion fluence has been observed in studies for different ion types in many different multilayer stacks, such as Pt/Co/Pt [165,167–169], Pt/Co/Ta [170], Pt/Co/MgO [171,172], Ir/Co/Pt [173], Ta/CoFeB/MgO [174,175], and W/CoFeB/MgO [176], which for the latter are shown in Figure 2.19. Increasing He^+ fluence results in interface mixing, which in turn shows a reduction of the coercive field and the interfacial anisotropy constant, with the sample showing in-plane anisotropy (i.e. negative K_{eff}) at large fluences.

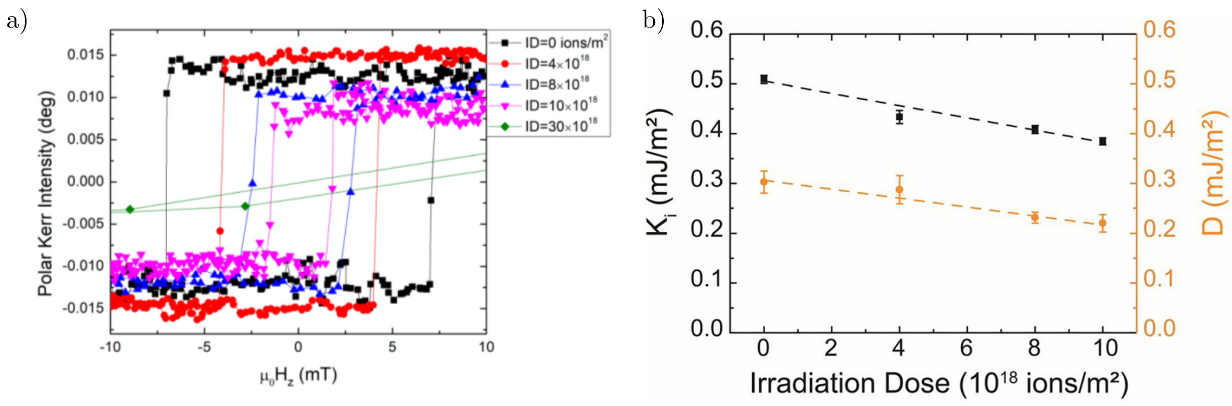

Fig. 2.19: Effect of He^+ irradiation on the properties of W/CoFeB/MgO | a) Polar MOKE hysteresis loops of W(4 nm)/$Co_{20}Fe_{60}B_{20}$(0.6 nm)/MgO(2 nm)/Ta(3 nm) irradiated with different He^+ fluences (irradiation dose - ID). b) Evolution of the interfacial anisotropy constant and DMI constant of W(4 nm)/$Co_{20}Fe_{60}B_{20}$(0.6 nm)/MgO(2 nm)/Ta(3 nm) as a function of He^+ fluence. Figures adapted from Ref. [176].

Interface intermixing also affects other interfacial properties, such as the DMI. Balk *et al.* [177] showed that the value and sign of H_{DMI} can be controlled in a Pt/Co/Pt stack, normally without DMI due to the lack of inversion symmetry, by tuning the top interface with low energy Ar^+ irradiation. Recent results show that the evolution of the DMI with ion irradiation is heavily dependent on the material stack that is investigated. Zhao *et al.* [176] showed a gradual decrease of the DMI in W/CoFeB/MgO with 15 keV He^+ irradiation, as shown in Figure 2.19b. The observed decrease has a simular form to the reduction in interface anisotropy. Conversely, in Ta/CoFeB/MgO, Herrera Diez *et al.* [178] showed an increase of the DMI in Ta/CoFeB/MgO irradiated with 15 keV He^+ at RT, as shown in Figure 2.20a. Nembach *et al.* [179] showed with Monte-Carlo simulations that the increase in DMI in Ta/CoFeB/Pt/MgO with 40 keV He^+ irradiation can be explained by an increase of Fert-Levy type FM-HM-FM triplets due to intermixing, shown in Figure 2.20b. This trend is opposite to the evolution of the interface anisotropy. In Pt/Co/X-based structures, intermixing at the Pt/Co interface only has a weak effect on the DMI. After an initial drop in the DMI, its value is stabilized and does not change significantly. This is observed in Pt/Co/Ta [170] and Pt/Co/MgO [171] for 25 keV and 15 keV He^+ irradiation, respectively, and is shown for Pt/Co/MgO in Figure 2.20c. This is in line with the theoretical predictions by Zimmermann *et al.* [180] that intermixing in the Pt/Co interface only results in a weak effect on the DMI. The evolution of the DMI in these systems does not follow the evolution of the interfacial anisotropy either, which gradually decreases with increasing He^+ fluence. For Ir/Co/Pt multilayers [173] irradiated with 30 keV Ga^+, a gradual decrease followed by a saturation of the DMI constant is observed with increasing fluence, which roughly follows a similar trend to the anisotropy. It is thus clear that the evident material dependence of the evolution of the DMI constant with increasing irradiation is not trivial, and requires further study to be fully understood. This should include a detailed study of the effects of the interfaces on both sides of the FM layer, as they both contribute to the DMI and can have different signs.

Intermixing can also affect the magnetization of the material, depending on the material stack. If the alloy that is formed after mixing is ferromagnetic, such as CoPt, the change in saturation magnetization is almost negligible [163]. Indeed, irradiation of Pt/Co/Pt [163] and Pt/Co/MgO

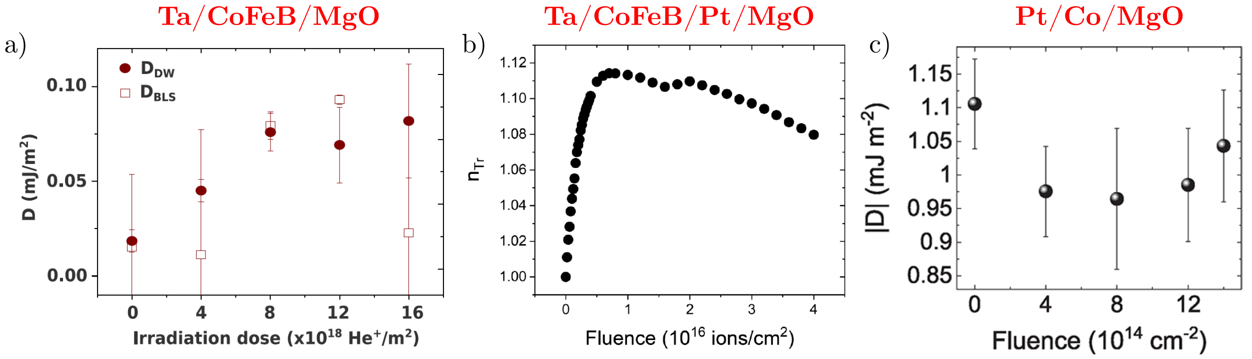

Fig. 2.20: Evolution of the DMI with He$^+$ irradiation in various systems | a) Results from Herrera Diez *et al.* [178] on the evolution of the DMI after 15 keV He$^+$ irradiation on Ta/CoFeB/MgO, as measured by domain wall expansion and BLS measurements. b) Results from Nembach *et al.* [179] on the evolution of the number of FM-HM-FM triplets (n_{tr}, thought to be proportional to the DMI) in Ta/CoFeB/Pt/MgO with 40 keV He$^+$ irradiation, extracted from Monte-Carlo simulations. c) Results from Juge *et al.* [171] on the evolution of the DMI after 15 keV He$^+$ irradiation on Pt/Co/MgO as measured with BLS.

[171] do not show a significant change in M_{s} with increasing fluence. However, alloys such as FeW and CoW, which are mostly paramagnetic [181], or FeTa and CoTa, which have a lower saturation magnetization than FeCo [182,183], can cause a reduction in the total magnetic moment, as observed in Ta/CoFeB/MgO [174] and W/CoFeB/MgO [176] for increasing He$^+$ fluence.

The changes in magnetization and anisotropy caused by progressive irradiation result in a temperature dependent reorientation of the anisotropy axis, and eventually a change in the magnetic phase at very large ion fluences [184]. Depending on the temperature and irradiation fluence, different magnetic phases and anisotropy axes are stabilized. It should be noted that each material has its own magnetic phase diagram, as it is heavily dependent on the magnetic properties. Samples with thicker FM layers or different elements can skip or add additional spin-orientation or phase transitions, or shift the phase diagram to lower or higher fluences.

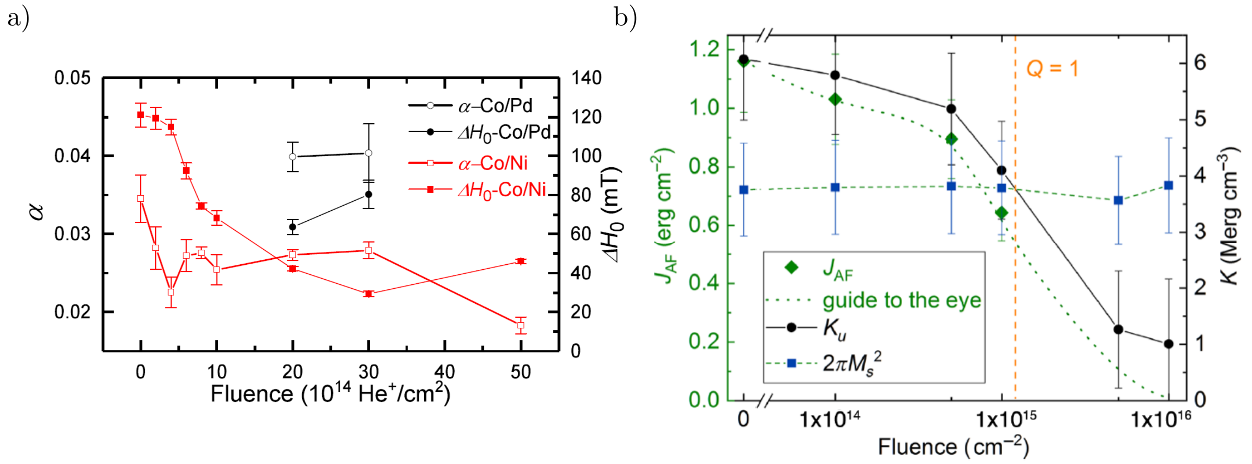

Fig. 2.21: Effects of He$^+$ irradiation on coupled layers | a) Data from Jiang *et al.* [185] showing the damping constant of the [Co/Ni] and [Co/Pd] multilayers in a Co/Ni]$_{\mathrm{x5}}$/Cu/[Co/Pd]$_{\mathrm{x4}}$ spin valve as a function of 15 keV He$^+$ fluence. b) Data from Koch *et al.* [186] showing the evolution of the interlayer exchange coupling and magnetic properties of a [(Co/Pt)$_{\mathrm{x5}}$/Co/Ru]$_{\mathrm{x3}}$/(Co/Pt)$_{\mathrm{x6}}$ synthetic anti-ferromagnet as a function of 4.5 keV He$^+$ fluence.

Irradiation also affects the damping constant. In Pt/Co/Ta, mixing has been observed to increase the damping constant [170] with increasing He$^+$ fluence. In [Co/Ni]$_{\mathrm{x5}}$/Cu/[Co/Pd]$_{\mathrm{x4}}$ spin valves, where the damping depends on the smoothness of the interface between the [Co/Ni]/Cu and Cu/[Co/Pd] interfaces, the damping was shown to decrease due to smoothing of the Cu/Co interface with 15 keV He$^+$ irradiation [185]. These results are shown in Figure 2.21a.

Other effects that are dependent on intermixing at interfaces between different materials, such as the the AOS of magnetization in Co/Gd ferrimagnetic layers [187], or the magnetostriction in Ni/Fe multilayers [188], are susceptible for tuning by ion irradiation [189,190], as we will show in more detail in Chapter 5 of this thesis. Moreover, materials that make use of the coupling between layers through interfaces, such as synthetic anti-ferromagnets (SAF) [191] or systems with exchange bias [192] can also be controlled with irradiation [186]. Figure 2.21b shows that the strength of the AF-coupling in a $[(Co/Pt)_{x5}/Co/Ru]_{x3}/(Co/Pt)_{x6}$ SAF is reduced with increasing He$^+$ fluence due to mixing at the Ru interface.

2.4.1.2 Irradiation induced ordering at low temperature

In the previous section we have discussed the effects caused by irradiation induced mixing. However, as we have seen in this chapter, irradiation performed at moderate temperatures can also result in ordering, which is what we discuss in this section. This irradiation induced ordering is typically performed at a much lower temperature than processes based on pure annealing.

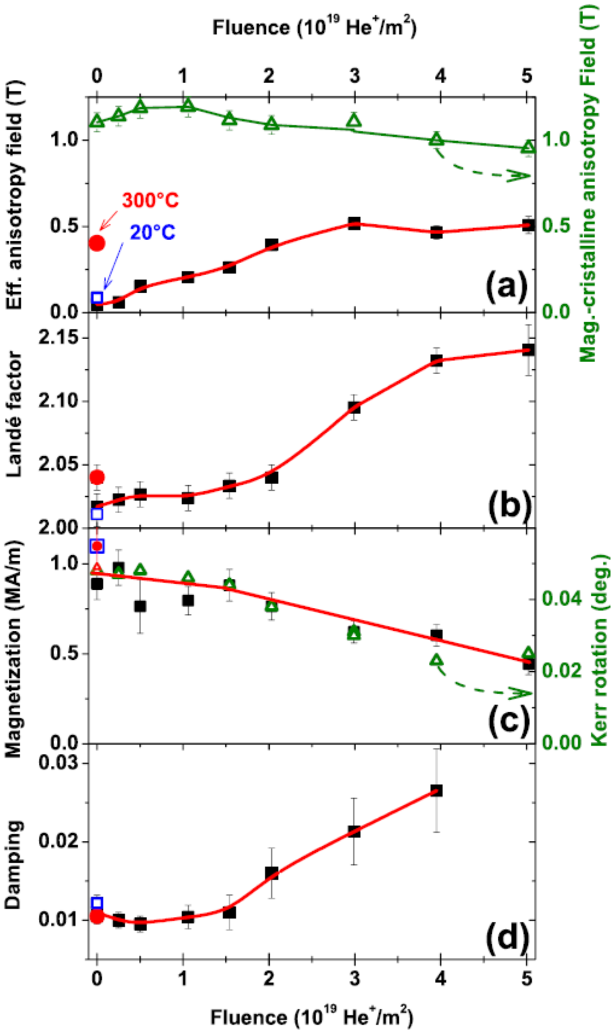

Fig. 2.22: Irradiation induced crystallization of Ta/CoFeB/MgO/Ta | Data from Devolder *et al.* [145] on the evolution of the magnetic properties of a Ta(5 nm)/$Co_{20}Fe_{60}B_{20}$ (1 nm)/MgO (2 nm)/Ta (5 nm) stack under 15 keV He$^+$ irradiation at 100°C. a) $H_{K_{\mathrm{eff}}}$ (black) and H_K (green). b) Landé g-factor. c) M_s (black) and Kerr rotation (green). d) α. In each figure, the amorphous initial state values are indicated in blue, and the value obtained after pure annealing at 300°C is indicated in red.

Most of the early work on irradiation induced ordering focused on intermetallic alloys such as FePt and FePd. Ravelosona *et al.* [193] showed that He^+ irradiation of FePt at 277°C results in increased ordering of films grown at room temperature, which normally requires high temperature processes around 427°C. The increased ordering results in a larger anisotropy. A more general study by Bernas *et al.* [194] showed that irradiation at large temperatures stabilizes the $L1_0$ phase, which has a larger anisotropy compared to the as-grown state.

In thin films based on CoFeB, ordering is typically induced through irradiation induced crystallization [145,195,196]. Devolder *et al.* [145] showed that irradiation of Ta/CoFeB/MgO with 15 keV He^+ ions at 100°C improves the anisotropy with increasing He^+ fluence, and that a similar anisotropy to that obtained through annealing at 300°C can be obtained. This is shown in Figure 2.22a. The other properties, such as the Landé g-factor, M_s and α, shown in Figures 2.22b, c, and d, respectively, are also affected, with an observed increase in the Landé factor and damping with increasing fluence. M_s decreases with increasing fluence. In our work, which is shown in more detail in Chapter 3, we show that other than the magnetic properties of a W/CoFeB/MgO thin film, the nanoscale disorder can also be controlled with irradiation induced crystallization [196].

It is clear from the extensive studies mentioned above that He^+ irradiation is an excellent tool to engineer magnetic properties and other interface effects. In the next section, we discuss the works that make use of this effect to control magnetic structures and that employ the ability to locally irradiate certain parts of a sample to engineer devices with these magnetic structures.

2.4.2 Domain walls, skyrmions, and devices

2.4.2.1 Domain walls in full films

The ability to control magnetic properties gives us the ability to control magnetic structures that have energies that depend on those magnetic properties. Indeed, DWs and skyrmions are prime candidates since their energy depends strongly on the anisotropy and DMI (Eq. 1.24). However, due to the effect of disorder on the DW structure and motion, the impact of ion irradiation, which modifies both disorder and magnetic properties, is not immediately obvious, and it remains to be fully understood.

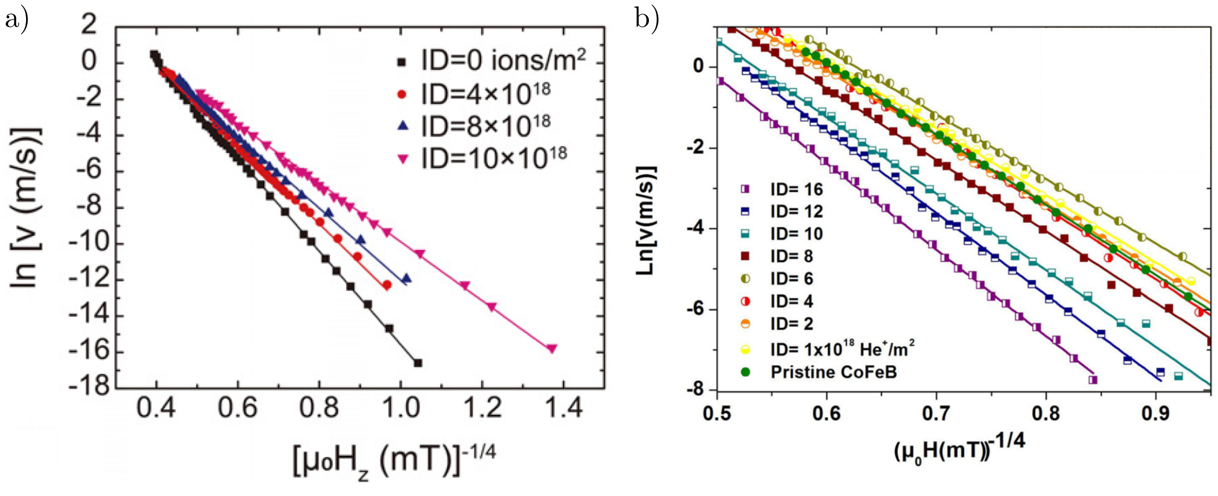

Fig. 2.23: The effect of He^+ irradiation on creep domain wall motion | a) Data from Zhao *et al.* [176] showing the DW velocity in the creep regime in W/CoFeB/MgO films irradiated with 15 keV He^+ ions. b) Data from Herrera Diez *et al.* [174] showing the DW velocity in the creep regime in Ta/CoFeB/MgO films irradiated with 15 keV He^+ ions.

Early studies in Pt/Co/Pt have shown that 30 keV He^+ irradiation homogenizes the pinning landscape [197,198]. Subsequently, Jamet *et al.* showed improved creep DW velocity in Pt/Co/Pt nanowires irradiated with Ga^+ at 25 keV [199]. This effect was also observed by Cayssol *et al.* [200] and Cormier *et al.* [201] for 10 keV and 30 keV He^+ irradiation, respectively. Zhao *et al.* [176]

observed an increased DW velocity in W/CoFeB/MgO after 15 keV He$^+$ irradiation, as shown in Figure 2.23a, however Herrera Diez *et al.* [174] have observed a decreased creep velocity in Ta/CoFeB/MgO after 15 keV He$^+$ irradiation, as shown in Figure 2.23b. In a follow-up study, the authors observed that in the flow regime, DW dynamics also evolved non-trivially with increasing irradiation fluence [178]. A clear understanding of the effect of ion irradiation induced structural and magnetic modifications on DW motion and pinning is thus still lacking. In Chapters 3 and 4 of this thesis, we aim to shed more light on the effect of irradiation on DW dynamics.

2.4.2.2 Devices and local irradiation

The strong interaction of DWs with pinning sites allows for the creation of artificial pinning sites through local irradiation. Lavrijsen *et al.* [202], and later Franken *et al.* [168,203], showed that DW pinning and depinning in Pt/Co/Pt can be precisely controlled with He$^+$ and Ga$^+$ irradiation through the engineering of anisotropy barriers. Burn and Atkinson [204] have seen a similar effect in NiFe nanowires after Ga$^+$ irradiation. Artificial DW pinning can be exploited to create so-called ratchet memories, where the position of the DW can be accurately controlled by anisotropy engineering with ion irradiation [205].

Similar effects have been observed for skyrmions, which have been of particular interest lately. It was found that skyrmions can be easily nucleated at artificial defects created with irradiation [206–208], with the nucleation density of skyrmions also controllable with ion irradiation [209,210]. This was exploited by Juge *et al.* [171], whose results are summarized in Figure 2.24. They showed that skyrmions can be nucleated in irradiated tracks (Fig. 2.24a), and that the movement of the skyrmion through the application of a current can be confined in the irradiated tracks (Fig. 2.24b-g). The motion of skyrmions can thus be accurately controlled in a track created by local He$^+$ irradiation. The effect of irradiation itself on the skyrmion velocity is not clear though, as both an increased velocity for Pt/Co/MgO after 15 keV He$^+$ irradiation [171] and a decreased velocity for W/CoFeB/MgO after 50 keV Ga$^+$ irradiation has been observed [211]. Kern *et al.* [209] have shown that by adding regularly spaced irradiation zones, the position of the skyrmion can be accurately controlled with current pulses. These recent advances in the control of skyrmion motion make them excellent candidates in various skyrmion circuits, as explored recently by Ahrens *et al.* [212].

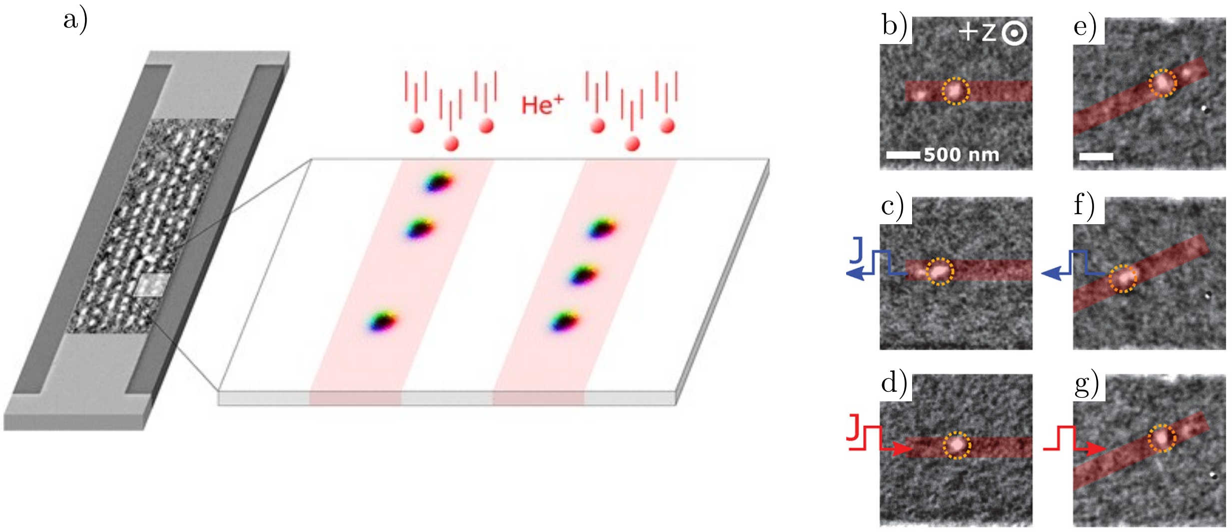

Fig. 2.24: He$^+$ puts skyrmions on the track | a) XMCD-PEEM image on top of a sketch of a Pt/Co/MgO wire with tracks created with local He$^+$ irradiation. The zoom shows a sketch of the irradiation tracks, where skyrmions can be nucleated after irradiation. b)-g) Sequence of XMCD-PEEM images demontrating current-induced skyrmion movement in the irradiated tracks (red shaded area). The tracks have an angle of 0° (b-d) and 22.5° (e-g). Figure adapted from Ref. [171].

Irradiation not only affects the motion of DWs and skyrmions themselves, but, in the case of DWs driven by currents [8], also the efficiency of the current to torque conversion. Yun *et al.* [213] showed that the current required to switch a Pt/Co/Ta stack is reduced after 500 eV Ar^+ irradiation, which was also observed for W/CoFeB/MgO [214] and Ta/Co/W [215] irradiated with He^+ ions at 15 and 30 keV, respectively. Recently, An *et al.* directly observed an increase of the current to torque efficiency in Pt/Co/MgO [172] after 30 keV He^+ irradiation, which is linked to an increased resistivity in the Pt layer.

2.5 Summary, conclusions, and outlook

In this chapter, we have discussed the basics of ion-matter physics, from the collisions of ions with individual matter atoms, to the evolution of the target material. We have seen that ion irradiation can induce atomic mixing and even crystallization, which can be exploited to enhance the properties of magnetic materials. Depending on the desired effect in the target material, one can chose different types of ions and irradiation energies. High energy heavy ions have strong effects in the target, but lack the control with lighter ions due to the large cascade collisions. It is thus clear that, when high control of the atomic arrangement is desired, light ions are the better tool to manipulate materials. This is exacerbated in magnetic thin films, as the nanometer thin layers that are involved are highly susceptible to small rearrangements of atoms, as are the magnetic properties.

There is an impressive body of work related to the control of magnetic phenomena with ion irradiation, from interfacial properties such as the anisotropy and DMI, to the stabilization and dynamics of complex magnetic structures such as DWs and skyrmions. However, this does not mean that we have extracted all the potential out of ion irradiation. As interfaces become increasingly important to control magnetism, so will the role that ion irradiation plays. As already briefly mentioned, effects that are heavily dependent on interfaces are prime candidates for modification with ion irradiation. This includes exchange coupling between layers, which opens up the possibility to create local FM and AF coupling with ion irradiation. Furthermore, the recent discovery of interlayer DMI [216,217] and its coupling through a spacer layer allows for similar modification with ion irradiation.

Irradiation induced ordering, particularly through irradiation induced crystallization, remains a topic that is under-investigated in thin films. A basic understanding of the evolution of the magnetic properties and structural characteristics with irradiation induced crystallization is still lacking, and the possibility to optimize the crystallization process would have a strong impact on the development of MRAM and MTJ-based devices. In Chapter 3, we kick-start this understanding by studying the effect of He^+ irradiation at moderate temperatures in W/CoFeB/MgO thin films.

In the case of DW motion, the interplay between the DW profile, velocity, and roughness is not completely understood. From previous results, the effect of ion irradiation seems to be heavily material dependent. However, with the use of nanoscale models, ion irradiation can be a prime candidate to study the role of disorder in more detail. Furthermore, by studying how we can tailor the defect structure with ion irradiation, we could potentially optimize the pinning landscape for easy DW motion. The recent push for spintronic devices based on the motion of DWs and skyrmions for storage [13], logic [14], and neuromorphic computing [20] opens new routes for ion irradiation. Proof of concept results in artificial DW and skyrmion pinning, and the control of their motion with ion irradiation pave the way for a use-case in a real spintronic device. In Chapters 3 and 4, we show that more can be revealed about the interplay between DW motion and nanoscale disorder with the use of ion irradiation in full films, particularly by disentangling the effects of magnetic properties and disorder. In Chapter 4 we extend this investigation to extrinsic edge defects that are created with a lithography process, which have been shown to also significantly hinder DWs and skyrmions [218,219].

Chapter 3

Tailoring order in W/CoFeB/MgO layers with He^+ irradiation induced crystallization

It's not about domain wall motion, it's about disorder!
André Thiaville

In this chapter, we present a study on the optimization and tailoring of the magnetic properties and order of thin films with He^+ irradiation. This chapter is divided in two distinct parts. In Section 3.1 we study the effect of ion beam induced crystallization on the magnetic properties of W/CoFeB/MgO thin films. Here we show that we can achieve improved magnetic properties using ion irradiation at moderate temperatures (< 250°C) compared to the standard industrial crystallization process based on pure annealing at high temperatures (> 350°C). In Section 3.2, we shift our focus on the intrinsic disorder after crystallization by presenting a method to measure said disorder with domain wall (DW) motion. By choosing samples with similar macroscopic magnetic parameters after an optimized crystallization process, we can selectively study the effects of disorder on the DW dynamics, without the contribution of the changes in magnetic properties.

3.1 Optimizing CoFeB/MgO materials through irradiation induced crystallization

In Chapter 2, we have seen that irradiation can induce the crystallization of bulk crystals, both by lowering the energy barrier for the onset of crystallization, allowing crystallization to happen at much lower temperatures under irradiation compared to pure thermal treatments, and by changing the crystallite growth dynamics, which results in a more homogeneous crystallite distribution. In this section, we apply irradiation induced crystallization to amorphous W/CoFeB/MgO ultra-thin films. We show that we can achieve similar or enhanced values of the anisotropy, damping, and DMI compared to a purely thermal crystallization method, which is the current industry standard.

3.1.1 Introduction: crystallization of CoFeB/MgO materials

With the myriad of new functionalities offered by spintronic devices [5], it becomes increasingly important to optimize the structural quality of the materials used in these devices. Novel spintronic devices make use of thin magnetic layers, where the interfaces between the different layers and their crystal structure play a large role in determining the strength of various magnetic parameters, such as the anisotropy and DMI (see Chapter 1). For applications such as data storage or sensing, spintronic devices like magnetic random access memory (MRAM) [220–223] and magnetic sensors [224] make use of a so-called magnetic tunnel junction (MTJ). MTJs are complicated stacks of different materials, typically containing over twenty different layers with a thickness on the scale of several ångström (10^{-10} m). In the improvement of these devices in terms of efficiency, stability, and storage density, a particular focus lies in obtaining a large anisotropy and tunnel magnetoresistance (TMR) together with a small distribution of magnetic properties [5,225].

The core element of current MTJs is based on CoFeB-MgO structures due to their low damping [226], strong anisotropy [49,227], and large TMR [228]. To induce high TMR, the MgO layer is often grown with a (001) orientation [229], which is achieved by growing it on top of an amorphous CoFeB layer [230]. A subsequent annealing step is then applied to crystallize the CoFeB layer, which induces a large anisotropy and further increases the TMR [231]. However, the large process temperatures that are involved can be detrimental to the magnetic structures by introducing structural disorder [229,232]. This includes intermixing, roughness, crystalline texture, different grain sizes and distributions, and more. The presence of such structural disorder results in a distribution of magnetic properties at the nanometer scale, which has detrimental effects on the performance of the devices [10]. Furthermore, these annealing processes are typically on the timescale of > 1 hour, which can act as a bottleneck to the wafer throughput.

To overcome these issues, is is crucial that alternative fast crystallization techniques are employed using a lower operating temperature and/or result in a more homogeneous material with a smaller defect rate. It is well known that irradiation can induce crystallization in bulk materials (see Chapter 2). However, its effects on the crystallization of thin films are not yet well understood. Devolder *et al.* [145] showed that 15 keV He^+ irradiation at 100°C can induce crystallization of Ta/CoFeB/MgO thin films, and that the samples crystallized by irradiation could reach similar magnetic properties to samples crystallized by thermal annealing at 300°C for 1h. Moreover, the irradiation crystallization process is on the timescale of seconds to minutes, significantly improving the process time over pure thermal annealing. However, they found that large ion fluences are typically required to reach these values, which can damage other parts of the sample. Furthermore, they only studied crystallization under a single irradiation temperature, while we have seen in Chapter 2 that irradiation enhanced crystallization is strongly temperature dependent.

Here, we study a crystallization process based on irradiation at moderate temperatures in W/CoFeB/MgO thin films. We study the effect of different irradiation temperatures on the effective anisotropy field, Gilbert damping, and inhomogeneous broadening of the samples. The latter gives us insight about the induced disorder. Additionally to previous work, we also investigate the evolution of the DMI, which is crucial for applications based on DW motion.

3.1.2 Crystallization of W/CoFeB/MgO materials by He^+ irradiation at moderate temperatures

We study the magnetic properties of two different thin films based on W/CoFeB/MgO with different CoFeB thicknesses, irradiated with 15 keV He^+ at moderate temperatures. The first stack is a W(4)/$Co_{20}Fe_{60}B_{20}$(1)/MgO(2)/Ta(3) (thickness in nm) ultra-thin film, deposited with a Singulus Rotaris sputtering system. The second stack is a W(4)/$Co_{20}Fe_{60}B_{20}$(0.7)/MgO/W(1)/Ta(2)/Ru(3) ultra-thin film, deposited with an Anelva-7100 system. Both stacks are deposited on a Si/SiO_2 substrate, and have amorphous CoFeB layers. Hereafter, these stacks will be referred to as stack 1 and stack 2, respectively. We use AGFM, FMR, and BLS measurements to investigate the magnetic parameters for different process characteristics such as irradiation temperature and irradiation fluence.

We first study the evolution of stack 1 under increasing He^+ fluence at different irradiation temperatures; room temperature (RT), 150°C, 200°C, and 250°C, which are all below the onset of thermal crystallization. At a fixed beam current, the process times range between a several seconds at the lowest fluences to a couple of minutes at the largest fluences. We measure the in-plane hysteresis loop with AGFM and fit a Stoner-Wolfarth model [28] to extract the effective anisotropy field $H_{K_{\mathrm{eff}}}$. The results are shown in Figure 3.1. For comparison, we also show the evolution of $H_{K_{\mathrm{eff}}}$ under pure annealing for 1h at different temperatures, which is shown in grey. The lines in-between the data points are guides to the eye. At RT, $H_{K_{\mathrm{eff}}}$ does not change with increasing fluence from its initial value. Increasing the irradiation temperature to more intermediate values of

150°C and 200°C, $H_{K_{\mathrm{eff}}}$ suddenly increases at low fluence, and subsequently reaches a plateau. This maximum attainable $H_{K_{\mathrm{eff}}}$ is increased with increasing irradiation temperature. The stabilization of $H_{K_{\mathrm{eff}}}$ suggests that, after initial nucleation, the crystallite growth is balanced by the ballistic destructive effects (see Section 2.2.3.1). At the largest irradiation temperature $T_{\mathrm{irr}} = 250°\mathrm{C}$, $H_{K_{\mathrm{eff}}}$ increases monotonically with increasing He^+ fluence. At larger fluences, i.e. 6×10^{15} ions/cm^2, values similar can be achieved to annealing at 400°C, which is associated to typical industrial back-end-of-line annealing. This threshold value is indicated by a horizontal dashed line. At this irradiation temperature, the results suggest that the crystallite growth is stronger than destructive ballistic effects, causing the progressive increase of $H_{K_{\mathrm{eff}}}$ with increasing He^+ fluence. This effect is similar to what has been observed previously in Ta/CoFeB/MgO systems [145].

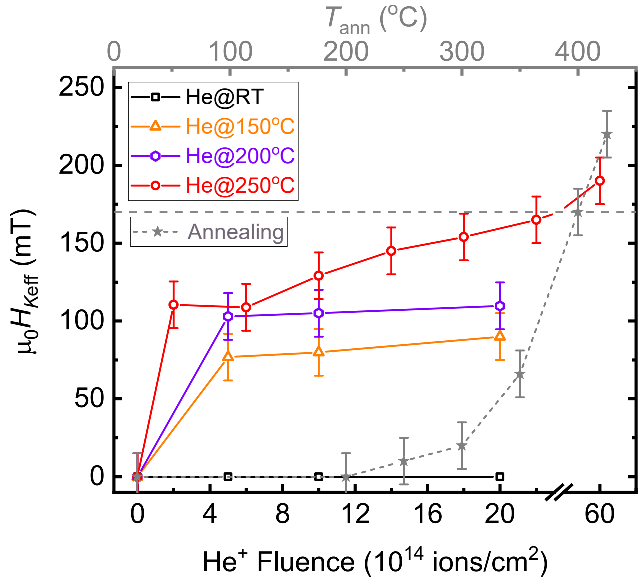

Fig. 3.1: Anisotropy field evolution of stack 1 at different irradiation temperatures | Evolution of $H_{K_{\mathrm{eff}}}$ as determined by AGFM of stack 1 under annealing (grey) progressive He^+ irradiation at different irradiation temperatures. The value for annealing at 400°C is indicated with a dashed horizontal line.

To gain more insight into the evolution of the damping constant α, we perform FMR measurements on selected samples irradiated at moderate temperatures. This also allows us to verify the evolution of $H_{K_{\mathrm{eff}}}$, as the Stoner-Wolfarth method has important limitations for in-plane magnetized samples, and to obtain information about the variation of magnetic properties through the inhomogeneous broadening ΔH_0. We restrict ourselves to irradiation at 250°C, as the results at this irradiation temperature are the most promising. The results of the FMR measurements on stack 1 and 2 after irradiation treatment are shown in Figures 3.2a-c and 3.2d-f, respectively. For comparison, we also show the evolution of the samples under pure annealing for 1h at different temperatures (in grey).

Figures 3.2a and 3.2d show the evolution of $H_{K_{\mathrm{eff}}}$ in stacks 1 and 2, respectively. We observe a progressive increase of $H_{K_{\mathrm{eff}}}$ with increasing irradiation fluence at 250°C for both stacks. In stack 1, values of $H_{K_{\mathrm{eff}}}$ obtained through irradiation surpass the values obtained with typical annealing, whereas in stack 2, $H_{K_{\mathrm{eff}}}$ can only reach similar values to annealing before the sample is deteriorated. The damping constant, shown in figures 3.2b and 3.2e, stays relatively constant for both stacks under the irradiation process. Some variations are observed, but no large changes in α are reported compared to the annealed samples. Only in stack 2 does α increase exponentially near the larger annealing temperatures, signaling a breakdown in sample quality. The latter is also observed when looking at the inhomogeneous broadening, shown in Figures 3.2c and 3.2f. Overall, a slight increase in ΔH_0 with increasing fluence is observed for the irradiation processes. In stack 1, this increase follows the evolution by annealing, with the irradiated sample showing overall slightly larger values. This signals that in stack 1, the irradiation treatment can result in slightly stronger bulk disorder

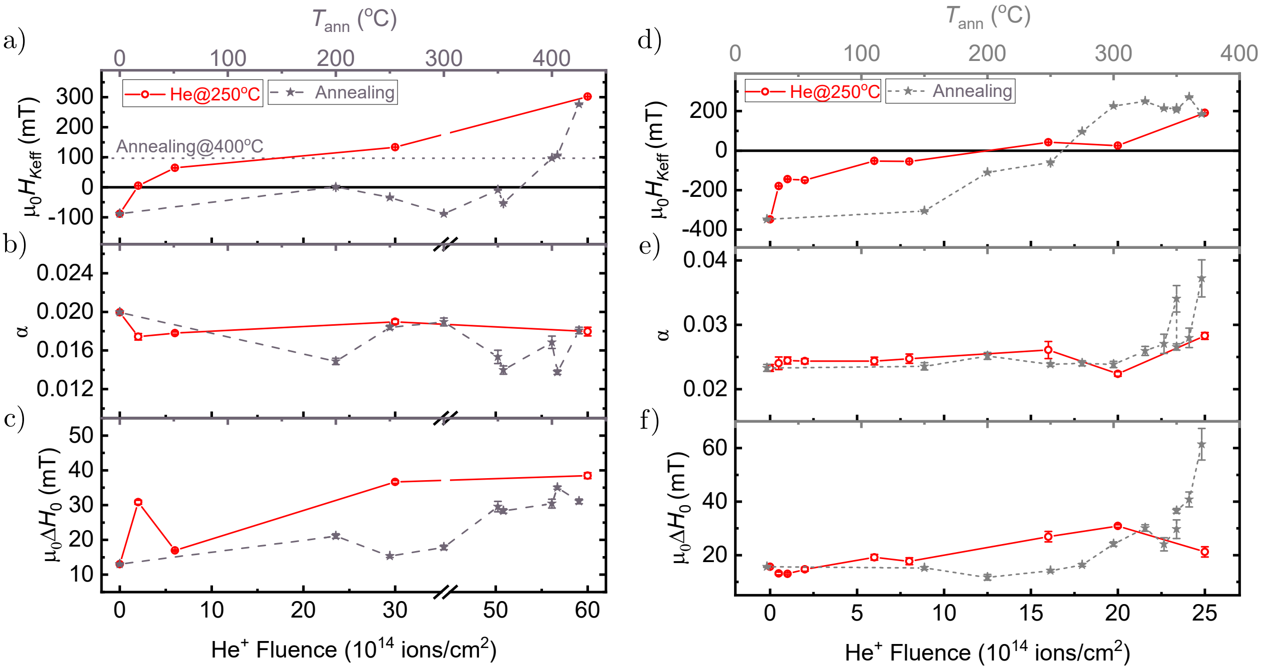

Fig. 3.2: Magnetic properties of W/CoFeB/MgO under He$^+$ irradiation at moderate temperatures | Properties of (a-c) stack 1 and (d-f) stack 2 as determined by FMR for different irradiation and annealing (grey) conditions. a) and d) show the effective anisotropy field, b) and e) show the damping, c) and f) show the inhomogeneous broadening.

compared to annealing. In stack 2, the irradiation treatments do not show the same trend as the annealing treatments, which, at large temperatures, result in an exponential increase of ΔH_0. This indicates a larger disorder after a certain threshold temperature.

We further study the evolution of the DMI for different irradiation conditions in stack 2 with BLS measurements. The results are shown in Figure 3.3a, along with the values for pure annealing for 1h at different temperatures. We find positive values for D which are in the range of values reported in the literature [35]. For progressive He$^+$ irradiation at 250°C, we observe an initial increase of the DMI constant, followed by a gradual decrease by further increasing He$^+$ fluences. D also gradually increases for pure annealing with increasing temperatures, but does not show a decrease. While in the range of expected values for DMI in W/CoFeB/MgO [35], the variation with irradiation nor annealing is not very strong. Furthermore, the value of the DMI is strongly dependent on the saturation magnetization, which follows a similar trend to the DMI constant. Getting rid of the M_s dependence, which is shown in Figure 3.3b, we see instead a progressive decrease of D/M_s, indicating a progressive deterioration of the material interfaces with increasing He$^+$ fluence. This deterioration is not observed for pure annealing.

3.1.3 Discussion and conclusion

With an irradiation induced crystallization process at low moderate temperature (250°C), we can obtain similar $H_{K_{eff}}$ values as conventional processes based on pure annealing at high temperatures. Depending on the thickness of the crystallized layer, the sample can show larger $H_{K_{eff}}$ values after irradiation at moderate temperatures compared to the values obtained by annealing at high temperatures. This is likely an effect that arises from the competition between bulk and interface effects. In thinner samples, the interfaces contribute more to the total value of the anisotropy compared to thicker samples, where the bulk contribution is increased. With irradiation, increasing fluences would progressively deteriorate the interfaces [176], with the W/CoFeB interface affected more than the CoFeB/MgO interface due to the positive enthalpy of mixing of Fe-Mg and Co-Mg and slightly negative enthalpy of mixing of Fe-W and Co-W (see Figure 2.13). Due to the large fluence required to grow the crystallites, we can thus expect a deterioration of the interfaces while

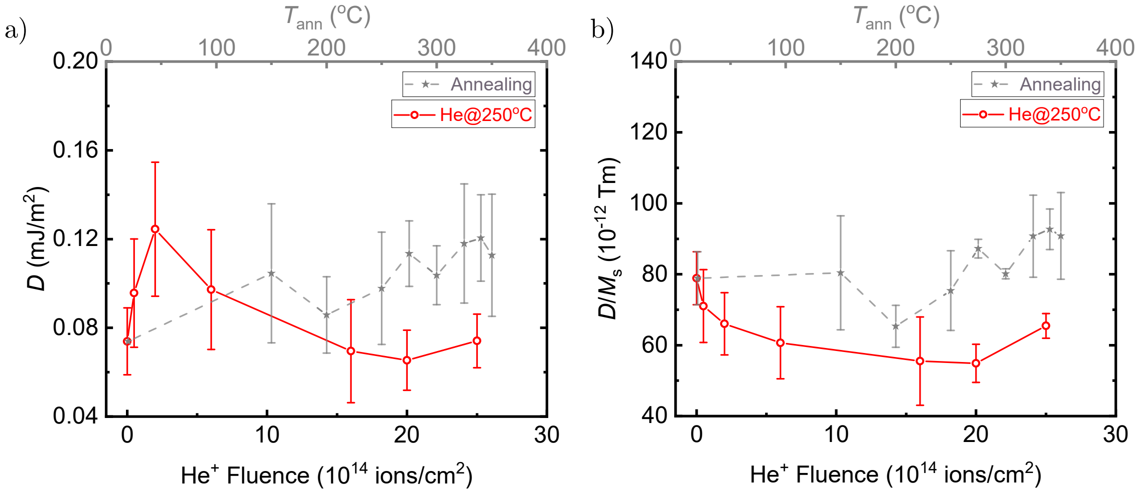

Fig. 3.3: Evolution of DMI with irradiation processes | a) DMI constant of stack 2 as determined by BLS for different crystallization processes and annealing (grey). b) Data from (a) independent of M_s.

the bulk crystal grows. The interface deteriorates at a similar rate no matter the thickness, but the effective reduction in H_{K_eff} in the thicker sample is smaller, as the bulk contribution is larger. Hence, a fluence range exists where the values obtained from annealing can be surpassed, whereas in the thinner samples, the interface quality is already too deteriorated when the crystalline component is strong enough to reach the values obtained from annealing. The strong reduction in interface quality is further supported in stack 2 by the observed reduction in D/M_s at larger fluences, as the DMI in W/CoFeB/MgO is strongly dependent on the quality of the W/CoFeB interface [35]. The fact that α and ΔH_0 do not significantly change with irradiation indicates that the bulk disorder is not significantly affected, although further structural investigation is required to confirm this effect. It should be noted that we have not studied the evolution of M_s and the magnetic dead layer in detail. Reductions in effective thickness as well as M_s can result in an increased H_{K_eff} value that is independent of crystallization. Similar to previous work [145], the fluence required to reach these H_{K_eff} values is still relatively large.

Summarizing, we show that by using a crystallization process based on He$^+$ irradiation at moderate temperatures, we can obtain similar anisotropy values as pure annealing, but at much lower temperatures and much faster process times (< 5 minutes). The evolution of H_{K_eff} is strongly dependent on sample characteristics, particularly on the thickness of the magnetic layer, and systematic characterizations have to be done to achieve the optimal H_{K_eff} values for each sample. Other magnetic properties such as damping, ΔH_0, and the DMI are only weakly affected. Further characterizations into the material disorder should be performed, as it is currently unclear from the magnetic properties how the nanoscale disorder is impacted by the irradiation induced crystallization. In the next section, we show that the nanoscale disorder can be measured with DW motion, and reveal that irradiation induced crystallization can result in an optimized disorder profile for DW motion.

3.2 Revealing nanoscale disorder with domain wall motion

Disorder in ultrathin films can significantly hinder domain wall (DW) motion. One of the main issues on the path towards efficient DW based devices remains the characterization of the pinning landscape at the nanoscale. In this section,[1] we will show that we can unlock information about the nanoscale disorder by studying DW motion in three differently crystallized samples with similar

---

[1] This section is based on results that have been published in *Physical Review Applied*: **J.W. van der Jagt** *et al.*, *Phys. Rev. Appl.* **18**, 054072 (2022) [196].

macroscopic magnetic parameters. We extract information about the nanoscale pinning parameters using an analytical model, which allows us to reveal important variations in the disorder of the crystallized samples. This work also offers a unique opportunity to selectively analyze the effects of disorder on the DW dynamics, without the contribution of changes in the magnetic properties. With the results in this section, we highlight that evaluation of the nanoscale pinning parameters is important when designing devices based on DW motion, which in return can be a powerful tool to probe disorder in ultrathin magnetic films.

3.2.1 Introduction: optimizing domain wall motion with disorder

As mentioned in the introduction to this thesis, spintronic devices based on magnetic DW motion are excellent candidates for logic [14–17], data-storage [11–13] and neuromorphic devices [18–22]. In these devices, the DWs can be efficiently driven by a current through spin-transfer torque [233] or spin-orbit torque (SOT) [8,234] above a current-density threshold. As we have seen in Chapter 1, the latter is related to pinning of the DW due to disorder in the material, which limits the efficiency of DW-motion-based devices. This disorder usually takes the form of spatial variation of magnetic properties due in particular to interface roughness, intermixing, crystalline texture, defects in the material, or grain boundaries. As a result, DWs are depinned only above a threshold force (f_d), below which their motion is thermally activated.

The optimization of DW motion in devices is usually based on improving the magnetic parameters, such as the damping, the Dzyaloshinskii-Moriya interaction (DMI) and/or the effective anisotropy. Another indication of efficient DW motion is the value of the depinning field H_dep. However, these different magnetic parameters and their contributions to the underlying physics are not well understood. Several techniques based on disorder modifications have already been shown to impact the DW motion, such as varying material growth conditions [235], layer thickness [236,237], or interface engineering by He$^+$ irradiation [176,178] (see also Chapter 2). However, these techniques modify both the magnetic parameters and the disorder landscape, making it difficult to extract the effect of the latter on DW motion. Mostly numerical investigations studying DW motion in different crystalline environments have been carried out [80–82,238], but experimental investigations without the influence of changing magnetic parameters are still lacking.

Understanding and optimizing DW motion in devices thus requires characterizing the disorder at the nanoscale. To this end, we study DW motion in W/CoFeB/MgO ultrathin films. Specifically, we study the DW dynamics measured in samples crystallized by either pure annealing at 400°C or optimized irradiation induced crystallization processes at different temperatures and He$^+$ fluences. Using a combination of Kerr microscopy, magnetic characterizations, micromagnetic simulations and analytic modeling [53,239], we can extract information about the nanoscale pinning landscape, such as the height of the average DW-pinning energy barrier, the characteristic pinning range, and pinning force, as well as the mean distance between pinning sites. In particular, by taking into account the minor differences in the magnetic parameters of the different samples, we show that the discrepancy observed in the DW dynamics in all regimes can only be ascribed to variations in the nanoscale pinning landscape, information that is out of reach of macroscopic measurement techniques.

This section is divided into two main parts. In Section 3.2.2, we discuss the magnetic and structural characterization of the W/CoFeB/MgO samples of this study. In Section 3.2.3, we study the DW motion in the creep, depinning, and flow regimes, the microscopic pinning parameters extracted from the analytical model, and the interplay between the domain wall velocity in the flow regime and intrinsic material disorder.

3.2.2 Sample characterization

For this study, we investigate the DW motion in the aforementioned stack 1. Three differently crystallized samples are studied, including one annealed at 400°C for 1h, and two obtained through an optimized process based on He$^+$ irradiation at moderated temperatures, as schematically shown in Figure 3.4. The irradiation treatments are hereafter denoted by irradiation treatment 1 and 2.

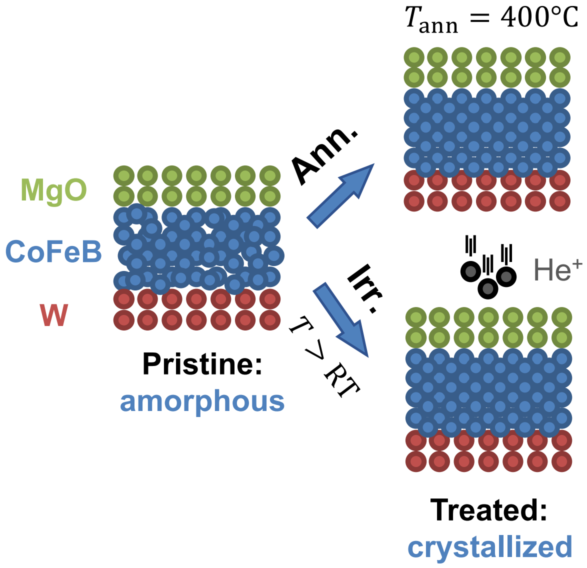

Fig. 3.4: Irradiation induced crystallization processes | A sketch showing the crystallization of an amorphous CoFeB layer in a W/CoFeB/MgO stack upon high temperature annealing and He^+ irradiation at $T > \text{RT}$.

To verify the crystallization and interface ordering, we perform AGFM and MOKE measurements on the as-deposited and crystallized samples. The results are shown in Figure 3.5a. All three samples have clear square loops with similar characteristics, indicating PMA, whereas the as-deposited sample (not shown) has in-plane anisotropy. The sample with irradiation treatment 1 has a larger coercive field compared to the other treated samples. This indicates an increased nucleation field, related to the absence of strong nucleation sites.

Furthermore, we perform time-of-flight secondary ion mass spectroscopy (ToF-SIMS) measurements. ToF-SIMS is a technique in which the material is sputtered from top to bottom with an ion beam [240–242] (see also Chapter 2 for more details on sputtering). The sputtered materials, or secondary ion, is then collected in a mass spectrometer. The resolution of the mass spectrometer can be enhanced to 10^{-3} amu by measuring the time-of-flight of the secondary ions. By tracking the elemental intensity as a function of sputtering time, we can essentially obtain a depth profile of the different elements across the layers.

Figure 3.5b shows the elemental depth profile of B for the three crystallized samples, as well as the as-deposited sample with an amorphous CoFeB layer. The spectra are obtained by sputtering with O^{2+} ions at 1 keV. The spectrum of each sample has been slightly shifted so that the position of the maximum of the B peaks overlap. By doing this, we can analyze the concentration differences between the different samples at different points in the spectra.

At the W/CoFeB interface, which is highlighted with a red box in Figure 3.5b, we see large differences in concentration between the treated samples and the as-deposited samples. All the treated samples have significantly more B around the location of the W layer. However, the difference in B concentration between the crystallized samples is negligible. The B-out diffusion from the CoFeB to the W layer in the treated samples, combined with the square hysteresis loops, are a strong indication of Co-Fe crystallization [243,244].

The magnetic properties of the crystallized samples are investigated further through SQUID-VSM, FMR, and BLS measurements. In the remainder of this section, we discuss these measurements in more detail. The results of all the magnetic characterizations are summarized in Table 3.1.

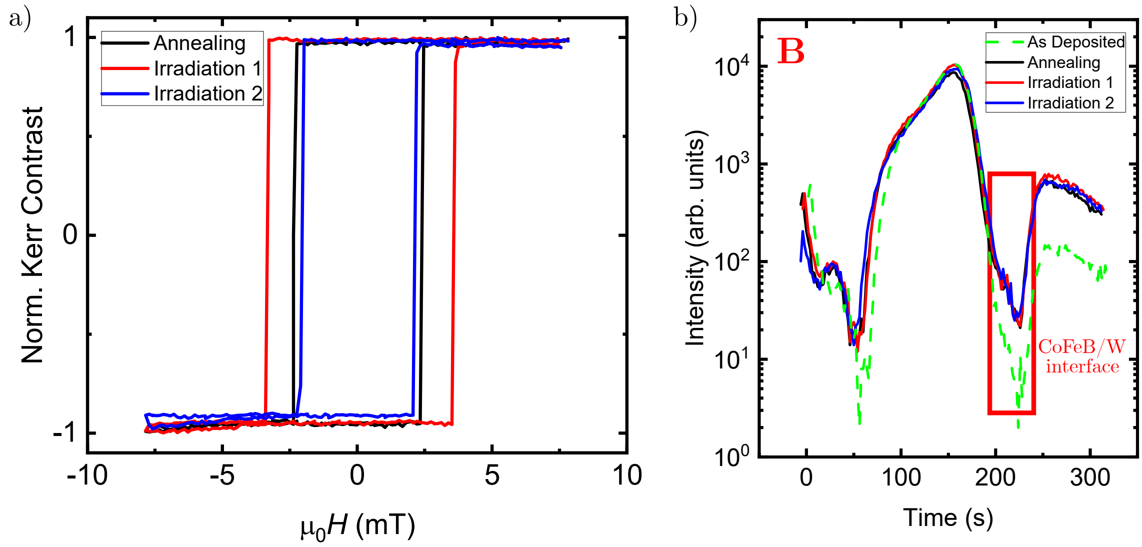

Fig. 3.5: Experimental magnetic evidence for crystallization | a) MOKE hysteresis loops of the three crystallized samples taken in an OOP field. Data has been treated to correct for linear offsets and slopes in the tails. b) The TOF-SIMS profile of B in the amorphous sample (green dashes) and in the three crystallized samples (black, red, and blue). The red box highlights the W/CoFeB interface. The profile is obtained by sputtering with O^{2+} ions at 1 keV.

Table 3.1: Macroscopic magnetic parameters | The macroscopic magnetic parameters for each sample. The table contains values for the saturation magnetization M_s, the effective anisotropy K_eff, the uniaxial anisotropy K_u, the Gilbert damping α, the DMI strength D, and the ratio of D/M_s.

	Annealed	Irradiation treatment 1	Irradiation treatment 2
M_s (MA/m)	1.25 ± 0.13	1.55 ± 0.16	1.60 ± 0.16
K_eff (MJ/m^3)	0.21 ± 0.03	0.20 ± 0.02	0.23 ± 0.02
K_u (MJ/m^3)	1.2 ± 0.2	1.7 ± 0.3	1.8 ± 0.3
α (10^{-3})	19 ± 2	17 ± 1	18 ± 1
D (mJ/m^2)	0.18 ± 0.02	0.16 ± 0.02	0.25 ± 0.04
D/M_s (nJ/A m)	0.14 ± 0.03	0.11 ± 0.03	0.16 ± 0.03

3.2.2.1 Saturation magnetization

M_s has been measured with SQUID-VSM, the results of which are reported in Table 3.1. We find that the irradiated samples have a larger M_s compared to the annealed sample, probably due to less intermixing at the W/CoFeB interface, since W-Fe and W-Co alloys are mostly paramagnetic [181].

3.2.2.2 Anisotropy and damping - FMR measurements

We measure the anisotropy and damping of the three crystallized samples with FMR. In our measurements, the static DC field is applied in the OOP direction, with the RF field in the IP direction. The measurements are performed in field-sweep mode, in a frequency range of 15-43 GHz, from which we obtain spectra similar to the one shown in Figure 1.15. The resulting resonance fields and linewidths are shown in Figure 3.6. The solid lines are fits with Equations 1.43 and 1.47 for the resonance fields (Fig. 3.6a) and linewidths (Fig. 3.6b), respectively. From the fits we can extract α, H_{K_eff}, *gamma* and ΔH_0. H_{K_eff} can be converted into K_eff with Equation 1.16. The values for α and K_eff are reported in Table 3.1, and the values for γ are reported in Section 3.4.2. Overall, the three samples have very similar damping and effective anisotropy. The values for ΔH_0 are reported in Table 3.2, as they will be used to describe the disorder later in this Chapter. We observe bigger differences between the samples in the values for ΔH_0, which is an indication that the sample indeed have different disorder landscapes.

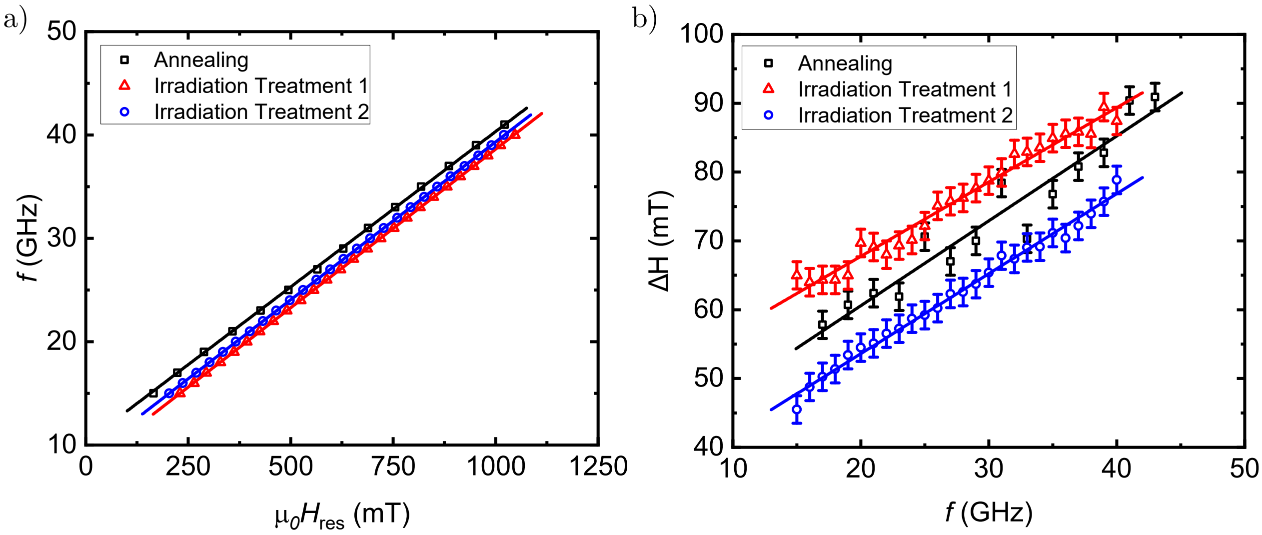

Fig. 3.6: FMR measurements of the crystallized samples | a) Frequency vs the measured perpendicular resonance field for the three crystallized samples. Solid lines are fits with Equation 1.43. b) Measured linewidth vs frequency for the three crystallized samples. Solid lines are fits with Equation 1.47.

We now calculate K_u using Equations 1.11 and 1.15. The values are also reported in Table 3.1. Similar to M_s, we find that the irradiated samples have a slightly larger K_u compared to the annealed sample. This could suggest that they have a smoother CoFeB/MgO interface [49].

3.2.2.3 DMI - BLS measurements

We use BLS to measure the DMI in the samples. The details of the measurement setup and parameters can be found in Section 1.4.2.2. Figure 3.7a shows the frequency shift Δf as a function of the spin-wave vector for the three samples. The solid lines are fits with Equation 1.49, which are forced through 0. The resulting values of the DMI are reported in Table 3.1. We find that the sample with irradiation treatment 2 has a larger DMI compared to the other two samples. Since the DMI in W/CoFeB/MgO mainly originates from the W/CoFeB interface [35], a larger DMI could suggest smoother interfaces [180].

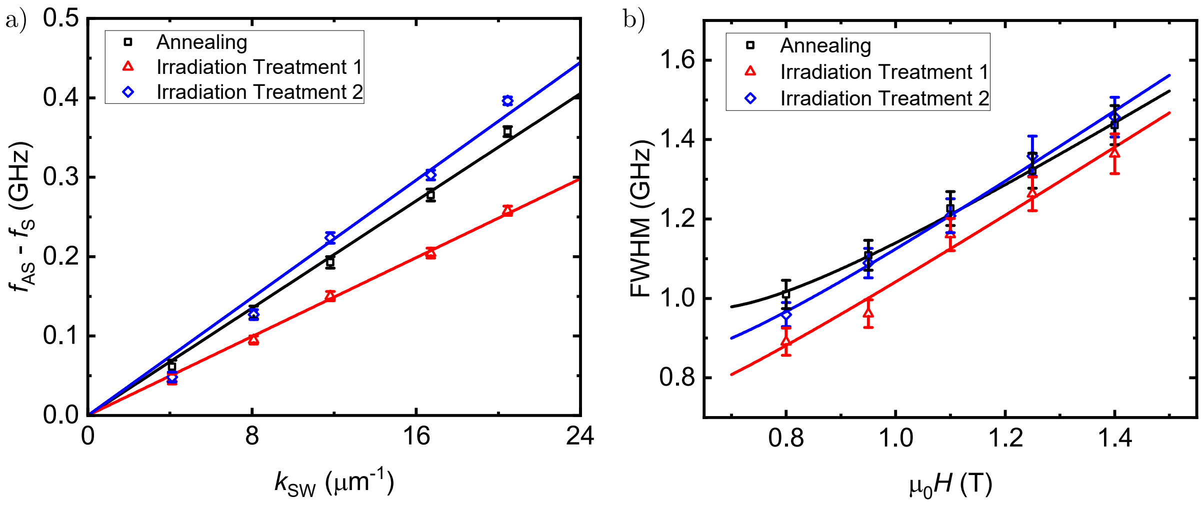

Fig. 3.7: BLS measurements of the crystallized samples | a) BLS frequency shift as a function of the wave vector k_SW for the three crystallized samples. Solid lines are fits with Equation 1.49). b) FWHM of the Lorentzian fits as a function of the applied magnetic field. Solid lines are fits with Equations 1.51 and 1.52.

Similar to FMR, we can obtain information about the variation of anisotropy from the BLS linewidth measurements using Equations 1.51 and 1.52. Figure 3.7b shows the linewidth as a function of the applied field, where we already subtracted the contribution of the spectrometer (0.38 GHz, equal to the width of the central peak that arises from the finesse of the spectrometer cavity, see Fig. 1.17). The solid lines are fits with Equations 1.51 and 1.52, where α and the anisotropy field variation $\Delta H_{K_{\mathrm{eff}}}$ are used as free fitting parameters. The resulting values for $\Delta H_{K_{\mathrm{eff}}}$ are reported in Table 3.2, and values for α are reported in Table 3.3. The three samples have very similar values for α, while bigger differences are observed in the $\Delta H_{K_{\mathrm{eff}}}$ values. The latter is an indication that the samples have different disorder landscapes.

3.2.2.4 Discussion and conclusion

From the results reported in Table 3.1, we see that the three crystallized samples have very similar magnetic properties. Taking the error bars into account, all parameters are within 10% variation and similar to what has been reported for crystallized W/CoFeB/MgO thin films [245]. Only slight variations in M_{s}, D, ΔH_0, and $\Delta H_{K_{\mathrm{eff}}}$ are observed between samples, which, as discussed in their relative sections, could point to slight differences in interface quality. These minor differences in magnetic parameters are taken into account in the remainder of this chapter. In particular, we show that these variations in magnetic parameters are not sufficient to explain the different DW dynamics observed in the three samples and that an investigation of the nanoscale pinning parameters is necessary to explain the DW dynamics. For a more in-depth discussion on the effect of M_{s} on the results, see Section 3.4.1.

3.2.3 Domain wall motion

We now study the DW motion in order to gain insight into the microscopic structure of the samples. To do so, we investigate the expansion profile and the velocity of the DW as a function of the OOP applied magnetic field using polar Kerr microscopy. By using an analytical model from Géhanne *et al.* [239] for the DW motion in the creep regime and micromagnetic simulations in the flow regime, we can extract more detailed information about the microscopic structure and pinning properties of the samples.

3.2.3.1 Creep and depinning

Figure 3.8 shows differential Kerr microscopy images for each sample at two different values of the reduced magnetic field; in the creep regime at $H/H_{\mathrm{dep}} = 0.4$, and closer to the depinning transition at $H/H_{\mathrm{dep}} = 0.9$. A striking result is that in the annealed sample the DW expansion exhibits fractal-like features, whereas the irradiated samples show bubble-like expansion with overall lower jaggedness. This difference in domain structure is an indication of stronger pinning effects in the annealed sample. Furthermore, smoother DWs have been linked to smoother interfaces [246]. We can also observe a smoothing of the DW profile when increasing the field toward the depinning transition, which is consistent with current models highlighting a reduction of the roughness amplitude at higher driving forces [247].

Figure 3.9a shows the DW velocity as a function of the applied magnetic field in the creep regime. We observe a strong variation of the DW velocity of several orders of magnitude, with the irradiated samples having a larger velocity than the annealed sample. The velocity difference is as high as 4 orders of magnitude at 0.94 $(\mathrm{mT})^{-1/4}$ (1.28 mT). Such higher DW velocity is consistent with easier DW motion as revealed by the bubble-like expansion.

To go further, we now use DW velocity as a function of an OOP applied magnetic field to extract more information about the DW motion mechanism in our samples. In the creep and depinning regimes, the velocity is given by Equations 1.38, 1.39, and 1.42. We use these expressions to fit the DW velocity reported in Figure 3.9. These fits are represented by solid and dashed lines for the creep and depinning regimes, respectively. The vertical dotted lines in Figure 3.9b, which shows the data from Figure 3.9a with linear axes, denote H_{dep}. Note that we perform the fit close to the

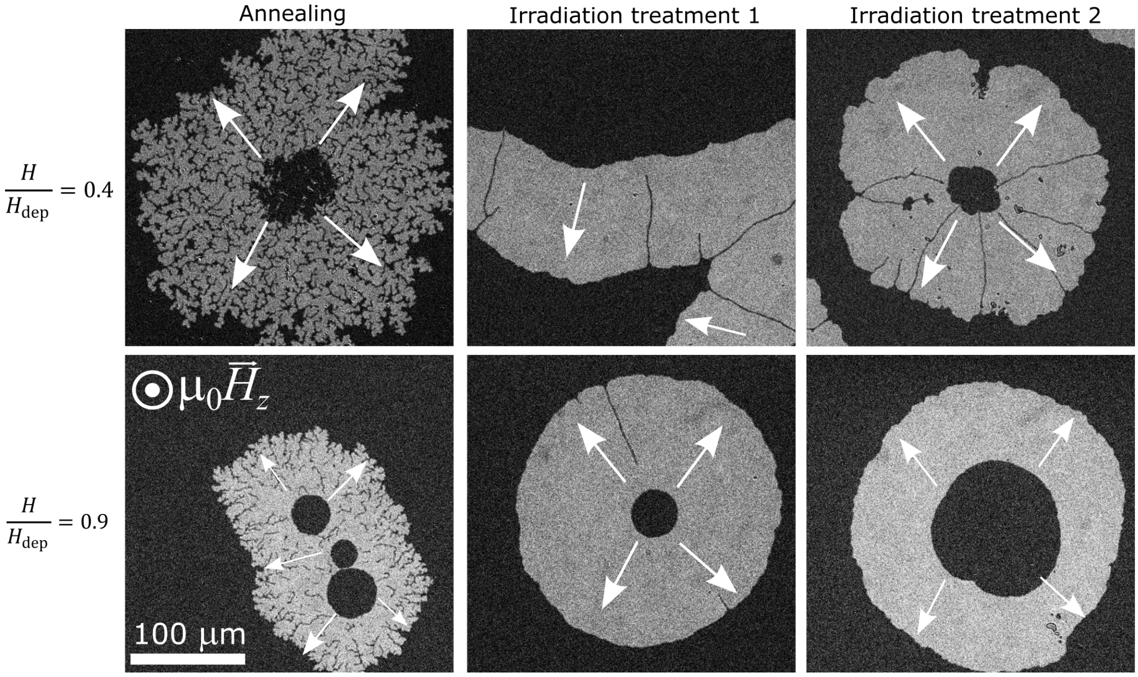

Fig. 3.8: Domain wall expansion in the three crystallized samples | DW expansion images for the three samples investigated in the creep regime at $H/H_{\mathrm{dep}} = 0.4$ and close to the depinning transition at $H/H_{\mathrm{dep}} = 0.9$. Images taken with (i) one pulse of 4 s at 1.83 mT, and 4 pulses of 10 μs at 4.45 mT, (ii) two pulses of 10 ms at 1.91 mT, and six pulses of 10 μs at 4.22 mT, and (iii) four pulses of 10 ms at 2.20 mT, and two pulses of 10 μs at 5.40 mT for the three samples at $H/H_{\mathrm{dep}} = 0.4$ and $H/H_{\mathrm{dep}} = 0.9$, respectively. All images are differential images, where the light-gray areas indicate the area over which the DW has moved during the OOP magnetic field pulse. The white arrows denote the direction of movement of the DW.

depinning transition. Due to the change in slope for the sample with irradiation treatment 2, the fit does not work deeper in the creep regime, and the following analysis is thus only valid close to the depinning regime. The other samples do not have this problem. The change in slope has been seen before, but its origin is still unknown [102]. The resulting values for the non-universal parameters are reported in Table 3.2.

We find that the irradiated samples have a significantly lower $k_{\mathrm{B}}T_{\mathrm{d}}$ than the annealed sample. In particular, $k_{\mathrm{B}}T_{\mathrm{d}}$ is 38% lower for the sample with irradiation treatment 1 and 31% lower for the sample with irradiation treatment 2, compared to the annealed sample. A larger pinning barrier for the annealed sample is consistent with stronger pinning sites, as seen in Figure 3.8. The depinning field remains fairly constant, where the sample with irradiation treatment 2 has a slightly larger $\mu_0 H_{\mathrm{dep}}$ than the others. While, typically, a larger depinning field is a signature of stronger pinning, our results indicate that it is not the sole contributor to the pinning strength, as can clearly be seen in Figure 3.8 for the annealed sample.

3.2.3.2 The role of microscopic pinning parameters

With the magnetic characterization and non-universal DW motion parameters extracted from Equations 1.38, 1.39, and 1.42, we can now use an analytical model to extract the microscopic pinning parameters [239]. The model considers a DW with width Δ given by Equation 1.19 and surface energy density σ given by Equation 1.20 interacting with the surrounding pinning sites, as schematically shown in Figure 3.10. For our calculations, we assume a constant $A = 15$ pJ/m [176].

We can then obtain the characteristic range ξ (nm) and strength f_{pin} (pJ/m) of the DW-defect interaction by using the following expressions:

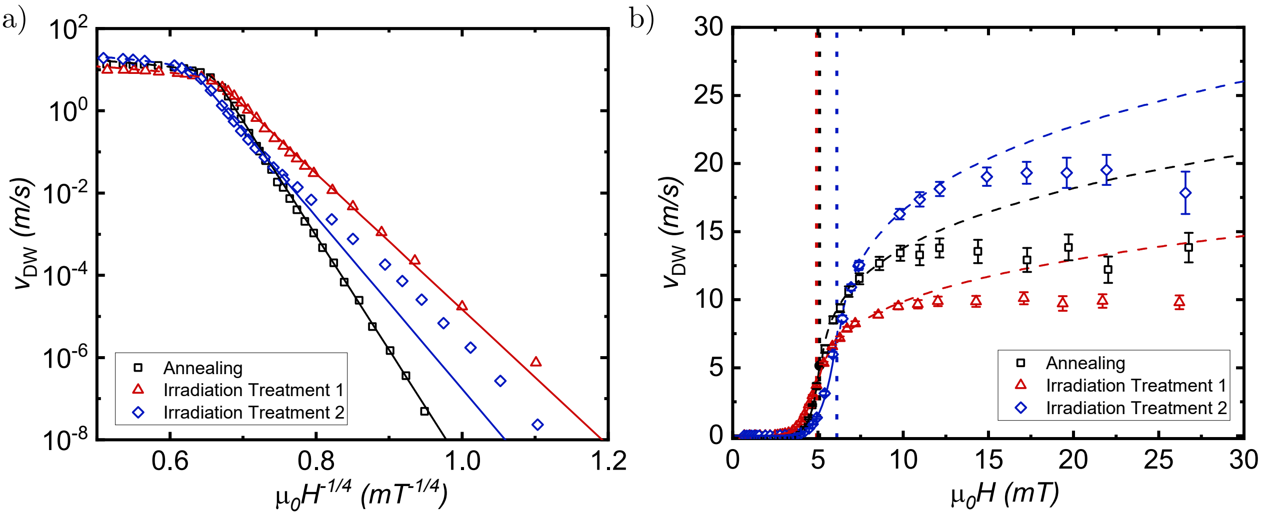

Fig. 3.9: Field driven domain wall velocity in the crystallized samples | a) The DW velocity as a function of the OOP applied magnetic field strength, rescaled to show creep-law behavior. The solid lines are fits in the creep regime, and the dashed lines are fits in the depinning regime. b) A representation of the data in a) with linear axes. The dotted vertical lines denote the depinning fields H_{dep}.

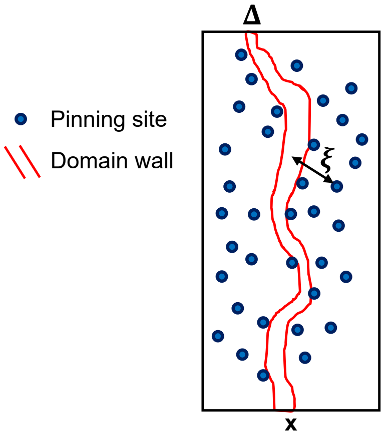

Fig. 3.10: Domain wall in a pinning landscape | A schematic representation of a DW with width Δ surrounded by pinning sites acting on it. ξ denotes the range of interaction between the pinning sites and the DW.

$$\xi \sim \left[\left(k_{\mathrm{B}} T_{\mathrm{d}}\right)^2 / \left(2\mu_0 H_{\mathrm{dep}} M_{\mathrm{s}} \sigma t^2\right)\right]^{1/3}, \tag{3.1}$$

$$f_{\mathrm{pin}} \sim \frac{1}{\sqrt{n}\xi} \sqrt{2\mu_0 H_{\mathrm{dep}} M_{\mathrm{s}} t k_{\mathrm{B}} T_{\mathrm{d}}}. \tag{3.2}$$

Here, t is the thickness of the magnetic film and $\frac{1}{\sqrt{n}} = b$ is the average distance between pinning sites, in which n is the pinning site density per unit area. We assume that the nominal thickness $t = 1$ nm of the magnetic layer does not change, since slight variations in dead layers are already taken into account in the M_{s} value. The value of $\frac{1}{\sqrt{n}}$ is based on the scaling between ξ, f_{pin}, Δ, and $\sigma \times t$ as proposed in Ref. [239], the values of which are all reported in table 3.2.

As proposed in Ref [239], f_{pin} should be proportional to $\sigma \times t$. When assuming that $f_{\mathrm{pin}} \approx \sigma t/20$ and that the three samples have the same average distance between pinning sites, we find that $\frac{1}{\sqrt{n}} = 12$ nm, which is close to the typical grain size in polycrystalline films [248]. The agreement

Table 3.2: Domain wall motion and microscopic pinning parameters | The creep and depinning parameters extracted from the DW-velocity curves using Equations 1.38, 1.39, and 1.42, DW parameters, microscopic pinning parameters extracted with Eqs. 3.1 and 3.2, and other disorder parameters extracted from FMR and BLS linewidth measurements. The table reports values for the depinning field H_{dep}, the pinning-barrier height $k_{\mathrm{B}}T_{\mathrm{d}}$, the DW width Δ, DW energy density times the thickness $\sigma \times t$, the characteristic pinning range ξ, the depinning force f_{pin}, the average distance between pinning sites $\frac{1}{\sqrt{n}}$ based on the scaling proposed in Ref. [239], the inhomogeneous broadening $\mu_0\Delta H_0$ as extracted by FMR, and both the raw effective-anisotropy-field variation $\Delta H_{K_{\mathrm{eff}}}$ and the reduced $\Delta H_{K_{\mathrm{eff}}}/H_{K_{\mathrm{eff}}}$ as extracted by BLS. Note that the reduced effective-anisotropy-field value is calculated with the anisotropy fields as extracted from BLS measurements.

	Annealed	Irradiation treatment 1	Irradiation treatment 2
	Creep and depinning parameters		
$\mu_0 H_{\mathrm{dep}}$ (mT)	5.1 ± 0.1	4.9 ± 0.1	6.1 ± 0.1
$k_{\mathrm{B}}T_{\mathrm{d}}$ (eV)	1.12 ± 0.09	0.69 ± 0.09	0.78 ± 0.09
	Domain wall parameters		
Δ (nm)	8.4 ± 0.4	8.6 ± 0.4	8.1 ± 0.4
$\sigma \times t$ (pJ/m)	7.2 ± 0.4	6.9 ± 0.3	7.4 ± 0.4
	Microscopic pinning parameters		
ξ (nm)	69 ± 5	47 ± 5	47 ± 4
$20 \times f_{\mathrm{pin}}$ (pJ/m)	5.2 ± 0.3	6.4 ± 0.5	7.9 ± 0.6
$\frac{1}{\sqrt{n}}$ (nm)	17 ± 2	13 ± 2	12 ± 2
	Other disorder parameters		
$\mu_0\Delta H_0$ (mT)	36 ± 3	46 ± 1	30 ± 1
$\mu_0\Delta H_{K_{\mathrm{eff}}}$ (mT)	24 ± 1	16 ± 3	20 ± 1
$\frac{\Delta H_{K_{\mathrm{eff}}}}{H_{K_{\mathrm{eff}}}}$ (%)	5.6 ± 0.4	5.3 ± 1.2	5.3 ± 0.5

between $20f_{\mathrm{pin}}$ and $\sigma \times t$ is good for the irradiated sample but not for the annealed sample. For the annealed sample, one way to obtain the proportionality is to increase the value of $\frac{1}{\sqrt{n}}$, which suggests that the microscopic structure of the three samples is indeed not the same. For each sample, the exact values of $\frac{1}{\sqrt{n}}$ obtained with this method are also reported in Table 3.2. Analysis of the microscopic pinning parameters thus shows that the annealed sample, while having strong pinning sites, has an overall larger mean spacing between pinning sites compared to the irradiated samples. This is further strengthened by the strongly reduced characteristic pinning range ξ for the irradiated samples. The decreased spacing between the pinning sites and the characteristic pinning range could potentially be an effect caused by a reduction of grain size in the irradiated samples.

Table 3.2 also contains other parameters that are often used to quantify disorder in materials, such as the inhomogeneous broadening $\mu_0\Delta H_0$ and effective anisotropy field variations $\Delta H_{K_{\mathrm{eff}}}/H_{K_{\mathrm{eff}}}$, which can be extracted from FMR and BLS linewidth experiments (see Chapter 1). The inhomogeneous broadening from FMR measurements shows significant variation between the three samples, with the sample with irradiation treatment 1 having the largest broadening. While this is an indication that the disorder is different between the three samples, no obvious trend between the broadening and domain wall motion is observed. Scale can be a potential reason for the discrepancy between the linewidth measurements and domain wall motion, since domain wall motion is typically measured over a much shorter length scale compared to FMR.

Contrary to the broadening measured in FMR, the raw effective anisotropy field variations measured with BLS show small changes that are consistent with the reduction in $k_{\mathrm{B}}T_{\mathrm{d}}$ and the increase in creep velocity showed in Figure 3.9, where the samples with lower $\mu_0\Delta H_{K_{\mathrm{eff}}}$ also have faster creep motion and a lower $k_{\mathrm{B}}T_{\mathrm{d}}$. However, when looking at the reduced effective anisotropy field variation $\Delta H_{K_{\mathrm{eff}}}/H_{K_{\mathrm{eff}}}$ the effect disappears. Furthermore, the values obtained from FMR and BLS do not agree, which we discuss in more detail in Section 3.4.2.

3.2.3.3 Disorder and the flow regime

We also study the domain wall velocity in the flow regime, which is shown in Figure 3.9b. We see that the domain wall velocity reaches a plateau above the depinning transition. This has been attributed to precessional losses inside the DW at fields larger than the Walker breakdown [64], the onset of the magnetization precession [28]. We observe that the plateau lies at different velocity values about 13 m/s, 10 m/s and 19 m/s for the annealed, irradiation treatment 1 and irradiation treatment 2 samples, respectively.

As discussed in Chapter 1, the height of the velocity plateau depends on D/M_s. While, qualitatively, the height of the velocity plateau scales with D/M_s in our samples (see Table 3.1), this scaling is too weak to explain the differences in plateau velocity. Recent simulation work in polycrystalline films has shown that the disorder can strongly influence the velocity in the precessional regime, mainly through the grain size and anisotropy variations [80].

To shed light on the variation of flow velocity in the three samples, we perform an extensive set of micromagnetic simulations using Mumax3 [82,249,250]. In the same vein as Ref. [80], we investigate DW velocity in the precessional regime in disordered samples. We will use the results of these simulations to argue that the variation of the flow velocity shown in Figure 3.9b cannot simply be explained by variation of magnetic parameters, and that instead the disorder has a role to play.

First, we study the effect of the disorder parameters on the flow velocity, where we focus specifically on the grain size and distribution of magnetic parameters. The system under study is the annealed sample, and thus we use the magnetic parameters reported in Table 3.1. We also assume $A = 15$ pJ/m. The computational window is $1 \times 2\mu\mathrm{m}^2$, with $2 \times 2\mathrm{nm}^2$ cells and a thickness of 1 nm. Grains are introduced using a Voronoi tessellation [82], and the grains are subsequently given a distribution of anisotropy values around their nominal value K_u with a distribution σ, and a deviation of anisotropy axis around the z-direction with the same distribution σ. A visualization of the resulting grain structure is shown in Figure 3.11a for grains ranging between 8 and 60 nm. Variations of other parameters are not considered, and the simulations are performed without the influence of temperature.

We investigate the velocity at an applied perpendicular field $B_z = 70$ mT, which is well above the depinning transition, but below the threshold for nucleation. Furthermore, the DW motion is in the precessional regime. We vary the average Voronoi grain size between 8 and 60 nm, for values of σ ranging between 3 and 8%. The DW is initialized in the center and allowed to relax before the magnetic field is applied. We calculate the displacement of the DW from its average position along its length, as visualized by the red dotted lines in Figure 3.11b. Each simulation is averaged over 10 different realizations of the grain distribution and anisotropy distribution. The results of this study are shown in Figure 3.11c and d.

Figure 3.11c shows that for all values of σ, the velocity increases sharply with increasing grain size up to roughly the value of the Bloch domain wall width $\pi\Delta = \pi\sqrt{A/K_\mathrm{eff}} = 26$ nm, after which it slightly decreases. This is in good agreement with previous simulations [80,251]. Furthermore, Figure 3.11c shows that the DW velocity in the flow regime is strongly impacted by the strength of the dispersion σ, with larger dispersions resulting in faster DW motion. This is also in agreement with previous simulations [81,82] and can be explained with an extra extrinsic component to the effective damping. The system dissipates energy through the emission of a spin wave at local DW depinning events, increasing the DW velocity [80] (see also Chapter 1 for more details). The curves in Figure 3.11c have a similar shape. Figure 3.11d shows the same data, but now normalized at 30 nm, revealing that the grain size has almost exactly the same effect no matter the strength of the anisotropy distribution.

We now simulate the DW velocity at different magnetic fields in the precessional regime, taking into account the measured micromagnetic properties and anisotropy variation of the samples. We set the grain size constant at 10 nm - a typical value in polycrystalline films [248] and consistent with the results reported in Table 3.2. The results of these simulations are shown with closed symbols in Figure 3.12a. Figure 3.12a also contains the experimental data as shown in Figure 3.9b, shown

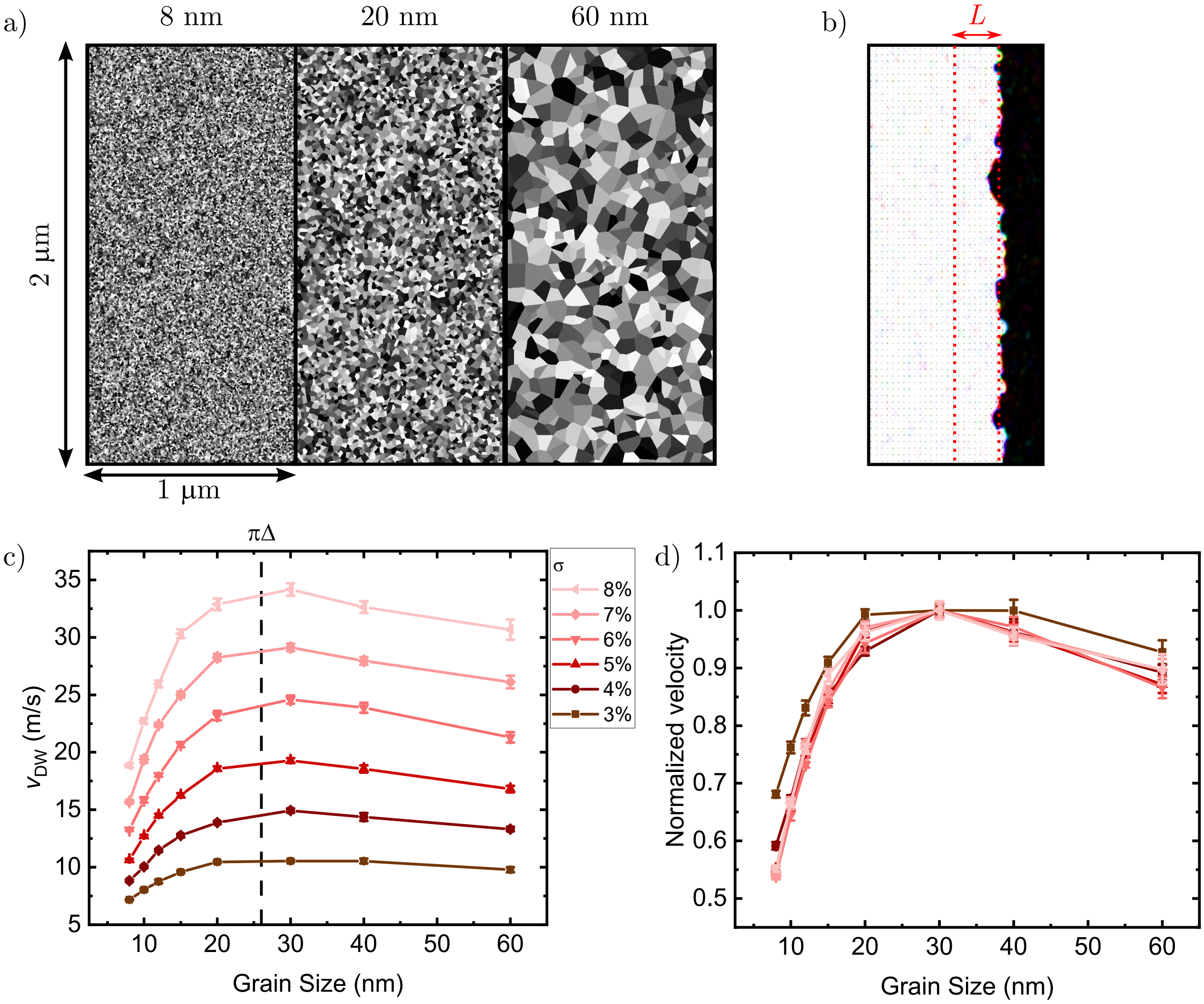

Fig. 3.11: Influence of disorder on the domain wall flow velocity | a) Examples of grain structures created with a Voronoi tesselation in the simulation window for average grain sizes of 8, 20, and 60 nm. The grey-scale colors indicate different regions i.e. grains. b) Example of a Mumax3 simulation window showing the simulation protocol. The local magnetization is visualized by color, with white showing the up-domain, black the down-domain, and the remaining colors visualize the in-plane magnetization in the DW. The displacement of the DW is measured from its average position compared to where it was initialized, visualized by L and the red-dotted lines. c) Micromagnetic simulations of the DW velocity at 70 mT as a function of the average Voronoi grain size for differing anisotropy distribution values σ. The dashed vertical line represents the Bloch DW width $\pi\Delta = \pi\sqrt{A/K_{\text{eff}}} = 26$ nm. The velocity is averaged over 10 different grain distributions, and the error bars denote the standard deviation in the average velocity over these grain distributions. d) Data of c) normalized at a grain size of 30 nm.

here with open symbols. The shaded area around the simulation data denotes the change in domain wall velocity based on the error in the variation of anisotropy field that we measured with BLS (see Table 3.2).

Figure 3.12a shows decent agreement between simulation and experiment for the annealed sample and the sample treated with irradiation treatment 2. However, the velocity for the sample with irradiation treatment 1 is about a factor 2 larger in the simulation compared to the experiment. Even when taking into account the error in the measured anisotropy field variation, the velocity is still too large.

Figure 3.12b shows the results for irradiation treatment 1 from Figure 3.12a, and includes simulation results performed with a smaller grain size of 7.5 nm. Although there is still a mismatch

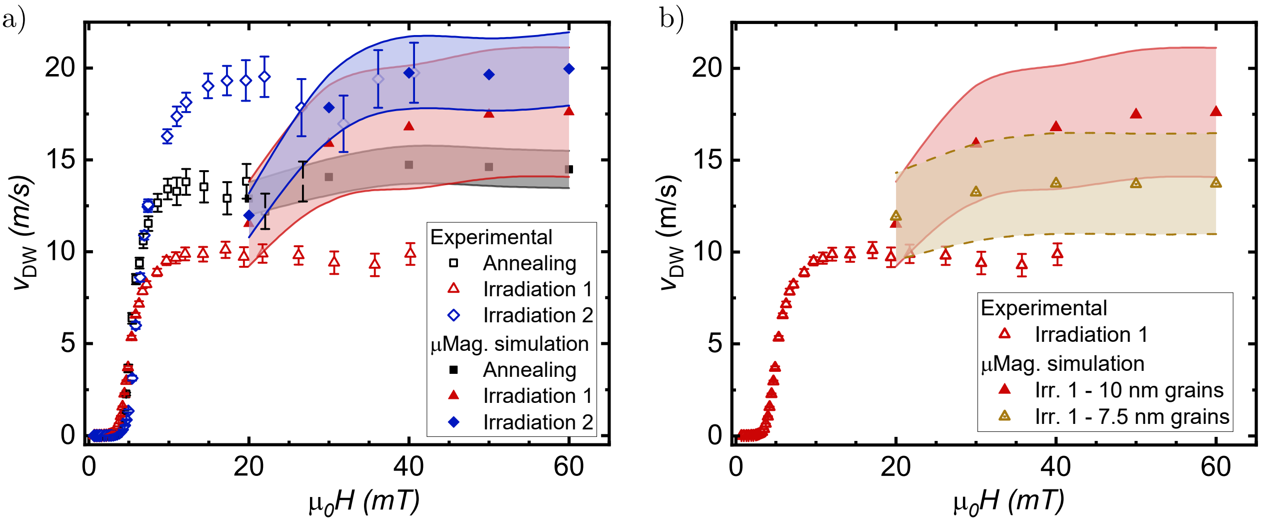

Fig. 3.12: Experimental and simulated DW velocity in the flow regime | a) The DW velocity as a function of the OOP applied magnetic field for the three samples. The figure contains experimental results (open symbols) and results from micromagnetic simulations with disorder (closed symbols). An average grain size of 10 nm is used in the simulations. The shaded area for the micromagnetic simulation denotes variation in domain wall velocity based on the measured anisotropy variation of BLS and the characterization results of the micromagnetic simulations. b) Experimental data (open symbols) and simulations (closed symbols) for irradiation treatment 1 from a) and simulations with a reduced average grain size at 7.5 nm (dotted open symbols).

between the simulation and experimental results, the mismatch has shrunk. This is an indication that the sample with irradiation treatment 1 could have a smaller average grain size than the other samples.

3.2.4 Discussion and conclusion

The effect of the changes in the microscopic pinning parameters reported in Table 3.2 can be seen when considering the pinning free energy $\delta F_{\text{pin}} = f_{\text{pin}}\sqrt{n\xi L}\xi$ of the collective pinning length of the DW $L_c \sim (\xi/n)^{1/3}(\sigma t/f_{\text{pin}})^{2/3} \approx 160$ nm [239], also called the Larkin length. We see a similar approximately 30% drop in pinning free energy due to the proportionality imposed with $k_B T_d$. Despite the decrease in the mean spacing of pinning sites (i.e., a higher defect density), a reduced energy barrier makes it easier for thermal excitations to induce DW motion, since the overall displacement of the DW in the creep regime is driven by the largest energy barriers [68].

A visual description of such an pinning energy landscape is shown in Figure 3.13. Here, two pinning landscapes are shown, in red for the annealed sample, and in blue for the irradiated samples. The lower maximum pinning energy of the irradiated samples corresponds to the reduction in pinning energy barrier, whereas the shorter spacing of the barriers represents the reduction in mean distance between pinning sites. The overall smoother landscape is a representation of the observations of smoother domain wall propagation in Figure 3.8.

Looking beyond the depinning transition, little is still known about the interplay between intrinsic material defects and the DW velocity in the velocity plateau. While disorder does impact the domain wall velocity in the precessional regime, only the sample with irradiation treatment 1 shows indications of significantly affected disorder, which is not consistent with our results from the creep regime. Moreover, the depinning fields, which also depend on the disorder, are significantly larger in the simulation compared to the experiment. One of the main causes is the absence of temperature in the simulations, but it shows that the grain size and anisotropy fluctuations have to be tuned further in order to reproduce the experimental values of the depinning field. Furthermore, the inclusion of DMI and thickness variations [252] can further help in reproducing both the depinning fields and the velocity in the precessional regime.

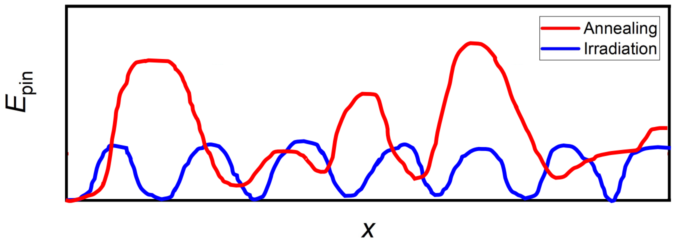

Fig. 3.13: Drawing the energy landscape | The proposed one-dimensional energy landscape for the annealed sample (red) and irradiated samples (blue).

Nonetheless, we can use the results from all DW motion regimes to gain insight into the disorder. A reduction in grain size upon irradiation would explain both the reduced average distance between pinning sites, as well as some of the discrepancies in the flow regime. A smaller grain size after irradiation is supported by the nanoparticle model for irradiation enhanced crystallization (see Chapter 2), both through the ballistic effects of irradiation reducing the stable particle size, as well as a likely increase in crystallite nucleation sites under irradiation. Using high resolution transmission electron microscopy (HR-TEM) measurements, it is not possible to see any grain size variations due to the nanometer scale origin of disorder (interface roughness, interface intermixing, etc.). Techniques with a larger field of view, such as high angle TEM or X-ray based techniques, could give further insight.

Overall, we can identify the grain size as a critical parameter for the optimization of DW motion in polycrystalline films. The pinning energy barrier also plays a significant role in the creep regime next to the depinning field, while in the flow regime the anisotropy variation can also have a significant impact [81]. However, more extensive simulations would be necessary to fully characterize the velocity in the flow regime and to make a link between the creep and depinning parameters and the flow regime.

Despite this fact, the extra information that can be obtained from DW motion measurements can aid in the characterization of disorder, since it provides information on the length scales involved in DW pinning, which is absent in a traditional magnetic study. Other techniques to independently access the same information are therefore required.

To summarize, we use DW motion to experimentally study the magnetic disorder of three differently crystallized W/CoFeB/MgO ultrathin films. The DW roughness and velocity in the samples are observed to be significantly different in the creep and flow regimes. These differences in the two regimes cannot be explained via pure magnetic characterizations and a deeper dive into the microscopic pinning parameters is required to fully understand the domain wall motion. We use an analytical model to link changes in the creep velocity to changes in the microscopic pinning parameters through the modulated pinning energy barrier. Furthermore, we use micromagnetic simulations and the domain wall velocity in the precessional regime to obtain information about structural differences between the samples. From the extensive measurement of all DW motion regimes we find that the pinning energy barrier $k_{\mathrm{B}}T_{\mathrm{d}}$, the scaled average distance between pinning sites $\frac{1}{\sqrt{n}}$, and the anisotropy variations are, on top of the depinning field H_{dep}, among the critical parameters in optimizing DW motion. Furthermore, we identified the grain size as an important physical parameter, although more research is required to confirm its relation to the microscopic parameters and the precessional DW velocity. Our results show that the extra information that can be obtained from DW motion measurements can be used in the characterization of material disorder and that measuring the microscopic pinning environment is a prerequisite when optimizing materials for devices based on DW motion. Not only are our results relevant for DW motion, but they could be applied to skyrmion motion as well, since it is also heavily impacted by disorder [251,253,254]. The fact that a more homogenized disorder landscape can be obtained with irradiation enhanced crystallization is very promising not only for racetrack applications, but also for STT/SOT MRAM, as the homogenized disorder would reduce variations in writing current, increasing overall yield.

3.3 Summary

In this chapter, we show that the magnetic properties and disorder of a W/CoFeB/MgO ultrathin film can be accurately controlled using an irradiation induced crystallization process at moderate temperatures. With irradiation at moderate temperatures, we show that similar or larger values of the effective anisotropy field $H_{K_{\mathrm{eff}}}$ can be obtained compared to the industrial standard of high temperature annealing. Furthermore, the irradiation process only weakly affects the other magnetic properties of the crystallized W/CoFeB/MgO film. We subsequently show that the disorder profile can be optimized to ensure easy DW motion throughout the film by using an improved irradiation induced crystallization process. We reveal the nanoscale disorder by using an analytical model based on the creep and depinning DW motion, and show that the pinning landscape can be effectively engineered with irradiation induced crystallization. Moreover, by using simulations of flow-regime dynamics we link the possible reduction of the grain size upon irradiation induced crystallization to the observed reductions in DW-pinning length scales. These results show not only that irradiation induced crystallization is an effective tool to control the magnetic properties of thin films, but also to optimize the structural properties of thin films. Furthermore, when designing devices based on DW motion, particular care should be taken in the design of the structural properties.

In the next chapter, we shift our focus from irradiation induced ordering to irradiation induced interface mixing of pre-crystallized samples. We investigate how the properties of, and the DW motion in a crystallized W/CoFeB/MgO film evolve with interface mixing. We then use these results to go beyond the interactions between DWs and intrinsic material defects, and study how extrinsic defects in the form of edge damage imposed by a (nano-)fabrication process are affected by He$^+$ irradiation.

3.4 Supplemental

3.4.1 Saturation magnetization and microscopic pinning parameters

The three crystallized samples that we study in Section 3.2 have very similar micromagnetic properties, except for the saturation magnetization. In this section we show that the results from this chapter do not depend significantly on the value of the saturation magnetization.

We perform the same analysis as described in Section 3.2.3.2, but now with constant $M_{\mathrm{s}} = 1.59$ MA/m. We also assumed $A = 10$ pJ/m, but the rest of the parameters are the same. Figure 3.14 shows the resulting values for the microscopic pinning length ξ from the two analysis. The analysis with constant M_{s} is shown in black, while the results with varying M_{s} are shown in red.

Figure 3.14 clearly shows that the resulting values for ξ are very similar, and not strongly dependent on the value of M_{s}, with a similar trend of reduced ξ for both analyses. The effect is similar for f_{pin} and $\frac{1}{\sqrt{n}}$ (not shown), where the trend for both analyses is the same. Furthermore, the extracted values for the creep energy barrier $k_{\mathrm{B}}T_{\mathrm{d}}$ come from the domain wall motion curve, and are thus independent of the value of M_{s}. From these results we can confirm that the conclusions regarding the pinning energy landscape from the main paper are not affected.

3.4.2 BLS vs FMR inhomogeneous broadening

In Section 3.2 we mentioned that the values for the inhomogeneous broadening obtained from BLS and FMR do not agree. In this section, we will elaborate and discuss potential causes. Table 3.3 contains the results from the FMR measurements and analysis using Equations 1.43 and 1.47, as well as the results of the BLS measurements and analysis using Equations 1.51, 1.52, and 1.48.

Regarding the reduced gyromagnetic factor $\gamma/2\pi$, we observe that the FMR values are very close with published measurements on nominally identical samples, for example 30.32 ± 0.04 GHz/T for the annealed sample [255]. The lower factor in the in-plane geometry measured by BLS is also consistent with the orbital contribution to the gyromagnetic ratio expected for samples with perpendicular easy axis [256].

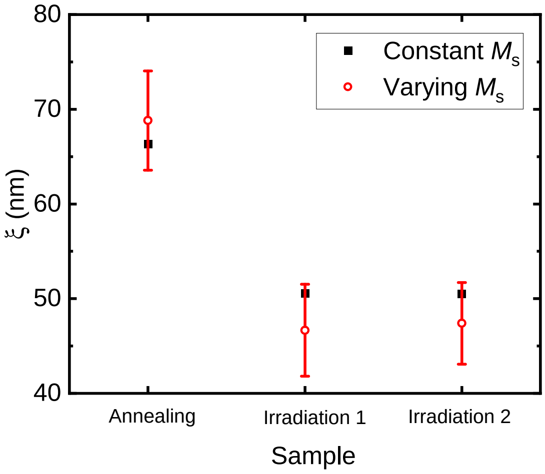

Fig. 3.14: Saturation magnetization and microscopic pinning | Microscopic pinning ranges in the three investigated samples from two different analyses. The analysis with constant M_s is shown in black, and the analysis with varying M_s from the main paper is shown in red.

Bigger differences are observed for the effective anisotropy field. They can be ascribed to the presence of a higher order contribution to the PMA, which is not detected in the perpendicular geometry but modifies the in-plane resonance frequency. For the samples considered here, the sign of the second order PMA appears to be positive, with values of the corresponding anisotropy field of 84, 54 and 80 mT for the annealed sample and the samples with irradiation treatment 1 and irradiation treatment 2, respectively. Another possible cause of the discrepancy between OOP and IP FMR could be the presence of a magnetic anisotropy within the sample plane, but such a term is not expected as the samples were grown under rotation within the sample plane. A last matter of concern is that the BLS measurements were performed at a finite wavevector $k_\mathrm{SW} = 11.81\ \mu\mathrm{m}^{-1}$. Comparing with the Kittel equation at $k_\mathrm{SW} = 0$ (Equation 1.43), one sees that a finite k amounts to replacing, in the ultra thin limit, the applied field H by $H + \frac{1}{2}ktM_\mathrm{s} + \frac{2A}{\mu_0 M_\mathrm{s}}k^2$, and the anisotropy field H_K by $H_K + ktM_\mathrm{s}$ (the first term in Equation 1.48). Using the magnetization values reported in Table 3.1 of the main text, one obtains for the linear term in $\mu_0 H$ values of 9, 11 and 12 mT, whereas for the quadratic term the values are all 3 mT. Therefore, despite the analysis at $k_\mathrm{SW} = 0$, the difference of anisotropy fields between FMR and BLS is real, and can be explained by the second order PMA constant.

Regarding the linewidth measurements, we note that FMR and BLS result in very similar values for the damping parameter, with α^FMR maybe slightly larger than α^BLS. However, larger differences are present when looking at the inhomogeneous broadening $\mu_0\Delta H_0$ and dispersion of the anisotropy field $\mu_0\Delta H^\mathrm{BLS}_{K_\mathrm{eff}}$. The values obtained from both techniques do not agree, with $\mu_0\Delta H_0$ larger than $\mu_0\Delta H^\mathrm{BLS}_{K_\mathrm{eff}}$. Note that, in the perpendicular geometry where FMR was performed, the additional relaxation channel called two-magnon scattering [257] is absent, so that $\mu_0\Delta H_0$ should be the true inhomogeneous broadening of the resonance line. For BLS, even if it is performed in the in-plane geometry, where the two-magnon scattering channel is active, no associated increase of the linewidth is expected. Indeed, magnons are not pumped at $k = 0$ in BLS, but probed at a specific k. From this analysis therefore, we expect that $\mu_0\Delta H_{K_\mathrm{eff}}$, evaluated by removing the non-linearity of in-plane resonance, should be equal to $\mu_0\Delta H_0$. In fact, we would even expect that $\mu_0\Delta H_{K_\mathrm{eff}} > \mu_0\Delta H_0$ as in the in-plane configuration the second PMA constant is active, whose dispersion adds to that of M_s and K_u. The experimental results, even when taking into account the larger error bars on $\mu_0\Delta H_{K_\mathrm{eff}}$ due to the small number of data points, are in stark opposition to these expectations, especially for the sample with irradiation treatment 1. This definitely calls for further studies. Despite these discrepancies, the values for $\Delta H^\mathrm{BLS}_{K_\mathrm{eff}}/H^\mathrm{BLS}_{K_\mathrm{eff}}$ obtained from BLS agree with previous work on similar samples [178], and hence we use them for the analysis where anisotropy variations come into play

Table 3.3: BLS vs FMR linewidth analysis | Parameters used for, and extracted from the linewidth measurements using FMR and BLS. The table reports values for the gyromagnetic ratio $\gamma/2\pi$ and the effective anisotropy field H_{K_eff} extracted from FMR and BLS. The table also reports the results of the analysis of the FMR linewidth measurements using Equation 1.47, namely α^FMR and ΔH_0, and $\Delta H_{K_\mathrm{eff}}^\mathrm{FMR}/H_{K_\mathrm{eff}}^\mathrm{FMR}$, as well as the results from analysis of the BLS linewidth measurements using Equations 1.51 and 1.52, namely α^BLS, $\mu_0\Delta H_{K_\mathrm{eff}}^\mathrm{BLS}$ and $\Delta H_{K_\mathrm{eff}}^\mathrm{BLS}/H_{K_\mathrm{eff}}^\mathrm{BLS}$.

	Annealing	Irradiation treatment 1	Irradiation treatment 2
$\gamma^\mathrm{FMR}/2\pi$ (GHz/T)	30.1 ± 0.1	30.67 ± 0.02	30.55 ± 0.02
$\mu_0 H_{K_\mathrm{eff}}^\mathrm{FMR}$ (mT)	342 ± 6	259 ± 1	287 ± 1
α^FMR (10^{-3})	19 ± 1	17 ± 1	18 ± 1
$\mu_0\Delta H_0$ (mT)	36 ± 3	46 ± 1	30 ± 1
$\gamma^\mathrm{BLS}/2\pi$ (GHz/T)	29.1 ± 0.6	29.3 ± 0.7	29.3 ± 0.6
$\mu_0 H_{K_\mathrm{eff}}^\mathrm{BLS}$ (mT)	426 ± 27	313 ± 38	367 ± 30
α^BLS (10^{-3})	15 ± 1	15 ± 1	16 ± 1
$\mu_0\Delta H_{K_\mathrm{eff}}^\mathrm{BLS}$ (mT)	24 ± 1	16 ± 3	20 ± 1
$\Delta H_{K_\mathrm{eff}}^\mathrm{BLS}/H_{K_\mathrm{eff}}^\mathrm{BLS}$ (%)	5.6 ± 0.6	5.3 ± 1.7	5.3 ± 0.8

(e.g. in Section 3.2.3.3).

Chapter 4

Tailoring disorder in W/CoFeB/MgO layers with irradiation induced mixing

> *Il y a encore des gens qui travaillent sur ça?*
> Thibaut Devolder

Magnetic domain walls (DW) are not only hindered by intrinsic defects that are related to material quality and inherent to granular films, but also by extrinsic defects, which can be introduced by (nano)fabrication processes. This is a major challenge to develop advanced racetrack memory applications where DWs or skyrmions propagate in very narrow wires. In this chapter, we show that we can use local He^+ irradiation at room temperature (RT) to reduce the interactions between DWs and extrinsic edge defects. First, we extensively study the effect of irradiation on the magnetic properties and intrinsic disorder of pre-crystallized W/CoFeB/MgO films through the mixing of interfaces. Then, we show that, depending on the ion fluence, the DW edge pinning can be controlled and even quenched by local irradiation at the edge of a microwire. Furthermore, by employing a magnetic planar patterning process without physical etching, we show that edge pinning can be significantly reduced on a larger scale. With this work we shed light on the effect of He^+ irradiation on both the intrinsic and extrinsic disorder of a W/CoFeB/MgO ultra-thin film, and show that He^+ irradiation can be used to accurately control the extrinsic DW pinning in a non-damaging way, which can be easily integrated into a lithography process.

4.1 Introduction

DWs interact with disorder, which typically arises in the form of spatial variations of magnetic parameters, crystallite boundaries, and interface roughness. Disorder slows down the dynamics of a DW through pinning, resulting in a stochastic behavior. In disordered materials, DWs are only able to move forward above a threshold force. This limits the efficiency of DW-motion based devices, and it is thus imperative that good control over the material disorder is obtained to improve the efficiency of such devices. Intrinsic material disorder can be controlled using a variation of techniques, such as material engineering [235–237], substrate patterning [258], and interface engineering with He^+ irradiation [174,176,178,196].

The use of DWs in devices generally requires lithography, which introduces additional extrinsic disorder in the form of edge effects. This additional extrinsic disorder has strong effects on the motion of DW through the device. In sub-micron wires, extrinsic pinning can significantly slow down [259] and even completely pin the DW [218]. Moreover, edge effects can significantly hinder the DW motion even in micrometer-sized wires [219], where edge effects normally play a small role. Edge pinning affects the DW motion through an increased DW curvature and a critical decrease in the DW velocity below the creep-law dependence. This is detrimental when designing devices based on DW motion, since the extrinsic pinning reduces the efficiency of the device.

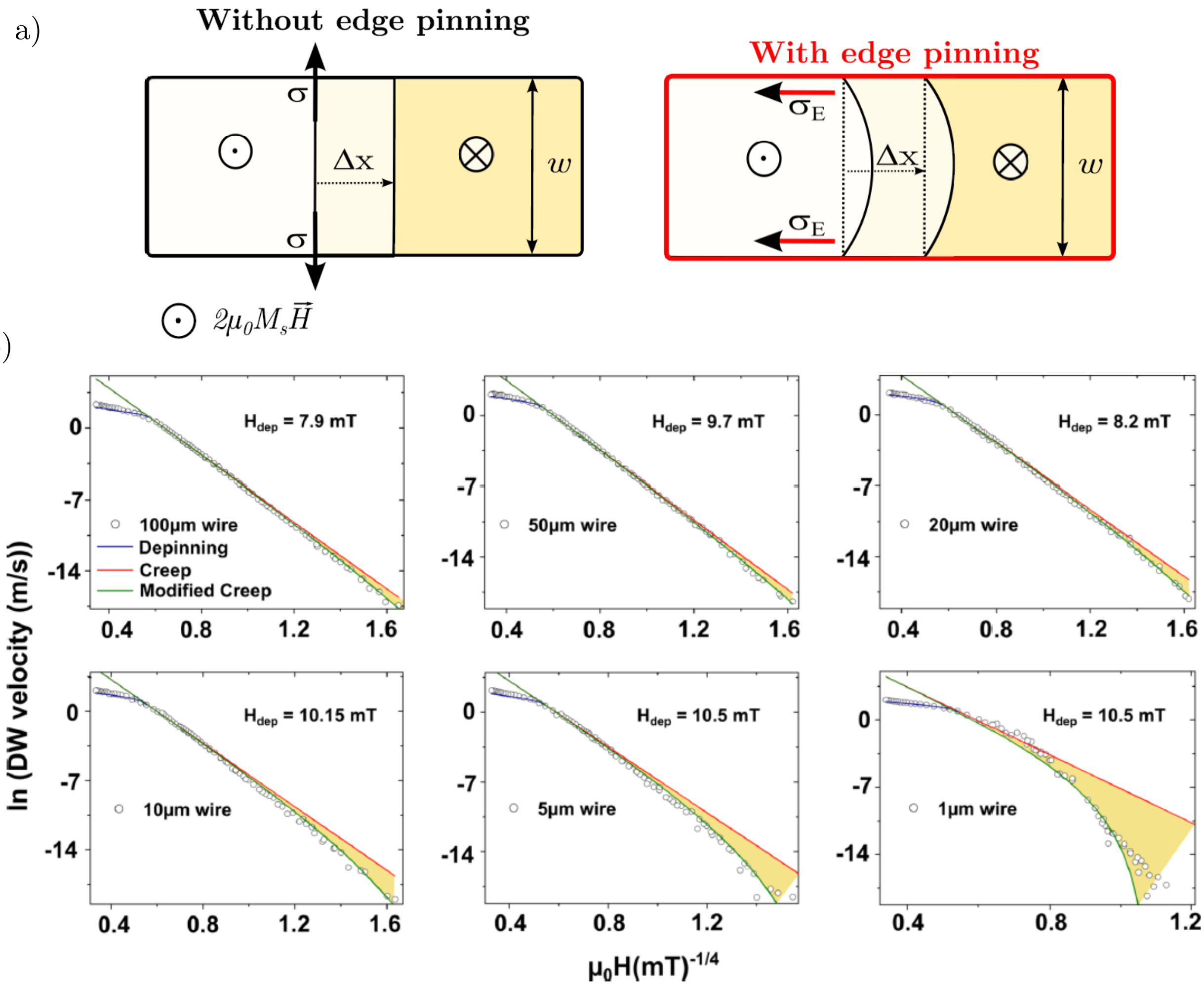

Fig. 4.1: Domain wall pinning at wire edge defects | a) Schematic showing a model for the displacement Δx of a DW in a wire with width w with and without edge pinning. b) Domain wall velocity in the creep regime in annealed Ta (5 nm)/$Co_{20}Fe_{60}B_{20}$ (1 nm)/MgO (2 nm)/Ta (3 nm) wires with widths ranging from 100µm to 1µm. The blue line denotes a fit in the depinning regime, the red line denotes the expected creep behavior in a wire without edge effects, and the green line shows the fit with a modified creep law that takes edge pinning into account. The depinning field is mentioned in each graph. Figures and data adapted from Ref. [219].

In microwires, edge pinning can be modeled as an additional pinning component at the edge [219,260], as schematically shown in Figure 4.1a. Upon the application of an external magnetic field, the DW moves forward so that the system gains Zeeman energy. The DW wants to reduce its tensile energy, and thus remains straight in a wire without edge pinning. The additional pinning component σ_E at the edges slows down the DW locally. To gain as much Zeeman energy as possible, the DW curves until the gained Zeeman energy is equal to the energy penalty that has to be paid to lengthen the DW. Depending on the strength of the edge pinning, the DW curvature thus changes, which in turn can significantly reduce its velocity. By the nature of the competition between the Zeeman and tensile energies, the effect of edge pinning is both dependent on the width of the wire, as well as the magnetic field. This dependence is observed in the data shown in Figure 4.1b. At larger fields, the contribution of the Zeeman energy is much larger than the additional edge pinning. This results in a flatter DW and a weaker relative[1] effect of the edge pinning on the DW velocity at larger fields [260]. Indeed for all wires in Figure 4.1b, the data follows the expected creep law (red line). The DW is only slowed down at low fields. Similarly, in narrower wires, less magnetic material is present in

---

[1] In the model, the edge pinning potential itself is not dependent on the magnetic field.

the bulk of the wire, meaning that a larger displacement is required to gain enough Zeeman energy to overcome the edge pinning, and thus the edges become increasingly important. This means that in narrower wires, the effects of the edge pinning on the DW velocity is stronger [219]. Indeed, in Figure 4.1b, the edge pinning effect is increased for wires with smaller widths.

For efficient DW-motion based devices, it is thus imperative that extrinsic edge roughness is minimized. Typically, this would be achieved by designing a lithography process that reduces edge roughness. However, a lithography process has a fundamental resolution that cannot be overcome (e.g. several hundreds of nm for UV lithography, or several nm for electron beam lithography (EBL)). On top of that, etching of the device with low-energy Ar^+ ions typically introduce strong edge effects, which further limits the resolution. In this work, we show that we can use local ion irradiation to correct edge damages from lithography processes. Through irradiation of the edges with a He^+ focused ion beam (FIB), we observe a significant increase of the DW velocity and, depending on the fluence, an almost complete quenching of edge defects. Moreover, we show that by irradiating through a mask we can create magnetic structures that have significantly reduced edge effects compared to typical structures formed by a regular UV lithography process.

This chapter is divided in two distinct parts. In Section 4.2, we study the evolution of a series of full-film W/CoFeB/MgO ultra-thin samples with He^+ irradiation to better understand the effects of irradiation on the magnetic and structural properties of the thin films. Then, in section 4.3, we show that the DW motion in wires is significantly affected by local He^+ irradiation, and we use the knowledge from Section 4.2 to discuss the local dose-dependent effect of the irradiation at the wire edge.

4.2 Controlling domain wall motion in W/CoFeB/MgO ultra-thin films with irradiation induced mixing

In the context of DW motion, the impact of intermixing the interfacial structure (and the subsequent changes in magnetic parameters) on the DW motion mechanisms and structural disorder is still unclear. Optimization of the structural disorder, such as interface intermixing and roughness, is one of the main challenges in the optimization of DW-motion based devices (see Chapter 3). In this section, we aim to shed more light on this phenomena by studying the effect of progressive interface intermixing induced by He^+ irradiation at room temperature on the motion of DWs in W/CoFeB/MgO ultra-thin films. Previous work on W/CoFeB/MgO [176] and Ta/CoFeB/MgO [174,178] films has already shown that the evolution of the magnetic parameters and DW motion is heavily dependent on the interface disorder and characteristics of the sample. We similarly study the evolution of magnetic parameters and DW-motion parameters, and we additionally investigate the effect of He^+ irradiation on the microscopic pinning parameters by using an analytical model for the DW-disorder interaction [239]. Furthermore, we also study the effect of He^+ irradiation in the flow regime.

4.2.1 Sample Characterization

We study the magnetic properties of a $\mathrm{W(4)/Co_{20}Fe_{60}B_{20}(1.1)/MgO(2)/Ta(5)}$ (thicknesses in nanometers) ultra-thin film, grown by a Singulus Rotaris sputtering tool on a 200-mm $\mathrm{Si/SiO_2}$ substrate, irradiated with increasing He^+ fluences. The samples have been annealed in-situ at 400°C for 1h prior to irradiation to induce crystallization and PMA. The irradiations are performed at 15 keV, with He^+ fluences ranging between 4×10^{14} and 5×10^{16} ions/cm^2. The magnetic properties are measured using a combination of AGFM, FMR, and BLS measurements.

Figure 4.2a shows the hysteresis loops of the irradiated samples, as measured with AGFM. The as-deposited sample shows PMA and a square hysteresis loop. Progressively irradiating the samples with He^+ ions only slightly affects the shape of the loops. Up to a He^+ fluence of 3×10^{15} ions/cm^2, all samples retain PMA and have square hysteresis loops. The coercive field and saturation magnetization are not significantly affected, as shown in Figure 4.2b. Only at very large

He$^+$ fluence, i.e. 5 × 10^{16} ions/cm^2, does the sample show a strongly reduced magnetic moment and a loss of PMA. This is most likely due to an almost total mixing of the metallic layers. In this case, the sample can almost be considered as paramagnetic. Note that contrary to previous studies [176], the samples do not go through tilted or in-plane anisotropy for the fluences studied here, but directly to a PM state.

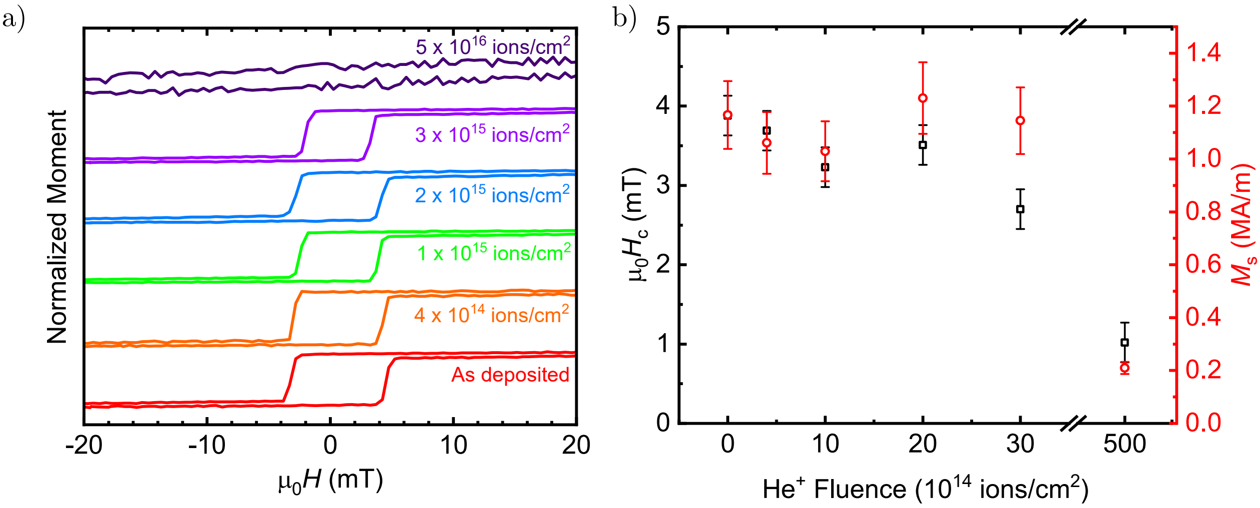

Fig. 4.2: Hysteresis properties of progressively irradiated W/CoFeB/MgO | a) Stacked hysteresis loops as measured by AGFM of W/CoFeB/MgO ultra-thin films progressively irradiated with He$^+$ ions. The magnetic moment of each loop is normalized. b) Coercive field H_c (black, left axis) and saturation magnetization M_s (red, right axis) as a function of He$^+$ fluence, extracted from the hysteresis loops.

Next, we study the evolution of the anisotropy and damping in the irradiated samples with FMR. The results are summarized in Figure 4.3. Figures 4.3a and b show the FMR frequency dependence on the resonance field and the FMR linewidth as a function of the FMR frequency, respectively, for the progressively irradiated samples. This data has been further analyzed using Equations 1.43 and 1.47 to extract H_{K_eff}, α, and ΔH_0, which are shown in Figures 4.3c, d, and e, respectively. We observe a gradual reduction in H_{K_eff} with increasing He$^+$ fluence, for which at the largest dose H_{K_eff} is reduced by roughly 29% compared to the as-deposited state. α does not vary strongly with irradiation, showing a stable value around 0.02 for all samples. ΔH_0 shows larger variations, albeit non-monotonically.

Finally, we study the evolution of the DMI in the irradiated samples with BLS measurements. The results are summarized in Figure 4.4. Figure 4.4a shows the frequency difference between the Stokes and Anti-Stokes peaks in the BLS spectra as a function of the probed wave-vector for the irradiated samples. From the slope, we can extract the DMI constant using Eq. 1.49. The results are shown in Figure 4.4b. We observe a small progressive reduction of D with increasing fluence. At a fluence of 3 × 10^{15} ions/cm^2, the DMI constant is reduced by roughly 33% compared to the as-deposited state.

Our results show that progressive He$^+$ irradiation indeed has an effect on the magnetic properties of W/CoFeB(1.1)/MgO. The reduction in H_{K_eff} can be linked to a reduction of the uniaxial anisotropy constant K_u, since M_s varies relatively little. Since $K_\mathrm{u} \propto K_\mathrm{s}/t$, and we assume the nominal thickness to remain constant, this indicates a reduction of K_s. Together with the drop in DMI with increasing fluence, we thus observe that it is mostly the interface properties that are changed with irradiation. Indeed, the more bulk-like properties, such as damping and M_s, remain relatively constant. This is very similar to earlier work on He$^+$ irradiation in W/CoFeB(0.6)/MgO [176], where D and K_s also reduce with irradiation. As mentioned in Chapter 3, the W/CoFeB interface is more susceptible to mixing than the CoFeB/MgO interface, due to the different enthalpies of mixing of the consituent elements, and thus it is expected that the reduction of K_s and D is mainly driven by the mixing of the W/CoFeB interface. Moreover, since the CoFeB/MgO interface is only

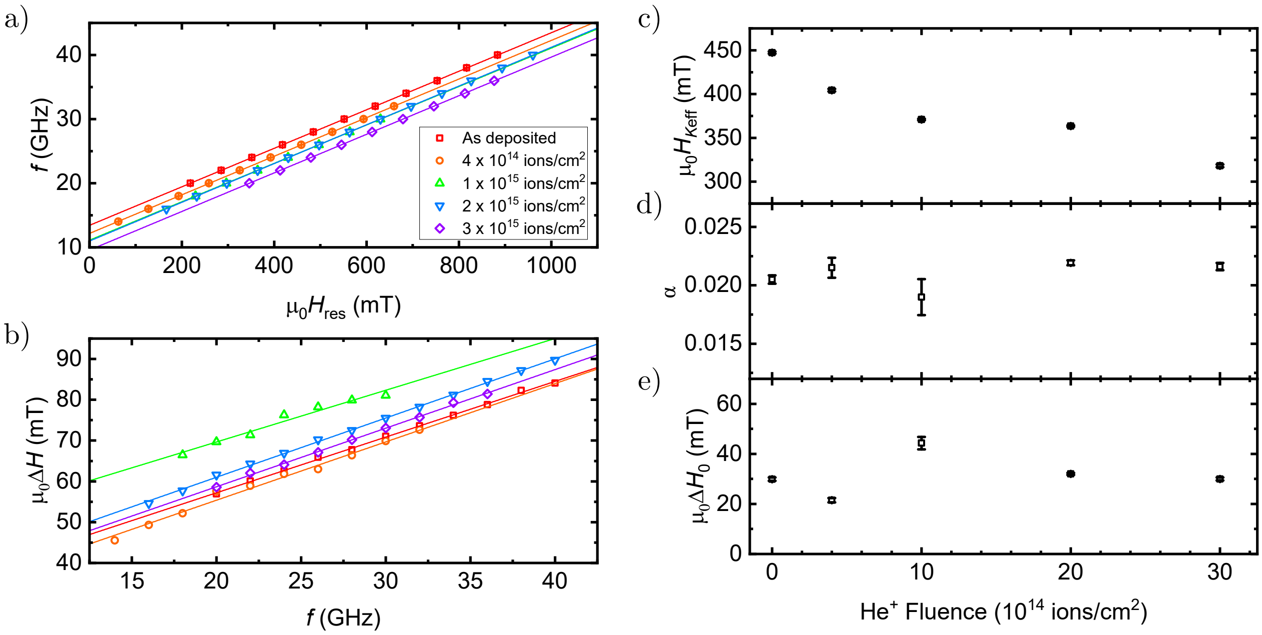

Fig. 4.3: FMR measurements of irradiated W/CoFveB/MgO | a) FMR frequency as a function of the resonance field in the progressively irradiated samples. The solid lines are fits with Eq. 1.43. b) FMR linewidth as a function of the FMR frequency in the progressively irradiated samples. The solid lines are fits with Eq. 1.47. c)-e) Magnetic properties extracted from the resonance field and linewidth measurements. c) Effective anisotropy field. d) Damping. e) Inhomogeneous broadening.

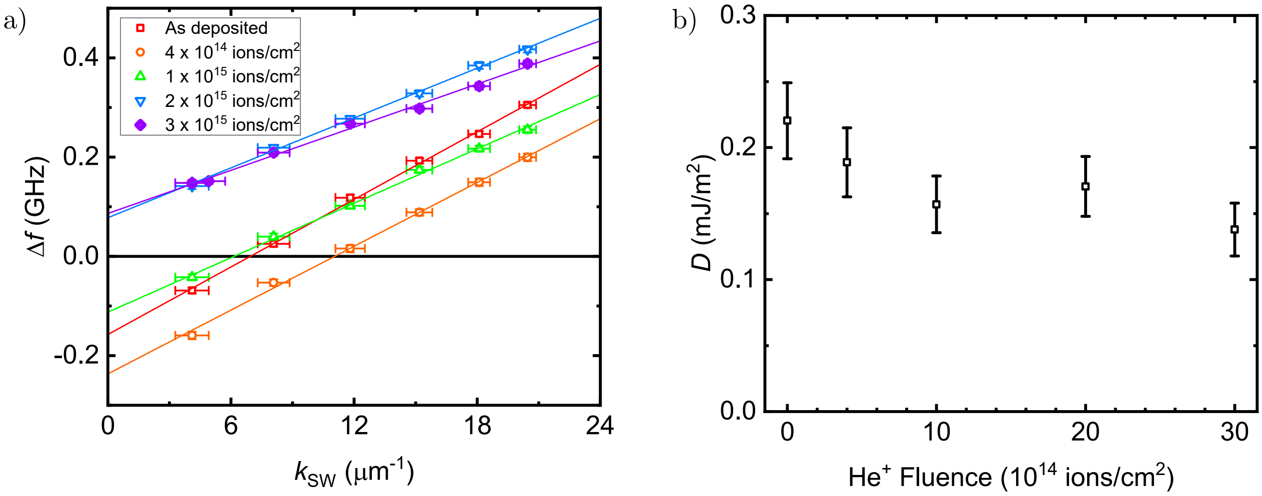

Fig. 4.4: BLS measurements of irradiated W/CoFeB/MgO | a) Frequency difference between the Stokes and Anti-Stokes peaks in the BLS spectra as a function of the probed spin-wave vector in the irradiated samples. The solid lines are fits with Eq. 1.49. b) DMI constant as a function of He$^+$ fluence as extracted from the data in (a).

weakly affected, this could explain why the sample retains its PMA for larger fluences. Another explanation for the reduced anisotropy is the migration of Fe atoms from the CoFeB/MgO interface, as observed in Ta/CoFeB/MgO under irradiation [174], although the effect on the DMI is unclear. Furthermore, the similarity between the observed decreases of $H_{K_{\text{eff}}}$ and D here and in Ref. [176] would suggest that Fe migration only plays a small role. ΔH_0 is often linked to the variation of $H_{K_{\text{eff}}}$ in the sample, but not much is known about the influence of interface intermixing on this parameter. Further detailed studies would be welcome to shed further light on this effect.

In the next section, we discuss how DW motion evolves with progressive He$^+$ irradiation, and we use the results from this section to further analyze the effect of irradiation on the microscopic DW-pinning parameters.

4.2.2 Domain wall motion

We study the field-driven motion of DWs in the progressively irradiated samples with polar Kerr microscopy. The DW velocity in each sample between fields of $\mu_0 H = 0.7$ mT and $\mu_0 H = 145$ mT is shown in Figure 4.5a. For all samples, we observe the different regimes; the creep regime at low fields, followed by a depinning transition at H_{dep} (indicated with gold stars) once the fields are large enough to overcome the DW pinning barrier. The velocity then reaches a plateau, related to 2D effects after the Walker breakdown (see Section 1.4), after which it enters the negative mobility regime which ends in the precessional regime. At the largest fields, we observe velocities that exponentially increase, away from the expected linear precessional motion. We relate this to increased nucleation effects throughout the sample, which interfere with the DW expansion. Figure 4.5b shows the DW velocity in the creep regime between 0.7 and 16 mT. The axes are rescaled to show creep-law behavior, which is observed for all samples. A zoom around the depinning transition is shown in the inset. One peculiarity is the change in slope close to the depinning transition, which is related to a change in DW roughness exponent [102]. It is unknown what is causing this effect, which in our data seems to reduce with increasing He$^+$ fluence, and further research would be required to understand it.

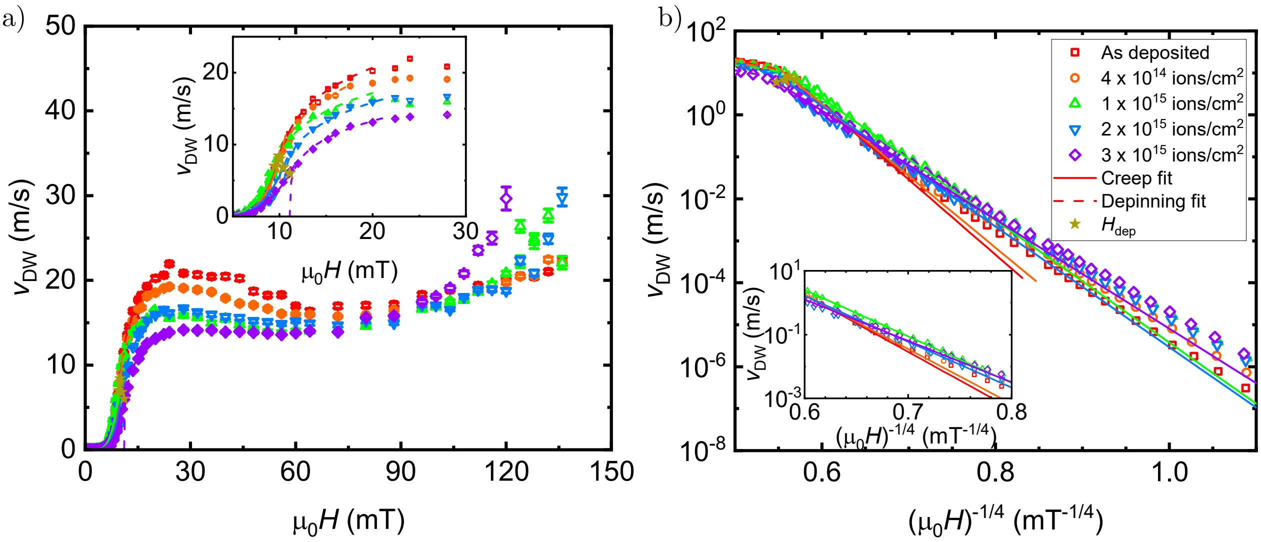

Fig. 4.5: Domain wall velocity in irradiated W/CoFeB/MgO | a) Full field driven DW velocity curve in W/CoFeB/MgO thin films progressively irradiated with He$^+$ ions. The inset shows a zoom that highlights the fits with the creep and depinning laws, shown with solid and dashed lines, respectively. The extracted depinning fields are shown with gold stars. b) Data of (a) with rescaled axes to show the creep-law behavior. Data shown between 0.7 and 16.0 mT. The inset contains a zoom of the depinning transition between 2.4 and 7.7 mT.

The effect of irradiation on the DW velocity in all regimes is clearly visible in Figure 4.5. Above the Walker breakdown and depinning transition (Fig. 4.5a), we observe a drop in the plateau velocity with increasing He$^+$ fluence. Furthermore, the apparent Slonczewski fields, corresponding to the end of the velocity plateau, seem to shift to lower values. At an irradiation fluence of 3 × 10^{15} ions/cm^2, the velocity plateau is no longer visible. For magnetic fields larger than the Slonczewski field and past the negative mobility regime, we observe indications of the beginning of the precessional regime, where the DW velocity changes negligibly with irradiation. Irradiation thus does not seem to have a strong impact on the precessional DW velocity in the range of fluences that we studied. We do observe that the nucleation threshold, identified by the exponential increase of the DW velocity in the precessional regime, is moved to lower fields, signaling that domain nucleation is enhanced with increased He$^+$ irradiation. In the creep regime (Fig. 4.5b), we see a progressive enhancement of the DW velocity at the lowest magnetic fields. At an irradiation fluence of 3×10^{15} ions/cm^2, the DW velocity is enhanced by almost two orders of magnitude at the lowest fields. This difference reduces at larger fields, as the slope of the creep velocity is decreased with increasing irradiation, signaling a change in the DW-pinning energy barrier by irradiation.

We now use the creep and depinning laws, given by Equations 1.38, 1.39, and 1.42, to analyze the evolution of the non-universal DW-motion parameters with He$^+$ irradiation by fitting them to our DW-motion data. These fits are represented in Figure 4.5 by solid and dashed lines for the creep and depinning law, respectively. Note that due to the observed change in slope close to the depinning transition, these fits are only valid close to the depinning field. The resulting values for H_{dep}, the depinning temperature T_{d}, and velocity at the depinning field $v\,(H_{\mathrm{dep}})$ are shown in Figures 4.6a, b, and c, respectively.

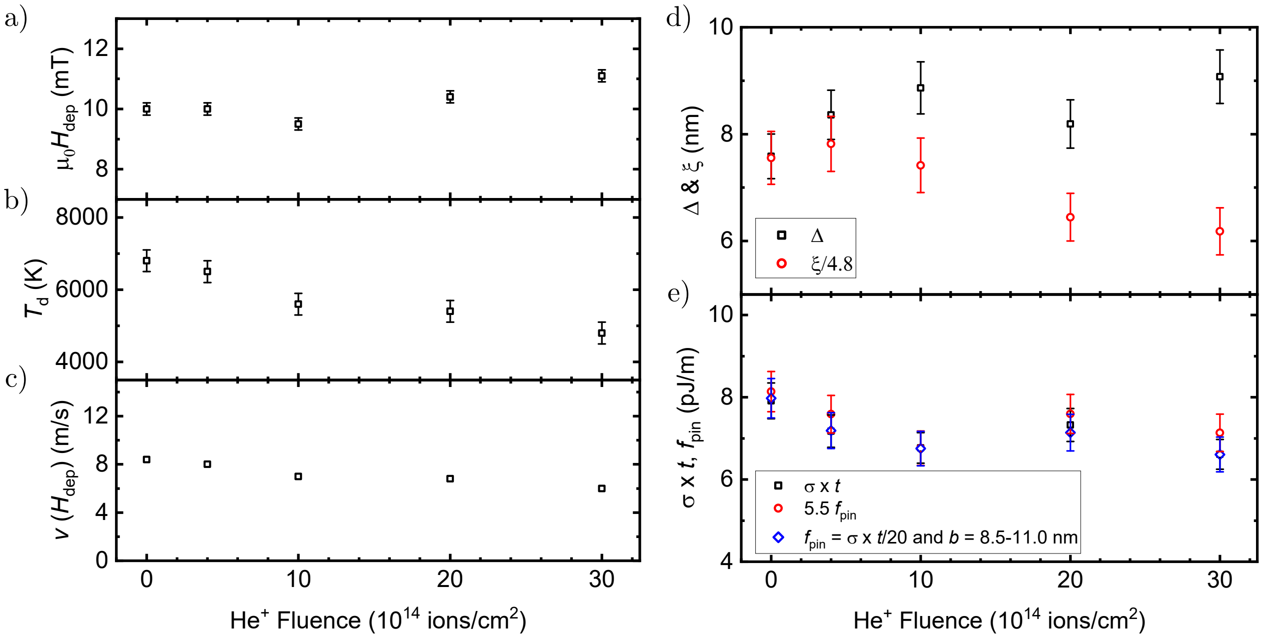

Fig. 4.6: Evolution of domain wall motion and pinning parameters with He$^+$ irradiation | a)-c) Evolution of the DW-motion parameters with progressive He$^+$ irradiation, extracted from the creep- and depinning- laws; a) Depinning field H_{dep}. b) Depinning temperature T_{d}. c) DW velocity at the depinning field $v\,(H_{\mathrm{dep}})$. d)-e) Evolution of the microscopic pinning parameters with progressive He$^+$ irradiation, extracted with the analytical model from Ref. [239].

From Figures 4.5a and c we observe only a weak effect of irradiation on H_{dep} and $v\,(H_{\mathrm{dep}})$. H_{dep} varies non-monotonically, decreasing slightly before increasing at higher fluences, but the change is limited to only a few mT. $v\,(H_{\mathrm{dep}})$ drops with increasing fluence, but not drastically. A stronger effect is seen in T_{d}, which drops monotonically with increasing fluence. Since T_{d} is linked to the creep energy barrier, this is a strong suggestion that irradiation reduces the energy barrier for DW motion in the creep regime.

To further analyze the effects of He$^+$ irradiation on the interaction between a DW and the microscopic pinning environment, we use the same analytical model we used in Section 3.2 [239]. For our calculations, we assume a constant $A = 15$ pJ/m [176]. We can then obtain the characteristic range ξ (nm) and strength f_{pin} (pJ/m) of the DW-defect interaction from Eqs. 3.1 and 3.2. We assume that the nominal thickness $t = 1.1$ nm of the magnetic layer does not change, since slight variations in dead layers are already taken into account in the M_{s} value. The value of b is based on the scaling between ξ, f_{pin}, Δ, and $\sigma \times t$ as proposed in Ref. [239], which are shown as a function of He$^+$ fluence in Figures 4.6d and e.

Figure 4.6d compares the evolution of ξ and Δ with increasing He$^+$ fluence. Rescaling ξ with an adjustable parameter ($\Delta = \xi/4.8$) shows overlap for the as-deposited sample, however Δ and

ξ diverge with increasing He$^+$ fluence. This divergence suggests that the DW pinning length-scale becomes less dependent on Δ with increasing He$^+$ fluence and that the distance between pinning sites b starts playing a larger role, although the effect is relatively small.

Figure 4.6e compares f_{pin} with $\sigma \times t$. In general, decent overlap is obtained in all samples for $\sigma \times t = 5.5 f_{\text{pin}}$ (shown in red), where the disorder is assumed to be the same for each sample. We can obtain an estimation of the variation of b with increasing He$^+$ fluence when setting $\sigma \times t = 20 f_{\text{pin}}$ for each sample, and rescaling using b (shown in blue). In this case, we find b in the range of 8.5-11.0 nm, which is close to the typical value of the grain size in textured CoFeB samples [248] and to the previously estimated grain size of similar W/CoFeB/MgO films as shown in Chapter 3. b does not significantly change with irradiation, which is a strong indication that RT He$^+$ irradiation does not significantly change the nanoscale disorder length scales.

4.2.3 Discussion and conclusion

Let us now discuss some of the phenomena that are most likely behind the observed changes in DW motion observed in the different regimes.

Below the depinning transition in the creep regime, only the creep energy barrier $k_B T_d$ is significantly affected by He$^+$ irradiation, while H_{dep} and the pinning length scales remain relatively stable. Since the transferred energy T to the lattice is very low due to the low mass of He$^+$ (see Chapter 2), no large change of the intrinsic disorder is expected at low irradiation temperatures. This is contrary to our results in Chapter 3, where the irradiation temperature is large enough to induce changes in the crystalline state. The observed changes in DW motion are thus likely driven by changes in the interface disorder and interfacial parameters. While the unchanged crystalline state can explain the constant defect density, a smoothed and reduced K_{eff} due to the interfacial mixing could help explain the reduction in creep energy barrier, as the pinning landscape becomes smoothened. A lower creep energy barrier would result in faster creep motion, especially at lower fields, since creep DW-motion is dominated by the lowest energy barriers [68]. A similar argument of interface smoothing was used in previous work on He$^+$ irradiation in W/CoFeB(0.6)/MgO [176] to explain a similar increase in creep velocity through the reduction of the creep energy barrier, although H_{dep} was found to decrease with irradiation, while here H_{dep} remains constant. In Ta/CoFeB/MgO, H_{dep} increases with irradiation, which could be explained through a change in the nanoscale disorder [174], however a similar analysis as performed here would be required to make any substantial conclusions. Comparing these results to our other work on Pt/Co/AlOx [261] suggests that the effect of He$^+$ irradiation might be heavily sample dependent. There, T_d is slightly increased with increasing fluence, while H_{dep} monotonically decreases. Irradiation also reduces the average distance between pinning sites, although here this could also be explained by an increase in domain wall width and thus a smoothed pinning interaction. It is clear that much remains unknown about the microscopic interactions between DWs and disorder, and in particular the effect that He$^+$ irradiation has on it. Unlike in the previous chapter, here, both the disorder and magnetic parameters vary simultaneously, meaning it is very difficult to separate the effects of ion irradiation on either property. A better understanding of the DW-defect interaction would also allow us to gain more insight into the evolution of H_{dep} with irradiation in the different systems.

Above the depinning transition, the changes in magnetic properties also play a role in the evolution of the DW motion. The reduction of the plateau velocity and the plateau length can be explained through the reduction of K_{eff} and D, as H_W and H_S depend on them (see Chapter 1). Given the weak effects of He$^+$ irradiation on the disorder, as evidenced by our results in the creep regime, it is not expected that the changes in disorder play a significant role on the observed changes of DW motion in the flow regime. Quantitative predictions about the correspondence of the reduction in the plateau velocity and length with the reduction in magnetic parameters cannot be made from our data, since we find $H_W \sim 1$ mT $< H_{\text{dep}}$ for all fluences, meaning the plateau is (partially) hidden by the depinning transition. After the negative mobility regime, we seem to observe regular precessional motion. However, when fitting the precessional DW velocity using Eq. 1.31 and using the values of Δ and γ_0 obtained with FMR, we obtain values of α that are two orders of magnitude too low (roughly $(70 \pm 1) \times 10^{-5}$) compared to values obtained with FMR (roughly $(20 \pm 1) \times 10^{-3}$). While values obtained from fitting with the precessional DW velocity are often larger than those obtained with FMR due to additional dissipation at defects [262], the difference here is too large and indicates that we might not have yet reached the full precessional motion. It is thus unclear what the full effect of He$^+$ irradiation is on the precessional DW motion, although even from the first indications in our data the effect seems to be small. The observed exponential increase of v_{DW} at the largest fields is then caused partly by nucleation events, which can also be explained by the reduction in K_{eff} with increasing He$^+$ fluence.

To conclude, we have shown that He$^+$ irradiation at room temperature decreases the effective anisotropy and DMI in W/CoFeB/MgO thin films through interface intermixing, while the bulk parameters are only slightly affected. This, in turn, has an effect on the DW motion in the creep and flow regimes. In the flow regime, the plateau velocity and length is reduced due to the reduction in D and K_{eff}, while the precessional regime remains mostly unaffected. In the creep regime, the pinning energy barrier is reduced with increasing irradiation, most likely due to the reduction in anisotropy and smoothing of interfaces, while the microscopic pinning parameters are also mostly unaffected. These results can help to further understand the interaction between nanoscale disorder and DW motion, specifically by investigating the link between the magnetic parameters and the microscopic pinning parameters. However, extended systematic studies are required to shed more light on the interaction between DWs and intrinsic disorder.

In the next section, we use the knowledge of the evolution of the sample properties with irradiation to locally manipulate the sample properties at the edges of microwires, which are expected to be able to counter-act the effect of extrinsic edge damages. Notably, we will show that by irradiation with large fluences, the interaction between DWs and edge defects can even be quenched.

4.3 Controlling extrinsic domain wall pinning in W/CoFeB/MgO wires with He$^+$ irradiation

We now shift our focus to the control of extrinsic defects with local He$^+$ irradiation. We will study both the effect of irradiation at the edges of micro-wires using a FIB, as well as the creation of magnetic patterns with significantly reduced edge pinning using magnetic planar patterning through a mask. To make both the micro-wires and the irradiation mask, we use a nanofabrication process based on UV lithography, which we discuss in more detail in the next section. Then we study the DW velocity with polar Kerr microscopy in both the sample containing wires with irradiated edges (Section 4.3.2), as well as the magnetic structures created with magnetic planar patterning through a mask (Section 4.2.

4.3.1 Nanofabrication process

The microwires masks were fabricated with a UV lithography process. A schematic overview of such a process is shown in Figures 4.7. Starting from our stack deposited on the substrate (Fig. 4.7a), we spin-coat a photosensitive resist AZ-5214 on top at 4000 RPM for 30 seconds with an acceleration of 2000 RPM (Fig. 4.7b). After baking the resist at 125°C for 60 seconds, the resist is locally exposed through a mask (black) to UV light for 14 seconds, which hardens the resist in the exposed area (Fig. 4.7c). The unexposed areas are then dissolved in a MIF-2026 developing agent for 50 seconds and rinsed with water, leaving only the area which was exposed to the UV light (Fig. 4.7d). The sample is subsequently cleaned in an oxygen plasma for 1 minute to reduce excess resist build-up at the edge. We then bombard the sample with 350 eV Ar$^+$ ions at an incidence of 20 degrees under continuous rotation for 200-300 seconds, which causes the material that is not protected by the mask to be etched down (Fig. 4.7e, see also Chapter 2 for more information on sputtering). The areas that are covered by a mask are protected, as the Ar$^+$ are stopped by the mask. The remaining mask is dissolved in remover PG at 80°C for up to 5h, leaving only the original stack material in the areas exposed with UV light (Fig. 4.7f).

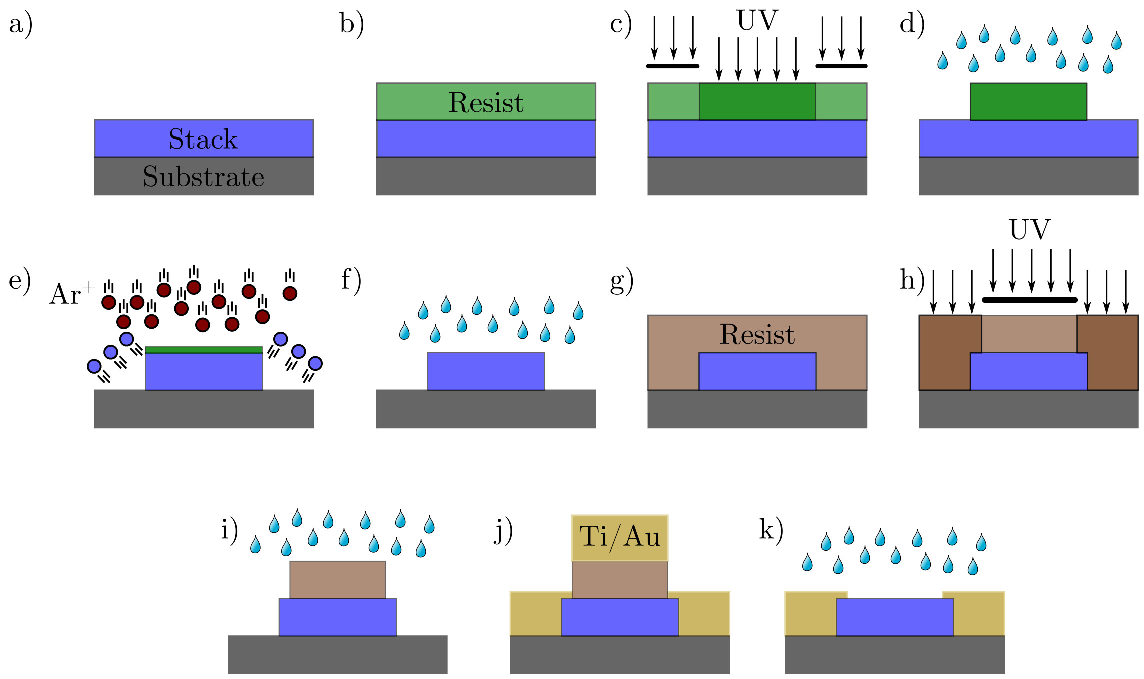

Fig. 4.7: Schematic of a nanofabrication process | a) Full film stack before nanofabrication. b) Spin-coating of resist (green). c) Local exposure of resist to UV. A mask (black) blocks the UV light in the areas that should not be exposed. d) Development of unexposed areas. e) Ar^+ ion beam etching (red), removing exposed material (blue). f) Dissolving of remaining resist. g) Spin-coating of resist (brown). h) Local exposure of resist to UV. i) Development of exposed areas. j) Ti/Au contact deposition. k) Lift-off of Ti/Au on top of resist, resulting in the final device.

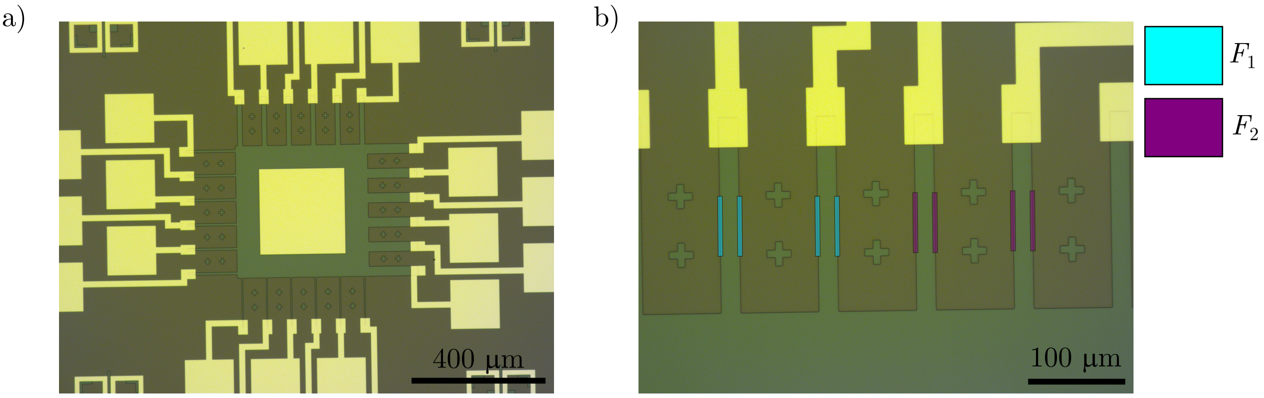

Fig. 4.8: Nanofabrication results and local ion irradiation | a) Microscopy image of a full device after the nanofabrication process. The Ti/Au contact pads are shown in gold, and the W/CoFeB/MgO magnetic reservoir and wires are shown in dark green/blue. b) Zoom in of wires with a width of 20 µm with schematic overlay of the local irradiation pattern with fluences F_1 (light blue) and F_2 (purple). The dimensions of the irradiated zones are 60 µm × 1 µm, centered on the wire edge. This means the actual irradiated zone at the edge of the wire has a width of 500 nm.

To allow for the application of current, a second lithography step is used, which is shown schematically in Figure 4.7g-k. Note that for the fabrication of the irradiation mask, we start the process here and no previous lithography is performed. The device is again covered in AZ-5214 resist by spin-coating (Fig. 4.7g) and subsequently exposed to UV light (Fig. 4.7h). AZ-5214 is a reversible resist, which is achieved by adding an additional baking step at 125°C for 60 seconds and a 30 second flood exposure to UV light without a mask after the initial exposure that defines the pattern. Upon development with MIF-2026 for 60 seconds and after rising with water (Fig. 4.7i), the exposed areas are now dissolved. The sample is again cleaned in an oxygen plasma for 1 minute, before Ti(20 nm)/Au(200 nm) contacts or an Al(500 nm) irradiation mask are deposited on the entire sample with electron beam evaporation (Fig. 4.7j). Dissolving the mask in acetone leaves behind the Ti/Au contacts only in the uncovered areas (Fig. 4.7k), resulting in the final device. The last stage is called a lift-off.

The resulting device from the above-described lithography process is showed in Figure 4.8a. The magnetic device from the first lithography sequence (Figs. 4.7a-f) is shown in green/blue, and the Ti/Au contacts from the second lithography sequence (Figs. 4.7g-k) are shown in gold. The device consists of a 500×500 µm^2 square, with six wires with varying widths coming from each side of the square. The wires have widths of 5, 10, 20, and 40 µm. Each device has four crosses in a square around the central device, which are used as alignment markers for the second lithography step. Crosses are placed in between the wires with a spacing of 60 µm (see also Figure 4.8b), which act as alignment markers for the FIB to increase the accuracy of the local irradiation.

4.3.2 Modulating edge pinning with local He$^+$ irradiation

We now study the DW edge pinning in microwires with- and without edge irradiation. We use Kerr microscopy to study the DW velocity and curvature in different parts of the device. We use a He$^+$ FIB to locally irradiate the edges of the microwires in between the FIB alignment markers, as shown in Figure 4.8b, which is a zoom-in around the wires with a width of 20 µm. Two irradiation fluences are investigated at 25 keV, $F_1 = 10^{15}$ ions/cm^2 and $F_2 = 5 \times 10^{16}$ ions/cm^2, shown in light blue and purple respectively. These fluences have been chosen to achieve two different scenarios. For F_1, the material in the irradiated zones retains PMA, albeit with reduced magnetic properties and enhanced DW motion. Here, it is expected that the increased DW velocity can (partly) compensate the edge pinning effects. For F_2, the magnetic phase of the irradiated zone is changed. We discussed the changes in magnetic properties and DW motion already in more detail in Section 4.2. The irradiation patterns have a length of 60 µm and a width of 1 µm, centered on the wire edge. This means that the actual irradiated zone at the edge of the wire has a width of 500 nm. For the un-irradiated wires, the results are shown in Figure 4.9.

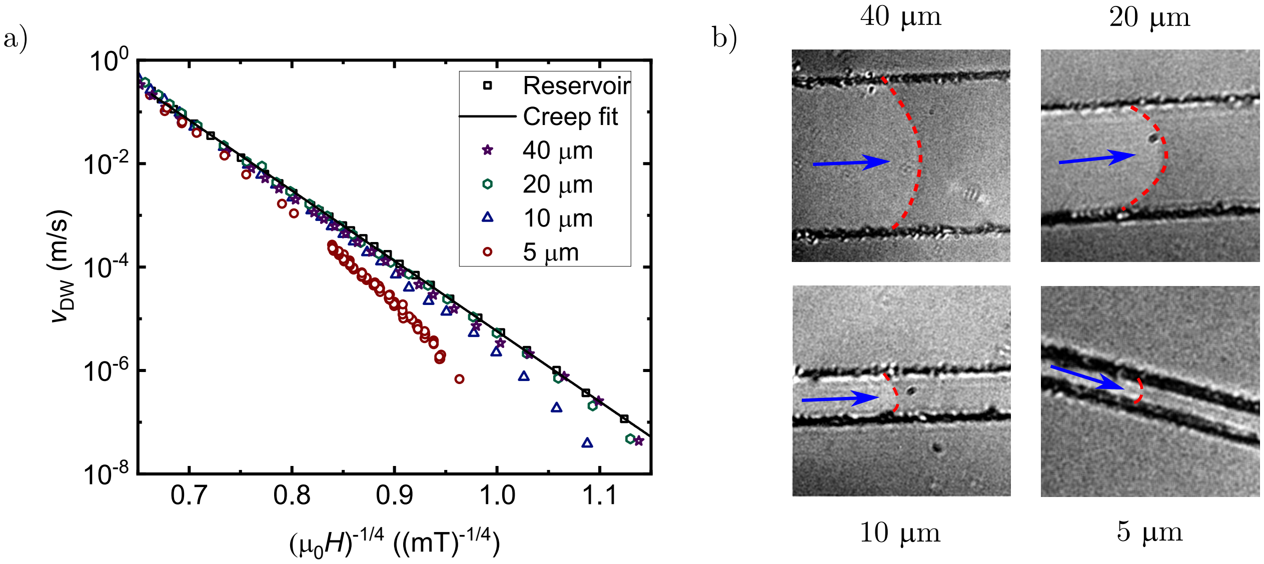

Fig. 4.9: Domain wall motion in unirradiated wires | a) DW velocity in W/CoFeB/MgO microwires with varying widths from 5 - 40 µm. Reservoir velocity mimics the expected full film velocity and creep dynamics. b) Kerr microscopy images of DWs in the microwires with varying widths. The DWs move from left to right (indicated with a blue arrow) under a field of 1.2 mT, and are indicated with a red dashed line.

Figure 4.9a shows the DW velocity as a function of the magnetic field in different areas of the device. The reservoir emulates the full film velocity, and follows creep-law behavior (Eqs. 1.38, 1.39). When progressively decreasing the width of the wire, a drop-off from creep behavior occurs at larger fields. The DW velocity in 40 µm and 20 µm wires still follows the creep behavior in the range of magnetic fields studied, but the DW velocity is strongly reduced at low fields in 10 µm and 5 µm wires. Figure 4.9b shows Kerr microscopy images of the DW shape in the microwires with different widths at a driving field of 1.2 mT. The DW moves from left to right (indicated with a blue arrow), and its position and shape is marked with a red dashed line. In all wires, the DW has a positively shaped curvature, with the DW lagging behind at the edges compared to the center due to the additional pinning at the edges. The curved shape of the DW, as well as the observed velocity drop-off and its dependence on the wire width are strong indications of edge pinning, even if the DW velocity in the wider wires is not impacted in the range of magnetic fields that were studied. It is also consistent with previous studies of DW edge pinning in microwires [219,260].

We now study the DW velocity and curvature in wires where the edges have been locally irradiated with He$^+$ ions. Figure 4.10 shows the DW velocity in the microwires with different widths and irradiated edges. Each figure shows the reservoir velocity and the velocity in the unirradiated wire as a reference. The data for reduced edges correspond to F_1, whereas magnetically dead edges correspond to F_2.

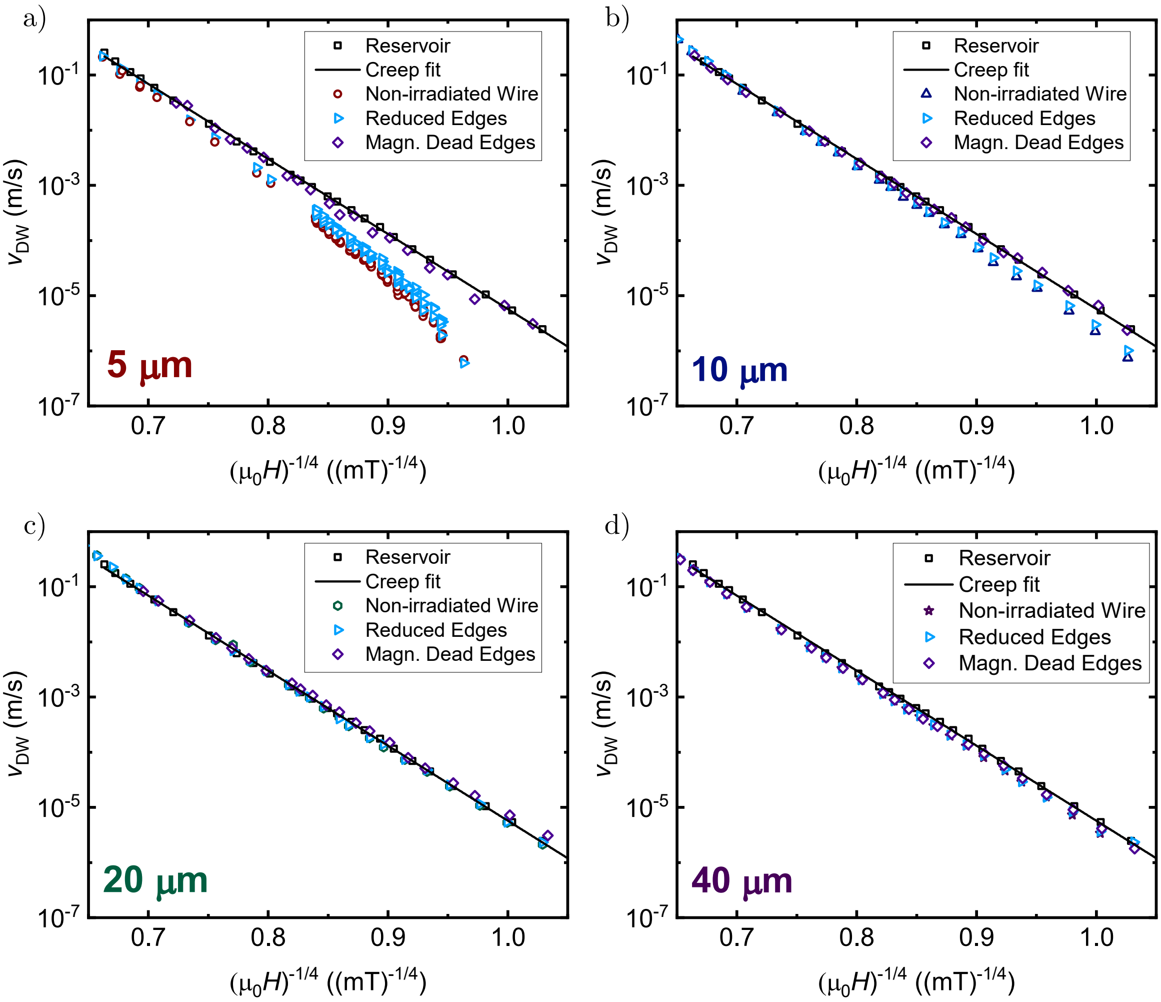

Fig. 4.10: Domain wall velocity in wires with irradiated edges | DW velocity in W/CoFeB/MgO microwires with irradiated edges. Data shown for wire widths of a) 5 µm. b) 10 µm. c) 20 µm. d) 40 µm. The reservoir velocity mimics the expected full film velocity and creep dynamics. Reduced edges correspond to edges irradiated with F_1. Magnetically dead edges corresponds to edges irradiated with F_2.

In the case of 5 µm wires (Fig. 4.10a), we do not observe a very significant increase in the velocity for wires with reduced edges. The velocity still shows a drop-off with respect to the expected creep behavior, although the velocity is about a factor 2 larger compared to the wire where the edges have not been irradiated. The drop-off from the creep law suggests that edge pinning still plays a large role, despite the slight increase of velocity. For wires with magnetically dead edges, we see a much larger effect. Indeed, the creep velocity is completely recovered and follows the creep law, at least in the range of fields that we study. Compared to the wire without edge irradiation, the velocity is increased by several orders of magnitude at the lowest fields.

The same effect for both irradiation fluences is also present in the 10 µm wire (Fig. 4.10b). Wires with reduced edges still show a drop in velocity at low magnetic fields, and wires with magnetically dead edges show a recovery of the creep behavior. In the 20 µm (Fig. 4.10c) and 40 µm wires (Fig. 4.10d), no significant change in the velocity is observed for any edge treatment. This is expected, as edge pinning did not significantly impact the velocity in these wires anyway (see Fig. 4.9).

Figure 4.11 shows Kerr microscopy images of DWs in wires with irradiated edges, with Figures 4.11a, b, c, and d showing images for wires with widths of 5, 10, 20, and 40 µm, respectively. The irradiation zones are indicated by colored bars, with the blue bar corresponding to irradiation fluence of F_1 and the purple bar corresponding to irradiation fluence F_2. The width of the colored bar is not to scale. The DW moves from left to right, as indicated by blue arrows. Its position and shape are indicated with a red dotted line.

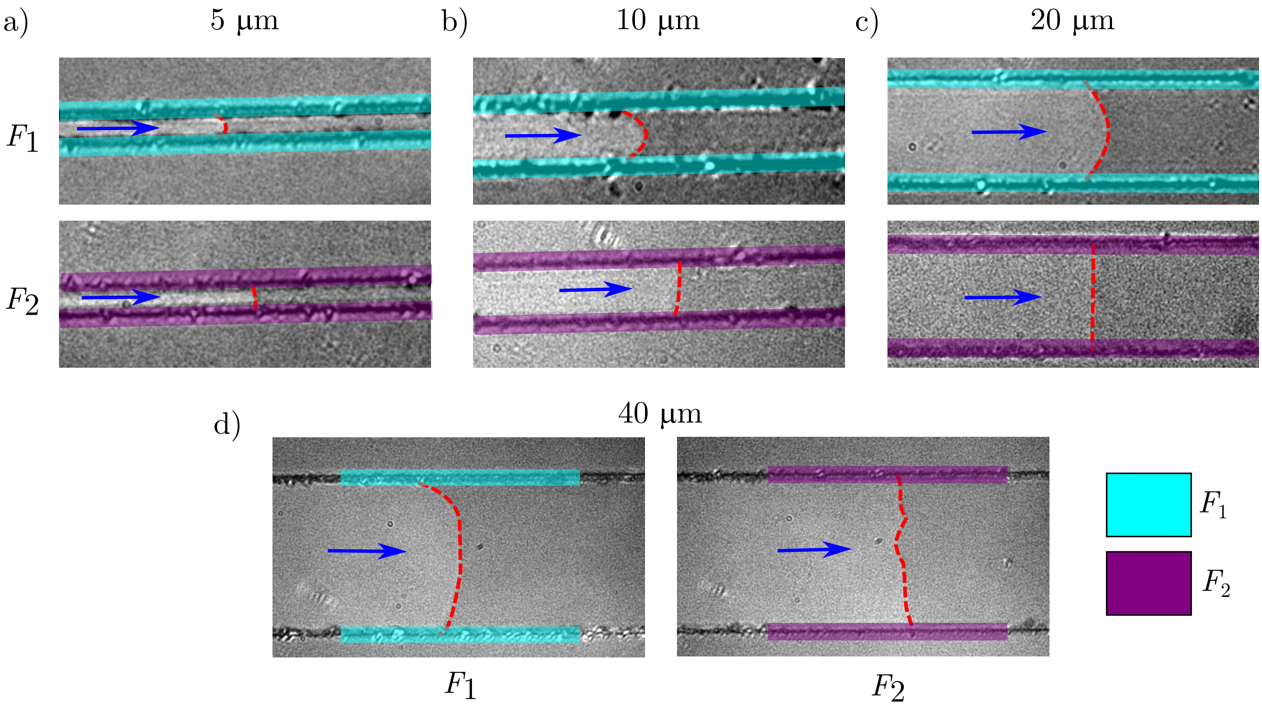

Fig. 4.11: Domain wall curvature in wires with irradiated edges | DW curvature in a 1.2 mT magnetic field in W/CoFeB/MgO microwires with irradiated edges. Data shown for wire widths of a) 5 µm. b) 10 µm. c) 20 µm. d) 40 µm. Colored bars show irradiated zone (not to scale), with light blue denoting F_1 and purple denoting F_2. The DW is identified with the red dashed line. Blue arrows show the direction in which the DW is moving.

For wires with reduced edges (light blue), we observe a positive DW curvature, with the edges lagging behind the center in all wires. We did not quantitatively study the curvature of the DW in the wires with reduced edges, and thus more statistical investigations are necessary to comment on a potential change in the curvature with respect to the unirradiated wires. Nonetheless, the positive DW curvature is another indication that edge pinning still plays a significant role in wires with reduced edges.

For wires with magnetically dead edges (purple), we observed a more-or-less flat DW in all wires.

The DW no longer lags behind at the edges, but instead travels at the same speed along its length. A flat DW and the recovery of the creep law dynamics in the wires with magnetically dead edges are a strong indication that edge pinning no longer plays a role. The effect is also visible in thicker wires, where the velocity was not changed by edge pinning in the range of magnetic fields probed in this study, indicating that we also change edge effects in the larger wires.

4.3.3 Modulating edge pinning with magnetic planar patterning

In the previous section we have seen that local irradiation can significantly impact DW edge pinning. In this section, we show that structures with significantly reduced edge pinning can easily be created with magnetic planar patterning.

We create the same structure as in Section 4.3.2, but instead of lithography we now employ magnetic planar patterning through a 500-nm thick Al mask. The sample is subsequently irradiated with 15 keV He$^+$ ions at F_2, at an incidence angle of 7° from the sample normal. The irradiations have been performed with a Helium-S$^{\mathrm{TM}}$ implantation machine from Spin-Ion Technologies [25]. This results in an average lateral resolution of roughly 50-75 nm. For more information about the fabrication process of the mask, see Section 4.3.1. After the process, only the structure covered by the mask is ferromagnetic (FM), the rest shows paramagnetic (PM) behavior. We then study DW motion in the FM pattern. The results are shown in Figure 4.12.

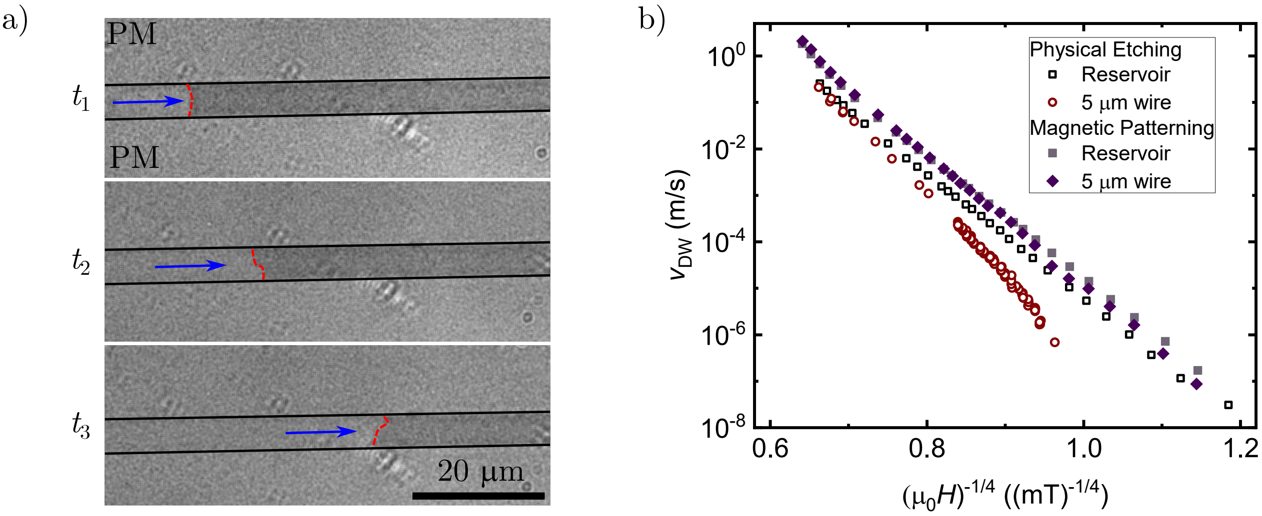

Fig. 4.12: Domain wall motion in a patterned microwire | a) Kerr microscopy images of a DW moving through a 5 µm wide FM wire (indicated with black lines) in a PM environment created with magnetic planar patterning. The position of the DW is shown for three different moments in time $t_1 < t_2 < t_3$ and is indicated with a red dashed line. The DW moves from left to right at an applied field of 1.0 mT, with the direction of motion indicated by the blue arrow. b) DW velocity as a function of magnetic field in the case of an etched device (open symbols, see also Figure 4.10) and in the case of magnetic planar patterning (closed symbols). The reservoir velocity mimics the expected full film velocity and creep dynamics.

Figure 4.12a shows a series of frames of a DW moving at 1.0 mT through a 5 µm wire, indicated with black lines, at three different times $t_1 < t_2 < t_3$. The DW moves from left to right (indicated by the blue arrow), and its position and shape are marked with a red dotted line. During the propagation of the DW through the wire, it does not show a steady shape; the DW is not consistently lagging behind at the edges, nor is it completely flat. This is expected, as the images do not show the DW in a relaxed state because of the presence of the magnetic field. However, the inconsistent DW shape during the propagation is an indication that edge pinning is not very strong in the wire.

Figure 4.12b shows the velocity of the DW in the pattern (closed symbols) versus the velocity of the DW in an etched wire (open symbols, as in Figure 4.10a). The reservoir again emulates the full film domain wall dynamics. We observe that, at low fields, the DW moving in the patterned 5 µm wire is significantly faster compared to the etched wire. Furthermore, it does not show a significant drop-off from the expected creep behavior, as is observed for the etched wire. Only a slight drop-off is observed at 0.96 mT$^{-1/4}$ (1.2 mT), but it is much less significant than the drop-off observed in the equivalent etched wire. The absence of a strong velocity drop-off and the more-or-less flat DW shape are strong indications that the patterned wires do not experience significant edge pinning.

4.3.4 Discussion and conclusion

It is worth discussing the two different fluence dependent effects that are at play in the wires with irradiated edges. As also discussed in more detail in Chapter 3, the material remains in the FM state after irradiation with F_1, while the material becomes PM, or magnetically dead, after irradiation with F_2. Hence, the interaction of the DW with the edge defects shows different effects.

In the reduced case, the DW is still allowed to exist in the irradiated zone. It thus still interacts with the edge defects, and has altered dynamics in the irradiated zone due to the changes in magnetic properties; the lower anisotropy in the irradiated zone causes the DW to move faster (see Chapter 3). If a DW moves faster at the edges compared to the center, it could even pull the DW forward. This has been observed before by Bernand-Mantel *et al.* [263] in Pt/Co/AlOx, where parts of the sample have altered magnetic properties through changes in oxidation at the Co/AlOx interface. In our wires, the effect of the edge roughness acts as a countering force to faster DW dynamics in the irradiated zone. It is unclear what happens exactly in this boundary, and more detailed studies are required to get a better idea of the physics at the edge. This could be achieved experimentally by studying a larger range of fluences to progressively change the balance between enhanced DW dynamics and edge roughness. Another irradiation parameter that can be tuned is the characteristics of the irradiation zone, such as width and shape. Furthermore, since the curvature of the DW can unlock more information about the dynamics in this zone [219], detailed statistical studies of the DW curvature in these wires, e.g. as performed in Ref. [260], could shed more light on the physics as well. Lastly, micromagnetic simulations could also aid in getting a better understanding of what is happening on this zone.

In the case of PM edges, the DW is not allowed to exist in the irradiated zone. The DW cannot interact with the physical edge roughness, which results in the recovery of the expected creep dynamics, as the intrinsic material disorder dominates the DW motion. In effect, wires with PM edges have a reduced wire width from the point of view of the DW. The roughness at the edges of these wires is now dependent on the resolution of the irradiation technique. The resolution of a FIB is smaller than the typical DW width, meaning that an almost perfect wire can be defined using the FIB. Due to the polycrystallinity of the sample, the grain size at the edges of the wire should play a role in the minimum roughness that can be achieved. If we assume that the grain stays intact after irradiation, which is likely as we used He$^+$ here, the roughness could be limited by the average grain size, i.e. roughly 10 nm in ultra-thin films [248]. To shine light on this issue, high resolution studies of the grains at the edges of the irradiated wire need to be performed. Nonetheless, even in the case where the roughness is limited by the grains, it is still a factor 20 lower than the typical UV lithography roughness - roughly 200 nm [219] - and thus it is still expected that the edge pinning plays a significantly lower role in the DW pinning.

When creating patterns with magnetic planar patterning, the roughness at the edges is larger due to the lower resolution of the technique compared to FIB. The resolution is dependent on the mask, which itself is created by a UV lithography process. Thinner parts of the mask would allow partial irradiation of the sample, and thus smooth the boundary between FM and PM regions. This smoothing is not on the same scale as the mask roughness though, as straggling in the mask can change the ion trajectory and thus reduce the lateral roughness resolution. In the case of the experiments in this chapter, it is expected to be in the range of 50-75 nm, which is also lower than the typical UV lithography roughness. Improvements to the resolution with our mask can be made by irradiating with a normal incidence compared to the irradiations at 7° performed here - which can introduce some shading - and by choosing a denser mask material to limit the height. Furthermore, higher resolution lithography techniques, such as electron beam lithography, can be used to define a sharper mask.

One can ask questions about the similarity of the pinning mechanisms at physical roughness and gradients in magnetic parameters due to irradiation at the edges. Furthermore, in each individual case, it is not well known what exactly drives the DW pinning effect. In the case of physical roughness, it is expected that the DW pinning is related to the fact that the DW has to change its length as it move through the wire, which changes its energy. For reduced edge roughness, the change in length is also reduced. Another effect that plays a role is that the physical roughness can reduce the magnetic properties at the edge. Some parts of the edges could be magnetically dead or have a strongly reduced magnetization, while others remain more-or-less unaffected. This would also introduce pinning effects for the DW. In the case of gradients in magnetic properties at the edge due to irradiation through a mask, the roughness of the mask is partly smoothed due to the ions straggling in the mask. This would create much smaller changes in width of the DW as it travels between FM, partly FM, and PM edge states. To confirm this however, more research into the physical mechanisms of edge pinning is required.

Nonetheless, we only observe a small velocity drop off and no significant DW curvature in structures created by magnetic planar patterning. Evidence for the latter was already observed in the first work on magnetic patterning in 1998 [24], although DW motion and curvature was never fully studied in these systems. In this work, we comprehensively show that the creep DW velocity is significantly improved when employing magnetic patterning and irradiation, unlocking new ways in the design of spintronic devices based on DW motion.

A possible issue with magnetic planar patterning that is worth mentioning is the integration of magnetic planar patterning with techniques based on current driven DW motion. If the irradiated material is still conductive, problems arise when trying to direct current through the patterned structures. A solution to this problem is to not employ magnetic planar patterning as the sole technique to create structures, but to use it as a corrective technique - i.e. an additional step in the lithography process - to create wires without edge effects where DWs can still be driven by current.

In conclusion, we show that we can reduce, and even quench, DW-edge pinning in W/CoFeB/MgO microwires with both local irradiation at the edges of the wire using a FIB and by employing magnetic planar patterning through a mask. For wires with irradiated edges, the effect on the DW motion is dependent on the irradiation fluence. For intermediate fluence, where the material remains perpendicular in the irradiated zone, the DW velocity is increased only by a small amount. The DW still experiences edge pinning, as evidenced by the curved DW shape in the irradiated zone. For large fluence, where the material becomes PM in the irradiated zone, the DW velocity is increased significantly at lower fields, and no longer shows a drop-off from the expected creep behavior. Furthermore, the DW shape is no longer curved in the irradiated zone, pointing to an absence of significant reduction of the edge pinning. A similar strong reduction of edge pinning is observed when employing magnetic planar patterning through a mask. As the DW moves through the FM wire, it does not show any curvature at the FM-PM boundary, and its velocity follows the expected creep behavior. Our results show that irradiation is an effective tool to correct edge effects, either locally through the use of a FIB, or by employing magnetic planar patterning. Not only are our results relevant for the optimization of DW based devices, the local tuning of edge pinning could be exploited in the design of pinning landscapes in DW-motion based devices. Moreover, it is expected that other forms of magnetic edge damages, such as in MTJ pillars for use in MRAM, can be easily corrected when employing ion irradiation, making it relevant for a larger application in the design of spintronic devices.

4.4 Summary

In this chapter, we discuss the effects of He$^+$ irradiation at RT on the magnetic properties and disorder of pre-crystallized W/CoFeB/MgO ultra-thin films, with a particular focus on the optimization of DW motion. We first show that RT He$^+$ irradiation results in a reduction of K_{eff} and D due to interface intermixing, which increases the DW velocity in the creep regime and reduces the plateau velocity in the flow regime. From an analytical model, we also show that the DW pinning at intrinsic defects is not significantly affected. We then show that RT He$^+$ irradiation significantly affects extrinsic defects, where we observe a massive improvement of creep DW velocity in wires with irradiated edges due to the absence of extrinsic pinning. Moreover, by employing magnetic planar patterning through a mask, we define a structure with significantly reduced edge pinning due to the absence of strong extrinsic defects.

He$^+$ irradiation at RT is not only a useful tool to tailor conventional interfacial magnetic properties, such as K_{eff} and D, but also more exotic effects that are interface dependent. In the next chapter, we will discuss results from several collaborations that show that the all-optical switching of magnetization in a Co/Gd artificial ferrimagnet and the magneto-elastic properties of a Ni/Fe multilayer can be efficiently tuned with He$^+$ irradiation, paving the way for the use of He$^+$ irradiation in novel applications.

Chapter 5

Application of ion irradiation to various magnetic phenomena

> *One irradiation a day, keeps the doctor away.*
> Giovanni Masciocchi

Throughout this thesis we show that He^+ irradiation can be used to effectively tune the magnetic properties of conventional W/CoFeB/MgO ultra-thin films through the manipulation of the interfaces, as well as the crystallization when irradiated at moderate temperatures. We focus mostly on conventional magnetic properties, such as anisotropy or DMI. However, as also mentioned in Section 2.4, other magnetic effects based on interfacial effects should also be susceptible to ion irradiation. In this chapter, we provide a study into two such effects. In Section 5.1, we show that the all-optical switching (AOS) of a Co/Gd artificial ferrimagnet can be tuned with He^+ irradiation. In Section 5.2, we show that the magneto-elasticiy of Ni/Fe multilayers can be quenched and even made to change sign with He^+ irradiation. The results shown in this chapter are based on collaborations with the Eindhoven University of Technology, published in Ref. [189], and with Sensitec GmbH, published in Ref. [190].

5.1 Enhancing all-optical switching of magnetization by He^+ ion irradiation

In this section, we explore the use of He^+ irradiation to enhance the all-optical switchting (AOS) of magnetization by a single femtosecond laser pulse in Co/Gd based synthetic ferrimagnets, which is one of the fastest magnetization switching processes that exist today [264,265]. The intermixing of the Co and Gd layers by He^+ irradiation is both numerically and experimentally investigated. We study the threshold fluence of AOS as a function of the He^+ fluence. We find that the AOS threshold fluence can be reduced by almost 30%. These results reveal that AOS can be accurately controlled by He^+ irradiation, which opens up new possibilities for AOS engineering.

5.1.1 Introduction: Enhancing all-optical switching by interface engineering

Single pulse AOS of the magnetization in 3d-4f ferrimagnets is one of the fastest and least dissipative ways of magnetization switching [264,266–269]. This mechanism not only offers means for ultrafast memory operations, but also allows for integration between photonics and spintronics [266,270], for which 3d-4f ferrimagnets are excellent materials [271]. Initially observed in a 3d-4f alloy [268], it was recently found that Co/Gd bilayer-based synthetic ferrimagnets [272,273] also exhibit AOS properties in the ps switching scale [274,275], with low switching threshold laser fluence [272,276,277]. Moreover, its high process tolerance [278] gives rise to an AOS-switchable MTJ with high TMR [275].

A unique advantage of the Co/Gd material platform is that the presence of AOS does not depend on the Co and Gd compositions [279], unlike in GdFeCo alloys [268] and $[\mathrm{Co/Tb}]_\mathrm{n}$ multilayers [280], where only a narrow composition window of ±2% results in AOS. This restriction is a result of the AOS reversal mechanism (more details can be found in Refs. [279,281]). Uniquely, the AOS in Co/Gd is not driven by the bulk, but instead by the Co/Gd interface, allowing us to exploit this degree of freedom when engineering AOS.

One of the methods to utilize this degree of freedom is exploring the intermixing at the Co and Gd interface [187,278]. It was found that the threshold laser fluence of AOS can be largely reduced when the sharp interface between Co and Gd is replaced by a very thin layer of CoGd alloy. Compared to the pure interface, the switching mechanism remains the same; however, the initial switching at the interface region requires less energy. As He^+ irradiation can induce interface intermixing, it is expected that AOS can be controlled by irradiation-induced interface intermixing.

In this work, we study the effect of He^+ irradiation on the AOS of a Co/Gd bilayer-based synthetic ferrimagnet. In Section 5.1.2, we first present the physical evidence of the layer intermixing as a result of He^+ irradiation, as well as the resulting change in magneto-static properties. In Section 5.1.3, we subsequently show experimentally that the AOS laser threshold fluence is reduced by almost 30% following irradiation.

5.1.2 He^+ irradiation induced mixing in Co/Gd bilayers

We study a Ta(4)/Pt(4)/Co(1)/Gd(3)/TaN(4) (thickness in nm) thin film stack, deposited on a $\mathrm{Si/SiO_2(100)}$ substrate using DC magnetron sputtering at a base pressure of 10^{-9} mbar. A detailed description of the magneto-static properties of these materials can be found in Ref. [272]. The samples are subsequently irradiated with 15 keV He^+ ions with fluences up to 5×10^{15} ions/cm^2.

Physical evidence of the induced intermixing is shown in Figure 5.1a, which shows a bright field scanning transmission electron microscopy (STEM) image of cross-sections of the as-deposited sample and a sample irradiated with 5×10^{15} ions/cm^2. STEM is a technique that uses the transmission of high energy electrons through a thin sample to obtain atomic resolution microscopy images [282]. The Pt/Co and Co/Gd interfaces (indicated with a white box) in the as-deposited sample are well separated, as found in comparable transition-metal/Gd interfaces [283,284]. A darker region on top of Pt and Gd can be observed (indicated by the dashed line in the white box) in the irradiated sample as a result of intermixing at the Pt/Co, Co/Gd, and Gd/TaN interfaces. Further evidence can extracted from quantified energy dispersive X-ray analysis (EDX) measurements, which use the generation of element characteristic X-rays from the scattering of a high-energy electron beam to obtain a compositional profile [282]. Elemental mappings obtained with EDX for the as-deposited sample and the sample irradiated with 5×10^{15} ions/cm^2 are shown in Figure 5.1b. The elements in the irradiated sample clearly have a broadened elemental distribution with respect to the thickness, which qualitatively indicates intermixing.

We further investigate the magneto-static properties of the samples as a function of He^+ irradiation. Figure 5.1c shows hysteresis loops of the irradiated samples, which are obtained with polar MOKE at a fixed scanning speed of 20 mT/s. We observe square hysteresis loops for the as-deposited and all irradiated samples. The shape of the hysteresis loop itself does not change, which indicates that all samples show PMA. The coercive field drops with increasing He^+ fluence, which is associated to the reduction of PMA caused by intermixing at the Pt/Co interface. We can quantify the change in interfacial anisotropy as a function of He^+ fluence with in-plane SQUID-VSM measurements. The results are shown in Figure 5.1d. We observe a decrease of the anisotropy with increasing He^+ fluence, which, while showing a similar trend to other ferromagnetic material systems [174,176], is much stronger. This can be attributed to the lowered magnetic moment of the intermixed Co-Gd.

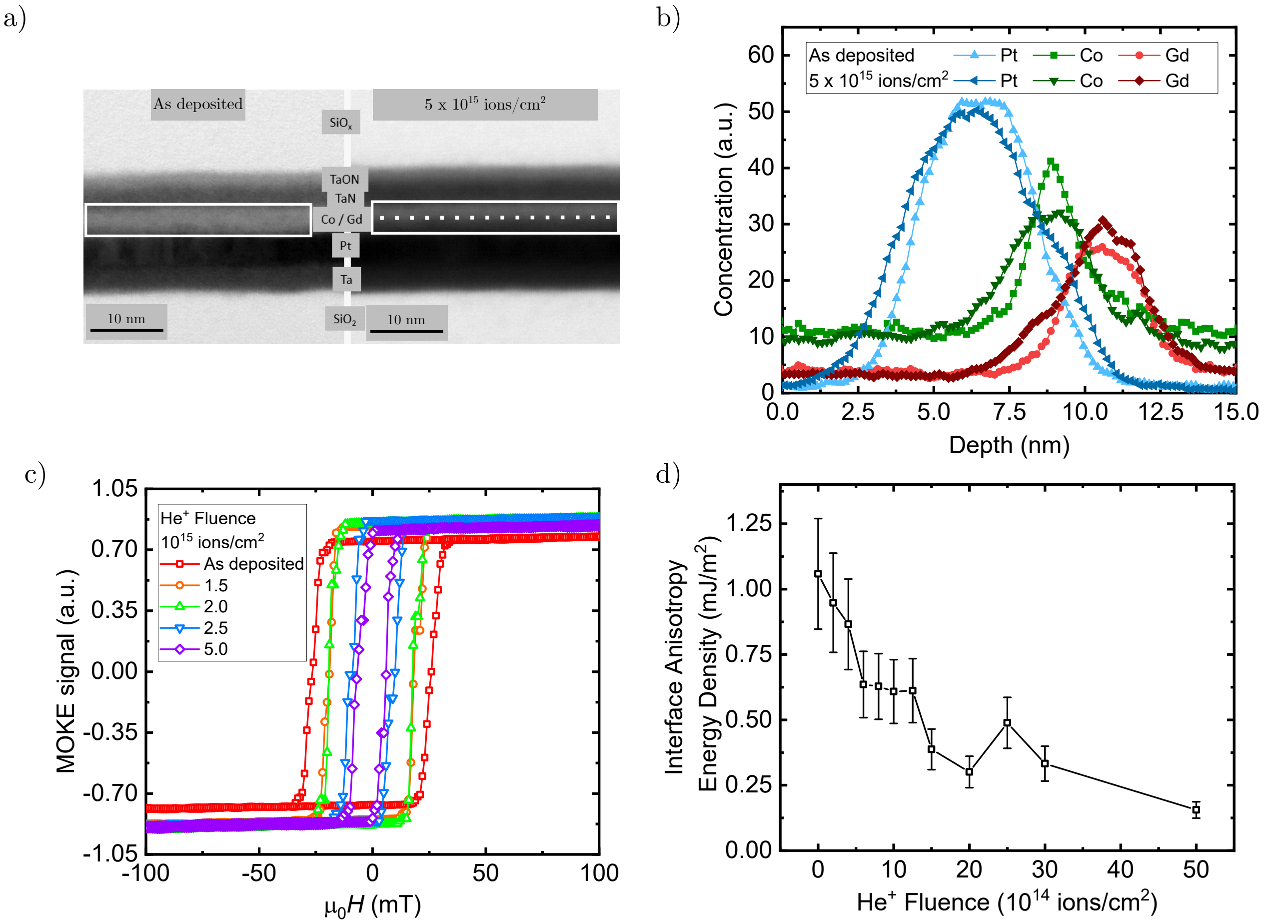

Fig. 5.1: He$^+$ irradiation in Co/Gd | a) Cross-section TEM image of the as-deposited sample and the sample treated with 5 × 10^{15} ions/cm^2. The scale bar as well as the label for each layer is marked in the figure. b) Depth profile of the elemental mapping (Pt, Co, and Gd) from EDX measurements for both the as-deposited sample and the irradiated sample with a fluence of 5 × 10^{15} ions/cm^2. c) Hysteresis loops, obtained with polar MOKE at the same field scanning speed, for samples irradiated with varying fluences of He$^+$ ions. d) The surface anisotropy energy density as a function of He$^+$ fluence, characterized with VSM-SQUID measurements in the hard-axis direction.

5.1.3 He$^+$ irradiation and all-optical switching

Next, we theoretically and experimentally investigate the effects of the induced intermixing on AOS. As an input for the intermixing, we numerically simulate the intermixing for different He$^+$ fluences using TRIDYN [285] (similar to the SRIM simulation package, see Chapter 2). A zoom in of the simulated intermixing near the Pt/Co/Gd interfaces is shown in Figure 5.2a. We observe progressive mixing of the interfaces with increasing He$^+$ fluence. These elemental profiles are then used as input in a theoretical model for AOS (the microscopic 3-temperature model, M3TM [286]). The Pt atoms are modelled as magnetically dead components, which do not significantly alter the AOS-ability nor the switching dynamics, as these are governed mostly by the Co/Gd interface. We extract the AOS threshold energy from the model, which is shown in Figure 5.2b. We see a monotonic decrease of the AOS threshold energy as the pristine Co/Gd interface is gradually replaced by a CoGdPt alloy with increasing intermixing.

Experimentally, we characterize the AOS threshold fluence of the as-deposited and irradiated samples. We adopt the same approach as in Ref. [272]. We illuminate the sample with a single ∼100 fs-laser pulse with various pulse energies and image the reversed domain using polar Kerr microscopy. Some examples are shown in Figure 5.2c, from which the threshold laser fluence is obtained by fitting the switched area as a function of the laser pulse energy. These results are plotted in Figure 5.2d. We find that the AOS threshold fluence reduces monotonically with increasing He$^+$ fluence at first,

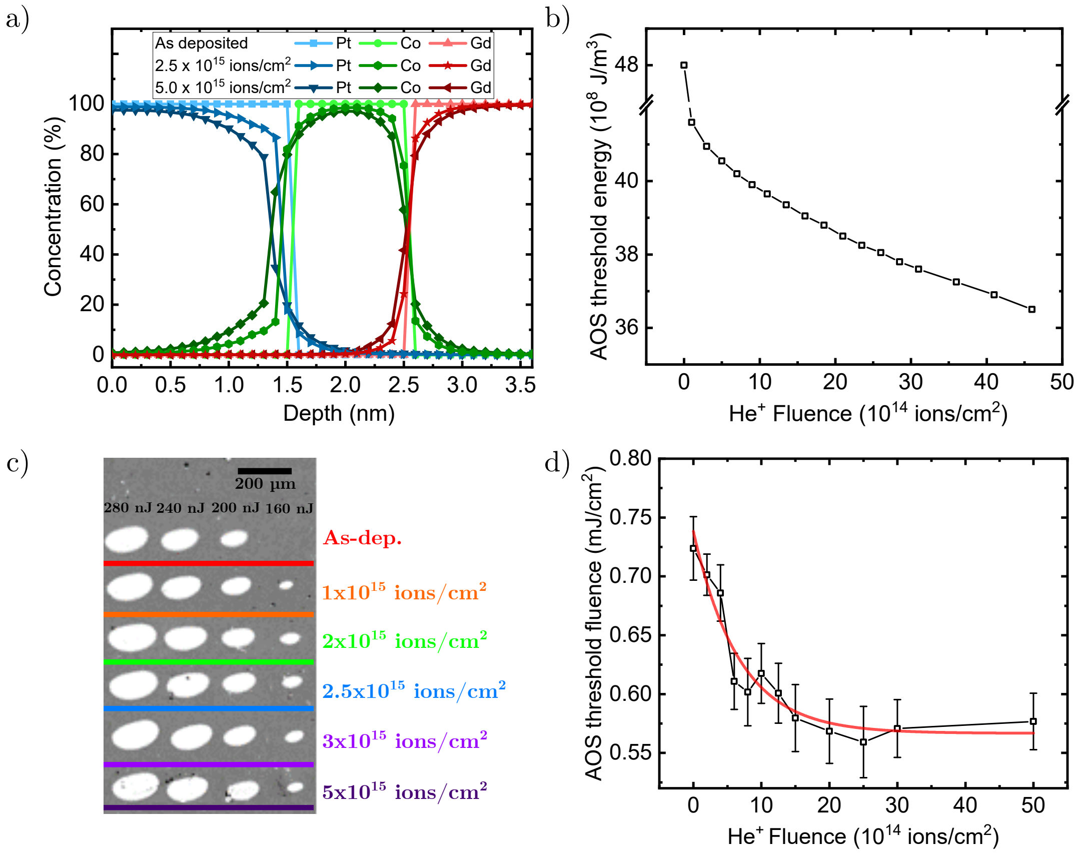

Fig. 5.2: He$^+$ irradiation and AOS | a) Depth profiles of the concentration of Pt, Co, and Gd, for various irradaition fluences, which are obtained from TRIDYN simulations. Note: the depth axis is relative with respect to the Pt/Co and Co/Gd interfaces. b) Simulated AOS threshold energy of Co/Gd as a function of the irradiation fluence, obtained through the TRIDYN concentration profile. c) Example Kerr microscopy images of domains for samples with different irradiation fluences, created by a single linearly polarized laser pulse of different pulse energies. d) AOS threshold fluences measurements of Pt/Co/Gd thin films irradiated with different He$^+$ fluences. The red curve is a guide to the eye.

followed by a saturation at large fluences. The AOS threshold fluence is reduced by as much as 30% for irradiation fluences below 2.5×10^{15} ions/cm^2. The qualitative trend of the AOS threshold fluence matches the theoretical predictions. Unraveling the origin of the saturation of the AOS threshold fluence with respect to the irradiation fluence is beyond the scope of this work.

5.1.4 Discussion and conclusion

In summary, we explore the use of He$^+$ irradiation to enhance AOS through the intermixing between the Co and Gd. We present the physical evidence of this intermixing as well as its effect on static magnetic properties. We show square hysteresis is maintained upon He$^+$ irradiation, while the anisotropy reduces monotonically. We theoretically predict the reduction of AOS threshold fluence upon intermixing. We verify experimentally that He$^+$ irradiation leads to a 30% reduction in threshold fluence, paving the way for local control of AOS.

5.2 Control of magneto-elastic coupling in Ni/Fe multilayers using He^+ ion irradiation

In this section, we report the effect of post-growth He^+ irradiation on the magneto-elastic properties of a Ni/Fe multi-layered stack. The progressive intermixing caused by He^+ irradiation at the interfaces of the multilayer allows us to tune the saturation magnetostriction value with increasing He^+ fluences and even to induce a reversal of the sign of the magnetostrictive effect. Additionally, we identify the critical fluence at which the absolute value of the magnetostriction is dramatically reduced. Therefore, insensitivity to strain of the magnetic stack is nearly reached after irradiation, as required for many sensor applications. All the above-mentioned effects are attributed to the combination of the negative saturation magnetostriction of sputtered Ni and Fe layers and the positive magnetostriction of the Ni_xFe_{1-x} alloy at the intermixed interfaces, whose contribution is gradually increased with irradiation. The possibility to locally tune the magnetostriction allows for new types of spintronic devices with locally varying magnetoelastic properties.

5.2.1 Introduction: Control of magnetoelasticity in Ni/Fe multilayers

The magnetoelastic properties of thin films, i.e. how the magnetic state behaves when strain is applied to the material itself, are of major interest for technological applications. The requirements for the magnetoelastic coefficient λ_s strongly depend on the application. For example, magnetic sensors often need strain immunity [287], i.e. zero magnetostriction, to reduce its strain sensitivity, while actuators require giant strain effects, achieved in materials such as $TbFe_2$ (terfenol) [288]. One way to obtain the optimal magnetostriction for a specific application is to use the combination of two or more materials with different magnetic and magnetoelastic properties in a multilayer fashion. Multilayer systems have been widely studied, exploiting the combination of different λ_s to achieve a target magnetostriction [188,289–291]. In these studies, intermixing at the multilayer interfaces has been identified to severely influence the total magnetostriction, and this interface magnetostriction has been exploited to engineer the total magnetoelastic coupling of the multilayer [188,289]. In sputtered films, where interface mixing naturally occurs, Nagai *et al.* [188] were able to change the sign of the magnetostriction of a multilayer stack by changing the relative thickness of the layers. However, a clear limit to this approach is the lack of control of the interlayer roughness and degree of intermixing. The latter is fixed by the deposition conditions. This imposes limitations to the usability of this method, as the magnetostriction can neither arbitrarily nor locally be changed.

These limitations can be resolved with ion irradiation, as this technique allows for precise control of interface mixing. Previous work [292] reported a change in the magnetostriction of $TbFe_2$/Co after irradiation with 700 MeV Pb ions. However, the use of high energy heavy ions is harmful to thin magnetic layers, as their structural properties can easily be degraded. Additionally, the long-range cascade collisions and thermal spikes make it difficult to precisely control the magnetic properties. Using a lighter ion such as He^+ would resolve these problems.

In this work, we study the effect of progressive intermixing at the interfaces of a Ni/Fe multilayer, caused by He^+ irradiation. The irradiation induced mixing is schematically shown in Figures 5.3a and b. We show that He^+ ion irradiation can be used to tune the magnetoelastic properties of in-plane magnetized Ni/Fe multilayers by promoting interface intermixing. Specifically, we observe a change in the sign of λ_s from negative to positive. Furthermore, we confirm in Ref. [190] that Ni/Fe multilayer retains its polycrystalline structure, and that the magnetic softness of the multilayer is improved.

5.2.2 He^+ ion irradiation induced intermixing in Ni/Fe multilayers

The samples are prepared by magnetron sputtering using a Singulus Rotaris system on a Si/SiO_2 substrate. A NiFeCr(5)/$[Ni(2)/Fe(2)]_8$/Ta(4) (thickness in nanometers) multilayer is sputtered in the presence of a rotating magnetic field of 5 mT. Circles with a diameter of 80 µm and spacing of 3 µm are subsequently patterned with optical lithography (see Chapter 4 for more details) in order to probe the local film properties. The samples are irradiated with 20 keV He$^+$ ions with different fluences ranging from 2×10^{14} to 1×10^{16} ions/cm^{-2}. TRIM simulations show that at these energies, the majority (95%) of the ions reach the substrate [190], which indicates uniform intermixing across the multilayer.

We obtain a more quantitative picture of the intermixing from a series of structural and chemical characterizations, the results of which are shown in Figures 5.3c and d for an as-deposited sample and the sample irradiated with 1×10^{16} ions/cm^2, respectively. In both figures, a high-angle annular dark field STEM (HAADF-STEM) image of a cross-section of the bottom three Ni/Fe repetitions on top of the NiFeCr seed layer is shown. HAADF-STEM is a particular form of STEM that utilizes electrons scattered at high angles to form an image where the brightness is dependent on the atomic number Z, with heavier ions showing up as brighter [282]. A vertical EDX profile (see also Ref. [282]) is shown on top of the HAADF-STEM image, denoting the concentrations of Ni (red), Fe (green), and Cr (purple). Next to the HAADF-STEM images with EDX overlays are the corresponding EDX maps, showing a 2D image of the concentrations of Ni and Fe along the cross-section.

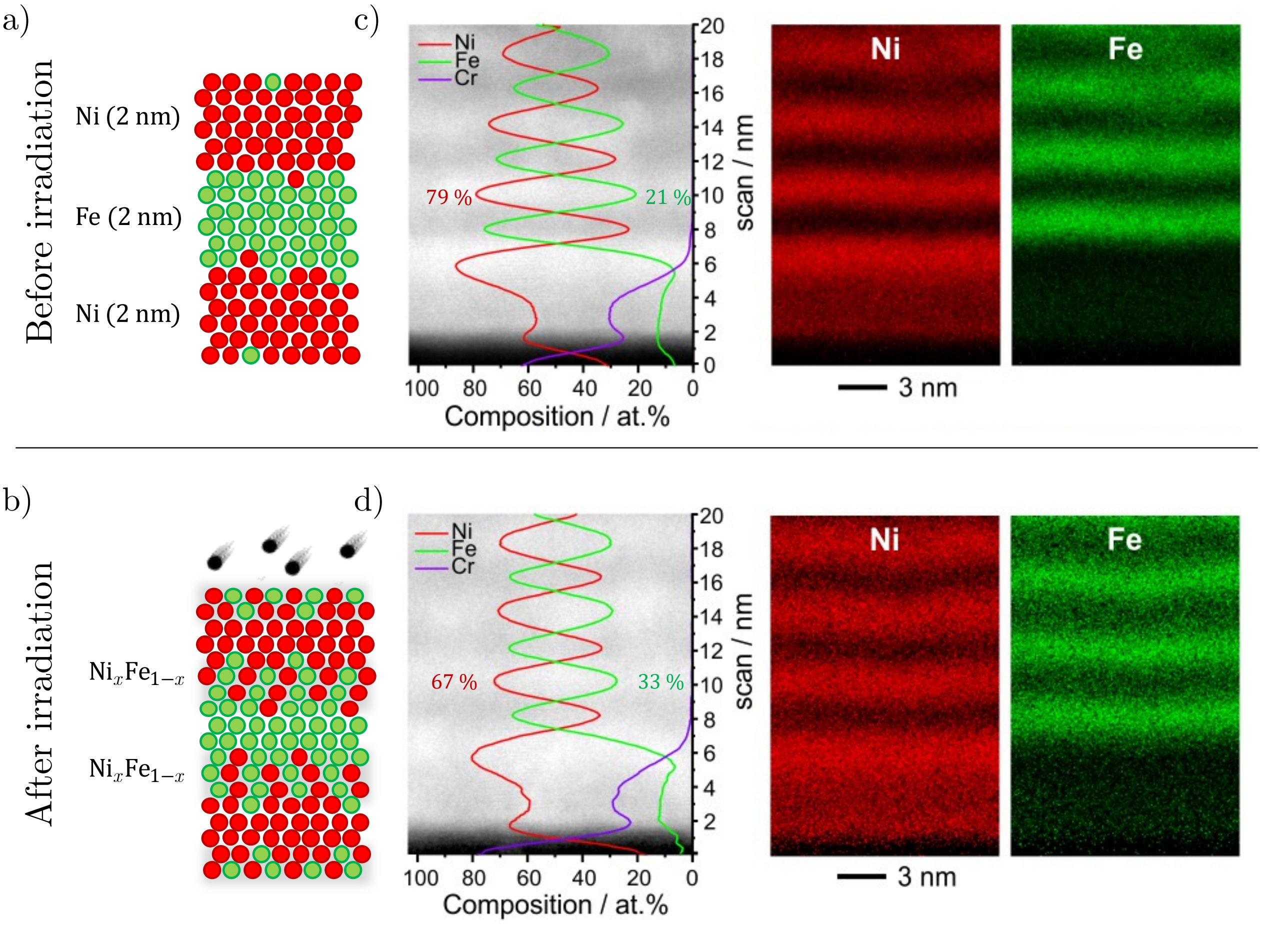

Fig. 5.3: He$^+$ irradiation of a Ni/Fe multilayer | a) and b) Sketches of the intermixing due to He$^+$ irradiation on a multilayer stack. c) and d) HAADF-STEM micrograph and EDX elemental maps of the Ni/Fe multilayer system before (c) and after (d) irradiation with 1×10^{16} ions/cm^2 measured across the first four repetitions on top of the NiFeCr seed layer. The HAADF-STEM micrograph is superimposed with a plot of the atomic composition quantified from the EDX measurements.

As deposited (Fig. 5.3c), the interfaces between the magnetic layers are relatively well defined. From the EDX profiles of the relative atomic compositions, we obtain an Fe concentration of 21 ± 2 % in a Ni layer before the irradiation. After irradiation (Fig. 5.3), the ratio of Fe atoms in a Ni layer is increased to 33 ± 4 %. This difference in stoichiometry is also observed in the EDX maps through the increased diffuse scattering of the signal intensity across the layer interfaces after irradiation. This suggests the formation of an alloy of $\mathrm{Ni}_x\mathrm{Fe}_{1-x}$ at the Ni/Fe interfaces when the different atoms are displaced under the effect of incoming He$^+$ ions.

5.2.3 Controlling magnetostriction with He$^+$ irradiation

To evaluate the effects that He$^+$ irradiation has on the magnetoelastic properties of the Ni/Fe multilayer, we measure the effective magnetic anisotropy under the application of mechanical strain by the three-point bending methods, as previously reported in Ref. [293]. With this method, the substrate is bent to exert a uniaxial strain on the sample. The coupling of the magnetization to the applied mechanical strain can be expressed with an additional anisotropy term [294]. This means we can measure this effect by probing changes in the hysteresis loops before and after mechanical deformations. The magnetoelastic anisotropy, which depends on the saturation magnetostriction λ_s, is given by [295]

$$K_\mathrm{ME} = \frac{3}{2}\lambda_\mathrm{s} Y \varepsilon, \tag{5.1}$$

where Y is Young's modulus and ε is the uniaxial tensile strain. If the directions of the crystalline and magnetoelastic uniaxial anisotropy are such that $K_\mathrm{u} \perp K_\mathrm{ME}$, the strain dependent effective in-plane anisotropy $K_\mathrm{eff,s}$[1] measured in the system can be written as the sum of two terms according to [296]

$$K_\mathrm{eff,s} = K_\mathrm{u} + K_\mathrm{ME}. \tag{5.2}$$

As the sign of K_ME depends on the sign of λ_s, the total magnetic anisotropy can increase or decrease in the presence of strain. To quantify $K_\mathrm{eff,s}$ hysteresis loops are measured using longitudinal Kerr microscopy, where the magnetic field and tensile strain are applied along the fixed direction $\Phi = 0°$. As the considered relatively thick magnetic system is dominated by shape anisotropy (included in K_u in Eq. 5.2) and, thus, in-plane magnetized, changes to the interface anisotropy as a result of ion irradiation can be neglected.

Some hysteresis loops under the applied strain of $\varepsilon_\mathrm{xx} = 0.06\%$ are shown in Figure 5.4a for samples irradiated with different He$^+$ fluences. In response to the applied strain, the samples have a different magnetic anisotropy field. We identify two potential scenarios from the comparison of the strained loops with the unstrained loop (dashed line). When a tensile strain increases the anisotropy field in the direction parallel to ε_xx, K_ME and λ_s are negative. In the as-deposited state, the sample shows negative magnetoelastic coupling. On the other hand, if the strain direction becomes an easy-axis of magnetization, K_ME and λ_s are positive. This behavior is present for samples irradiated with larger He$^+$ fluences.

We can use Equations 5.1 and 5.2 to estimate the saturation magnetostriction as a function of He$^+$ fluence [297–299]. The results are shown in Figure 5.4b. In agreement with the behavior of the magnetic hysteresis loops, the as-deposited sample shows $\lambda_\mathrm{s} = -2.6 \pm 0.5$ ppm, indicated by the horizontal dotted line in Figure 5.4b. For increasing He$^+$ fluence, the absolute value of the magnetostriction is gradually reduced, and then increased through positive values. The magnetostriction changes sign between 1×10^{15} and 2×10^{15} ions/cm^2.

An additional confirmation of the change in magnetic behavior under strain after irradiation is obtained by imaging domain formation using longitudinal Kerr microscopy. A vector image of the in-plane magnetization is obtained by the sum of horizontal and vertical components of the magnetic contrast; some examples for the as-deposited sample and two samples irradiated with 2×10^{15} and 5×10^{15} ions/cm^2 are shown in Figures 5.4c-e. The left-hand image shows the magnetic state without strain, whereas the right-hand image shows the magnetic state under the

---

[1] N.B.: the effective in-plane anisotropy under strain is not exactly the same as the effective anisotropy discussed in Chapter 1 (Eq. 1.15). K_eff as discussed in chapter one is limited to samples with a surface anisotropy term favoring a magnetization direction normal to the plane and a shape anisotropy term favoring in-plane magnetization. Here, $K_\mathrm{eff,s}$ describes an in-plane magnetized system.

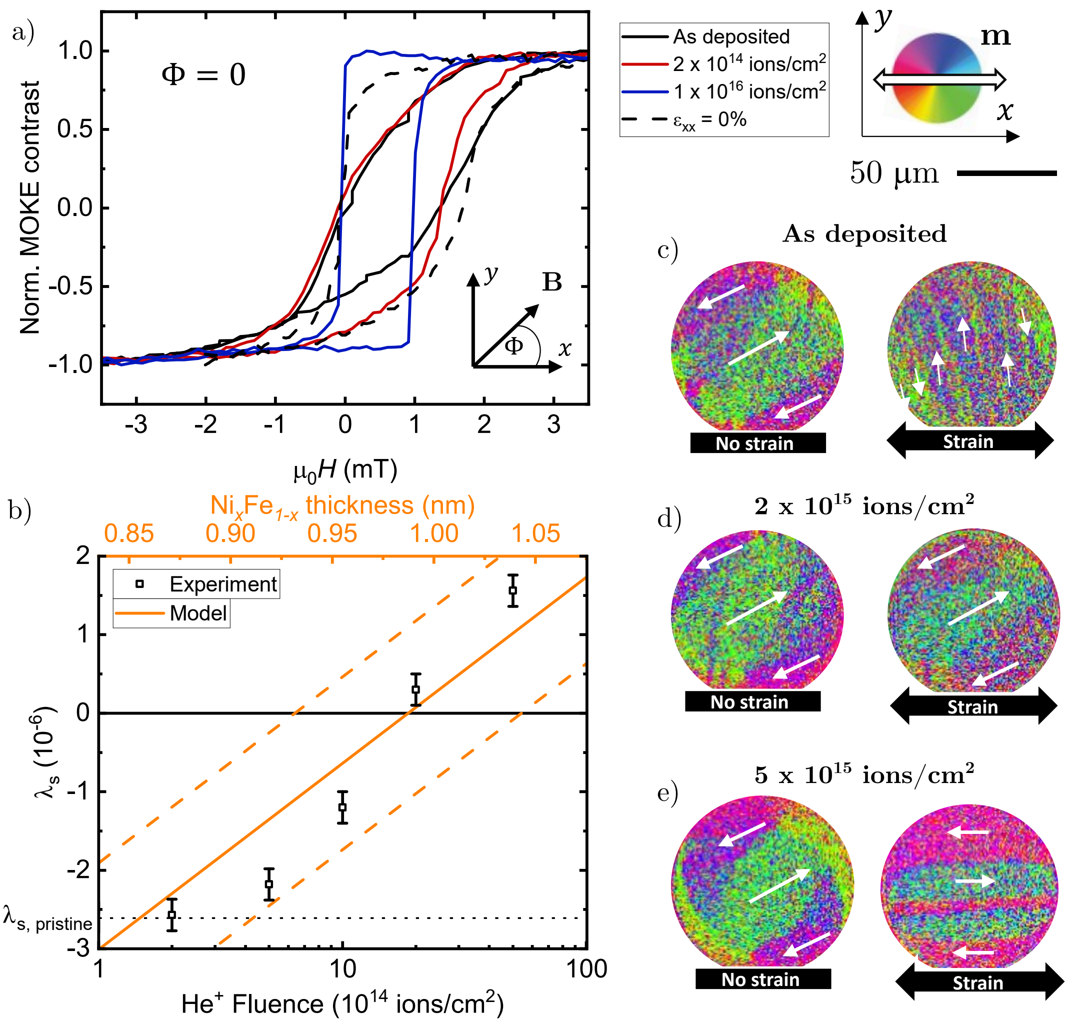

Fig. 5.4: The effects of He$^+$ irradiation on the magnetostriction of Ni/Fe | a) Hysteresis loops measured along the direction of the applied strain ($\varepsilon_{xx} = 0.06\%$) for different He$^+$ fluences (solid lines) are compared with the unstrained magnetic loop (dashed line). b) Measured saturation magnetostriction λ_s (black dots) as a function of the He$^+$ fluence and calculated values using Eq. 5.3 (orange lines) as a function of the intermixed alloy thickness $t_{\mathrm{Ni}_x\mathrm{Fe}_{1-x}}$. A central value of $\lambda_\mathrm{s}^{\mathrm{Ni}_x\mathrm{Fe}_{1-x}} = 19 \times 10^{-6}$ with $\pm 20\%$ variation is considered (dashed lines). The dotted horizontal line indicates λ_s of the as-deposited sample. c)-e) Kerr microscope images of the remanent magnetic domain state, respectively, before (left) and after (right) the application of strain are compared for c) the as deposited case, d) 2×10^{15} ions/cm^2, and e) 5×10^{15} ions/cm^2. The white arrows represent the direction of the in-plane magnetization in the domains according to the color wheel.

application of 0.06% strain. White arrows show the overall direction of the magnetization in the domains, with the color also showing the direction of the magnetization according to the color wheel. In all samples, the magnetization aligns with a crystalline axis before the application of strain. Differences between the samples are observed when applying strain. In the as-deposited sample (Fig. 5.4c), the magnetic domains orient along the y-direction, perpendicular to the applied strain. This is a clear indication of stress induced magnetic anisotropy $K_\mathrm{ME} \sim 450$ J/m^3, which overcomes the initial uniaxial anisotropy. K_ME is perpendicular to the strain direction, because λ_s is negative. For the sample irradiated with 2×10^{15} ions/cm^2 (Fig. 5.4d), which has nearly no magnetostriction, the orientation of the domains are unchanged. Indeed, K_ME is not strong enough to overcome the initial uniaxial anisotropy. For larger fluences (Fig. 5.4e), i.e. 5×10^{15} ions/cm^2, where the magnetostriction becomes stronger again, the magnetic domains now align parallel to the applied strain. This is a direct indication that the magnetoelastic coupling has been altered by ion irradiation, as the coupling has changed from negative to positive.

5.2.4 Discussion and conclusion

As previously reported [289], the small value of the magnetostriction in the as-deposited periodic system is caused by the balance of the negative magnetostriction of Ni ($\lambda_\mathrm{s}^\mathrm{Ni} = -30 \times 10^{-6}$) and Fe ($\lambda_\mathrm{s}^\mathrm{Fe} = -9 \times 10^{-6}$), and the strongly positive magnetostriction of the Ni$_x$Fe$_{1-x}$ alloy ($\lambda_\mathrm{s}^{\mathrm{NiFe}_{50}} = 19 \times 10^{-6}$) with a relative composition close to 50% [300]. The STEM and EDX measurements in Figure 5.3 show the formation of an intermixed interface region of Ni$_x$Fe$_{1-x}$ at the boundary between the Ni and Fe layers with progressive He$^+$ irradiation. This gradually shifts the magnetostriction of the full stack to positive values. A common way to describe the effective magnetostriction in the presence of intermixing is [188,289–291,301–303]

$$\lambda_\mathrm{s} = \frac{\lambda_\mathrm{s}^\mathrm{Ni} + \lambda_\mathrm{s}^\mathrm{Fe}}{2} + \left(2\lambda_\mathrm{s}^{\mathrm{Ni}_x\mathrm{Fe}_{1-x}} - \lambda_\mathrm{s}^\mathrm{Ni} - \lambda_\mathrm{s}^\mathrm{Fe}\right) \frac{t_{\mathrm{Ni}_x\mathrm{Fe}_{1-x}}}{t_\mathrm{p}}, \tag{5.3}$$

where $t_\mathrm{p} = t_\mathrm{Ni} + t_\mathrm{Fe} = 4$ nm is the period thickness, $t_{\mathrm{Ni}_x\mathrm{Fe}_{1-x}}$ describes the thickness of the alloy created through the intermixing, and $\lambda_\mathrm{s}^{\mathrm{Ni}_x\mathrm{Fe}_{1-x}}$ is the saturation magnetostriction of the intermixed alloy. By using the appropriate magnetostriction values, Equation 5.3 describes different material systems. We can use the solution to Equation 5.3 to describe the formation of Ni$_x$Fe$_{1-x}$ under irradiation, which is shown with an orange line in Figure 5.4b for a central value of $\lambda_\mathrm{s}^{\mathrm{Ni}_x\mathrm{Fe}_{1-x}} = 19\times10^{-6}$. The dashed lines denote the result when taking a 20% variation in $\lambda_\mathrm{s}^{\mathrm{Ni}_x\mathrm{Fe}_{1-x}}$ into account. For the as-deposited sample, we find $t_{\mathrm{Ni}_x\mathrm{Fe}_{1-x}} \approx 0.85$ nm, under the assumption $t_\mathrm{Fe}/t_\mathrm{p} = 0.5$. For this value, Equation 5.3 gives $\lambda_\mathrm{s} = -2.8 \pm 0.2 \times 10^{-6}$, closed to the measured value after deposition. Moreover, the amount of induced intermixing by He$^+$ irradiation can be estimated from Equation 5.3. The calculated $t_{\mathrm{Ni}_x\mathrm{Fe}_{1-x}}$ is 0.98 ± 0.02 nm at $\lambda_\mathrm{s} = 0$, and 1.05 ± 0.02 nm for the highest fluence, where the magnetostriction is positive due to the dominant effect of the alloy. This corresponds to a 20% increase in the alloy thickness induced by He$^+$ irradiation between 2×10^{14} and 5×10^{15} ions/cm^2, in agreement with the information extracted from HAADF-STEM and EDX measurements (Figure 5.3).

In conclusion, in the section we present an experimental investigation into the magnetoelastic properties of sputtered Ni/Fe multilayers after He$^+$ irradiation. Using different experimental techniques for structural analysis, the presence of moderate roughness and alloying is observed after sputtering at the Ni/Fe interface. This can justify the small negative value of magnetostriction in the as-deposited state. In the same way, we find that light ion irradiation promotes the intermixing at the interfaces proportional to the irradiation fluence. This process can explain the reported changes in the saturation magnetostriction of the magnetic stack. The increasing irradiation fluence progressively changes the saturation magnetostriction, inducing a change in the sign of the magnetoelastic coupling of the material - from negative to positive. Remarkably, strain insensitivity on the magnetic properties of the proposed material can be obtained with ion fluences between 1×10^{15} and 2×10^{15} ions/cm^2. Importantly, the polycrystalline structure of the layers is confirmed to be unchanged after the used irradiation conditions [190].

As a result, post growth He$^+$ irradiation can finely tune the magnetoelasic properties of multilayer magnetic samples, and is applicable to several material combinations. Accordingly, this technique offers the possibility to have local patterning of magnetostriction with high control and flexibility, allowing the realization of highly demanding applications, in particular magnetic sensors.

5.3 Summary

In this chapter, we present the results of two collaborations the discuss how the all-optical switching (AOS) of a Co/Gd synthethic anti-ferromagnet and the magnetostriction in a Ni/Fe multilayer are changed with RT He^+ irradiation. We show that the AOS efficiency can be enhanced by 30% through the creation of a CoGdPt alloy at the Co/Gd interface as a result of irradiation induced mixing at the Co/Gd layer. Furthermore, we show that we can tune the strength of the magnetostriction of a Ni/Fe multilayer with increasing intermixing of the Fe and Ni layers, eventually resulting in a sign change of the magnetostrictive constant. We also identify a regime where the magnetostriction is almost zero, resulting in a magnetization state that is insensitive to strain. The results shown in this chapter indicate that He^+ irradiation is a broadly applicable technique that allows for the engineering of AOS and magnetoelastic systems, which in turn can be used to create new device application based on the local modification of these properties.

Chapter 6

Summary and perspectives

In this chapter, we summarize the key concepts and results in this thesis, and discuss potential future research on the subjects presented.

6.1 Summary

Spintronics has the potential to further revolutionize data storage, sensing, logic, and artificial intelligence. However, spintronic devices face challenges in terms of magnetic and structural properties of the materials used in these devices, often based on HM/FM/NM ultra-thin films. These films are susceptible to large variations in structural disorder, which negatively impacts device operation for example through the pinning of a magnetic domain wall (DW) in racetrack memory or low data retention in MRAM, and introduces variations between devices created on the same wafer. Additionally, it can be difficult to design a universal material that is suitable for multiple use-cases, as different combinations of magnetic properties are required depending on the application.

In this thesis, we explore how irradiation with He^+ ions can be used to control not only the atomic arrangement within each layer, but also the atomic arrangement at the interfaces between layers, which subsequently affects the magnetic behavior of these materials. We particularly address several remaining challenges:

1. Improvement of the crystallization process of W/CoFeB/MgO ultra-thin films by designing a fast He^+ irradiation process at moderate temperature, as the current crystallization processes based on high temperature annealing are plagued with long annealing times and structural damages induced by the large temperatures required.

2. Improvement of the DW motion in W/CoFeB/MgO materials and better understanding of the role of disorder through irradiation induced crystallization and irradiation induced interface intermixing.

3. Improvement of DW motion in W/CoFeB/MgO wires by reducing the influence of extrinsic edge defects through He^+ irradiation.

In the following we will review the different results and findings we have reached through different experiments, and how they contribute resolve the challenges listed above. In this sense, the results in this thesis are divided into three distinct parts.

In Chapter 3, we employ He^+ irradiation at moderate temperatures to study the crystallization of an amorphous W/CoFeB/MgO ultra-thin film and subsequently study the DW motion in the crystallized films to further study the changes in intrinsic defects and their effect on DW motion. We observe that by increasing the irradiation temperature and He^+ fluence, $H_{K_{\mathrm{eff}}}$ is also increased, surpassing even the values typically obtained for high-temperature annealing for certain fluence-temperature combinations. Surprisingly, the other magnetic properties remain relatively unaffected.

We then study the nanoscale disorder in more detail by employing DW motion. Particularly, we investigate three samples with similar magnetic properties but with different disorder landscapes, which allows us to study the effects of He^+ irradiation at moderate temperatures on the defect structure and DW motion, without the influence of changing magnetic properties. We observe significant differences in DW motion at all magnetic fields between the differently crystallized samples. Subsequently, we use a microscopic model for the creep regime to identify that the typical length scales that are involved in the DW-defect interaction are reduced, along with the pinning energy barrier itself. We then use micromagnetic simulations to study the DW motion in the flow regime for various different microstructures, and identify that a reduction in the grain size and changes in the anisotropy distribution are most likely behind the observed changes in DW motion.

Our results not only show that DW motion is an efficient method to study the microscopic structure of a textured ultra-thin films in more detail, but also that the microscopic structure is a very important factor to consider when designing devices based on DW motion and that He^+ irradiation gives us excellent control over the microscopic structure of ultra-thin films [196].

In Chapter 4, we focus on He^+ irradiation induced intermixing at the interfaces of a pre-crystallized W/CoFeB/MgO film to study how the interface configuration affects the magnetic properties and the intrinsic disorder. We expand this investigation to study how irradiation can be used to optimize extrinsic defects as well. We show that RT He^+ irradiation mainly reduces $H_{K_{\mathrm{eff}}}$ and D, while the other properties remain relatively unchanged. This, in turn, has an effect on the DW motion in the creep and flow regimes. In the flow regime, we observe a reduction of the plateau velocity - related to 2D effects after the Walker breakdown. In the creep regime, we show an enhancement of the velocity at very low fields, which is linked to a reduction of the creep energy barrier. With an analytical model, we reveal no significant changes in the disorder after irradiation, suggesting the changes in DW motion are caused mainly by the changes in magnetic properties after interface mixing.

We then go beyond the interaction between DWs and intrinsic defects, and show that the interaction between DWs and extrinsic defects can be reduced, and even quenched, by local He^+ irradiation at the edges of wires through use of a focused ion beam (FIB) and magnetic planar patterning through a mask. In the case of wires with irradiated edges, we show a fluence dependent effect on the DW motion. Low fluences keep the irradiated edges perpendicularly magnetized and only slightly affect the DW dynamics. The DW motion in the whole wire is only slightly increased at low fields, as the increased velocity in the irradiated zone counteracts the additional pinning. However, a steep drop-off in velocity is still observed at low fields. For large fluences, the material at the edges becomes paramagnetic, and we observe a massive improvement in DW motion in the entire wire. The DW loses its curvature - something that is inherent in the case of strong edge pinning and low bulk pinning - after irradiation with high fluence, pointing to an absence of significant edge pinning. Wires created through magnetic planar patterning with a mask show a similar strongly reduced edge pinning. With these results we show that irradiation can be an effective tool to correct edge effects created by nanofabrication processes, which can be achieved either locally by use of a FIB, or by employing magnetic planar patterning with a mask.

In Chapter 5, we show results from several collaborations on how He^+ irradiation induced interface mixing can be used to optimize the all-optical switching (AOS) of a Co/Gd artificial ferrimagnet [189] and the magnetoelasticity of Ni/Fe multi-layers [190]. We show that the AOS efficiency can be enhanced by 30% and that the magnetostriction can be quenched and even made to change sign, all through the mixing of the constituent layers. These results show that He^+ irradiation is not only useful for conventional spintronic materials, but can also be employed for novel spintronic phenomena that are heavily interface dependent.

6.2 Perspectives

While we have addressed several challenges in this thesis, further development and challenges remain, which we summarize in this section.

The improvement of $H_{K_{\mathrm{eff}}}$ through irradiation enhanced crystallization of W/CoFeB/MgO films is a promising result that invites further study into the effects of irradiation induced crystallization in a full MTJ stack, which is currently a subject of development at Spin-Ion Technologies. An MTJ does not only contain a single FM layer, but also a reference FM layer, which is also part of a synthetic antiferromagnet, which in turn consists of many other FM layers coupled antiferromagnetically through a Ru spacer layer. As the ion travels through the entire MTJ during the irradiation process, the effect of the irradiation on each constituent layer and the overall behavior should be thoroughly investigated before irradiation enhanced crystallization can be integrated into devices that rely on MTJs, such as MRAM. Moreover, the effects of irradiation at moderate temperatures on the tunneling magnetoresistance (TMR) are important factors to consider, and should be studied as the TMR directly represents the efficiency of an MTJ. Many of these properties have already been studied after irradiation at RT (see Ref. [155] and references therein), but a full investigation that includes irradiation temperature is needed. In this way, one could tune an MTJ to achieve the desired combination of properties for different applications with a single post-growth irradiation technique.

When it comes to the application of DW motion, irradiation induced crystallization seems to challenge the conventional method to design devices based on DW motion by also unlocking the ability to tune the microscopic structure. While promising, many challenges still remain when it comes to better understanding the interactions between DWs and disorder and the exact relationship between various irradiation parameters and the resulting crystalline texture. For example, the exact relationship between H_{dep} and the magnetic and microscopic pinning properties is still an open question. Irradiation can play a role in shedding more light on this interaction, as it allows us to modify the magnetic parameters and microscopic structure, either simultaneously or separately depending on the irradiation conditions.

Increasing the understanding of DW pinning will further develop DW motion as a method to *measure* disorder. In Chapter 3 we obtain information about the disorder in the samples from the creep and flow regimes separately, but no direct link between the two investigations exists. A systematic study that takes into account different sample thicknesses, irradiation temperatures, and irradiation fluences, as well as advances in the modelling of disorder using micromagnetic simulations and the understanding of the impact of disorder on the flow-regime dynamics are required to fully bridge the gap between the two regimes. Other methods of measuring disorder with micromagnetic phenomena, notably using FMR and BLS linewidth measurements to obtain the inhomogeneous broadening, also require further investigation before they can be linked to sample disorder. As we mentioned in Chapter 3, BLS and FMR do not always result in the same values between the two techniques, and further lack a direct link to the various types of disorder present in the sample, such as anisotropy, DMI, thickness, and saturation magnetization variations. A similar systematic study like the one mentioned above could resolve some of these issues. Comparing the various studies mentioned above to direct structural characterizations is a must, although directly imaging nanoscale disorder is often challenging. In the case of TEM measurements, a Ga^{+} FIB is often employed to create the TEM lamallae [304], which can alter the sample disorder further and prevent a clean image. Similarly, ToF-SIMS also uses an ion beam to sputter sample atoms. This means non-destructive measurements based on X-rays, such as X-ray reflectometry (XRR) and X-ray diffraction (XRD), would be the best option to study the sample disorder, and can even be used to study the evolution of the sample during the crystallization process when used in-situ at a beamline, for example.

Magnetic patterning, either by FIB or through a mask, is not a new concept. Nonetheless, our results are the first that show the correction of edge damage using this technique. This sparks some interesting follow-up opportunities. On the fundamental side, the flexibility offered by the irradiation process in terms of fluence could help us shed more light on the physical mechanism that is behind edge pinning, as He^+ irradiation process allows us to selectively turn off the magnetic properties while keeping the structural damages to a minimum. By further playing with different edge irradiation patterns, a better understanding of the range of the edge pinning effect can be gained as well. On the applications side, one can create interesting irradiation patterns to further enhance the DW motion in the wire. For example, DWs in edge irradiation zones, where they are faster than the bulk DWs, could pull along the entire DW, increasing the total velocity (inversely to the edge pinning effect). Furthermore, magnetic patterning can be employed to control DW motion through artificial pinning sites and anisotropy gradients [205], without introducing more complex geometries, such as notches [305], through lithography. As DWs are typically driven by currents in devices, our study should be expanded to include the effect of edge irradiation on current driven DW motion. As edge irradiation results in less pinning, it is expected that the critical current required to move DWs forward (essentially the *depinning current*) is reduced, which would enhance the efficiency of any DW-motion-based device.

Lastly, as also mentioned at the end of Chapter 2, the rising importance of interfacial effects in magnetism, as well as the discovery of novel interfacial interactions and the many existing proof of concepts on changing individual magnetic parameters, only enhance the flexibility of ion irradiation to create new device functionalities. This is not solely limited to magnetostriction in Ni/Fe multilayers or AOS in Co/Gd bi-layers, like shown in this thesis. For example, recent work shows that the magnonic index of refraction in yttrium iron garnet (YIG) can be controlled by ion irradiation [306], and the transmission of spin-waves in devices can further be controlled by designing anisotropy landscapes [307,308], paving the way for the design of spin-wave devices with irradiation. Irradiation could also be used to affect other methods that change interfaces, such as the control of magnetism through manipulation of the oxidation state of a FM in contact with an oxide layer with large ionic mobility using electric fields, also known as magneto-ionics [309–311]. Not only has it already been shown that the crystalline state of a $W/CoFeB/HfO_2$ thin film strongly affects the magneto-ionic behavior [311], irradiation of, and implantation of foreign ion species could potentially enhance oxygen mobility through the creation of additional vacancies. Additionally, irradiation and magneto-ionics can work in tandem to create volatile and non-volatile control of the magnetization state simultaneously, for example by enhancing DW motion with irradiation and creating pinning sites through gating with magneto-ionics.

References

[1] Baibich M. N., Broto J. M., Fert A., Van Dau F. N., Petroff F., Etienne P., Creuzet G., Friederich A. & Chazelas J., *Giant Magnetoresistance of (001)Fe/(001)Cr Magnetic Superlattices*, Physical Review Letters **61**, 2472–2475 (1988). [p. 1]

[2] Binasch G., Grünberg P., Saurenbach F. & Zinn W., *Enhanced magnetoresistance in layered magnetic structures with antiferromagnetic interlayer exchange*, Physical Review B **39**, 4828–4830 (1989). [p. 1]

[3] Julliere M., *Tunneling between ferromagnetic films*, Physics Letters A **54**, 225–226 (1975). [p. 1]

[4] Moodera J. S., Kinder L. R., Wong T. M. & Meservey R., *Large Magnetoresistance at Room Temperature in Ferromagnetic Thin Film Tunnel Junctions*, Physical Review Letters **74**, 3273–3276 (1995). [p. 1]

[5] Dieny B., Prejbeanu I. L., Garello K., Gambardella P., Freitas P., Lehndorff R., Raberg W., Ebels U., Demokritov S. O., Akerman J., Deac A., Pirro P., Adelmann C., Anane A., Chumak A. V., Hirohata A., Mangin S., Valenzuela S. O., Onbaşlı M. C., d'Aquino M., Prenat G., Finocchio G., Lopez-Diaz L., Chantrell R., Chubykalo-Fesenko O. & Bortolotti P., *Opportunities and challenges for spintronics in the microelectronics industry*, Nature Electronics **3**, 446–459 (2020). [pp. 1, 71, 72]

[6] Slonczewski J., *Current-driven excitation of magnetic multilayers*, Journal of Magnetism and Magnetic Materials **159**, L1–L7 (1996). [p. 1]

[7] Myers E. B., Ralph D. C., Katine J. A., Louie R. N. & Buhrman R. A., *Current-Induced Switching of Domains in Magnetic Multilayer Devices*, Science **285**, 867–870 (1999). [p. 1]

[8] Manchon A., Železný J., Miron I. M., Jungwirth T., Sinova J., Thiaville A., Garello K. & Gambardella P., *Current-induced spin-orbit torques in ferromagnetic and antiferromagnetic systems*, Reviews of Modern Physics **91**, 035004 (2019). [pp. 1, 69, 76]

[9] Jung S., Lee H., Myung S., Kim H., Yoon S. K., Kwon S.-W., Ju Y., Kim M., Yi W., Han S., Kwon B., Seo B., Lee K., Koh G.-H., Lee K., Song Y., Choi C., Ham D. & Kim S. J., *A crossbar array of magnetoresistive memory devices for in-memory computing*, Nature **601**, 211–216 (2022). [p. 1]

[10] Wu L., Taouil M., Rao S., Marinissen E. J. & Hamdioui S. *Survey on STT-MRAM Testing: Failure Mechanisms, Fault Models, and Tests* (2020). [pp. 1, 72]

[11] Parkin S. S. P., Hayashi M. & Thomas L., *Magnetic Domain-Wall Racetrack Memory*, Science **320**, 190–194 (2008). [pp. 1, 76]

[12] Zhao W. S., Duval J., Ravelosona D., Klein J.-O., Kim J. V. & Chappert C., *A compact model of domain wall propagation for logic and memory design*, Journal of Applied Physics **109**, 07D501 (2011). [pp. 1, 76]

[13] Kumar D., Jin T., Sbiaa R., Kläui M., Bedanta S., Fukami S., Ravelosona D., Yang S.-H., Liu X. & Piramanayagam S., *Domain wall memory: Physics, materials, and devices*, Physics Reports **958**, 1–35 (2022). [pp. 1, 69, 76]

[14] Luo Z., Hrabec A., Dao T. P., Sala G., Finizio S., Feng J., Mayr S., Raabe J., Gambardella P. & Heyderman L. J., *Current-driven magnetic domain-wall logic*, Nature **579**, 214–218 (2020). [pp. 1, 69, 76]

[15] Currivan J. A., Youngman Jang, Mascaro M. D., Baldo M. A. & Ross C. A., *Low Energy Magnetic Domain Wall Logic in Short, Narrow, Ferromagnetic Wires*, IEEE Magnetics Letters **3**, 3000104–3000104 (2012). [pp. 1, 76]

[16] Alamdar M., Leonard T., Cui C., Rimal B. P., Xue L., Akinola O. G., Patrick Xiao T., Friedman J. S., Bennett C. H., Marinella M. J. & Incorvia J. A. C., *Domain wall-magnetic tunnel junction spin–orbit torque devices and circuits for in-memory computing*, Applied Physics Letters **118**, 112401 (2021). [pp. 1, 76]

[17] Raymenants E., Bultynck O., Wan D., Devolder T., Garello K., Sourlau L., Thlam A., Tsvetanova D., Canvel Y., Nikonov D. E., Young I. A., Heyns M., Soree B., Asselberghs I., Radu I., Couet S. & Nguyen V. D., *Nanoscale domain wall devices with magnetic tunnel junction read and write*, Nature Electronics **4**, 392–398 (2021). [pp. 1, 76]

[18] Currivan-Incorvia J. A., Siddiqui S., Dutta S., Evarts E. R., Zhang J., Bono D., Ross C. A. & Baldo M. A., *Logic circuit prototypes for three-terminal magnetic tunnel junctions with mobile domain walls*, Nature Communications **7**, 10275 (2016). [pp. 1, 76]

[19] Lequeux S., Sampaio J., Cros V., Yakushiji K., Fukushima A., Matsumoto R., Kubota H., Yuasa S. & Grollier J., *A magnetic synapse: Multilevel spin-torque memristor with perpendicular anisotropy*, Scientific Reports **6**, 31510 (2016). [pp. 1, 76]

[20] Grollier J., Querlioz D., Camsari K. Y., Everschor-Sitte K., Fukami S. & Stiles M. D., *Neuromorphic spintronics*, Nature Electronics **3**, 360–370 (2020). [pp. 1, 69, 76]

[21] Liu S., Xiao T. P., Cui C., Incorvia J. A. C., Bennett C. H. & Marinella M. J., *A domain wall-magnetic tunnel junction artificial synapse with notched geometry for accurate and efficient training of deep neural networks*, Applied Physics Letters **118**, 202405 (2021). [pp. 1, 76]

[22] Brigner W. H., Hassan N., Hu X., Bennett C. H., Garcia-Sanchez F., Cui C., Velasquez A., Marinella M. J., Incorvia J. A. C. & Friedman J. S., *Domain Wall Leaky Integrate-and-Fire Neurons With Shape-Based Configurable Activation Functions*, IEEE Transactions on Electron Devices **69**, 2353–2359 (2022). [pp. 1, 76]

[23] Fassbender J., Ravelosona D. & Samson Y., *Tailoring magnetism by light-ion irradiation*, Journal of Physics D: Applied Physics **37**, R179–R196 (2004). [pp. 2, 63]

[24] Chappert C., Bernas H., Ferré J., Kottler V., Jamet J.-P., Chen Y., Cambril E., Devolder T., Rousseaux F., Mathet V. & Launois H., *Planar Patterned Magnetic Media Obtained by Ion Irradiation*, Science **280**, 1919–1922 (1998). [pp. 2, 63, 106]

[25] https://www.spin-ion.com/. [pp. 2, 60, 104]

[26] https://magnefi.c2n.u-psud.fr/. [p. 2]

[27] Hubert A. & Schäfer R., *Magnetic domains: The analysis of magnetic microstructures*, Springer, Berlin ; New York (2009). [pp. 6, 31]

[28] Coey J. M. D., *Magnetism and magnetic materials*, Cambridge University Press, Cambridge (2010). [pp. 6, 9, 10, 11, 12, 24, 72, 84]

[29] Dzyaloshinsky I., *A thermodynamic theory of "weak" ferromagnetism of antiferromagnetics*, Journal of Physics and Chemistry of Solids **4**, 241–255 (1958). [p. 7]

[30] Moriya T., *Anisotropic Superexchange Interaction and Weak Ferromagnetism*, Physical Review **120**, 91–98 (1960). [pp. 7, 8]

[31] Fert A. & Levy P. M., *Role of Anisotropic Exchange Interactions in Determining the Properties of Spin-Glasses*, Physical Review Letters **44**, 1538–1541 (1980). [pp. 7, 8]

[32] Kim K.-W., Lee H.-W., Lee K.-J. & Stiles M. D., *Chirality from Interfacial Spin-Orbit Coupling Effects in Magnetic Bilayers*, Physical Review Letters **111**, 216601 (2013). [pp. 7, 8]

[33] Franken J. H., Herps M., Swagten H. J. M. & Koopmans B., *Tunable chiral spin texture in magnetic domain-walls*, Scientific Reports **4**, 5248 (2014). [p. 7]

[34] Meijer M. J. *Imaging the magnetic chirality of spin textures*. Ph.D. thesis Eindhoven University of Technology, Eindhoven (2022). [p. 8]

[35] Kuepferling M., Casiraghi A., Soares G., Durin G., Garcia-Sanchez F., Chen L., Back C. H., Marrows C. H., Tacchi S. & Carlotti G., *Measuring interfacial Dzyaloshinskii-Moriya interaction in ultrathin magnetic films*, Reviews of Modern Physics **95**, 015003 (2023). [pp. 8, 28, 74, 75, 79]

[36] Rashba E. I., *Properties of semiconductors with an extremum loop. I. Cyclotron and combinational resonance in a magnetic field perpendicular to the plane of the loop*, Soviet Physics, Solid State **2**, 1224–1238 (1960). [p. 8]

[37] Bychkov Y. A. & Rashba E. I., *Oscillatory effects and the magnetic susceptibility of carriers in inversion layers*, Journal of Physics C: Solid State Physics **17**, 6039–6045 (1984). [p. 8]

[38] Krupin O., Bihlmayer G., Starke K., Gorovikov S., Prieto J. E., Döbrich K., Blügel S. & Kaindl G., *Rashba effect at magnetic metal surfaces*, Physical Review B **71**, 201403 (2005). [p. 8]

[39] Miron I. M., Gaudin G., Auffret S., Rodmacq B., Schuhl A., Pizzini S., Vogel J. & Gambardella P., *Current-driven spin torque induced by the Rashba effect in a ferromagnetic metal layer*, Nature Materials **9**, 230–234 (2010). [p. 8]

[40] Yang H., Boulle O., Cros V., Fert A. & Chshiev M., *Controlling Dzyaloshinskii-Moriya Interaction via Chirality Dependent Atomic-Layer Stacking, Insulator Capping and Electric Field*, Scientific Reports **8**, 12356 (2018). [p. 8]

[41] Thiaville A., Rohart S., Jué É., Cros V. & Fert A., *Dynamics of Dzyaloshinskii domain walls in ultrathin magnetic films*, EPL (Europhysics Letters) **100**, 57002 (2012). [pp. 8, 17, 18]

[42] Rohart S. & Thiaville A., *Skyrmion confinement in ultrathin film nanostructures in the presence of Dzyaloshinskii-Moriya interaction*, Physical Review B **88**, 184422 (2013). [p. 8]

[43] Chappert C. & Bruno P., *Magnetic anisotropy in metallic ultrathin films and related experiments on cobalt films (invited)*, Journal of Applied Physics **64**, 5736–5741 (1988). [p. 9]

[44] Néel L., *Anisotropie magnétique superficielle et surstructures d'orientation*, Journal de Physique et le Radium **15**, 225–239 (1954). [p. 9]

[45] Gradmann U., *Magnetic surface anisotropies*, Journal of Magnetism and Magnetic Materials **54–57**, 733–736 (1986). [p. 9]

[46] Chappert C., Dang K. L., Beauvillain P., Hurdequint H. & Renard D., *Ferromagnetic resonance studies of very thin cobalt films on a gold substrate*, Physical Review B **34**, 3192–3197 (1986). [p. 9]

[47] Bruno P. & Renard J. P., *Magnetic surface anisotropy of transition metal ultrathin films*, Applied Physics A Solids and Surfaces **49**, 499–506 (1989). [p. 9]

[48] Johnson M. T., Bloemen P. J. H., den Broeder F. J. A. & de Vries J. J., *Magnetic anisotropy in metallic multilayers*, Reports on Progress in Physics **59**, 1409–1458 (1996). [p. 9]

[49] Dieny B. & Chshiev M., *Perpendicular magnetic anisotropy at transition metal/oxide interfaces and applications*, Reviews of Modern Physics **89**, 025008 (2017). [pp. 10, 72, 79]

[50] Griffiths D. J., *Introduction to electrodynamics*, Fourth edition, Pearson, Boston (2013). [p. 11]

[51] Juge R. *Exploring different facets of magnetic skyrmion nucleation and dynamics in ultra-thin films*. Ph.D. thesis Université Grenoble Alpes, Grenoble (2020). [pp. 13, 14, 15, 16, 22, 23]

[52] DeJong M. D. & Livesey K. L., *Analytic theory for the switch from Bloch to Néel domain wall in nanowires with perpendicular anisotropy*, Physical Review B **92**, 214420 (2015). [p. 12]

[53] Géhanne P. *Dynamique de parois de domaines magnétiques chirales en présence de défauts*. Ph.D. thesis Université Paris-Saclay (2021). [pp. 12, 13, 14, 16, 17, 19, 33, 76]

[54] Landau L. & Lifshitz E. *On the theory of the dispersion of magnetic permeability in ferromagnetic bodies*, in *Perspectives in Theoretical Physics*, Elsevier (1992). [p. 15]

[55] Gilbert T. L., *A phenomenological theory of damping in ferromagnetic materials*, IEEE Transactions on Magnetics **40**, 7 (2004). [p. 15]

[56] Walker L. R. *Unpublished.* Tech. Rep., Bell Telephone Laboratories Memorandum (1956). [p. 16]

[57] Dillon J., Jr. *Domains and Domain Walls*, in *Spin Arrangements and Crystal Structure, Domains, and Micromagnetics: A Treatise on Modern Theory and Materials*, Second, Academic Press Inc. (1963). [p. 16]

[58] Schryer N. L. & Walker L. R., *The motion of 180° domain walls in uniform dc magnetic fields*, Journal of Applied Physics **45**, 5406–5421 (1974). [p. 16]

[59] Slonczewski J. C. *Dynamics of magnetic domain walls.* in *AIP Conference Proceedings*, vol. 5, 170–174 (Chicago, IL, USA, 1972). [p. 16]

[60] Ha Pham T., Vogel J., Sampaio J., Vaňatka M., Rojas-Sánchez J.-C., Bonfim M., Chaves D. S., Choueikani F., Ohresser P., Otero E., Thiaville A. & Pizzini S., *Very large domain wall velocities in Pt/Co/GdOx and Pt/Co/Gd trilayers with Dzyaloshinskii-Moriya interaction*, EPL (Europhysics Letters) **113**, 67001 (2016). [p. 18]

[61] Beach G. S. D., Nistor C., Knutson C., Tsoi M. & Erskine J. L., *Dynamics of field-driven domain-wall propagation in ferromagnetic nanowires*, Nature Materials **4**, 741–744 (2005). [p. 18]

[62] Yoshimura Y., Kim K.-J., Taniguchi T., Tono T., Ueda K., Hiramatsu R., Moriyama T., Yamada K., Nakatani Y. & Ono T., *Soliton-like magnetic domain wall motion induced by the interfacial Dzyaloshinskii–Moriya interaction*, Nature Physics **12**, 157–161 (2016). [p. 18]

[63] Krizakova V., Garcia J. P., Vogel J., Rougemaille N., Chaves D. d. S., Pizzini S. & Thiaville A., *Study of the velocity plateau of Dzyaloshinskii domain walls*, Physical Review B **100**, 214404 (2019). [p. 18]

[64] Garcia J. P., Fassatoui A., Bonfim M., Vogel J., Thiaville A. & Pizzini S., *Magnetic domain wall dynamics in the precessional regime: Influence of the Dzyaloshinskii-Moriya interaction*, Physical Review B **104**, 014405 (2021). [pp. 18, 21, 22, 84]

[65] Metaxas P. J. *Creep and Flow Dynamics of Magnetic Domain Walls: Weak Disorder, Wall Binding and Periodic Pinning*, in *Solid State Physics*, Elsevier/Academic Press, Amsterdam (2010). [p. 19]

[66] Jeudy V., Mougin A., Bustingorry S., Savero Torres W., Gorchon J., Kolton A. B., Lemaître A. & Jamet J.-P., *Universal Pinning Energy Barrier for Driven Domain Walls in Thin Ferromagnetic Films*, Physical Review Letters **117**, 057201 (2016). [pp. 19, 20]

[67] Kolton A. B., Rosso A., Giamarchi T. & Krauth W., *Dynamics below the Depinning Threshold in Disordered Elastic Systems*, Physical Review Letters **97**, 057001 (2006). [p. 19]

[68] Kolton A. B., Rosso A., Giamarchi T. & Krauth W., *Creep dynamics of elastic manifolds via exact transition pathways*, Physical Review B **79**, 184207 (2009). [pp. 19, 86, 98]

[69] Ferrero E. E., Foini L., Giamarchi T., Kolton A. B. & Rosso A., *Spatiotemporal Patterns in Ultraslow Domain Wall Creep Dynamics*, Physical Review Letters **118**, 147208 (2017). [p. 19]

[70] Ferrero E. E., Foini L., Giamarchi T., Kolton A. B. & Rosso A., *Creep motion of elastic interfaces driven in a disordered landscape*, Annual Review of Condensed Matter Physics **12**, 111–134 (2021). [p. 19]

[71] Kleemann W., *Universal Domain Wall Dynamics in Disordered Ferroic Materials*, Annual Review of Materials Research **37**, 415–448 (2007). [p. 19]

[72] Bonamy D. & Bouchaud E., *Failure of heterogeneous materials: A dynamic phase transition?*, Physics Reports **498**, 1–44 (2011). [p. 19]

[73] Nicolas A., Ferrero E. E., Martens K. & Barrat J.-L., *Deformation and flow of amorphous solids: Insights from elastoplastic models*, Reviews of Modern Physics **90**, 045006 (2018). [p. 19]

[74] Le Doussal P., Wiese K. J., Moulinet S. & Rolley E., *Height fluctuations of a contact line: A direct measurement of the renormalized disorder correlator*, EPL (Europhysics Letters) **87**, 56001 (2009). [p. 19]

[75] Lemerle S., Ferré J., Chappert C., Mathet V., Giamarchi T. & Le Doussal P., *Domain Wall Creep in an Ising Ultrathin Magnetic Film*, Physical Review Letters **80**, 849–852 (1998). [p. 20]

[76] Chauve P., Giamarchi T. & Le Doussal P., *Creep and depinning in disordered media*, Physical Review B **62**, 6241–6267 (2000). [p. 20]

[77] Diaz Pardo R., Savero Torres W., Kolton A. B., Bustingorry S. & Jeudy V., *Universal depinning transition of domain walls in ultrathin ferromagnets*, Physical Review B **95**, 184434 (2017). [p. 20]

[78] Ferrero E. E., Bustingorry S. & Kolton A. B., *Nonsteady relaxation and critical exponents at the depinning transition*, Physical Review E **87**, 032122 (2013). [p. 20]

[79] Bustingorry S., Kolton A. B. & Giamarchi T., *Thermal rounding of the depinning transition*, EPL (Europhysics Letters) **81**, 26005 (2008). [p. 20]

[80] Voto M., Lopez-Diaz L. & Torres L., *Effects of grain size and disorder on domain wall propagation in CoFeB thin films*, Journal of Physics D: Applied Physics **49**, 185001 (2016). [pp. 21, 22, 76, 84]

[81] Min H., McMichael R. D., Donahue M. J., Miltat J. & Stiles M. D., *Effects of Disorder and Internal Dynamics on Vortex Wall Propagation*, Physical Review Letters **104**, 217201 (2010). [pp. 21, 22, 76, 84, 87]

[82] Leliaert J., Van de Wiele B., Vansteenkiste A., Laurson L., Durin G., Dupré L. & Van Waeyenberge B., *Current-driven domain wall mobility in polycrystalline Permalloy nanowires: A numerical study*, Journal of Applied Physics **115**, 233903 (2014). [pp. 21, 22, 76, 84]

[83] Voto M., Lopez-Diaz L., Torres L. & Moretti S., *Disorder-induced domain wall velocity shift at high fields in perpendicularly magnetized thin films*, Physical Review B **94**, 174438 (2016). [p. 22]

[84] Foner S., *Versatile and Sensitive Vibrating-Sample Magnetometer*, Review of Scientific Instruments **30**, 548–557 (1959). [p. 24]

[85] Foner S., *Further improvements in vibrating sample magnetometer sensitivity*, Review of Scientific Instruments **46**, 1425–1426 (1975). [p. 24]

[86] Foner S., *Review of magnetometry*, IEEE Transactions on Magnetics **17**, 3358–3363 (1981). [p. 24]

[87] Philo J. S. & Fairbank W. M., *High-sensitivity magnetic susceptometer employing superconducting technology*, Rev. Sci. Instrum. **48**, 9 (1977). [p. 24]

[88] Flanders P. J., *An alternating-gradient magnetometer (invited)*, Journal of Applied Physics **63**, 3940–3945 (1988). [p. 25]

[89] Lucassen J. *Exploring chiral magnetism with spin waves and domain walls.* Ph.D. thesis Technische Universiteit Eindhoven, Eindhoven (2020). [pp. 25, 31]

[90] Noel P. *Dynamical spin injection and spin to charge current conversion in oxide-based Rashba interfaces and topological insulators.* Ph.D. thesis Université Grenoble Alpes (2019). [p. 26]

[91] Farle M., *Ferromagnetic resonance of ultrathin metallic layers*, Reports on Progress in Physics **61**, 755 (1998). [p. 26]

[92] Arias R. & Mills D. L., *Extrinsic contributions to the ferromagnetic resonance response of ultrathin films*, Physical Review B **60**, 7395–7409 (1999). [p. 27]

[93] Patton C. E., *Magnetic Excitations in Solids*, Physics Reports **103**, 251–315 (1984). [p. 28]

[94] Demokritov S. & Tsymbal E., *Light scattering from spin waves in thin films and layered systems*, Journal of Physics: Condensed Matter **6**, 7145–7188 (1994). [p. 28]

[95] Damon R. & Eshbach J., *Magnetostatic modes of a ferromagnet slab*, Journal of Physics and Chemistry of Solids **19**, 308–320 (1961). [p. 28]

[96] Belmeguenai M., Adam J.-P., Roussigné Y., Eimer S., Devolder T., Kim J.-V., Cherif S. M., Stashkevich A. & Thiaville A., *Interfacial Dzyaloshinskii-Moriya interaction in perpendicularly magnetized Pt/Co/AlO x ultrathin films measured by Brillouin light spectroscopy*, Physical Review B **91**, 180405(R) (2015). [p. 29]

[97] Moon J.-H., Seo S.-M., Lee K.-J., Kim K.-W., Ryu J., Lee H.-W., McMichael R. D. & Stiles M. D., *Spin-wave propagation in the presence of interfacial Dzyaloshinskii-Moriya interaction*, Physical Review B **88**, 184404 (2013). [p. 29]

[98] Cortés-Ortuño D. & Landeros P., *Influence of the Dzyaloshinskii–Moriya interaction on the spin-wave spectra of thin films*, Journal of Physics: Condensed Matter **25**, 156001 (2013). [p. 29]

[99] Capua A., Yang S.-h., Phung T. & Parkin S. S. P., *Determination of intrinsic damping of perpendicularly magnetized ultrathin films from time-resolved precessional magnetization measurements*, Physical Review B **92**, 224402 (2015). [p. 30]

[100] Kerr J., *XLIII.* On rotation of the plane of polarization by reflection from the pole of a magnet, The London, Edinburgh, and Dublin Philosophical Magazine and Journal of Science **3**, 321–343 (1877). [p. 30]

[101] Qiu Z. Q. & Bader S. D., *Surface magneto-optic Kerr effect*, Review of Scientific Instruments 1243 (2000). [p. 30]

[102] Caballero N. B., Fernández Aguirre I., Albornoz L. J., Kolton A. B., Rojas-Sánchez J. C., Collin S., George J. M., Diaz Pardo R., Jeudy V., Bustingorry S. & Curiale J., *Excess velocity of magnetic domain walls close to the depinning field*, Physical Review B **96**, 224422 (2017). [pp. 33, 81, 96]

[103] Bernas H. (ed.) *Materials science with ion beams*, Springer, Berlin (2010). [p. 35]

[104] Hellborg R., Whitlow H. J. & Zhang Y. (eds.) *Ion Beams in Nanoscience and Technology*, Springer Berlin Heidelberg, Berlin, Heidelberg (2010). [p. 35]

[105] Wesch W. & Wendler E. (eds.) *Ion beam modification of solids*, Springer Berlin Heidelberg, New York, NY (2016). [pp. 35, 51, 55, 56, 57, 59]

[106] Möller W. *Fundamentals of Ion-Solid Interaction - A Compact Introduction* (2017). [pp. 35, 36, 37, 39, 40, 45, 46, 48, 49, 50, 51]

[107] Lindhard J., Nielsen V. & Scharff M., *Approximation methods in classical scattering by screened coulomb fields (Notes on atomic collisions I)*, Matematisk-fysiske Meddelelser **36**, 10 (1968). [pp. 37, 38, 40]

[108] Thomas L. H., *The calculation of atomic fields*, Mathematical Proceedings of the Cambridge Philosophical Society **23**, 542–548 (1927). [p. 38]

[109] Fermi E., *Statistical method to determine some properties of atoms*, Rendiconti Lincei **6**, 602–607 (1927). [p. 38]

[110] Ziegler J. F., Biersack J. P. & Littmark U., *The stopping and range of ions in solids*, Pergamon, New York (1985). [p. 38]

[111] Lindhard J., Scharff M. & Schiøtt H., E., *Range concepts and heavy ion ranges (Notes on atomic collisions, II)*, Matematisk-fysiske Meddelelser **33**, 44 (1963). [p. 41]

[112] Fermi E., Teller E. & Weisskopf V., *The Decay of Negative Mesotrons in Matter*, Physical Review **71**, 314–315 (1947). [p. 42]

[113] Lindhard J. & Scharff M., *Energy Dissipation by Ions in the kev Region*, Physical Review **124**, 128–130 (1961). [p. 42]

[114] Bohr N., *II.* On the theory of the decrease of velocity of moving electrified particles on passing through matter, The London, Edinburgh, and Dublin Philosophical Magazine and Journal of Science **25**, 10–31 (1913). [p. 42]

[115] Bohr N., *LX.* On the decrease of velocity of swiftly moving electrified particles in passing through matter, The London, Edinburgh, and Dublin Philosophical Magazine and Journal of Science **30**, 581–612 (1915). [p. 42]

[116] Bethe H., *Zur Theorie des Durchgangs schneller Korpuskularstrahlen durch Materie*, Annalen der Physik **397**, 325–400 (1930). [p. 42]

[117] Ziegler J. F., Ziegler M. & Biersack J., *SRIM – The stopping and range of ions in matter (2010)*, Nuclear Instruments and Methods in Physics Research Section B: Beam Interactions with Materials and Atoms **268**, 1818–1823 (2010). [p. 42]

[118] Winterbon K., Sigmund P. & Sanders J., *Spatial distribution of energy deposited by atomic particles in elastic collisions*, Matematisk-fysiske Meddelelser **37**, 14 (1970). [p. 44]

[119] Schiøtt H., *Range-Energy relations for low-energy ions*, Matematisk-fysiske Meddelelser **35** (1966). [p. 45]

[120] Sigmund P., *Collision theory of displacement damage, ion ranges and sputtering I*, Rev. Roum. Phys. **17**, 823–870 (1972). [p. 47]

[121] Sigmund P., *Collision theory of displacement damage, ion ranges and sputtering II*, Rev. Roum. Phys. **17**, 969–1000 (1972). [p. 47]

[122] Sigmund P., *Collision theory of displacement damage, ion ranges and sputtering III*, Rev. Roum. Phys. **17**, 1079–1106 (1972). [p. 47]

[123] Winterbon K. B., *Calculations of implanted-ion range and energy-deposition distributions: ^{11} B in Si*, Radiation Effects **30**, 199–206 (1976). [p. 48]

[124] Kinchin G. H. & Pease R. S., *The Displacement of Atoms in Solids by Radiation*, Reports on Progress in Physics **18**, 1–51 (1955). [p. 49]

[125] Devolder T. *Structuration et nanostructuration de couches magnetiques Co/Pt par irradiation ionique.* Ph.D. thesis Paris XI, Bures-sur-Yvette (2000). [pp. 50, 62, 63]

[126] Konobeyev A.Yu., Fischer U., Korovin Yu.A. & Simakov S., *Evaluation of effective threshold displacement energies and other data required for the calculation of advanced atomic displacement cross-sections*, Nuclear Energy and Technology **3**, 169–175 (2017). [p. 49]

[127] Averback R., Benedek R. & Merkle K., *Efficiency of defect production in cascades*, Journal of Nuclear Materials **69–70**, 786–789 (1978). [p. 50]

[128] Vook F. L. & Stein H. J., *Relation of neutron to ion damage annealing in Si and Ge*, Radiation Effects **2**, 23–30 (1969). [p. 51]

[129] Dienes G. J. & Damask A. C., *Radiation Enhanced Diffusion in Solids*, Journal of Applied Physics **29**, 1713–1721 (1958). [p. 51]

[130] Sizmann R., *The effect of radiation upon diffusion in metals*, Journal of Nuclear Materials **69–70**, 386–412 (1978). [p. 52]

[131] Golubov S., Barashev A. & Stoller R. *Radiation damage theory*, in *Comprehensive Nuclear Materials*, Elsevier, Amsterdam (2012). [p. 52]

[132] Cheng Y.-T., *Thermodynamic and fractal geometric aspects of ion-solid interactions*, Materials Science Reports **5**, 45–97 (1990). [p. 52]

[133] Nastasi M. & Mayer J., *Ion beam mixing in metallic and semiconductor materials*, Materials Science and Engineering: R: Reports **12**, 1–52 (1994). [p. 52]

[134] Bolse W., *Mechanisms of ion beam induced atomic mixing in solids*, Materials Science and Engineering: A **253**, 194–201 (1998). [p. 52]

[135] Sigmund P. & Gras-Marti A., *Theoretical aspects of atomic mixing by ion beams*, Nuclear Instruments and Methods **182–183**, 25–41 (1981). [p. 52]

[136] Johnson W., Cheng Y., Van Rossum M. & Nicolet M.-A., *When is thermodynamics relevant to ion-induced atomic rearrangements in metals?*, Nuclear Instruments and Methods in Physics Research Section B: Beam Interactions with Materials and Atoms **7–8**, 657–665 (1985). [pp. 53, 54]

[137] Miedema A., *The heat of formation of alloys*, Phillips Technical Review **36**, 8 (1976). [p. 54]

[138] Debski A., Debski R. & Gasior W., *New Features of Entall Database: Comparison of Experimental and Model Formation Enthalpies/ Nowe Funkcje Bazy Danych Entall: Porównanie Doświadczalnych I Modelowych Entalpii Tworzenia*, Archives of Metallurgy and Materials **59**, 1337–1343 (2014). [p. 54]

[139] Traverse A., Boité M. G. L. & Martin G., *Quantitative Description of Mixing with Light Ions*, Europhysics Letters (EPL) **8**, 633–637 (1989). [p. 54]

[140] Yuasa S., Suzuki Y., Katayama T. & Ando K., *Characterization of growth and crystallization processes in CoFeB/MgO/CoFeB magnetic tunnel junction structure by reflective high-energy electron diffraction*, Applied Physics Letters **87**, 242503 (2005). [p. 55]

[141] Rumaiz A. K., Woicik J. C., Wang W. G., Jordan-Sweet J., Jaffari G. H., Ni C., Xiao J. Q. & Chien C. L., *Effects of annealing on the local structure of Fe and Co in CoFeB/MgO/CoFeB tunnel junctions: An extended x-ray-absorption fine structure study*, Applied Physics Letters **96**, 112502 (2010). [p. 55]

[142] Wang S., Li M., Zhang S., Fang S., Wang D. & Yu G., *High annealing tolerance and the microstructure study in perpendicular magnetized MgO/CoFeB/MgO structures with thin W spacer layer*, Journal of Magnetism and Magnetic Materials **479**, 121–125 (2019). [p. 55]

[143] Im J. S. & Atwater H. A., *Ion irradiation enhanced crystal nucleation in amorphous Si thin films*, Applied Physics Letters **57**, 1766–1768 (1990). [pp. 55, 59]

[144] Spinella C., Lombardo S. & Priolo F., *Crystal grain nucleation in amorphous silicon*, Journal of Applied Physics **84**, 5383–5414 (1998). [pp. 55, 58, 59]

[145] Devolder T., Barisic I., Eimer S., Garcia K., Adam J.-P., Ockert B. & Ravelosona D., *Irradiation-induced tailoring of the magnetism of CoFeB/MgO ultrathin films*, Journal of Applied Physics **113**, 203912 (2013). [pp. 55, 66, 67, 72, 73, 75]

[146] Frost H. & Russell K., *Recoil resolution and particle stability under irradiation*, Journal of Nuclear Materials **104**, 1427–1432 (1981). [p. 58]

[147] Martin G., *Phase stability under irradiation: Ballistic effects*, Physical Review B **30**, 1424–1436 (1984). [p. 58]

[148] Olson G. & Roth J., *Kinetics of solid phase crystallization in amorphous silicon*, Materials Science Reports **3**, 1–77 (1988). [p. 59]

[149] Williams J. S., Elliman R. G., Brown W. L. & Seidel T. E., *Dominant Influence of Beam-Induced Interface Rearrangement on Solid-Phase Epitaxial Crystallization of Amorphous Silicon*, Physical Review Letters **55**, 1482–1485 (1985). [p. 59]

[150] Metherell A. J. *Energy Analyzing and Energy Selecting Electron Microscopes - Reprinted from Advances in Optical and Electron Microscopy volume 4 (1971) 263–360.*, in *Advances in Imaging and Electron Physics*, Elsevier (2017). [p. 60]

[151] Hill R., Notte J. A. & Scipioni L. *Scanning Helium Ion Microscopy*, in *Advances in Imaging and Electron Physics*, Elsevier (2012). [p. 61]

[152] Fassbender J. & McCord J., *Magnetic patterning by means of ion irradiation and implantation*, Journal of Magnetism and Magnetic Materials **320**, 579–596 (2008). [pp. 61, 63]

[153] McCord J., Gemming T., Schultz L., Fassbender J., Liedke M. O., Frommberger M. & Quandt E., *Magnetic anisotropy and domain patterning of amorphous films by He-ion irradiation*, Applied Physics Letters **86**, 162502 (2005). [p. 63]

[154] Devolder T., Chappert C., Chen Y., Cambril E., Bernas H., Jamet J. P. & Ferré J., *Sub-50 nm planar magnetic nanostructures fabricated by ion irradiation*, Applied Physics Letters **74**, 3383–3385 (1999). [p. 63]

[155] Mahendra A., Gupta P., Granville S. & Kennedy J., *Tailoring of magnetic anisotropy by ion irradiation for magnetic tunnel junction sensors*, Journal of Alloys and Compounds **910**, 164902 (2022). [pp. 63, 121]

[156] Fert A., Reyren N. & Cros V., *Magnetic skyrmions: Advances in physics and potential applications*, Nature Reviews Materials **2**, 17031 (2017). [p. 63]

[157] Bernas H., Devolder T., Chappert C., Ferré J., Kottler V., Chen Y., Vieu C., Jamet J., Mathet V., Cambril E., Kaitasov O., Lemerle S., Rousseaux F. & Launois H., *Ion beam induced magnetic nanostructure patterning*, Nuclear Instruments and Methods in Physics Research Section B: Beam Interactions with Materials and Atoms **148**, 872–879 (1999). [p. 63]

[158] Terris B. D., Folks L., Weller D., Baglin J. E. E., Kellock A. J., Rothuizen H. & Vettiger P., *Ion-beam patterning of magnetic films using stencil masks*, Applied Physics Letters **75**, 403–405 (1999). [p. 63]

[159] Warin P., Hyndman R., Glerak J., Chapman J. N., Ferré J., Jamet J. P., Mathet V. & Chappert C., *Modification of Co/Pt multilayers by gallium irradiation—Part 2: The effect of patterning using a highly focused ion beam*, Journal of Applied Physics **90**, 3850–3855 (2001). [p. 63]

[160] Blomeier S., Hillebrands B., Demidov V. E., Demokritov S. O., Reuscher B., Brodyanski A. & Kopnarski M., *Magnetic patterning of Fe/Cr/Fe(001) trilayers by Ga+ ion irradiation*, Journal of Applied Physics **98**, 093503 (2005). [p. 63]

[161] Aziz A., Bending S. J., Roberts H., Crampin S., Heard P. J. & Marrows C. H., *Artificial domain structures realized by local gallium focused Ion-beam modification of Pt/Co/Pt trilayer transport structure*, Journal of Applied Physics **98**, 124102 (2005). [p. 63]

[162] Ferré J., Chappert C., Bernas H., Jamet J.-P., Meyer P., Kaitasov O., Lemerle S., Mathet V., Rousseaux F. & Launois H., *Irradiation induced effects on magnetic properties of Pt/Co/Pt ultrathin films*, Journal of Magnetism and Magnetic Materials **198–199**, 191–193 (1999). [p. 63]

[163] Devolder T., *Light ion irradiation of Co/Pt systems: Structural origin of the decrease in magnetic anisotropy*, Physical Review B **62**, 5794–5802 (2000). [pp. 63, 64]

[164] Hyndman R., Warin P., Gierak J., Ferré J., Chapman J. N., Jamet J. P., Mathet V. & Chappert C., *Modification of Co/Pt multilayers by gallium irradiation—Part 1: The effect on structural and magnetic properties*, Journal of Applied Physics **90**, 3843–3849 (2001). [p. 63]

[165] Rettner C. T., Anders S., Baglin J. E. E., Thomson T. & Terris B. D., *Characterization of the magnetic modification of Co/Pt multilayer films by He+, Ar+, and Ga+ ion irradiation*, Applied Physics Letters **80**, 279–281 (2002). [pp. 63, 64]

[166] Vieu C., Gierak J., Launois H., Aign T., Meyer P., Jamet J. P., Ferré J., Chappert C., Devolder T., Mathet V. & Bernas H., *Modifications of magnetic properties of Pt/Co/Pt thin layers by focused gallium ion beam irradiation*, Journal of Applied Physics **91**, 3103–3110 (2002). [p. 63]

[167] Devolder T., Bernas H., Ravelosona D., Chappert C., Pizzini S., Vogel J., Ferré J., Jamet J.-P., Chen Y. & Mathet V., *Beam-induced magnetic property modifications: Basics, nanostructure fabrication and potential applications*, Nuclear Instruments and Methods in Physics Research Section B: Beam Interactions with Materials and Atoms **175–177**, 375–381 (2001). [p. 64]

[168] Franken J. H., Hoeijmakers M., Lavrijsen R. & Swagten H. J. M., *Domain-wall pinning by local control of anisotropy in Pt/Co/Pt strips*, Journal of Physics: Condensed Matter **24**, 024216 (2012). [pp. 64, 68]

[169] Sakamaki M., Amemiya K., Sveklo I., Mazalski P., Liedke M. O., Fassbender J., Kurant Z., Wawro A. & Maziewski A., *Formation of Co nanodisc with enhanced perpendicular magnetic anisotropy driven by Ga + ion irradiation on Pt/Co/Pt films*, Physical Review B **94**, 174422 (2016). [p. 64]

[170] Sud A., Tacchi S., Sagkovits D., Barton C., Sall M., Diez L. H., Stylianidis E., Smith N., Wright L., Zhang S., Zhang X., Ravelosona D., Carlotti G., Kurebayashi H., Kazakova O. & Cubukcu M., *Tailoring interfacial effect in multilayers with Dzyaloshinskii–Moriya interaction by helium ion irradiation*, Scientific Reports **11**, 23626 (2021). [pp. 64, 65]

[171] Juge R., Bairagi K., Rana K. G., Vogel J., Sall M., Mailly D., Pham V. T., Zhang Q., Sisodia N., Foerster M., Aballe L., Belmeguenai M., Roussigné Y., Auffret S., Buda-Prejbeanu L. D., Gaudin G., Ravelosona D. & Boulle O., *Helium Ions Put Magnetic Skyrmions on the Track*, Nano Letters acs.nanolett.1c00136 (2021). [pp. 64, 65, 68]

[172] An S., Baek E., Kim J.-A., Lee K.-S. & You C.-Y., *Improved spin–orbit torque induced magnetization switching efficiency by helium ion irradiation*, Scientific Reports **12**, 3465 (2022). [pp. 64, 69]

[173] de Jong M. C. H., Meijer M. J., Lucassen J., van Liempt J., Swagten H. J. M., Koopmans B. & Lavrijsen R., *Local control of magnetic interface effects in chiral Ir / Co / Pt multilayers using Ga + ion irradiation*, Physical Review B **105**, 064429 (2022). [p. 64]

[174] Herrera Diez L., García-Sánchez F., Adam J.-P., Devolder T., Eimer S., El Hadri M. S., Lamperti A., Mantovan R., Ocker B. & Ravelosona D., *Controlling magnetic domain wall motion in the creep regime in He + -irradiated CoFeB/MgO films with perpendicular anisotropy*, Applied Physics Letters **107**, 032401 (2015). [pp. 64, 65, 67, 68, 91, 93, 95, 98, 110]

[175] Mendisch S., Riente F., Ahrens V., Gnoli L., Haider M., Opel M., Kiechle M., Ruo Roch M. & Becherer M., *Controlling Domain-Wall Nucleation in Ta / Co - Fe - B / Mg O Nanomagnets via Local Ga + Ion Irradiation*, Physical Review Applied **16**, 014039 (2021). [p. 64]

[176] Zhao X., Zhang B., Vernier N., Zhang X., Sall M., Xing T., Diez L. H., Hepburn C., Wang L., Durin G., Casiraghi A., Belmeguenai M., Roussigné Y., Stashkevich A., Chérif S. M., Langer J., Ocker B., Jaiswal S., Jakob G., Kläui M., Zhao W. & Ravelosona D., *Enhancing domain wall velocity through interface intermixing in W-CoFeB-MgO films with perpendicular anisotropy*, Applied Physics Letters **115**, 122404 (2019). [pp. 64, 65, 67, 74, 76, 81, 91, 93, 94, 95, 97, 98, 110]

[177] Balk A. L., Kim K.-W., Pierce D. T., Stiles M. D., Unguris J. & Stavis S. M., *Simultaneous control of the Dzyaloshinskii-Moriya interaction and magnetic anisotropy in nanomagnetic trilayers*, Physical Review Letters **119**, 077205 (2017). [p. 64]

[178] Herrera Diez L., Voto M., Casiraghi A., Belmeguenai M., Roussigné Y., Durin G., Lamperti A., Mantovan R., Sluka V., Jeudy V., Liu Y. T., Stashkevich A., Chérif S. M., Langer J., Ocker B., Lopez-Diaz L. & Ravelosona D., *Enhancement of the Dzyaloshinskii-Moriya interaction and domain wall velocity through interface intermixing in Ta/CoFeB/MgO*, Physical Review B **99**, 054431 (2019). [pp. 64, 65, 68, 76, 89, 91, 93]

[179] Nembach H. T., Jué E., Poetzger K., Fassbender J., Silva T. J. & Shaw J. M., *Tuning of the Dzyaloshinskii–Moriya interaction by He + ion irradiation*, Journal of Applied Physics **131**, 143901 (2022). [pp. 64, 65]

[180] Zimmermann B., Legrand W., Maccariello D., Reyren N., Cros V., Blügel S. & Fert A., *Dzyaloshinskii-Moriya interaction at disordered interfaces from* ab initio *theory: Robustness against intermixing and tunability through dusting*, Applied Physics Letters **113**, 232403 (2018). [pp. 64, 79]

[181] Nicolenco A., Tsyntsaru N., Fornell J., Pellicer E., Reklaitis J., Baltrunas D., Cesiulis H. & Sort J., *Mapping of magnetic and mechanical properties of Fe-W alloys electrodeposited from Fe(III)-based glycolate-citrate bath*, Materials & Design **139**, 429–438 (2018). [pp. 65, 78]

[182] Chien C. L., Liou S. H., Ha B. K. & Unruh K. M., *Rapidly quenched Fe $_x$ Ta $_{100-x}$ alloys*, Journal of Applied Physics **57**, 3539–3541 (1985). [p. 65]

[183] Varga L. & Doyle W. D., *Measurement of the crystalline anisotropy in sputtered single-crystal FeTaN thin films*, Journal of Applied Physics **79**, 4995 (1996). [p. 65]

[184] Ferré J., Devolder T., Bernas H., Jamet J. P., Repain V., Bauer M., Vernier N. & Chappert C., *Magnetic phase diagrams of He ion-irradiated Pt/Co/Pt ultrathin films*, Journal of Physics D: Applied Physics **36**, 3103–3108 (2003). [p. 65]

[185] Jiang S., Chung S., Herrera Diez L., Le T. Q., Magnusson F., Ravelosona D. & Åkerman J., *Tuning the magnetodynamic properties of all-perpendicular spin valves using He $^+$ irradiation*, AIP Advances **8**, 065309 (2018). [pp. 65, 66]

[186] Koch L., Samad F., Lenz M. & Hellwig O., *Manipulating the Energy Balance of Perpendicular-Anisotropy Synthetic Antiferromagnets by He $^+$ -Ion Irradiation*, Physical Review Applied **13**, 024029 (2020). [pp. 65, 66]

[187] Beens M., Lalieu M. L. M., Duine R. A. & Koopmans B., *The role of intermixing in all-optical switching of synthetic-ferrimagnetic multilayers*, AIP Advances **9**, 125133 (2019). [pp. 66, 110]

[188] Nagai Y., Senda M. & Toshima T., *Properties of ion-beam-sputtered Ni/Fe artificial lattice film*, Journal of Applied Physics **63**, 1136–1140 (1988). [pp. 66, 113, 117]

[189] Li P., van der Jagt J. W., Beens M., Hintermayr J., Verheijen M. A., Bruikman R., Barcones B., Juge R., Lavrijsen R., Ravelosona D. & Koopmans B., *Enhancing all-optical switching of magnetization by He ion irradiation*, Applied Physics Letters **121**, 172404 (2022). [pp. 66, 109, 120]

[190] Masciocchi G., van der Jagt J. W., Syskaki M.-A., Lamperti A., Wolff N., Lotnyk A., Langer J., Kienle L., Jakob G., Borie B., Kehlberger A., Ravelosona D. & Kläui M., *Control of magnetoelastic coupling in Ni/Fe multilayers using He $^+$ ion irradiation*, Applied Physics Letters **121**, 182401 (2022). [pp. 66, 109, 113, 114, 117, 120]

[191] Duine R. A., Lee K.-J., Parkin S. S. P. & Stiles M. D., *Synthetic antiferromagnetic spintronics*, Nature Physics **14**, 217–219 (2018). [p. 66]

[192] Nogués J., Sort J., Langlais V., Skumryev V., Suriñach S., Muñoz J. & Baró M., *Exchange bias in nanostructures*, Physics Reports **422**, 65–117 (2005). [p. 66]

[193] Ravelosona D., Chappert C., Mathet V. & Bernas H., *Chemical order induced by ion irradiation in FePt (001) films*, Applied Physics Letters **76**, 236–238 (2000). [p. 67]

[194] Bernas H., Attané J.-P., Heinig K.-H., Halley D., Ravelosona D., Marty A., Auric P., Chappert C. & Samson Y., *Ordering Intermetallic Alloys by Ion Irradiation: A Way to Tailor Magnetic Media*, Physical Review Letters **91**, 077203 (2003). [p. 67]

[195] Ravelosona D. *Process for treating a magnetic structure* (2016). [p. 67]

[196] van der Jagt J. W., Jeudy V., Thiaville A., Sall M., Vernier N., Herrera Diez L., Belmeguenai M., Roussigné Y., Chérif S. M., Fattouhi M., Lopez-Diaz L., Lamperti A., Juge R. & Ravelosona D., *Revealing Nanoscale Disorder in W / Co - Fe - B / MgO Ultrathin Films Using Domain-Wall Motion*, Physical Review Applied **18**, 054072 (2022). [pp. 67, 75, 91, 120]

[197] Devolder T., Ferré J., Chappert C., Bernas H., Jamet J.-P. & Mathet V., *Magnetic properties of He + -irradiated Pt/Co/Pt ultrathin films*, Physical Review B **64**, 064415 (2001). [p. 67]

[198] Repain V., Bauer M., Jamet J.-P., Ferré J., Mougin A., Chappert C. & Bernas H., *Creep motion of a magnetic wall: Avalanche size divergence*, Europhysics Letters (EPL) **68**, 460–466 (2004). [p. 67]

[199] Jamet J., Ferre J., Meyer P., Gierak J., Vieu C., Rousseaux F., Chappert C. & Mathet V., *Giant enhancement of the domain wall velocity in irradiated ultrathin magnetic nanowires*, IEEE Transactions on Magnetics **37**, 2120–2122 (2001). [p. 67]

[200] Cayssol F., Menéndez J. L., Ravelosona D., Chappert C., Jamet J.-P., Ferré J. & Bernas H., *Enhancing domain wall motion in magnetic wires by ion irradiation*, Applied Physics Letters **86**, 022503 (2005). [p. 67]

[201] Cormier M., Mougin A., Ferré J., Jamet J.-P., Weil R., Fassbender J., Baltz V. & Rodmacq B., *Fast propagation of weakly pinned domain walls and current-assisted magnetization reversal in He $^+$ -irradiated Pt/Co/Pt nanotracks*, Journal of Physics D: Applied Physics **44**, 215002 (2011). [p. 67]

[202] Lavrijsen R., Franken J. H., Kohlhepp J. T., Swagten H. J. M. & Koopmans B., *Controlled domain-wall injection in perpendicularly magnetized strips*, Applied Physics Letters **96**, 222502 (2010). [p. 68]

[203] Franken J. H., Hoeijmakers M., Lavrijsen R., Kohlhepp J. T., Swagten H. J. M., Koopmans B., van Veldhoven E. & Maas D. J., *Precise control of domain wall injection and pinning using helium and gallium focused ion beams*, Journal of Applied Physics **109**, 07D504 (2011). [p. 68]

[204] Burn D. M. & Atkinson D., *Control of domain wall pinning by localised focused Ga + ion irradiation on Au capped NiFe nanowires*, Journal of Applied Physics **116**, 163901 (2014). [p. 68]

[205] Franken J. H., Swagten H. J. M. & Koopmans B., *Shift registers based on magnetic domain wall ratchets with perpendicular anisotropy*, Nature Nanotechnology **7**, 499–503 (2012). [pp. 68, 122]

[206] Sapozhnikov M. V., Vdovichev S. N., Ermolaeva O. L., Gusev N. S., Fraerman A. A., Gusev S. A. & Petrov Yu. V., *Artificial dense lattice of magnetic bubbles*, Applied Physics Letters **109**, 042406 (2016). [p. 68]

[207] Zhang S., Petford-Long A. K. & Phatak C., *Creation of artificial skyrmions and antiskyrmions by anisotropy engineering*, Scientific Reports **6**, 31248 (2016). [p. 68]

[208] Fallon K., Hughes S., Zeissler K., Legrand W., Ajejas F., Maccariello D., McFadzean S., Smith W., McGrouther D., Collin S., Reyren N., Cros V., Marrows C. H. & McVitie S., *Controlled Individual Skyrmion Nucleation at Artificial Defects Formed by Ion Irradiation*, Small **16**, 1907450 (2020). [p. 68]

[209] Kern L.-M., Pfau B., Deinhart V., Schneider M., Klose C., Gerlinger K., Wittrock S., Engel D., Will I., Günther C. M., Liefferink R., Mentink J. H., Wintz S., Weigand M., Huang M.-J., Battistelli R., Metternich D., Büttner F., Höflich K. & Eisebitt S., *Deterministic Generation and Guided Motion of Magnetic Skyrmions by Focused He $^+$ -Ion Irradiation*, Nano Letters acs.nanolett.2c00670 (2022). [p. 68]

[210] Hu Y., Zhang S., Zhu Y., Song C., Huang J., Liu C., Meng X., Deng X., Zhu L., Guan C., Yang H., Si M., Zhang J. & Peng Y., *Precise Tuning of Skyrmion Density in a Controllable Manner by Ion Irradiation*, ACS Applied Materials & Interfaces acsami.2c07268 (2022). [p. 68]

[211] Ahrens V., Gnoli L., Giuliano D., Mendisch S., Kiechle M., Riente F. & Becherer M., *Skyrmion velocities in FIB irradiated W/CoFeB/MgO thin films*, AIP Advances **12**, 035325 (2022). [p. 68]

[212] Ahrens V., Kiesselbach C., Gnoli L., Giuliano D., Mendisch S., Kiechle M., Riente F. & Becherer M., *Skyrmions Under Control – FIB Irradiation as a Versatile Tool for Skyrmion Circuits*, Advanced Materials 2207321 (2022). [p. 68]

[213] Yun J., Zuo Y., Mao J., Chang M., Zhang S., Liu J. & Xi L., *Lowering critical current density for spin-orbit torque induced magnetization switching by ion irradiation*, Applied Physics Letters **115**, 032404 (2019). [p. 69]

[214] Zhao X., Liu Y., Zhu D., Sall M., Zhang X., Ma H., Langer J., Ocker B., Jaiswal S., Jakob G., Kläui M., Zhao W. & Ravelosona D., *Spin–orbit torque driven multi-level switching in He $^+$ irradiated W–CoFeB–MgO Hall bars with perpendicular anisotropy*, Applied Physics Letters **116**, 242401 (2020). [p. 69]

[215] Dunne P., Fowley C., Hlawacek G., Kurian J., Atcheson G., Colis S., Teichert N., Kundys B., Venkatesan M., Lindner J., Deac A. M., Hermans T. M., Coey J. M. D. & Doudin B., *Helium Ion Microscopy for Reduced Spin Orbit Torque Switching Currents*, Nano Letters **20**, 7036–7042 (2020). [p. 69]

[216] Vedmedenko E. Y., Riego P., Arregi J. A. & Berger A., *Interlayer Dzyaloshinskii-Moriya Interactions*, Physical Review Letters **122**, 257202 (2019). [p. 69]

[217] Yang H., Liang J. & Cui Q., *First-principles calculations for Dzyaloshinskii–Moriya interaction*, Nature Reviews Physics (2022). [p. 69]

[218] Zhang X., Vernier N., Zhao W., Vila L. & Ravelosona D., *Extrinsic pinning of magnetic domain walls in CoFeB-MgO nanowires with perpendicular anisotropy*, AIP Advances **8**, 056307 (2018). [pp. 69, 91]

[219] Herrera Diez L., Jeudy V., Durin G., Casiraghi A., Liu Y. T., Voto M., Agnus G., Bouville D., Vila L., Langer J., Ocker B., Lopez-Diaz L. & Ravelosona D., *Wire edge dependent magnetic domain wall creep*, Physical Review B **98**, 054417 (2018). [pp. 69, 91, 92, 93, 102, 105]

[220] Kawahara T., Ito K., Takemura R. & Ohno H., *Spin-transfer torque RAM technology: Review and prospect*, Microelectronics Reliability **52**, 613–627 (2012). [p. 71]

[221] Kent A. D. & Worledge D. C., *A new spin on magnetic memories*, Nature Nanotechnology **10**, 187–191 (2015). [p. 71]

[222] Apalkov D., Dieny B. & Slaughter J. M., *Magnetoresistive Random Access Memory*, Proceedings of the IEEE **104**, 1796–1830 (2016). [p. 71]

[223] Khvalkovskiy A. V., Apalkov D., Watts S., Chepulskii R., Beach R. S., Ong A., Tang X., Driskill-Smith A., Butler W. H., Visscher P. B., Lottis D., Chen E., Nikitin V. & Krounbi M., *Basic principles of STT-MRAM cell operation in memory arrays*, Journal of Physics D: Applied Physics **46**, 074001 (2013). [p. 71]

[224] Freitas P. P., Ferreira R. & Cardoso S., *Spintronic Sensors*, Proceedings of the IEEE **104**, 1894–1918 (2016). [p. 71]

[225] Hirohata A., Sukegawa H., Yanagihara H., Zutic I., Seki T., Mizukami S. & Swaminathan R., *Roadmap for Emerging Materials for Spintronic Device Applications*, IEEE Transactions on Magnetics **51**, 1–11 (2015). [p. 72]

[226] Liu X., Zhang W., Carter M. J. & Xiao G., *Ferromagnetic resonance and damping properties of CoFeB thin films as free layers in MgO-based magnetic tunnel junctions*, Journal of Applied Physics **110**, 033910 (2011). [p. 72]

[227] Ikeda S., Miura K., Yamamoto H., Mizunuma K., Gan H. D., Endo M., Kanai S., Hayakawa J., Matsukura F. & Ohno H., *A perpendicular-anisotropy CoFeB–MgO magnetic tunnel junction*, Nature Materials **9**, 721–724 (2010). [p. 72]

[228] Ikeda S., Hayakawa J., Ashizawa Y., Lee Y. M., Miura K., Hasegawa H., Tsunoda M., Matsukura F. & Ohno H., *Tunnel magnetoresistance of 604% at 300K by suppression of Ta diffusion in CoFeB/MgO/CoFeB pseudo-spin-valves annealed at high temperature*, Applied Physics Letters **93**, 082508 (2008). [p. 72]

[229] Butler W. H., Zhang X.-G., Schulthess T. C. & MacLaren J. M., *Spin-dependent tunneling conductance of Fe | MgO | Fe sandwiches*, Physical Review B **63**, 054416 (2001). [p. 72]

[230] Djayaprawira D. D., Tsunekawa K., Nagai M., Maehara H., Yamagata S., Watanabe N., Yuasa S., Suzuki Y. & Ando K., *230% room-temperature magnetoresistance in CoFeB/MgO/CoFeB magnetic tunnel junctions*, Applied Physics Letters **86**, 092502 (2005). [p. 72]

[231] Hayakawa J., Ikeda S., Lee Y. M., Matsukura F. & Ohno H., *Effect of high annealing temperature on giant tunnel magnetoresistance ratio of CoFeB/MgO/CoFeB magnetic tunnel junctions*, Applied Physics Letters **89**, 232510 (2006). [p. 72]

[232] Chatterjee J., Tahmasebi T., Swerts J., Kar G. S. & De Boeck J., *Impact of seed layer on post-annealing behavior of transport and magnetic properties of Co/Pt multilayer-based bottom-pinned perpendicular magnetic tunnel junctions*, Applied Physics Express **8**, 063002 (2015). [p. 72]

[233] Brataas A., Kent A. D. & Ohno H., *Current-induced torques in magnetic materials*, Nature Materials **11**, 372–381 (2012). [p. 76]

[234] Emori S., Bauer U., Ahn S.-M., Martinez E. & Beach G. S. D., *Current-driven dynamics of chiral ferromagnetic domain walls*, Nature Materials **12**, 611–616 (2013). [p. 76]

[235] Lavrijsen R., Hartmann D. M. F., van den Brink A., Yin Y., Barcones B., Duine R. A., Verheijen M. A., Swagten H. J. M. & Koopmans B., *Asymmetric magnetic bubble expansion under in-plane field in Pt/Co/Pt: Effect of interface engineering*, Physical Review B **91**, 104414 (2015). [pp. 76, 91]

[236] Metaxas P. J., Jamet J. P., Mougin A., Cormier M., Ferré J., Baltz V., Rodmacq B., Dieny B. & Stamps R. L., *Creep and Flow Regimes of Magnetic Domain-Wall Motion in Ultrathin Pt / Co / Pt Films with Perpendicular Anisotropy*, Physical Review Letters **99**, 217208 (2007). [pp. 76, 91]

[237] Quinteros C. P., Bustingorry S., Curiale J. & Granada M., *Correlation between domain wall creep parameters of thin ferromagnetic films*, Applied Physics Letters **112**, 262402 (2018). [pp. 76, 91]

[238] Caballero N. B., Ferrero E. E., Kolton A. B., Curiale J., Jeudy V. & Bustingorry S., *Magnetic domain wall creep and depinning: A scalar field model approach*, Physical Review E **97**, 062122 (2018). [p. 76]

[239] Géhanne P., Rohart S., Thiaville A. & Jeudy V., *Strength and length scale of the interaction between domain walls and pinning disorder in thin ferromagnetic films*, Physical Review Research **2**, 043134 (2020). [pp. 76, 80, 81, 82, 83, 86, 93, 97]

[240] Benninghoven A., *Chemical Analysis of Inorganic and Organic Surfaces and Thin Films by Static Time-of-Flight Secondary Ion Mass Spectrometry (TOF-SIMS)*, Angewandte Chemie International Edition in English **33**, 1023–1043 (1994). [p. 77]

[241] Van Vaeck L., Adriaens A. & Gijbels R., *Static secondary ion mass spectrometry (S-SIMS) Part 1: Methodology and structural interpretation*, Mass Spectrometry Reviews **18**, 1–47 (1999). [p. 77]

[242] Adriaens A., Van Vaeck L. & Adams F., *Static secondary ion mass spectrometry (S-SIMS) Part 2: Material science applications*, Mass Spectrometry Reviews **18**, 48–81 (1999). [p. 77]

[243] Pellegren J. P. & Sokalski V. M., *Thickness and Interface-Dependent Crystallization of CoFeB Alloy Thin Films*, IEEE Transactions on Magnetics **51**, 1–3 (2015). [p. 77]

[244] Greer A. A., Gray A. X., Kanai S., Kaiser A. M., Ueda S., Yamashita Y., Bordel C., Palsson G., Maejima N., Yang S.-H., Conti G., Kobayashi K., Ikeda S., Matsukura F., Ohno H., Schneider C. M., Kortright J. B., Hellman F. & Fadley C. S., *Observation of boron diffusion in an annealed Ta/CoFeB/MgO magnetic tunnel junction with standing-wave hard x-ray photoemission*, Applied Physics Letters **101**, 202402 (2012). [p. 77]

[245] Soucaille R., Belmeguenai M., Torrejon J., Kim J.-V., Devolder T., Roussigné Y., Chérif S.-M., Stashkevich A. A., Hayashi M. & Adam J.-P., *Probing the Dzyaloshinskii-Moriya interaction in CoFeB ultrathin films using domain wall creep and Brillouin light spectroscopy*, Physical Review B **94**, 104431 (2016). [p. 80]

[246] Magni A., Carlotti G., Casiraghi A., Darwin E., Durin G., Diez L. H., Hickey B. J., Huxtable A., Hwang C. Y., Jakob G., Kim C., Kläui M., Langer J., Marrows C. H., Nembach H. T., Ravelosona D., Riley G. A., Shaw J. M., Sokalski V., Tacchi S. & Kuepferling M., *Key points in the determination of the interfacial Dzyaloshinskii-Moriya interaction from asymmetric bubble domain expansion*, IEEE Transactions on Magnetics **58**, 1–16 (2022). [p. 80]

[247] Cortés Burgos M. J., Guruciaga P. C., Jordán D., Quinteros C. P., Agoritsas E., Curiale J., Granada M. & Bustingorry S., *Field-dependent roughness of moving domain walls in a Pt/Co/Pt magnetic thin film*, Physical Review B **104**, 144202 (2021). [p. 80]

[248] Zeissler K., Mruczkiewicz M., Finizio S., Raabe J., Shepley P. M., Sadovnikov A. V., Nikitov S. A., Fallon K., McFadzean S., McVitie S., Moore T. A., Burnell G. & Marrows C. H., *Pinning and hysteresis in the field dependent diameter evolution of skyrmions in Pt/Co/Ir superlattice stacks*, Scientific Reports **7**, 15125 (2017). [pp. 82, 84, 98, 105]

[249] Vansteenkiste A., Leliaert J., Dvornik M., Helsen M., Garcia-Sanchez F. & Van Waeyenberge B., *The design and verification of MuMax3*, AIP Advances **4**, 107133 (2014). [p. 84]

[250] Mulkers J., Van Waeyenberge B. & Milošević M. V., *Effects of spatially engineered Dzyaloshinskii-Moriya interaction in ferromagnetic films*, Physical Review B **95**, 144401 (2017). [p. 84]

[251] Kim J.-V. & Yoo M.-W., *Current-driven skyrmion dynamics in disordered films*, Applied Physics Letters **110**, 132404 (2017). [pp. 84, 87]

[252] Gross I., Akhtar W., Hrabec A., Sampaio J., Martínez L. J., Chouaieb S., Shields B. J., Maletinsky P., Thiaville A., Rohart S. & Jacques V., *Skyrmion morphology in ultrathin magnetic films*, Physical Review Materials **2**, 024406 (2018). [p. 86]

[253] Legrand W., Maccariello D., Reyren N., Garcia K., Moutafis C., Moreau-Luchaire C., Collin S., Bouzehouane K., Cros V. & Fert A., *Room-Temperature Current-Induced Generation and Motion of sub-100 nm Skyrmions*, Nano Letters **17**, 2703–2712 (2017). [p. 87]

[254] Juge R., Je S.-G., Chaves D. d. S., Buda-Prejbeanu L. D., Peña-Garcia J., Nath J., Miron I. M., Rana K. G., Aballe L., Foerster M., Genuzio F., Menteş T. O., Locatelli A., Maccherozzi F., Dhesi S. S., Belmeguenai M., Roussigné Y., Auffret S., Pizzini S., Gaudin G., Vogel J. & Boulle O., *Current-Driven Skyrmion Dynamics and Drive-Dependent Skyrmion Hall Effect in an Ultrathin Film*, Physical Review Applied **12**, 044007 (2019). [p. 87]

[255] Devolder T., Ducrot P.-H., Adam J.-P., Barisic I., Vernier N., Kim J.-V., Ockert B. & Ravelosona D., *Damping of* $Co_x Fe_{80-x} B_{20}$ *ultrathin films with perpendicular magnetic anisotropy*, Applied Physics Letters **102**, 022407 (2013). [p. 88]

[256] Shaw J. M., Nembach H. T., Silva T. J. & Boone C. T., *Precise determination of the spectroscopic* g *-factor by use of broadband ferromagnetic resonance spectroscopy*, Journal of Applied Physics **114**, 243906 (2013). [p. 88]

[257] Mills D. L. & Rezende Sergio. M. *Spin Damping in Ultrathin Magnetic Films*, in *Spin Dynamics in Confined Magnetic Structures II*, Springer, Berlin ; New York (2003). [p. 89]

[258] Digiacomo A., Mantovan R., Vernier N., Devolder T., Garcia K., Tallarida G., Fanciulli M., Lamperti A., Ocker B., Baldi L., Mariani M. & Ravelosona D., *Engineering Domain-Wall Motion in Co - Fe - B / Mg O Ultrathin Films with Perpendicular Anisotropy Using Patterned Substrates with Subnanometer Step Modulation*, Physical Review Applied **10**, 064053 (2018). [p. 91]

[259] Cayssol F., Ravelosona D., Chappert C., Ferré J. & Jamet J. P., *Domain Wall Creep in Magnetic Wires*, Physical Review Letters **92**, 107202 (2004). [p. 91]

[260] Herrera Diez L., Ummelen F., Jeudy V., Durin G., Lopez-Diaz L., Diaz-Pardo R., Casiraghi A., Agnus G., Bouville D., Langer J., Ocker B., Lavrijsen R., Swagten H. J. M. & Ravelosona D., *Magnetic domain wall curvature induced by wire edge pinning*, Applied Physics Letters **117**, 062406 (2020). [pp. 92, 102, 105]

[261] Balan C., van der Jagt J. W., Garcia J. P., Vogel J., Ranno L., Bonfim M., Ravelosona D., Pizzini S. & Jeudy V. *Control of domain wall and pinning disorder interaction by light He+ ion irradiation in Pt/Co/AlOx* (2022). [p. 98]

[262] Mougin A., Cormier M., Adam J. P., Metaxas P. J. & Ferre J., *Domain wall mobility, stability and Walker breakdown in magnetic nanowires*, Europhysics Letters (EPL) **78**, 57007 (2007). [p. 99]

[263] Bernand-Mantel A., Herrera Diez L., Ranno L., Pizzini S., Vogel J., Givord D., Auffret S., Boulle O., Miron I. M. & Gaudin G., *Electric-field control of domain wall nucleation and pinning in a metallic ferromagnet*, Applied Physics Letters **102**, 122406 (2013). [p. 105]

[264] Kimel A. V. & Li M., *Writing magnetic memory with ultrashort light pulses*, Nature Reviews Materials **4**, 189–200 (2019). [p. 109]

[265] Xu Y. & Mangin S., *Magnetization manipulation using ultra-short light pulses*, Journal of Magnetism and Magnetic Materials **564**, 170169 (2022). [p. 109]

[266] Polley D., Pattabi A., Chatterjee J., Mondal S., Jhuria K., Singh H., Gorchon J. & Bokor J., *Progress toward picosecond on-chip magnetic memory*, Applied Physics Letters **120**, 140501 (2022). [p. 109]

[267] Radu I., Vahaplar K., Stamm C., Kachel T., Pontius N., Dürr H. A., Ostler T. A., Barker J., Evans R. F. L., Chantrell R. W., Tsukamoto A., Itoh A., Kirilyuk A., Rasing Th. & Kimel A. V., *Transient ferromagnetic-like state mediating ultrafast reversal of antiferromagnetically coupled spins*, Nature **472**, 205–208 (2011). [p. 109]

[268] Ostler T., Barker J., Evans R., Chantrell R., Atxitia U., Chubykalo-Fesenko O., El Moussaoui S., Le Guyader L., Mengotti E., Heyderman L., Nolting F., Tsukamoto A., Itoh A., Afanasiev D., Ivanov B., Kalashnikova A., Vahaplar K., Mentink J., Kirilyuk A., Rasing Th. & Kimel A., *Ultrafast heating as a sufficient stimulus for magnetization reversal in a ferrimagnet*, Nature Communications **3**, 666 (2012). [pp. 109, 110]

[269] El-Ghazaly A., Gorchon J., Wilson R. B., Pattabi A. & Bokor J., *Progress towards ultrafast spintronics applications*, Journal of Magnetism and Magnetic Materials **502**, 166478 (2020). [p. 109]

[270] Lalieu M. L. M., Lavrijsen R. & Koopmans B., *Integrating all-optical switching with spintronics*, Nature Communications **10**, 110 (2019). [p. 109]

[271] Kim S. K., Beach G. S. D., Lee K.-J., Ono T., Rasing T. & Yang H., *Ferrimagnetic spintronics*, Nature Materials **21**, 24–34 (2022). [p. 109]

[272] Lalieu M. L. M., Peeters M. J. G., Haenen S. R. R., Lavrijsen R. & Koopmans B., *Deterministic all-optical switching of synthetic ferrimagnets using single femtosecond laser pulses*, Physical Review B **96**, 220411 (2017). [pp. 109, 110, 111]

[273] Li P., Kools T. J., Lavrijsen R. & Koopmans B. *Ultrafast racetrack based on compensated Co/Gd-based synthetic ferrimagnet with all-optical switching* (2022). [p. 109]

[274] Peeters M. J. G., van Ballegooie Y. M. & Koopmans B., *Influence of magnetic fields on ultrafast laser-induced switching dynamics in Co/Gd bilayers*, Physical Review B **105**, 014429 (2022). [p. 109]

[275] Wang L., Cheng H., Li P., van Hees Y. L. W., Liu Y., Cao K., Lavrijsen R., Lin X., Koopmans B. & Zhao W., *Picosecond optospintronic tunnel junctions*, Proceedings of the National Academy of Sciences **119**, e2204732119 (2022). [p. 109]

[276] van Hees Y. L. W., van de Meugheuvel P., Koopmans B. & Lavrijsen R., *Deterministic all-optical magnetization writing facilitated by non-local transfer of spin angular momentum*, Nature Communications **11**, 3835 (2020). [p. 109]

[277] Li P., Peeters M. J. G., van Hees Y. L. W., Lavrijsen R. & Koopmans B., *Ultra-low energy threshold engineering for all-optical switching of magnetization in dielectric-coated Co/Gd based synthetic-ferrimagnet*, Applied Physics Letters **119**, 252402 (2021). [p. 109]

[278] Wang L., van Hees Y. L. W., Lavrijsen R., Zhao W. & Koopmans B., *Enhanced all-optical switching and domain wall velocity in annealed synthetic-ferrimagnetic multilayers*, Applied Physics Letters **117**, 022408 (2020). [pp. 109, 110]

[279] Beens M., Lalieu M. L. M., Deenen A. J. M., Duine R. A. & Koopmans B., *Comparing all-optical switching in synthetic-ferrimagnetic multilayers and alloys*, Physical Review B **100**, 220409 (2019). [p. 110]

[280] Avilés-Félix L., Olivier A., Li G., Davies C. S., Álvaro-Gómez L., Rubio-Roy M., Auffret S., Kirilyuk A., Kimel A. V., Rasing Th., Buda-Prejbeanu L. D., Sousa R. C., Dieny B. & Prejbeanu I. L., *Single-shot all-optical switching of magnetization in Tb/Co multilayer-based electrodes*, Scientific Reports **10**, 5211 (2020). [p. 110]

[281] Gerlach S., Oroszlany L., Hinzke D., Sievering S., Wienholdt S., Szunyogh L. & Nowak U., *Modeling ultrafast all-optical switching in synthetic ferrimagnets*, Physical Review B **95**, 224435 (2017). [p. 110]

[282] Williams D. B. & Carter C. B., *Transmission electron microscopy: A textbook for materials science*, 2. ed, Springer, New York (2009). [pp. 110, 114]

[283] Hintermayr J., Ullrich A. & Albrecht M., *Structure and magnetic properties of ferrimagnetic [Gd/Fe]* $_{\mathrm{n}}$ *multilayer and Gd* $_{\mathrm{x}}$ *Fe* $_{100-\mathrm{x}}$ *thin films*, AIP Advances **11**, 095214 (2021). [p. 110]

[284] Hintermayr J., Safonova N. Y., Ullrich A. & Albrecht M., *Magnetic properties and structure of Gd-implanted* $\mathbf{L}\,\boldsymbol{1}_{0}$ *FePt thin films*, AIP Advances **9**, 055020 (2019). [p. 110]

[285] Möller W., Eckstein W. & Biersack J., *Tridyn-binary collision simulation of atomic collisions and dynamic composition changes in solids*, Computer Physics Communications **51**, 355–368 (1988). [p. 111]

[286] Schellekens A. J. & Koopmans B., *Microscopic model for ultrafast magnetization dynamics of multisublattice magnets*, Physical Review B **87**, 020407 (2013). [p. 111]

[287] Ota S., Ando A. & Chiba D., *A flexible giant magnetoresistive device for sensing strain direction*, Nature Electronics **1**, 124–129 (2018). [p. 113]

[288] García-Miquel H., Barrera D., Amat R., Kurlyandskaya G. & Sales S., *Magnetic actuator based on giant magnetostrictive material Terfenol-D with strain and temperature monitoring using FBG optical sensor*, Measurement **80**, 201–206 (2016). [p. 113]

[289] Senda M. & Nagai Y., *Magnetic properties of Fe/Co, Fe/CoFe, and (Fe/Co)/SiO* $_{2}$ *multilayer films*, Journal of Applied Physics **65**, 3151–3156 (1989). [pp. 113, 117]

[290] Rengarajan S., Yun E. J., Kang W. S. & Walser R. M., *Effect of intermixing on the magnetic properties of Co50Fe50/Ni80Fe20 multilayers*, Journal of Applied Physics **81**, 4761–4763 (1997). [pp. 113, 117]

[291] Jen S. & Lin C., *Magnetostriction and Young's modulus of [Fe15Ni85/Fe25Ni75] multilayers*, Thin Solid Films **471**, 218–223 (2005). [pp. 113, 117]

[292] Juraszek J., Grenier A., Teillet J., Tiercelin N., Petit F., Ben Youssef J. & Toulemonde M., *Swift ion irradiation of magnetostrictive multilayers*, Nuclear Instruments and Methods in Physics Research Section B: Beam Interactions with Materials and Atoms **245**, 157–160 (2006). [p. 113]

[293] Masciocchi G., Fattouhi M., Kehlberger A., Lopez-Diaz L., Syskaki M.-A. & Kläui M., *Strain-controlled domain wall injection into nanowires for sensor applications*, Journal of Applied Physics **130**, 183903 (2021). [p. 115]

[294] Bur A., Wu T., Hockel J., Hsu C.-J., Kim H. K. D., Chung T.-K., Wong K., Wang K. L. & Carman G. P., *Strain-induced magnetization change in patterned ferromagnetic nickel nanostructures*, Journal of Applied Physics **109**, 123903 (2011). [p. 115]

[295] Finizio S., Foerster M., Buzzi M., Krüger B., Jourdan M., Vaz C. A. F., Hockel J., Miyawaki T., Tkach A., Valencia S., Kronast F., Carman G. P., Nolting F. & Kläui M., *Magnetic Anisotropy Engineering in Thin Film Ni Nanostructures by Magnetoelastic Coupling*, Physical Review Applied **1**, 021001 (2014). [p. 115]

[296] Martin N., McCord J., Gerber A., Strache T., Gemming T., Mönch I., Farag N., Schäfer R., Fassbender J., Quandt E. & Schultz L., *Local stress engineering of magnetic anisotropy in soft magnetic thin films*, Applied Physics Letters **94**, 062506 (2009). [p. 115]

[297] Choe G. & Megdal B., *High precision magnetostriction measurement employing the B-H looper bending method*, IEEE Transactions on Magnetics **35**, 3959–3961 (1999). [p. 115]

[298] Raghunathan A., Snyder J. E. & Jiles D. C., *Comparison of Alternative Techniques for Characterizing Magnetostriction and Inverse Magnetostriction in Magnetic Thin Films*, IEEE Transactions on Magnetics **45**, 3269–3273 (2009). [p. 115]

[299] Hill C. B., Hendren W. R., Bowman R. M., McGeehin P. K., Gubbins M. A. & Venugopal V. A., *Whole wafer magnetostriction metrology for magnetic films and multilayers*, Measurement Science and Technology **24**, 045601 (2013). [p. 115]

[300] Cullity B. D. & Graham C. D., *Introduction to magnetic materials*, 2nd ed, IEEE/Wiley, Hoboken, N.J (2009). [p. 117]

[301] Hollingworth M. P., Gibbs M. R. J. & Murdoch S. J., *Magnetostriction and surface roughness of ultrathin NiFe films deposited on SiO2*, Journal of Applied Physics **94**, 7235–7239 (2003). [p. 117]

[302] Favieres C., Vergara J. & Madurga V., *Interface effects on magnetostriction in pulsed laser deposited Co/Fe/Co cylindrical soft magnetic multilayers*, Journal of Physics D: Applied Physics **40**, 4101–4108 (2007). [p. 117]

[303] Jen S., Wu T., Lin C. & Chang K., *Anisotropic magnetoresistance and magnetostriction of [Fe15Ni85/Fe25Ni75] and [Co35Ni65/Fe25Ni75] multilayers*, Solid State Communications **132**, 259–262 (2004). [p. 117]

[304] Mayer J., Giannuzzi L. A., Kamino T. & Michael J., *TEM Sample Preparation and FIB-Induced Damage*, MRS Bulletin **32**, 400–407 (2007). [p. 121]

[305] Yuan H. Y. & Wang X. R., *Domain wall pinning in notched nanowires*, Physical Review B **89**, 054423 (2014). [p. 122]

[306] Kiechle M., Papp A., Mendisch S., Ahrens V., Golibrzuch M., Bernstein G. H., Porod W., Csaba G. & Becherer M. *Spin-Wave Optics in YIG by Ion-Beam Irradiation* (2022). [p. 122]

[307] Mohseni M., Hillebrands B., Pirro P. & Kostylev M., *Controlling the propagation of dipole-exchange spin waves using local inhomogeneity of the anisotropy*, Physical Review B **102**, 014445 (2020). [p. 122]

[308] Deenen A. J. M. *Simulating spin waves in electrically gated thin film Co.* MSc. Thesis Eindhoven University of Technology, Eindhoven (2021). [p. 122]

[309] Nichterwitz M., Honnali S., Kutuzau M., Guo S., Zehner J., Nielsch K. & Leistner K., *Advances in magneto-ionic materials and perspectives for their application*, APL Materials **9**, 030903 (2021). [p. 122]

[310] Pachat R., Ourdani D., van der Jagt J., Syskaki M.-A., Di Pietro A., Roussigné Y., Ono S., Gabor M., Chérif M., Durin G., Langer J., Belmeguenai M., Ravelosona D. & Diez L. H., *Multiple Magnetoionic Regimes in Ta/Co 20 Fe 60 B 20 / Hf O 2*, Physical Review Applied **15**, 064055 (2021). [p. 122]

[311] Pachat R., Ourdani D., Syskaki M.-A., Lamperti A., Roy S., Chen S., Pietro A. D., Largeau L., Juge R., Massouras M., Balan C., van der Jagt J. W., Agnus G., Roussigné Y., Gabor M., Chérif S. M., Durin G., Ono S., Langer J., Querlioz D., Ravelosona D., Belmeguenai M. & Herrera Diez L., *Magneto-Ionics in Annealed W/CoFeB/HfO $_2$ Thin Films*, Advanced Materials Interfaces 2200690 (2022). [p. 122]

Curriculum Vitae

Johannes Wilhelmus (Gyan) van der Jagt was born on December 14, 1995 in Ter Aar, the Netherlands. After finishing high school in 2014 at the Pax Christi College in Druten, the Netherlands, he studied Applied Physics at the Eindhoven University of Technology. In 2017 he obtained his Bachelor degree with his project on Magnetic Force Microscopy on Skyrmionic Systems in the Physics of Nanostructures Group under the supervision of dr. ir. J. Lucassen and prof. dr. ir. H.J.M. Swagten.

Gyan continued his studies at the Eindhoven University of Technology and obtained his Master's degree in Applied Physics in 2019. During this time he carried out an external internship in the Materials and Condensed Matter Physics group of prof. dr. Steven McVitie at the University of Glasgow, United Kingdom, where he worked on a Lorentz TEM investigation of skyrmion grain boundary effects in B20 FeGe helimagnets, under the supervision or dr. Damien McGrouther. He graduated with a project in the Physics of Nanostructures Group at Eindhoven University of Technology under the supervision of dr. Marielle Meijer and dr. ir Reinoud Lavrijsen on Ga^+ irradiation for zero-field skyrmion stabilization: Towards imaging skyrmions with SEMPA.

After obtaining his Master's degree, Gyan continued with a PhD project at the Université de Paris-Saclay in Palaiseau, France. The PhD project is conducted in the start-up company Spin-Ion Technologies and at the Centre de Nanosciences et de Nanotechnologies, under the supervision of dr. Dafiné Ravelosona and under the co-supervision of dr. Liza Herrera Diez. His PhD project is part of the MagnEFi ITN, funded by the European Union's Horizon 2020 research and innovation programme under the Marie Skłodowska-Curie grant agreement No. 860060 "Magnetism and the effect of Electric Field" (MagnEFi). The main results of this project are presented in this thesis.

Publications

1. G. Masciocchi, **J.W. van der Jagt**, M.-A. Syskaki, J. Langer, G. Jakob, J. McCord, B. Borie, A. Kehlberger, D. Ravelosona, and M. Kläui, "Optimization of Permalloy properties for magnetic field sensors using He^+ irradiation," *Submitted to Physical Review Applied*, ArXiv:2302.14455 (2023); Link
2. C. Balan, **J.W. van der Jagt**, A. Fassatoui, J.P. Garcia, V. Jeudy, A. Thiaville, J. Vogel, M. Bonfim, L. Ranno, D. Ravelosona, and S. Pizzini, "Improving Néel domain walls dynamics and skyrmion stability using He ion irradiation," *Submitted to Small*, ArXiv:2303.04543 (2023); Link
3. C. Balan, **J.W. van der Jagt**, J.P. Garcia, J. Vogel, L. Ranno, M. Bonfim, D. Ravelosona, S. Pizzini, and V. Jeudy, "Control of the interaction between pinning disorder and domain walls in Pt/Co/AlOx ultrathin films by He^+ ion irradiation," *Accepted in Applied Physics Letters*, ArXiv:2303.04577 (2023); Link
4. **J.W. van der Jagt**, V. Jeudy, A. Thiaville, M. Sall, N. Vernier, L. Herrera Diez, M. Belmeguenai, Y. Roussigné, S.M. Chérif, M. Fattouhi, L. Lopez-Diaz, A. Lamperti, R. Juge, and D. Ravelosona, "Revealing Nanoscale Disorder in W/Co-Fe-B/MgO Ultrathin Films Using Domain-Wall Motion," *Physical Review Applied* **18**, 054072 (2022); Link
5. G. Masciocchi, **J.W. van der Jagt**, M.-A Syskaki, A. Lamperti, N. Wolff, A. Lotnyk, J. Langer, L. Kienle, G. Jakob, B. Borie, A. Kehlberger, D. Ravelosona, and M. Kläui, "Control of magnetoelastic coupling in Ni/Fe multilayers using He^+ ion irradiation," *Applied Physics Letters*, **121**, 182401 (2022); Link
6. P. Li, **J.W. van der Jagt**, M. Beens, J. Hintermayr, M.A. Verheijen, R. Bruikman, B. Barcones, R. Juge, R. Lavrijsen, D. Ravelosona, and B. Koopmans,"Enhancing all-optical switching of magnetization by He ion irradiation," *Applied Physics Letters* **121**, 172404 (2022); Link
7. R. Pachat, D. Ourdani, M.-A. Syskaki, A. Lamperti, S. Roy, S. Chen, A. Di Pietro, L. Largeau, R. Juge, M. Massouras, C. Balan, **J.W. van der Jagt**, G. Agnus, Y. Roussigné, M. Gabor, S.M. Chérif, G. Durin, S. Ono, J. Langer, D. Querlioz, M. Belmeguenai, and L. Herrera Diez, "Magneto-Ionics in Annealed W/CoFeB/HfO_2 Thin films," *Advanced Materials Interfaces*, 2200690 (2022); Link
8. A. Di Pietro, R. Pachat, L. Qiao, L. Herrera Diez, **J.W. van der Jagt**, D. Ravelosona, and G. Durin, "*Ab-initio* study of magneto-ionic mechanisms in ferromagnet/oxide multilayers," *Submitted to Physical Review B*, ArXiv:2204.11699 (2022); Link
9. R. Pachat, D. Ourdani, **J.W. van der Jagt**, M.-A. Syskaki, A. Di Pietro,, Y. Roussigné, S. Ono, M.S. Gabor, M. Chérif, G. Durin, J. Langer, M. Belmeguenai, D. Ravelosona, and L. Herrera Diez, "Multiple Magnetoionic Regimes in Ta/$Co_{20}Fe_{60}B_{20}$/HfO_2," *Physical Review Applied* **15**, 064055 (2021); Link
10. F. Rendell-Bhatti, R.J. Lamb, **J.W. van der Jagt**, G.W. Peterson, H.J.M. Swagten, and D. McGrouther, "Spontaneous creation and annihilation dynamics and strain-limited stability of magnetic skyrmions," *Nature Communications* **11**, 3536 (2020); Link

Résumé en Français

Avec l'avènement du big data, de l'informatique quantique et de l'intelligence artificielle, le stockage et le traitement des informations sont soumis à une demande exponentielle. Le besoin d'accroître sans cesse la capacité de stockage des données, la vitesse et réduire la faible consommation d'énergie représente un défi de taille pour le développement de dispositifs de stockage et de calcul de nouvelle génération. Une catégorie prometteuse de dispositifs capables de relever ces défis concerne le domaine de la spintronique où sont utilisés non seulement la charge des électrons mais aussi leur moment magnétique (ou spin).

Le domaine de la spintronique a été initié par la découverte de la magnétorésistance géante (GMR, giant magnetoresistance), puis développé avec l'avènement de la magnétorésistance tunnel (TMR, tunnel magnetoresistance) et du transfert de spin. Ces percées ont conduit au développement d'un nouveau type de mémoire non-volatile, la MRAM (magnetic random access memory). La MRAM code les informations dans des jonctions tunnel magnétique (MTJ, magnetic tunnel junction), où la valeur du bit (1 ou 0) dépend de l'orientation relative de deux couches ferromagnétiques (FM). Cette orientation peut être contrôlée par un courant électrique par l'intermédiaire du couple de transfert de spin (STT, spin-transfer torque) ou du couple spin-orbite (SOT, spin-orbit torque). Malgré des progrès importants avec la commercialisation des MRAM en 2019, la technologie est toujours confrontée à des verrous technologiques majeurs tels que la faible densité de stockage et les courants d'écriture élevés, liés en particulier à la présence de désordre structurale et de propriétés magnétiques des matériaux qui sont limitantes.

Un autre dispositif spintronique prometteur est le «racetrack memory »où les données sont stockées sous la forme de l'orientation de domaines magnétiques le long d'une piste. La région qui sépare deux domaines est appelée paroi magnétique et peut être mis en mouvement par STT ou SOT. Comme pour la MRAM, le concept de racetrack memory présente des verrous importants. Le principal obstacle est lié au désordre intrinsèque du matériau et au désordre extrinsèque induit par les procédés de nanofabrication, qui induisent un fort piégeage des parois magnétiques et augmentent les courants critiques pour faire avancer la paroi. De manière général, il est donc essentiel de réduire le désordre des matériaux et des nanocomposants à l'échelle atomique pour améliorer les performances des dispositifs spintroniques.

Dans cette thèse, nous utilisons une technique innovante basée sur l'irradiation post dépôt avec des ions He^+ pour réduire l'influence du désordre structural dans des dispositifs spintroniques. Les matériaux utilisés consistent en des structures de métal lourd (HM, heavy metal)/ferromagnétique (FM)/non-magnétique (NM) à anisotropie magnétique perpendiculaire, où chaque couche est seulement constituée de quelques atomes d'épaisseur. Les propriétés magnétiques de ces matériaux dépendent fortement de la structure des interfaces entre les différentes couches. Par exemple, l'anisotropie magnétique - importante pour obtenir une densité de stockage de données élevée - et l'interaction Dzyaloshinskii-Moriya - importante pour obtenir un mouvement des parois magnétiques rapide - dépendent toutes deux fortement de la structure de l'interface. Le mélange des interfaces, une forme importante de désordre dans ces films ultraminces, affecte fortement les performances. En particulier, les procédés de recuit thermique à haute température pour cristalliser ces films ainsi que les procédés de nanofabrication induisent des défauts qui limitent les fonctionnalités de ces dispositifs.

Comme nous le démontrons dans cette thèse, l'irradiation par des ions He^+ post-dépôt donne un nouveau degré de liberté pour optimiser les propriétés structurales et magnétiques des matériaux et des nanocomposants spintroniques. Comme les ions He^+ ont une faible masse, ils transfèrent une faible énergie aux atomes cibles, et seuls des déplacements inter-atomiques sont induits sans collisions en cascade ni pulvérisation de surface. Cette propriété unique fait de l'irradiation He^+ une technique post-croissance extrêmement polyvalente pour contrôler les propriétés structurales et magnétiques des films ultra-minces.

L'irradiation ionique des matériaux magnétiques est utilisée depuis la découverte par Chappert et al. que les propriétés magnétiques d'un film ultra-mince de Co/Pt peuvent être contrôlées par le mélange des interfaces Co/Pt induit par l'irradiation par des ions He^+. Depuis, de nombreux nouveaux défis technologiques sont apparus avec le développement en particulier des technologies MRAM et du concept de racetrack memory. Dans cette thèse, nous nous concentrons particulièrement sur les matériaux W/CoFeB/MgO, qui sont des matériaux archétypiques dans les MTJs et les dispositifs basés sur le mouvement des parois magnétiques en raison de leur forte TMR, leur anisotropie élevée et leur faible amortissement qui augmentent l'efficacité de ces dispositifs. Comme mentionné précédemment, le désordre intrinsèque et extrinsèque est l'un des principaux obstacles à la poursuite de l'intégration de la MRAM et du racetrack memory. C'est pourquoi, dans cette thèse, nous nous sommes focalisés sur la possibilité de relever plusieurs défis :

1. Amélioration du processus de cristallisation de films ultra-minces W/CoFeB/MgO par un procédé d'irradiation He^+ à température modérée.

2. Amélioration du mouvement des parois magnétiques dans les matériaux W/CoFeB/MgO et meilleure compréhension du rôle du désordre après la cristallisation et le mélange d'interfaces induit par irradiation par ions He^+.

3. Amélioration du mouvement des parois magnétiques dans les fils de W/CoFeB/MgO en réduisant l'influence des défauts de bord extrinsèques par irradiation par ions He^+.

Cette thèse a été préparée à Spin-Ion Technologies, une start-up issue du Centre de Nanosciences et de Nanotechnologies (Université Paris-Saclay et CNRS) qui développe des procédés d'irradiation ionique afin d'améliorer les matériaux magnétiques pour des applications dans le domaine de la spintronique, et qui fait partie d'un réseau international de formation (ITN) financé par l'Union Européenne nommé «Magnetism and the effects of Electric Fields (MagnEFi) ». Ce projet ITN a stimulé de nombreuses opportunités de collaborations qui nous ont permis d'explorer les effets de l'irradiation He^+ pour d'autres concepts spintroniques tels que la commutation tout-optique (AOS, all-optical switching), la magnétostriction, la transmission d'ondes de spin et la magnéto-ionique. Cette thèse contient les résultats de plusieurs de ces collaborations pour démontrer le potentiel majeur de l'irradiation par des ions He^+.

Nous donnons ci-dessous un bref résumé de nos principaux résultats qui répondent aux défis ci-dessus.

L'amélioration de la cristallisation des films ultra-minces de W/CoFeB/MgO est essentielle pour augmenter les performances des dispositifs MRAM et racetrack. En effet, la cristallisation est indispensable pour obtenir de grandes valeurs de TMR et d'anisotropie, mais les procédés actuels basés sur le recuit à haute température (>350°C) peuvent introduire des défauts structuraux dans les matériaux et entrainent généralement de grandes variations de propriétés entre les dispositifs. En outre, les procédés de recuit sont généralement longs (>1 heure), ce qui peut constituer un verrou pour le rendement de production.

Pour améliorer le procédé de cristallisation, nous nous nous sommes focalisés sur la cristallisation induite par irradiation, afin de répondre aux verrous technologiques induits par un pure recuit thermique (présence de défauts, fortes températures, temps de recuit long). L'irradiation à des températures modérées peut induire la cristallisation car l'énergie cinétique des ions qui est transférée au réseau contribue à la réduction de la barrière énergétique de la cristallisation. En outre, les modèles développés pour des nanoparticules suggèrent que les cristallites formés sous irradiation sont plus homogènes.

Nous étudions l'effet d'une irradiation à des températures modérées sur les propriétés magnétiques de films ultra-minces de W(4 nm)/$Co_{20}Fe_{60}B_{20}$(0.7 nm)/MgO/W(1 nm)/Ta(2 nm)/Ru(3 nm) intégrant dans l'état initial une couche amorphe de CoFeB. Pour étudier l'évolution de l'anisotropie magnétique, nous utilisons des mesures de résonance ferromagnétique (FMR, ferromagnetic resonance). La Figure 6.1a montre l'évolution du champ d'anisotropie effectif $H_{K_{\text{eff}}}$ en fonction de la fluence pour une irradiation à 250°C. La Figure 6.1a montre une augmentation de $H_{K_{\text{eff}}}$ lorsque la fluence augmente pour atteindre la même valeur qu'un pur recuit thermique. Ceci indique qu'une cristallisation complète peut être obtenue par irradiation a des températures modérées et avec des temps de traitement ultra-rapides (<5 minutes).

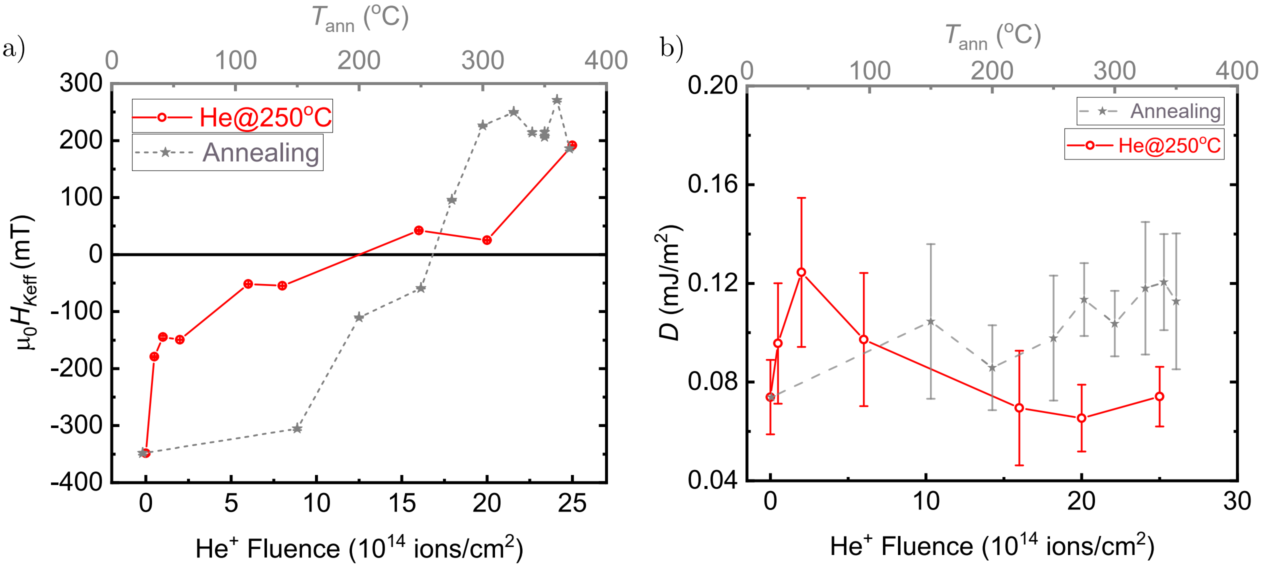

Fig. 6.1: Propriétés magnétiques de W/CoFeB/MgO sous irradiation He$^+$ à des températures modérées | a) Champ d'anisotropie effectif et b) Constante de DMI de la couche mince de W(4 nm)/$Co_{20}Fe_{60}B_{20}$(0.7 nm)/MgO/W(1 nm)/Ta(2 nm)/Ru(3 nm) sous irradiation par des ions He$^+$ à 250°C en fonction de la fluence (rouge) et recuit en fonction du temperature (gris).

Nous étudions également l'évolution de la constante DMI, qui est importante pour le mouvement de parois magnétiques, en utilisant des mesures de diffusion de la lumière Brillouin (BLS, Brillouin light scattering). L'évolution de la constante DMI pour une irradiation à 250°C et un recuit est représentée sur la Figure 6.1b. Lorsque que la fluence augmente, la constante DMI augmente d'abord avant de diminuer progressivement à des fluences plus importantes, signalant un mélange complet des interfaces à forte fluence. Cette transition n'est pas observée pour le recuit, qui n'indique qu'une faible augmentation de la constante DMI.

Les résultats de la Figure 6.1 indiquent donc que la cristallisation par irradiation de films minces amorphes de W/CoFeB/MgO peut répondre à l'exigence de grandes valeurs d'anisotropie et à des temps de traitement beaucoup plus faibles.

Par la suite, nous montrons que nous pouvons obtenir plus d'informations sur le désordre à l'échelle nanométrique des échantillons cristallisés par irradiation en étudiant le mouvement des parois magnétiques.

Dans le cadre de cette étude, nous étudions le mouvement des parois magnétiques dans trois films ultraminces de W(4 nm)/$Co_{20}Fe_{60}B_{20}$(1 nm)/MgO(2 nm)/Ta(3 nm) cristallisés différemment : par recuit à 400°C pendant 1h, et par irradiation à $T < 250$°C à deux fluences He$^+$ différentes, dénommés respectivement traitement d'irradiation 1 et traitement d'irradiation 2. Ces traitements ont été choisis pour disposer d'échantillons présentant les mêmes propriétés magnétiques mais des profils de désordre à l'échelle nanométrique différents. Cela nous permet non seulement de déterminer si la cristallisation induite par irradiation donne lieu à un plus faible désordre, mais nous offre également une occasion unique d'étudier indépendamment les effets du désordre sur la propagation de parois magnétiques sans modifications des propriétés magnétiques.

Afin d'étudier le mouvement des parois magnétiques, nous utilisons la microscopie Kerr. Les images de l'expansion de la paroi magnétique pour différents champs magnétiques dans les trois échantillons cristallisés sont présentées sur la Figure 6.2a. Ici, les champs magnétiques permettent d'étudier le mouvement des parois magnétiques dans le régime de reptation qui est dominé par le désordre et l'activation thermique. Les images de la Figure 6.2a montrent un comportement radicalement différent pour les trois échantillons cristallisés. Pour l'échantillon recuit, l'expansion de la paroi magnétique est de type fractal, avec de nombreux sites de piégeages forts, alors que dans les deux échantillons irradiés, l'expansion de la paroi magnétique est lisse, avec très peu de sites de piégeages forts. Ce résultat est une indication d'un désordre beaucoup plus faible dans les échantillons cristallisés par irradiation.

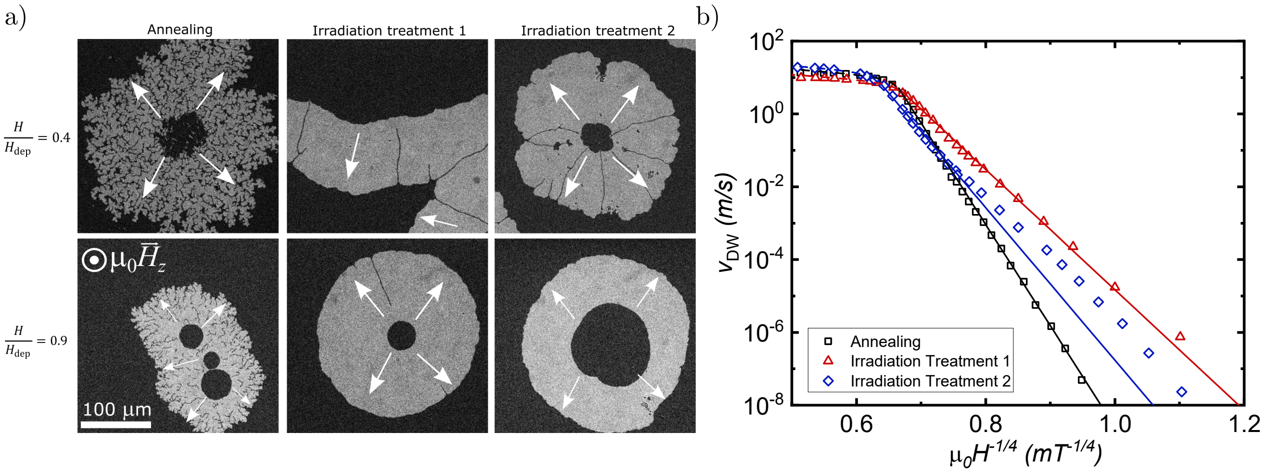

Fig. 6.2: Mouvement de la paroi dans des couches minces cristallisées par recuit thermique et irradiation en température | a) Images de microscopie Kerr de l'expansion d'une paroi magnétique dans trois échantillons W(4 nm)/$Co_{20}Fe_{60}B_{20}$(1 nm)/MgO(2 nm)/Ta(3 nm) cristallisés par recuit (à gauche), traitement d'irradiation 1 (au milieu), et traitement d'irradiation 2 (à droite) à des champs $H/H_{\text{dep}} = 0.4$ et proche de la transition de dépiégeage à $H/H_{\text{dep}} = 0.9$ où H_{dep} est le champ de dépiégeage. Les zones gris clair indiquent la zone où la paroi s'est déplacé pendant l'application du champ. Les flèches blanches indiquent la direction de mouvement de la paroi. b) Vitesse de parois magnétique en fonction du champ magnétique appliqué dans les couches cristallisées, dans la régime de reptation de parois. L'adéquation avec la loi de reptation est montrée par la ligne pleine, et l'adéquation avec la loi de dépiégeage est montrée par la ligne pointillée.

Cette amélioration est encore plus visible en comparant les vitesses de parois magnétiques, comme on peut le voir sur la Figure 6.2b. A faible champ, dans le régime de reptation, nous observons une augmentation de plusieurs ordres de grandeur de la vitesse de propagation de paroi magnétique dans les films cristallisés par irradiation. Il s'agit d'une preuve supplémentaire que, malgré des propriétés magnétiques similaires, le traitement par irradiation donne lieu à un désordre plus faible favorable au mouvement de paroi magnétique.

Dans la suite, nous nous intéressons à l'effet du mélange aux interfaces induit par l'irradiation à température ambiante dans des couches pré-cristallisées par recuit thermique.

Dans cette étude, nous examinons comment les propriétés magnétiques, la dynamique des parois magnétiques et le désordre des films ultraminces pré-cristallisés W(4 nm)/$Co_{20}Fe_{60}B_{20}$(1.1 nm)/MgO(2 nm)/Ta(3 nm) évoluent sous irradiation à température ambiante. Nous observons d'abord une diminution progressive de $H_{K_{\text{eff}}}$ et de la constante DMI avec l'augmentation de la fluence He^+ en raison de l'augmentation du mélange des interfaces. Nous nous concentrons ensuite sur la vitesse des parois magnétiques. La Figure 6.3 montre la vitesse des parois magnétiques dans les échantillons irradiés lorsque la fluence augmente.

Nous observons que le mélange aux interfaces a un impact sur la vitesse des parois magnétiques au-dessus du champ de dépiégeage. La vitesse atteint un plateau - lié aux effets bidimensionnels et au désordre, proportionnel au DMI - qui est réduit en hauteur et en largeur avec l'augmentation de la fluence. La transition de dépiégeage elle-même n'est que faiblement affectée. Dans le régime de reptation, la vitesse est augmentée aux champs les plus faibles. Pour comprendre ces résultats, nous

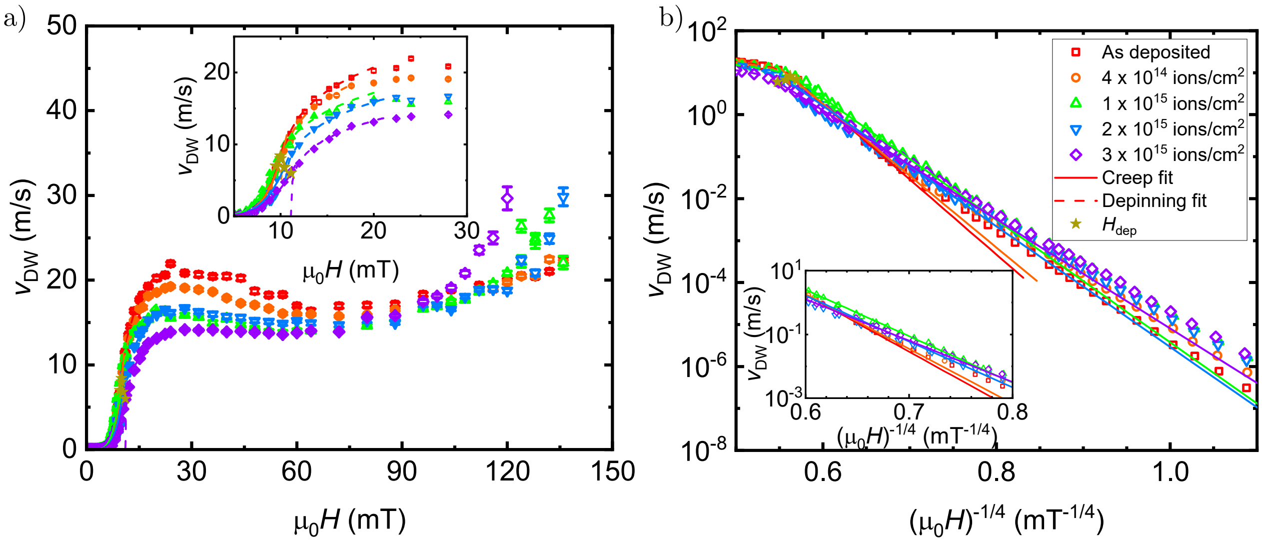

Fig. 6.3: Vitesse de la paroi dans des couches irradiées de W/CoFeB/MgO pré-cristallisés | a) Courbe de vitesse de paroi dans des films minces W(4 nm)/Co$_{20}$Fe$_{60}$B$_{20}$(1.1 nm)/MgO(2 nm)/Ta(3 nm) progressivement irradiés par des ions He$^+$. L'encart montre un zoom qui indique l'adéquations avec les lois de reptation et dépiégeage, indiquées respectivement par des lignes pleines et pointillées. Les champs de dépiégeage sont représentés par des étoiles dorées. b) Données de (a) avec des axes remis à l'échelle pour montrer le comportement de la loi de reptation. Les données sont représentées entre 0,7 et 16,0 mT. L'encart contient un zoom de la transition de dépiégeage entre 2,4 et 7,7 mT.

analysons plus en détail le mouvement des parois magnétiques à l'aide d'un modèle analytique pour étudier les propriétés de piégeage des parois magnétiques à l'échelle nanométrique, comme pour les échantillons cristallisés par irradiation. Nous constatons que l'irradiation ne réduit que la barrière d'énergie de reptation, mais que les autres paramètres de piégeage restent relativement inchangés, ce qui indique que l'irradiation à température ambiante ne modifie pas de manière significative la structure cristalline des films minces W/CoFeB/MgO pré-cristallisés. Cela suggère également que la diminution de la hauteur du plateau est causée par la réduction du DMI, et nous pouvons établir un lien entre la barrière d'énergie de reptation et la réduction de $H_{K_{\text{eff}}}$ avec l'irradiation.

Dans la suite, nous nous focalisons sur la réduction du désordre extrinsèque. Les défauts de bord dans une piste lithographiée peuvent provoquer un piégeage important des parois magnétiques, ce qui est un frein majeur pour les applications. Les défauts des bords sont introduits par les procédés de nanofabrication, en particulier la gravure physique par faisceaux d'ions Ar$^+$. Ce piégeage sur les bords domine pour les films où le piégeage intrinsèque est faible, comme dans le cas de W/CoFeB/MgO. En particulier, la paroi magnétique se propageant dans une piste acquière une courbure significative du à un ralentissement de sa vitesse sur les bords. Dans cette étude, nous testons l'effet sur le mouvement de paroi magnétique d'une irradiation locale aux bords de microfils fabriqués par lithographie UV à l'aide d'un faisceau d'ions He$^+$ focalisé (FIB, focused ion beam) et par irradiation au travers d'un masque. Les résultats de l'irradiation en utilisant un FIB sont présentés sur la Figure 6.4.

La vitesse des parois magnétiques est comparée à la situation d'un film non structuré (noir, désigné comme réservoir sur la Figure 6.4a). Dans un fil sans irradiation aux bords, les défauts de bord affectent fortement la vitesse des parois magnétiques. À faible champ, la vitesse dans le fil non irradié s'éloigne du comportement de reptation attendu dans un film non structuré de plusieurs ordres de grandeur, ce qui est une signature d'un fort piégeage des bords.

Nous vérifions ensuite l'effet de l'irradiation des bords en utilisant deux fluences He$^+$ différentes, F$_1$ et $F_2 > F_1$. Dans le cas de F_1, le bord irradié est toujours ferromagnétique et présente une anisotropie magnétique perpendiculaire réduite. Comme le montre la Figure 6.4a, (bleu clair), la vitesse de la paroi magnétique est améliorée d'un facteur 2, mais présente toujours une vitesse inférieure à celle du film non structuré. L'effet des défauts de bord est également visible sur la Figure 6.4b, qui montre

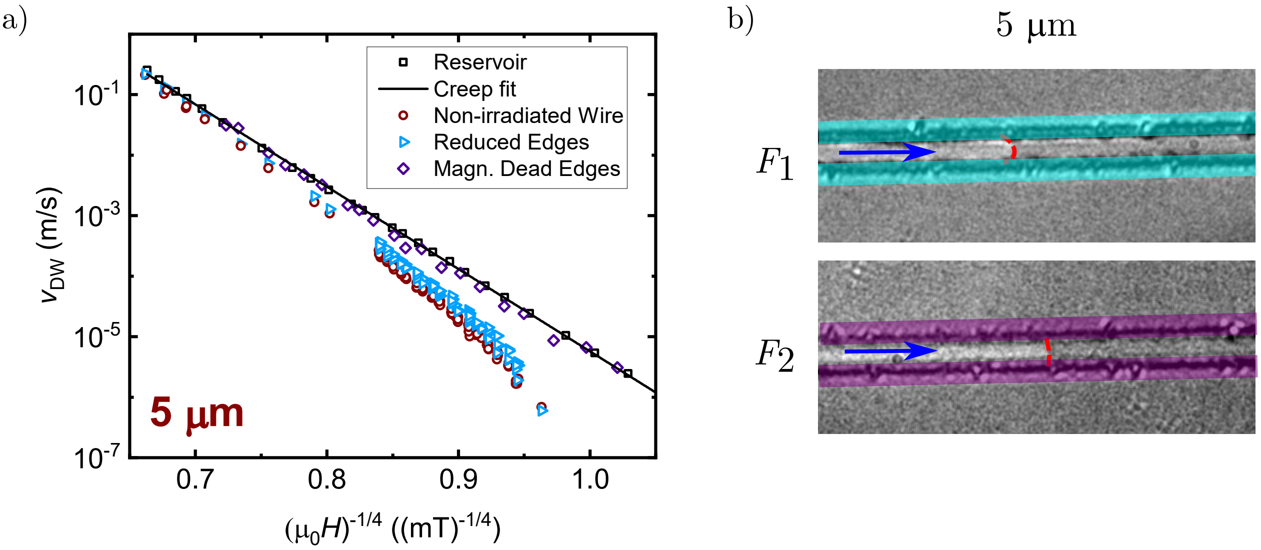

Fig. 6.4: Augmentation de la vitesse de parois après irradiation par He$^+$ en bords de fils | a) Vitesse d'une paroi magnétique en fonction du champ appliqué dans une structure de W(4 nm)/$Co_{20}Fe_{60}B_{20}$(1.1 nm)/MgO(2 nm)/Ta(3 nm) dans differentes situations; le réservoir, un fil pas irradié aux bords, un fil irradié aux bords avec F_1 (bords réduit), et un fil irradié aux bords avec F_2 (bords magnétiquement morts). La largeur du fil est 5 µm. Le réservoir indique la vitesse de la paroi dans un film non structuré. Le ligne noir indique l'adéquation avec le loi de reptation. b) Images de microscopie Kerr d'une paroi qui traverse un fil de largeur 5 µm où les bords sont irradiés avec F_1 (haut) et F_2 (bas), indiqué par les zones blues et violets. La courbure de la parois est indiqué par une ligne pointillée rouge. La direction du mouvement de la paroi est indiqué par la flèche bleue.

des images de microscopie Kerr de la paroi magnétique lors de son déplacement dans la zone irradiée. La courbure de la paroi magnétique est toujours présente mais moins importante que pour la piste non irradiée. Dans le cas de F_2, les bords irradiés sont devenus non magnétiques. Dans ce cas, la vitesse de propagation de paroi est similaire à celle du film non structuré et la courbure de parois a disparu, indiquant que les effets de piégeage en bord de piste sont réduits. Nous montrons aussi que le piégeage des bords peut également être éliminé par irradiation d'un film continu au travers d'un masque.

Finalement, pour montrer que le champ d'application de l'irradiation He$^+$ dans le domaine de la spintronique est vaste, nous mentionnons brièvement d'autres applications possibles. Ces résultats ont été obtenus grâce à des collaborations au sein du projet MagnEFi. Nous nous concentrons spécifiquement sur deux effets : l'AOS dans les bicouches artificielles de Co/Gd et la magnétostriction dans des multicouches de Ni/Fe. Dans notre première étude, nous induisons un mélange d'interfaces dans des films de Ta(4 nm)/Pt(4 nm)/Co(1 nm)/Gd(3 nm)/TaN(4 nm), ce qui, comme le montre la Figure 6.5a, entraîne une réduction de 30% de la fluence seuil du AOS. Dans une autre étude, nous montrons également que la valeur initialement négative de la magnétostriction λ_s d'une multicouche NiFeCr(5 nm)/[Ni(2 nm)/Fe(2 nm)]$_8$/Ta(4 nm) peut être progressivement réduite et changer de signe en augmentant la fluence comme le montre la Figure 6.5b. De plus, il est possible d'obtenir une magnétostriction nulle, une propriété importante pour les capteurs magnétiques.

De manière général, ces résultats montrent que l'irradiation par He$^+$ a fort potentiel pour manipuler précisément les propriétés magnétiques dépendant des interfaces dans le domaine de la spintronique.

En conclusion, dans cette thèse nous montrons que la cristallisation induite par irradiation permet d'obtenir des propriétés magnétiques similaires à un pur recuit thermique mais avec des temps et des températures de traitement plus faibles et un désordre réduit. En outre, nous montrons que dans ces films cristallisés par irradiation, les vitesses de parois sont plus importantes et l'analyse des régimes de reptation nous permet d'accéder aux paramètres du désordre. Nous montrons aussi que l'irradiation

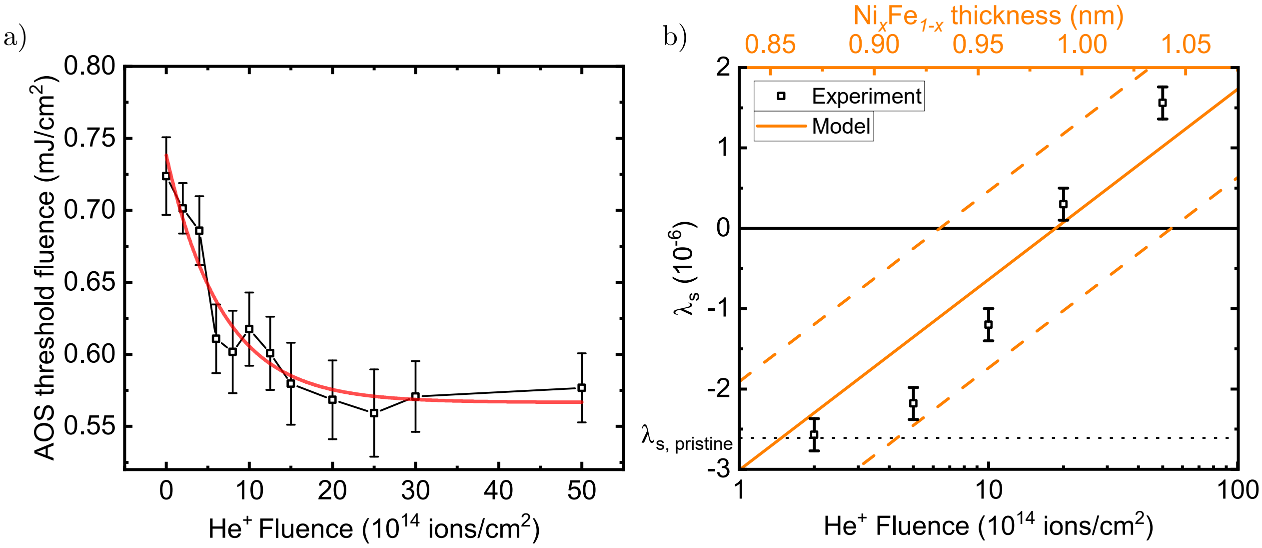

Fig. 6.5: Effet de l'irradiation par des ions He$^+$ sur l'AOS et la magnétostriction | a) Energie de seuil de l'AOS dans des couches Ta(4 nm)/Pt(4 nm)/Co(1 nm)/Gd(3 nm)/TaN(4 nm) en fonction de la fluence He$^+$. La ligne rouge est un guide pour l'œil. b) Constante de magnétostriction λ_s mesurée dans des multicouches NiFeCr(5 nm)/[Ni(2 nm)/Fe(2 nm)]$_8$/Ta(4 nm) en fonction de la fluence He$^+$ et calculée avec un modèle pour l'épaisseur d'un alliage NiFe aux interfaces (orange). Les lignes oranges en pointillés dénotent la variation de λ_s prise en compte dans le modèle. La ligne noire en pointillés dénote la valeur de λ_s dans l'échantillon vierge.

à température ambiante d'échantillons déjà cristallisés permet de contrôler le mélange aux interfaces. Ce mélange affecte considérablement le mouvement des parois magnétiques, dû à une modification des propriétés magnétiques (anisotropie, DMI), sans impact significatif sur le désordre intrinsèque. Par la suite, nous démontrons qu'une irradiation locale des bords de micro-fils lithographiés peut améliorer de manière significative la vitesse des parois magnétiques en supprimant les défauts de bord. Finalement, nous montrons que l'irradiation par des ions He$^+$ peut modifier le AOS dans des couches ferrimagnétiques de Co/Gd et la magnétostriction dans des multicouches Ni/Fe, ce qui montre que l'irradiation par des ions He$^+$ a un large champ d'application dans le domaine de la spintronique.